UNIMORE
UNIVERSITÀ DEGLI STUDI DI
MODENA E REGGIO EMILIA

UNIVERSITÀ DEGLI STUDI
DI MODENA E REGGIO EMILIA

Dottorato di ricerca in
"Ingegneria industriale e del territorio"

Ciclo XXXVIII

Maisotsenko cycle evaporative cooling of confined thermal environments: numerical modelling and energy simulation

Candidate: Michele Cossu

Tutor: Prof. Alberto Muscio

First Co-Tutor: Prof. Nicolò Morselli

Second Co-tutor: Prof. Marco Puglia

Coordinator of the PhD Course: Prof. Alberto Muscio

Index

List of figures

List of tables

Abstract

The rising energy demand for summer cooling represents a critical challenge for the sustainability of the building sector. In this context, evaporative cooling systems based on the Maisotsenko cycle (M-cycle) have emerged as a promising technology capable of overcoming the theoretical wet-bulb temperature limit and approaching the dew point, ensuring a drastic reduction in electricity consumption compared to conventional vapor compression systems.

This research systematically addresses the modeling, experimental validation, and application analysis of M-cycle heat and mass exchangers. A substantial part of the work is dedicated to the development of predictive numerical models. Starting from a critical analysis of existing modeling approaches, an alternative numerical formulation is proposed. This approach enables a more rigorous description of coupled heat and mass transfer phenomena and allows accurate prediction of thermo-hygrometric gradients within the channels.

To overcome the high computational cost associated with physical simulations under dynamic conditions, an artificial neural network was implemented. The model demonstrates a strong capability in predicting intermediate operating conditions, enabling near-instantaneous evaluation of system performance at each time step and facilitating integration into building energy simulation tools.

The theoretical framework is supported by experimental investigations. Tests performed on commercial heat exchanger modules validate the numerical models and confirm the reliability of the theoretical predictions.

Finally, the effectiveness of the technology is assessed through real-world case studies across different climatic conditions. The results show that, through proper management of airflow rates and recirculation ratios, the energy efficiency ratio can be

optimized under varying operating conditions. The study demonstrates that M-cycle systems can provide high indoor comfort and air quality with minimal energy consumption in different climatic scenarios.

This work identifies the Maisotsenko cycle as a technologically mature solution, with strong potential for large-scale adoption in sustainable HVAC applications.

1. Introduction

The present chapter provides the contextual and technological framework underlying the development of evaporative cooling systems as an alternative to conventional mechanical refrigeration. It first outlines the global energy and environmental challenges associated with the growing demand for space cooling in the building sector. The text highlights the limitations of vapor compression technologies in terms of efficiency, sustainability, and environmental impact. The chapter then introduces evaporative cooling as a viable low-energy solution. It describes its fundamental thermodynamic principles, main system configurations, and recent technological advancements. Particular attention is devoted to the classification of direct, indirect, and regenerative evaporative systems. The discussion also covers the role of materials and design parameters that govern heat and mass transfer processes. This overview establishes the basis for the analytical and modeling approaches developed in the subsequent chapters.

1.1. Energy context and environmental concerns

The building sector is widely recognized as one of the main contributors to global energy consumption and greenhouse gas emissions. As of 2014, buildings accounted for more than 30% of global final energy consumption and 55% of final electricity demand. When upstream energy generation is considered, the sector is responsible for over one quarter of global energy-related CO_2 emissions [1]. In light of the record levels reached by energy-related CO_2 emissions in 2023, the decarbonization of the building sector has become a central objective of international energy and climate policies [2].

Within the overall building energy balance, space cooling represents the fastest-growing end-use. As early as 2016, it already accounted for nearly 20% of total electricity consumption in buildings worldwide. Projections indicate that, in the

absence of strong policy interventions, cooling-related energy demand could more than triple by 2050. This increase is driven by rising global temperatures, population growth, and urbanization as well as by improving living standards in emerging economies, particularly in regions characterized by hot climates [3].

This evolution creates a self-reinforcing feedback loop. Increasing ambient temperatures lead to higher demand for mechanical cooling, which in turn raises electricity consumption, still largely supplied by fossil fuel-based generation. At the same time, waste heat rejected into the environment further intensifies local thermal conditions. In densely populated urban areas, this contributes to the Urban Heat Island (UHI) effect, increasing nighttime temperatures by more than $1\,°C$ and amplifying cooling demand. Moreover, space cooling significantly contributes to peak electricity loads, placing additional stress on electrical grids and requiring costly investments in generation capacity and infrastructure [3].

These challenges highlight the urgent need for alternative cooling technologies that are not only energy-efficient but also capable of decoupling thermal comfort from intensive electricity consumption.

1.2. Conventional cooling systems

Vapor Compression Refrigeration (VCR) systems currently represent the dominant technology for air conditioning and refrigeration worldwide, owing to their scalability, reliability, and compactness. Their operation is based on a reverse Rankine cycle consisting of four main components: a compressor, a condenser, an expansion valve, and an evaporator [4]. Despite the availability of alternative technologies, such as absorption systems, vapor compression continues to meet the vast majority of space cooling demand in developed markets.

However, increasing energy consumption and growing environmental concerns are progressively challenging their long-term sustainability. One of the intrinsic

limitations of VCR systems lies in their reduced efficiency when simultaneously handling sensible and latent loads. In order to achieve dehumidification, the supply air must be cooled below its dew point to induce condensation, forcing the evaporator to operate at low temperatures and thereby reducing the system Energy Efficiency Ratio (EER) [5]. Under conditions characterized by low Sensible Heat Ratio (SHR), where latent loads dominate, post-heating of the supply air is often required to maintain comfort conditions, resulting in additional energy penalties and further efficiency losses [5].

These limitations become more pronounced in regions with high ambient temperatures. As outdoor temperature increases, the temperature gradient between the condenser and the surrounding air decreases, impairing heat rejection. Consequently, the compressor must operate at higher pressure ratios, leading to increased energy consumption and a higher risk of system shutdown due to excessive discharge temperatures [4].

In addition to performance limitations, vapor compression systems rely on refrigerants with significant environmental impacts. The transition from chlorofluorocarbons (CFCs) and hydrochlorofluorocarbons (HCFCs) to hydrofluorocarbons (HFCs) eliminated ozone depletion concerns but introduced high Global Warming Potential (GWP). As a result, international regulations such as the Montreal Protocol and EU Regulation No. 517/2014 are progressively phasing out high-GWP refrigerants, including R134a, R404A, and R410A. For instance, R404A and R410A are primary targets for replacement due to their high GWP values. Low-GWP alternatives, such as hydrofluoroolefins (HFOs) or natural refrigerants (e.g., hydrocarbons, CO_2), present technical challenges. Some of these fluids are flammable (such as R600a or R32), toxic, or require very high operating pressures (such as CO_2 in transcritical cycles) [6]. Moreover, refrigerant replacement can lead to a decrease in overall efficiency if the system is not adequately redesigned.

Recent international regulations, such as the Kigali Amendment to the Montreal Protocol, mandate a drastic phase-down of these fluids. This effort aims to prevent further global warming of up to 0.5 $°C$ by the end of the century [7].

It is therefore essential to consider that any solution reducing direct emissions but increasing electricity consumption may lead to higher overall environmental impact, typically evaluated through the Total Equivalent Warming Impact (TEWI). These limitations have stimulated research into alternative or hybrid cooling technologies. In this context, evaporative cooling has emerged as a promising solution, either as a standalone system or as an auxiliary technology. For instance, evaporative pre-cooling of condenser inlet air can reduce condensation temperature, thereby improving compressor efficiency, particularly in hot and dry climates [4]. More broadly, non-vapor compression technologies, such as indirect evaporative cooling, offer a pathway to reduce electricity consumption and dependence on high-GWP refrigerants [8], [9].

1.3. Evaporative cooling

Evaporative cooling systems represent a promising alternative to conventional vapor compression cycles, offering significantly lower energy consumption, particularly in hot and arid climates [10]. Unlike compression-based systems, they operate without compressors or synthetic refrigerants, using water as the working fluid. This eliminates environmental risks associated with refrigerant leakage, flammability, toxicity, and ozone depletion [6]. Moreover, since compressors are typically the most energy-intensive and failure-prone components of conventional systems [11], their absence results in lower capital and maintenance costs, as well as reduced peak electricity demand [12].

From a thermodynamic perspective, evaporative cooling exploits the natural tendency of water to evaporate when exposed to unsaturated air. The vapor pressure gradient between the water-air interface and the bulk airflow drives mass transfer [13], while

the associated latent heat of vaporization is extracted from the surrounding air. This process converts sensible heat into latent heat, resulting in a reduction of air temperature [14].

Over time, a variety of system architectures have been developed to adapt evaporative cooling to different climatic conditions and application requirements. These configurations are generally classified into three main categories [15]:

1. **Direct Evaporative Coolers (DEC)**, where air and water are in direct contact.
2. **Indirect Evaporative Coolers (IEC)**, where a separating surface prevents direct contact between the product air and water.
3. **Combined systems**, which integrate multiple stages or technologies.

The following sections examine the key design aspects of evaporative systems, with particular focus on heat and mass transfer materials and system configurations, leading to advanced concepts such as the Maisotsenko cycle.

1.3.1. Evaporative materials

Before examining specific evaporative system configurations, it is essential to analyze the role of materials used for heat and mass transfer. Material selection directly affects cooling effectiveness, water consumption, durability, and operating costs [16].

Efficient evaporative cooling relies on the ability to promote simultaneous heat and mass transfer between air and water. This performance depends on material properties such as wettability, water retention, capillary transport, and the ability to ensure uniform water distribution. While thermal conductivity and porosity remain relevant, several studies emphasize that practical aspects (e.g. mechanical strength, manufacturability, resistance to biological growth, and compatibility with surface treatments) often play a decisive role in real applications [17].

An ideal material must rapidly form and sustain a uniform water film, preventing the formation of dry spots that reduce the effective evaporation area. At the same time, it must maintain structural integrity under repeated wetting and drying cycles [16]. Both industrial practice and patent literature indicate that absorbent layers may be either hydrophilic or hydrophobic, provided that the surface is properly engineered to ensure effective wetting. These layers can be manufactured in various forms, including films, woven or braided structures, continuous or discontinuous fibers, particle beds, or hybrid configurations. Common materials include cellulose, fiberglass, organic and synthetic fibers, porous plastics, carbon-based fibers, polyesters, polypropylene, silicon-based fibers, and their combinations. Widely used spunbonded materials include polyolefins, polyethylene terephthalate (PET), and nylon [18].

Among these options, fibrous materials are the most adopted due to their high porosity and low cost. Synthetic fibers, particularly polymers such as polyester (e.g., Coolmax, Coolpass) and nylon, have demonstrated superior performance compared to traditional Kraft paper [19] , offering enhanced absorption, diffusion, and evaporation characteristics. Advanced synthetic structures, including next-generation fibers resembling basalt paper, exhibit exceptional capillary transport capabilities [20].

Natural fibers such as jute, loofah, palm fiber, and cotton have also been extensively investigated due to their availability and sustainability. Jute, for instance, has demonstrated high initial cooling efficiency, although it is prone to biological degradation and mold formation [21]. Luffa shows improved resistance to microbial growth despite slightly lower performance. Kraft paper remains the industrial benchmark for evaporative pads, although it typically exhibits lower performance and reduced durability compared to advanced synthetic materials [19], [22].

Beyond fibrous materials, alternative solutions have been explored to overcome structural or thermal limitations. Porous ceramics offer excellent hydrophilicity, high specific surface area, and strong water retention, reducing the need for continuous

irrigation. However, their brittleness, high weight, and production costs limit widespread application [17]. Metals such as aluminum and copper provide high thermal conductivity but exhibit poor natural wettability. Their effectiveness therefore depends on surface engineering techniques, including porous coatings, sintered capillary structures, or micro-structured geometries. Aluminum is generally preferred over copper due to its lower cost [17]. More recently, treated polymers have emerged as a promising solution. For example, materials such as PTFE can be rendered super-hydrophilic through laser etching and the deposition of silicon dioxide (SiO_2) nanoparticles, reducing the water contact angle to nearly zero. This significantly enhances wettability and improves combined evaporation and dehumidification performance [23].

The evaluation of these materials requires rigorous experimental characterization. To identify the most suitable solution, several laboratory tests are employed to quantify water transport capacity, evaporation rate, and long-term durability. It should be noted, however, that many characterization methods are strongly influenced by sample thickness. Parameters such as absorption time, capillary rise height, and diffusion speed may vary significantly with thickness, making comparisons between different materials unreliable unless proper normalization is applied or tests are conducted on samples of comparable dimensions [22].

The main testing methods adopted in the literature are described below:

- **Wicking Height Test**: This test measures the rate and height of water rising vertically through the porous structure due to capillary forces. Capillary rise results from the balance between liquid–solid adhesion forces and surface tension, which promote upward motion within the micro-channels formed by the fibers, and the opposing effect of gravity acting on the water column. The equilibrium height is reached when capillary pressure balances the fluid weight, while the rise velocity decreases rapidly, especially within the first few

minutes [22]. Experimentally, fabric samples are suspended vertically with their lower end immersed in a water reservoir, often colored to facilitate visualization. The advancement of the liquid front is recorded over time using image acquisition systems or graduated rulers [16], [22], [24]. Results have highlighted the superiority of technical synthetic fabrics. Materials such as Coolpass recorded rise heights exceeding 17 cm in 15 min. This performance is significantly better than the approximately 6 cm of Kraft paper [19]. Cellulose/PET composite fibers have also demonstrated excellent rapid wetting properties [24]. It has also been observed that capillary rise and diffusion results depend on environmental conditions. In particular, increasing ambient temperature reduces water surface tension, thereby decreasing the capillary force available for vertical transport. This emphasizes the importance of controlled testing conditions and accurate reporting of environmental parameters, especially for evaporative cooling applications that are strongly climate-dependent [22].

- **Diffusivity Test**: This test evaluates the ability of water to spread horizontally across a flat surface. A controlled amount of water is deposited at the center of a horizontally positioned sample, and the expansion of the wetted area is monitored over time, typically through image analysis [16], [19], [22]. Results show that some materials, despite good mechanical properties, exhibit poor immediate diffusion, retaining the droplet locally instead of spreading it. This behavior makes them unsuitable for vertical applications, where water may slide off before evaporating. In contrast, treated synthetic materials and composites can exhibit diffusion rates up to 300% higher than conventional paper materials [19].
- **Evaporation Rate Test**: This parameter directly affects the cooling capacity of the system. It is typically evaluated by monitoring the mass loss of a saturated

sample over time or by tracking the reduction of the wetted area until complete drying under controlled conditions [16], [22], [25]. Results indicate that technical fabrics such as Coolmax and cellulose/PET composites achieve evaporation rates comparable to or higher than wood pulp paper [25]. A high evaporation rate is generally associated with greater porosity and with structures that prevent the formation of excessively thick water films, which would otherwise introduce additional thermal resistance [19], [22].

- **Durability Test**: Resistance to degradation is essential to reduce maintenance costs and ensure long-term reliability. To assess this aspect, materials are subjected to stress tests including repeated wetting/drying cycles, immersion in saline solutions (to simulate salt accumulation or the use of liquid desiccants), or exposure to high-pressure water flows [23]. Tests confirm that synthetic fibers and non-wovens possess superior durability compared to natural materials like Kraft paper, which tend to deform or structurally degrade after repeated cycles [20]. Furthermore, super-hydrophilic coatings on plastic substrates have been shown to maintain their surface properties unaltered even after 48 hours of continuous high-speed washing [23].

Overall, material selection cannot be based on a single parameter but must consider a balance between capillary transport, diffusion, evaporation rate, structural durability, and cost. In this context, synthetic materials and advanced composites are emerging as the most promising solutions for high-efficiency evaporative cooling applications.

1.3.2. Direct evaporative cooling (DEC)

Direct Evaporative Cooling (DEC) systems represent the simplest configuration among evaporative cooling technologies. In this architecture, a single airstream flows through a porous medium saturated with water, enabling direct contact between air and liquid (Figure 1.1). The evaporation process extracts latent heat from the air,

resulting in a simultaneous reduction in dry-bulb temperature and an increase in humidity. Under ideal conditions, the process approaches the inlet wet-bulb temperature, which represents its theoretical lower limit. The transformation can be considered approximately adiabatic, assuming the enthalpy contribution of the make-up water is negligible.

From a construction perspective, DEC systems are mechanically simple, typically consisting of a fan, ductwork, a wetted medium, and a water distribution system. However, the direct interaction between air and water introduces important limitations. The water source may contain contaminants, and the supply air may carry droplets containing pathogens, such as Legionella [26]. For this reason, these systems are generally unsuitable for occupied indoor environments unless strict maintenance protocols are enforced. Additionally, droplet carryover can pose risks in applications involving sensitive equipment. Another limitation arises from the increase in air humidity, which may lead to thermal discomfort if indoor relative humidity exceeds recommended levels (e.g., 50 %).

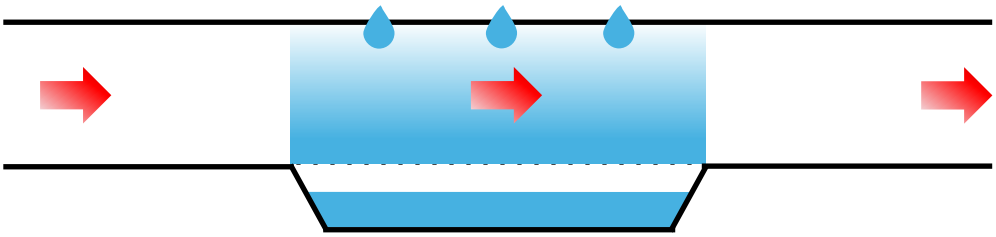

Figure 1.1. Schematic representation of a direct evaporative cooling configuration.

This configuration offers considerable flexibility in material selection, as the evaporative medium is directly exposed to the airflow. A wide range of organic materials has been investigated, including palm fibers [21], [27], aspen [28], [29], coconut [29], jute [21], and eucalyptus [30], as well as rigid structures assembled from such materials [31]. However, these solutions are often affected by biological degradation and mold formation [21].

To increase the air–water contact surface, granular media such as plastic pellets, rice husk [32], volcanic tuff, and pumice stones [33] have been explored. More advanced solutions include synthetic polymer fibers [34], as well as rigid inorganic materials such as pottery cylinders [35] and porous bricks [36], where controlled porosity is essential to ensure effective water transport to the air interface. Hybrid approaches have also been proposed, such as the incorporation of biochar into concrete matrices to enhance absorbency [37]. Despite these alternatives, the most widely adopted commercial solutions remain structured pads made of impregnated cellulose or PVC [38], consisting of corrugated sheets arranged to form tortuous airflow channels [39]. This configuration enables precise control of geometric parameters such as channel geometry [40], flute angle, and depth [41], allowing optimization of the trade-off between pressure drop and cooling efficiency.

Numerous studies have evaluated the performance of alternative materials in comparison with commercial media, highlighting the trade-offs between thermal efficiency, durability, and hydraulic resistance. For example, Jain and Hindoliya [29] demonstrated that material selection significantly affects performance even in low-cost systems. Similarly, comparisons involving recycled HDPE pellets and rice husk [32], showed that, although rice husk provides superior cooling, it suffers from poor durability. Granular media generally exhibit higher pressure drops than structured pads, resulting in increased operating costs. Comparable trends were observed for pumice stones [33], where finer granulometry enhances cooling performance but leads to excessive hydraulic resistance.

Air velocity and water flow rate are key operational parameters. Increasing air velocity typically reduces wet-bulb effectiveness while increasing pressure losses. Similarly, excessive water supply can increase flow resistance, negatively affecting performance [33]. Dynamic studies [42] have shown that mass transfer coefficients peak immediately after water injection ceases, when the medium remains fully wetted but

aerodynamic resistance is minimized. This behavior highlights the importance of optimizing water distribution strategies, including intermittent supply.

Water consumption is another critical aspect. To address freshwater scarcity, alternative sources such as seawater have been investigated. Kabeel and Bassuoni [43] demonstrated that seawater use can reduce freshwater demand, although it leads to higher supply temperatures and potential salt deposition, which may reduce effective evaporation area and accelerate material degradation.

Due to their simplicity and low cost, DEC systems are widely used in agricultural storage [44], [45], greenhouses [46], and livestock facilities [42], as well as in industrial contexts such as data center pre-cooling [47].

For performance prediction, exponential models based on log-mean temperature difference are commonly used, assuming the inlet wet-bulb temperature as the reference condition for the heat exchange surface. These models enable estimation of wet-bulb effectiveness as a function of mass flow rate [48] and have been applied to both conventional Celdek pads [49] and unconventional media [50]. However, their accuracy may decrease under varying operating conditions [51]. Similar formulations have also been extended to mass transfer modeling based on vapor density [29], [34], [35].

In summary, DEC systems are particularly suitable for applications where humidity control is not critical and where supply temperatures below the wet-bulb limit are not required. Design optimization typically involves maximizing frontal area to reduce air velocity, thereby increasing residence time and improving cooling effectiveness while limiting pressure losses. Additionally, minimizing water flow to the required evaporation rate and adopting intermittent supply strategies can further enhance system performance.

1.3.3. Indirect evaporative cooling (IEC)

Indirect evaporative cooling (IEC) systems were developed to overcome the limitations of direct evaporative cooling. In these systems, a heat exchanger separates two airstreams: the primary (product) air, which is supplied to the conditioned space, and the secondary (working) air, which is used to reject heat. This separation prevents direct contact between water and supply air, eliminating the risk of droplet carryover and avoiding humidity increase. As a result, IEC systems are better suited for indoor environments and applications requiring strict humidity control.

Depending on the configuration, IEC systems can be classified as dry-surface or wet-surface systems [52]. In dry-surface configurations, evaporation occurs upstream of a sensible heat exchanger, where the secondary air is cooled and humidified before exchanging heat with the primary air. In wet-surface configurations, heat and mass transfer occur simultaneously within the heat exchanger itself, as water is introduced directly into the secondary channels. In this case, evaporation absorbs heat from both the working air and the separating wall, enabling indirect cooling of the primary airflow through conduction. A schematic representation of the two types of IEC is shown in Figure 1.2.

As in conventional heat exchangers, various flow arrangements can be adopted, including co-current, counter-current, and cross-flow configurations. Although IEC systems provide purely sensible cooling and are therefore particularly suitable for comfort applications, their cooling effectiveness is generally lower than that of direct systems.

A wide range of materials has been proposed for IEC applications, including porous fibers, carbon-based materials, metal foams, ceramics, and zeolite structures [17]. The most common geometry consists of parallel plates arranged vertically or horizontally [53], often in cross-flow configuration [54]. Surface design plays a critical role in

performance: flat plates promote wettability but may limit heat transfer and structural stiffness, while enhanced geometries can improve heat transfer at the expense of uniform water distribution [55]. Orientation also affects performance, as horizontal configurations may lead to the formation of dry spots in the wet channels, reducing evaporation efficiency [56].

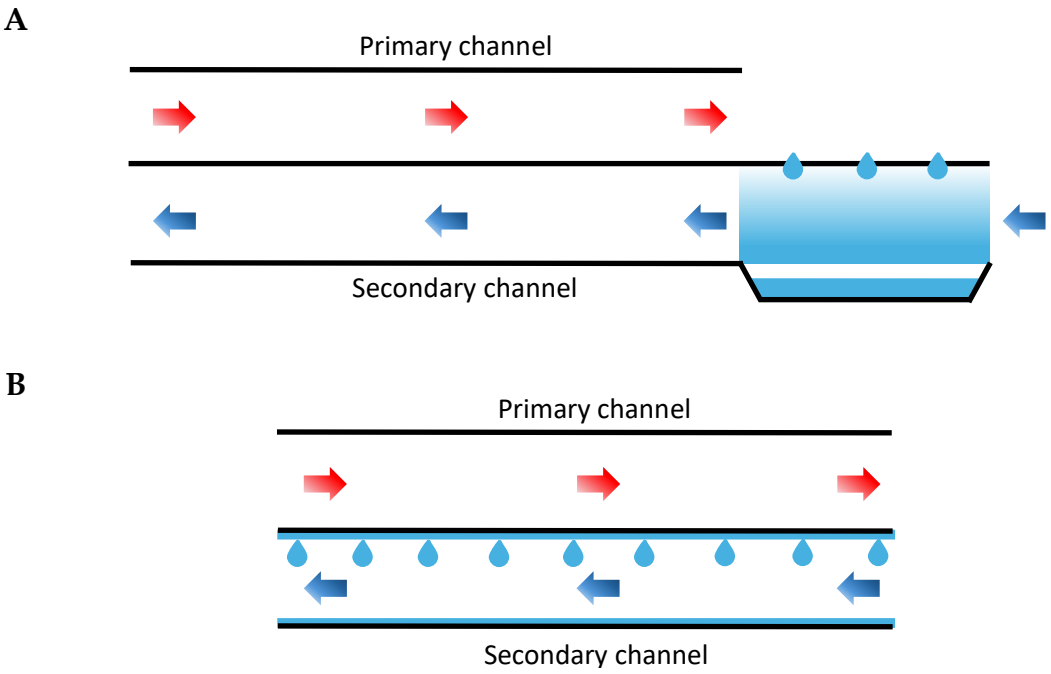

Figure 1.2. Schematic representation of indirect evaporative cooling in counter-current configuration: dry-surface IEC (A) and wet-surface IEC (B).

Water distribution strategies significantly influence system performance. In dry-surface systems, spray-based humidification can replace traditional evaporative pads. Studies have shown that counter-current spray injection relative to the working airflow improves wet-bulb effectiveness compared to co-current configurations [57]. In wet-surface exchangers, porous materials can retain water within the structure [58], enabling stable performance even under intermittent water supply conditions [59].

1.3.4. Combined system IEC-DEC

The main limitation hindering the widespread adoption of conventional indirect evaporative cooling systems is their relatively low cooling capacity. In single-stage configurations, the achievable temperature reduction is thermodynamically bounded by the inlet air wet-bulb temperature. This constraint often results in insufficient performance, particularly in humid climates, and may not justify the additional cost associated with the heat exchanger. To overcome this limitation, a two-stage configuration can be employed, combining an IEC with a downstream DEC stage [52]. Figure 1.3 shows a schematic representation of the IEC-DEC two-stage evaporative system.

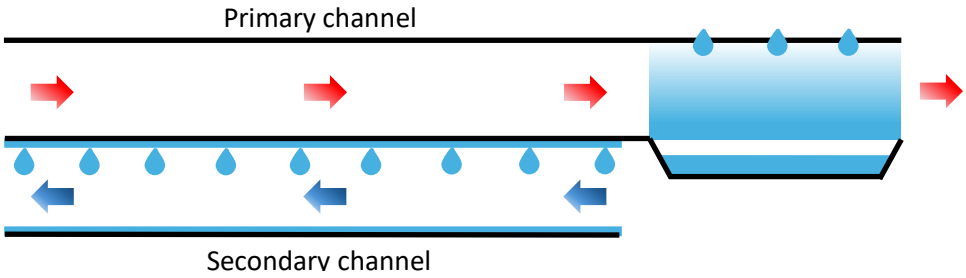

Figure 1.3. Schematic representation of two-stage evaporative cooling (IEC-DEC) configuration.

In this arrangement, the product air first undergoes sensible cooling within the indirect exchanger, reducing its dry-bulb temperature while maintaining constant specific humidity. This pre-cooling process lowers both the air enthalpy and its corresponding wet-bulb temperature. Subsequently, the pre-cooled air enters the direct evaporative stage, where it is further cooled through adiabatic humidification. Since the wet-bulb temperature at the inlet of the second stage is now lower than that of the ambient air, the system can deliver supply air at temperatures below the theoretical limit achievable by standalone direct or conventional indirect evaporative systems.

1.3.5. M-cycle

The most advanced development in evaporative cooling technology is represented by the Maisotsenko cycle (M-cycle) [60], which introduces a fundamental modification to conventional indirect evaporative cooling. While maintaining the distinction between dry and wet channels, the key innovation lies in a regenerative flow arrangement, in which the working air is not an independent stream but a fraction of the air exiting the dry channel, diverted and redirected into the wet channel.

In this configuration, the primary airflow undergoes sensible cooling along the dry channel. A portion of this pre-cooled air is then extracted and used as working air in the wet channel, where it is humidified. Thanks to this configuration, the working air enters the wet channel at the lowest temperature achieved in the primary channel, increasing overall heat transfer. The latent heat required for evaporation is extracted both from the working air and from the separating wall. This mechanism indirectly cools the primary airflow through conduction across the wall.

A key characteristic of this system is that the temperature of the working air at the wet channel inlet corresponds to the dry channel outlet temperature. As a result, increasing the length of the heat exchanger progressively lowers the working air temperature, maintaining a favorable thermal gradient along the device. Since cooling in the dry channel occurs at constant humidity, the theoretical limit approaches the inlet air dew point, enabling performance beyond the wet-bulb limitation of conventional evaporative systems.

Recent literature highlights a growing interest in dew-point evaporative cooling systems [61], [62], which, despite their increased complexity, offer significantly improved thermodynamic performance [63]. The most commonly studied configurations involve parallel plate geometries in vertical or horizontal arrangements [64] , with various combinations of counter-flow [65] or cross-flow [66] air streams and

different water flow orientations [67]. Materials and water injection systems remain similar to those of conventional indirect systems [68], although several studies have proposed the use of mesh screens derived from cooling tower technologies [69].

In cross-flow configurations, particular attention has been devoted to the design of air diversion mechanisms from dry to wet channels. Proposed solutions include configurations where dry channels are partially blocked at a specific length, with intermediate perforations connecting to wet channels [70], [71], as well as designs featuring distributed perforations along the entire channel length [72] . More advanced geometries incorporate variable perforation patterns to optimize local mass flow distribution and enhance overall performance [73], [74].

The influence of surface treatments on wettability has been investigated through the development of finned heat and mass exchangers coated with polymeric and porous materials [75]. Other studies adapted ceramic pads for application inside the wet channels [76]. With the increasing research focus on M-cycle systems, more advanced geometric configurations have been proposed to intensify heat and mass transfer. These include corrugated plates with optimized geometries [77], [78], [79], the addition of internal baffles within dry channels to enhance convective heat transfer coefficients [80], [81], and the use of transverse ceramic tubes to strengthen the thermal coupling between dry and wet channels [82].

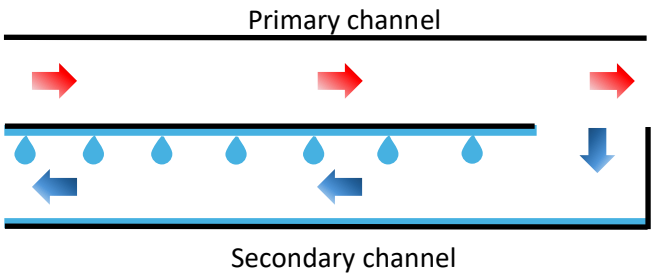

Figure 1.4. Schematic representation of a regenerative evaporative cooling system based on the M-cycle.

The growing geometric complexity of these solutions has also motivated the adoption of advanced manufacturing techniques. Additive manufacturing has been employed to enable the realization of intricate internal channel structures that are difficult to achieve with conventional fabrication methods [83]. In parallel, data-driven approaches based on machine learning have been introduced to provide generalized predictive capabilities of system performance, reducing the need for repeated, case-specific CFD simulations [84].

Despite these advancements, several fundamental aspects remain critical for system performance. Ensuring uniform wettability in the wet channel is essential to maximize evaporation. As in other evaporative systems, increasing air velocity generally reduces cooling effectiveness while increasing pressure losses. Channel spacing also plays a key role: narrower gaps enhance heat transfer but may significantly increase hydraulic resistance.

Finally, the working-to-inlet mass flow ratio represents a key design parameter. Increasing this ratio enhances the temperature reduction of the primary airflow by providing a larger mass flow for evaporation. However, it simultaneously reduces the airflow rate delivered to the conditioned space. Consequently, beyond a certain threshold, further increases in this ratio may lead to a reduction in overall cooling capacity, despite lower outlet temperatures.

2. Theoretical background

The analysis and modeling of evaporative cooling systems require a rigorous understanding of the fundamental principles of thermodynamics, fluid mechanics, and transport phenomena. Unlike systems operating with pure substances, evaporative cooling relies entirely on the interaction between two distinct chemical species: dry air and water vapor. Consequently, the working fluid must be treated as a multicomponent mixture, whose properties depend not only on temperature and pressure but also on its chemical composition.

In thermodynamics, a mixture is defined as a substance composed of two or more chemical species that are not chemically bonded to each other but are mixed at the molecular level. To accurately predict the behavior of such systems, it is essential to define the fundamental quantities that describe the composition, the thermodynamic state, and the constitutive laws governing the mixture.

This chapter establishes the physical and mathematical foundations necessary for the subsequent modeling. The discussion begins with the thermodynamic properties of ideal gas mixtures and the specific principles of psychrometry, which describe the state of moist air. Subsequently, the conservation laws for mass, momentum, and energy are introduced to describe the fluid flow and the associated transport mechanisms. Special attention is given to the dimensionless parameters that characterize the flow regimes and the heat and mass transfer rates. Finally, the analogy between heat and mass transfer is explored through the Lewis relation, and the numerical methods employed to solve the governing differential equations are presented.

2.1. Dalton's and Amagat's laws

When dealing with a gas composed of multiple substances, one refers to a gas mixture. Assuming that all components of the mixture obey the ideal gas law, the mixture itself

behaves as an ideal gas. To describe its behavior, it is necessary to consider the collective contribution of the individual components. In this framework, Dalton's and Amagat's laws provide the fundamental relations for the thermodynamic modeling of gas mixtures.

Dalton's law states that, in an ideal gas mixture, the total pressure p is equal to the sum of the partial pressures of each component p_i. The partial pressure p_i is defined as the pressure the i-th component would exert if it alone occupied the entire volume of the mixture at the same temperature

$$p = \sum_i p_i \qquad 2.1$$

Amagat's law, complementary to Dalton's, states that the total volume of a gas mixture V is equal to the sum of the partial volumes of the individual components V_i. The partial volume V_i is the volume the i-th component would occupy if it alone were subject to the total mixture pressure at the same temperature

$$V = \sum_i V_i \qquad 2.2$$

In both expressions, the index i denotes a specific component within the mixture.

These laws can be combined with the ideal gas equation to describe the state of each component in the mixture. When Dalton's law is applied

$$p_i\, V = n_i\, R\, T \qquad 2.3$$

or, when Amagat's law is considered

$$p\, V_i = n_i\, R\, T \qquad 2.4$$

In these expressions, n_i denotes the number of moles of the i-th component, which quantifies its amount of substance in the mixture, R is the universal gas constant and

T denotes the absolute temperature of the mixture. Summing the equations of state for all components yields

$$\sum_i p_i\, V = \sum_i p\, V_i = \sum_i n_i\, R\, T \qquad 2.5$$

By factoring out the global properties from the summation, one obtains

$$V \sum_i p_i = p \sum_i V_i = R\, T \sum_i n_i \qquad 2.6$$

Noting that the total number of moles of the mixture n corresponds to the sum of the moles of all individual components n_i

$$n = \sum_i n_i \qquad 2.7$$

The equation of state for the ideal gas mixture can then be expressed in the familiar form

$$p\, V = n\, R\, T \qquad 2.8$$

This final relation retains the same form as the equation of state for a single ideal gas. Consequently, an ideal gas mixture behaves thermodynamically like a single homogenous ideal gas, provided that the global properties are considered. This links the microscopic contributions of individual components i to the macroscopic behavior of the mixture.

2.2. Partial mass and density in ideal gas mixtures

The number of moles n of a substance is defined as the ratio between its mass m and its molar mass M

$$n = \frac{m}{M} \qquad 2.9$$

When applied to the i-th component of a gas mixture, this definition can be substituted into equation 2.3 to express the state equation in terms of mass

$$p_i\, V = \frac{m_i}{M_i}\, R\, T \qquad 2.10$$

From this relation, the partial mass of the i-th component can be expressed as

$$m_i = \frac{p_i\, V\, M_i}{R\, T} \qquad 2.11$$

The partial density of a species i, denoted as ρ_i, is defined as the mass of the species per unit volume of the mixture

$$\rho_i = \frac{m_i}{V} \qquad 2.12$$

By combining this definition with equation 2.11, the partial density can be expressed as

$$\rho_i = \frac{p_i\, M_i}{R\, T} \qquad 2.13$$

This section established the dependencies of the partial mass and density for components within an ideal gas mixture.

2.3. Total mass and density in ideal gas mixtures

The total mass of a gas mixture m is the sum of the partial masses m_i of all its components

$$m = \sum_i m_i \qquad 2.14$$

By substituting the expression for partial mass derived in equation 2.11, the total mass can be expressed in terms of the partial pressures p_i and molar masses M_i

$$m = \sum_i \frac{p_i\, V\, M_i}{R\, T} \qquad 2.15$$

Factoring out the global properties from the summation gives

$$m = \frac{V}{R\, T} \sum_i p_i\, M_i \qquad 2.16$$

The density of the mixture ρ, is defined as the ratio between the total mass of the mixture and its volume V. By dividing the expression above by the total volume, the mixture density is written as

$$\rho = \frac{1}{R\, T} \sum_i p_i\, M_i \qquad 2.17$$

This derives the fundamental relations for calculating the total mass and overall density of the mixture based on its constituents.

2.4. Relative humidity

In specific systems, a mixture may contain one or more components at temperatures below their critical point. Under these conditions, liquid and vapor phases can coexist in equilibrium, provided that the partial pressure of the component does not exceed its saturation pressure at the given temperature. The maximum amount of vapor the mixture can hold is determined solely by the system temperature and the corresponding saturation pressure.

The relative humidity φ quantifies how close the system is to this saturation limit. It is defined as the ratio of the actual vapor mass m_v to the saturation vapor mass $m_{v,sat}$ that would exist under the same thermodynamic conditions (same volume and temperature)

$$\varphi = \frac{m_v}{m_{v,sat}} \qquad 2.18$$

Here, and in the following formulations, the subscript v denotes quantities associated with the vapor, while the subscript v, sat refers to the vapor saturated conditions. Applying equation 2.11 to both the actual vapor mass and the saturation vapor mass yields

$$\varphi = \frac{p_v\, V\, M_v}{R\, T}\, \frac{R\, T}{p_{v,sat}\, V\, M_v} \qquad 2.19$$

Since the temperature, volume, molar mass, and the universal gas constant are identical for both states, these terms cancel out, reducing the expression to

$$\varphi = \frac{p_v}{p_{v,sat}} \qquad 2.20$$

This shows that relative humidity is equivalent to the ratio between the actual partial vapor pressure in the mixture and the saturation vapor pressure at the same temperature.

In an experimental context, measuring the relative humidity of moist air via dedicated sensors, and knowing the saturation vapor pressure (which is a known function of temperature), allows for the calculation of the vapor partial pressure

$$p_v = \varphi\, p_{v,sat} \qquad 2.21$$

This relation provides a straightforward method to determine the thermodynamic state of the vapor component within the mixture.

2.5. Saturation vapor pressure

As established in the previous section, the saturation vapor pressure $p_{v,sat}$, represents the maximum partial pressure that water vapor can exert in a mixture at a given temperature before condensation begins. From a thermodynamic perspective, this value corresponds to the pressure at which the liquid and gaseous phases of a substance coexist in equilibrium at a specific temperature.

According to the Gibbs phase rule, for a single-component system with two phases in equilibrium, the system possesses only one degree of freedom [85]. Consequently, the saturation pressure is a function of temperature only

$$p_{v,sat} = f(T) \tag{2.22}$$

While the fundamental relationship between vapor pressure and temperature is described by the Clausius-Clapeyron equation, in engineering applications and psychrometry, semi-empirical correlations are preferred for their balance of accuracy and computational efficiency. For water vapor in air, within the temperature ranges typical of evaporative cooling applications, the Magnus-Tetens formula with coefficients optimized by Murray [86] is one of the most widely adopted models

$$p_{v,sat}(T) = 610.78\, e^{\left(\frac{17.27\,T}{T+237.3}\right)} \tag{2.23}$$

In this expression, $p_{v,sat}$ is the saturation vapor pressure expressed in Pascals $[Pa]$, T is the temperature expressed in degrees Celsius $[°C]$ and the constants are empirical coefficients optimized for the liquid water phase.

This correlation enables the calculation of relative humidity and other psychrometric properties essential for modeling the performance of evaporative heat exchangers.

2.6. Specific humidity

In the study of moist air thermodynamics, it is essential to quantify the relative contributions of water vapor and dry air to the total mixture. While relative humidity provides a measure of how close the vapor phase is to saturation, it does not directly indicate the actual mass of vapor present relative to the dry air mass. To address this, the specific humidity ω is introduced.

Specific humidity is defined as the ratio between the mass of vapor m_v and the mass of dry air m_{da} contained in a given volume of moist air

$$\omega = \frac{m_v}{m_{da}} \qquad 2.24$$

Here, as in the following formulations, the subscript v denotes quantities associated with the vapor, while the subscript da denotes quantities associated with the dry air, i.e. the gaseous mixture not considered as vapor.

By applying the ideal gas law 2.11 to both the vapor and the dry air, the following expression is obtained

$$\omega = \frac{p_v\, V\, M_v}{R\, T}\, \frac{R\, T}{p_{da}\, V\, M_{da}} \qquad 2.25$$

Since both components occupy the same volume at the same temperature, and because the universal gas constant R is invariant, the equation simplifies to the ratio of molar masses and partial pressures

$$\omega = \frac{M_v}{M_{da}}\, \frac{p_v}{p_{da}} \qquad 2.26$$

According to Dalton's law 2.1, the partial pressure of dry air corresponds to the difference between the total pressure p of the mixture and the vapor partial pressure

$$p_{da} = p - p_v \qquad 2.27$$

The total pressure p can be measured experimentally using a manometer. The vapor partial pressure p_v, on the other hand, can be derived indirectly from measurements of temperature and relative humidity φ via equation 2.21. Substituting relations 2.21 and 2.27 into equation 2.26 yields a practical expression for specific humidity

$$\omega = \frac{M_v}{M_{da}} \frac{\varphi\, p_{v,sat}}{p - \varphi\, p_{v,sat}} \qquad 2.28$$

This formulation highlights that specific humidity can be fully determined from measurable macroscopic quantities: temperature, total pressure, and relative humidity.

2.7. Enthalpy

In thermodynamics, enthalpy represents the total energy content of a system, accounting for both its internal energy and the flow work required to displace its environment at constant pressure. In psychrometry, it is standard convention to define the specific enthalpy of moist air per unit mass of dry air, rather than per unit mass of the total mixture.

Assuming dry air behaves as an ideal gas, its enthalpy varies linearly with temperature. Referred to a reference temperature T_0, the total enthalpy of the dry air component I_{da} is expressed as

$$I_{da} = m_{da}\, c_{p,da}\, (T - T_0) \qquad 2.29$$

where $c_{p,da}$ is the specific heat of dry air at constant pressure.

The enthalpy of the vapor I_v includes both the latent heat of vaporization and the sensible heat associated with the superheating of the vapor. It can be written as

$$I_v = m_v \left[i_{lv} + c_{p,v} \left(T - T_0 \right) \right] \qquad 2.30$$

where i_{lv} is the latent heat of vaporization at the reference temperature T_0, and $c_{p,v}$ is the specific heat of vapor at constant pressure.

The total enthalpy of the moist air mixture I is obtained by summing the contributions of the dry air and the water vapor

$$I = I_{da} + I_v \qquad 2.31$$

By substituting equations 2.29 and 2.30 into equation 2.31 and dividing the total enthalpy by the mass of dry air, the specific enthalpy of moist air i is defined as

$$i = c_{p,da} \left(T - T_0 \right) + \omega \left[i_{lv} + c_{p,v} \left(T - T_0 \right) \right] \qquad 2.32$$

Here, ω is the specific humidity of the mixture as defined in the previous section. From the derivative of the specific enthalpy with respect to temperature, it is useful to define the specific heat of moist air, denoted as $c_{p,u}$. Consistent with the definition of specific enthalpy, this parameter is expressed per unit mass of dry air (not per unit mass of the total mixture). It represents the amount of heat required to raise the temperature of the mixture associated with 1 kg of dry air by 1 Kelvin.

By grouping the terms dependent on temperature in equation 2.32, the specific heat of moist air is given by

$$c_{p,u} = c_{p,da} + \omega \, c_{p,v} \qquad 2.33$$

Consequently, the simplified expression for the sensible enthalpy change of moist air becomes $di = c_{p,u} \, dT$.

2.8. Wet-bulb and dew-point temperatures

The thermodynamic limits of evaporative cooling processes are intrinsically linked to the psychrometric properties of moist air. Among these, the dry-bulb temperature, the wet-bulb temperature, and the dew-point temperature play a central role, as they define the thermal state of the humid air and the theoretical boundaries of achievable cooling.

The dry-bulb temperature (T_{db}) is the temperature of air measured by a standard thermometer freely exposed to the air stream and shielded from radiation. It represents the sensible thermal energy content of the air and is independent of its moisture content.

The wet-bulb temperature (T_{wb}) is defined as the equilibrium temperature attained by an air stream when it is brought into contact with a wetted surface under adiabatic conditions, allowing water to evaporate until thermodynamic equilibrium is reached. Physically, it represents the result of a balance between sensible heat transfer from the air and latent heat absorption associated with water evaporation. In direct evaporative cooling systems, the wet-bulb temperature constitutes the minimum achievable air temperature. As evaporation proceeds, the air temperature decreases while its humidity increases, and further cooling becomes impossible once saturation conditions corresponding to the wet-bulb temperature are reached. For this reason, the wet-bulb temperature has traditionally been regarded as the fundamental thermodynamic limit of conventional evaporative cooling technologies.

The dew-point temperature (T_{dp}) is defined as the temperature at which an air–water vapor mixture becomes saturated when cooled at constant humidity ratio. At this temperature, the partial pressure of water vapor equals the saturation vapor pressure, and any further reduction in temperature leads to condensation. Unlike the wet-bulb temperature, the dew-point temperature depends solely on the specific humidity of

the air and is independent of its dry-bulb temperature. In regenerative evaporative cooling systems, such as the M-cycle, the dew-point temperature emerges as the ultimate thermodynamic lower bound for air cooling.

2.9. Dimensionless numbers in internal flows

To generalize the analysis of fluid dynamics and simultaneous heat and mass transfer phenomena, it is essential to introduce specific dimensionless groups. These parameters arise naturally from the non-dimensionalization of the governing conservation equations, revealing the relative magnitude of the competing physical mechanisms that determine the flow regime and transport characteristics.

Consider the governing equations for the steady flow of an incompressible Newtonian fluid with constant properties. The momentum conservation equation (Navier-Stokes) can be expressed in vector form as

$$\rho\left(\underline{v}\cdot\nabla\underline{v}\right) = -\nabla p + \mu\,\nabla^2\underline{v} \qquad 2.34$$

Where ρ is the density, $\underline{v}$ is the velocity vector, p is the pressure, and μ is the dynamic viscosity. To render this equation dimensionless, characteristic reference scales are introduced: a characteristic length L_c (e.g., hydraulic diameter), a reference velocity v_c, and a reference dynamic pressure ($\rho\ {v_c}^2$). Introducing the dimensionless variables

$$\underline{v}^* = \frac{\underline{v}}{v_c} \qquad 2.35$$

$$\nabla^* = L_c\,\nabla \qquad 2.36$$

$$p^* = \frac{p}{\rho\ v_c^2} \qquad 2.37$$

equation 2.34 becomes

$$\underline{v}^* \cdot \nabla^* \underline{v}^* = -\nabla p^* + \frac{\mu}{\rho\, v_c\, L_c}\, \nabla^{*2} \underline{v}^* \qquad 2.38$$

The dimensionless coefficient appearing in the viscous term is recognized as the inverse of the Reynolds number (Re). This parameter represents the ratio of inertial forces to viscous forces. For internal flow through a duct, it is defined as

$$Re = \frac{\rho\, v_c\, L_c}{\mu} \qquad 2.39$$

The magnitude of Re governs the flow regime; values below approximately 2300 typically indicate a laminar regime.

Similarly, the energy conservation equation, neglecting viscous dissipation, is given by

$$\rho\, c_p \left(\underline{v} \cdot \nabla T\right) = k\, \nabla^2 T \qquad 2.40$$

Where c_p is the specific heat capacity and k is the thermal conductivity. To render this equation dimensionless, a dimensionless temperature T^* is defined based on a reference fluid temperature T_c and a characteristic constant temperature difference ΔT_c

$$T^* = \frac{T - T_c}{\Delta T_c} \qquad 2.41$$

Substituting dimensionless variables into equation 2.40 yields

$$\underline{v}^* \cdot \nabla^* T^* = \frac{k}{\rho\, c_p\, v_c\, L_c}\, \nabla^{*2} T^* \qquad 2.42$$

To relate the thermal field to the flow field, the coefficient on the right-hand side can be rearranged to explicitly factor out the Reynolds number

$$\frac{k}{\rho\, c_p\, v_c\, L_c} = \frac{\mu}{\rho\, v_c\, L_c}\,\frac{k}{\mu\, c_p} = \frac{1}{Re\, Pr} \qquad 2.43$$

The resulting new group is the Prandtl number (Pr), defined as the ratio of momentum diffusivity to thermal diffusivity α

$$Pr = \frac{\mu\, c_p}{k} = \frac{\mu}{\rho\, k}\,\frac{\rho\, c_p}{k} = \frac{\nu}{\alpha} \qquad 2.44$$

In this context, ν represents the cinematic viscosity of the fluid, while α indicates its thermal diffusivity. The product of Reynolds and Prandtl numbers is often grouped as the Péclet number

$$Pe = Re\, Pr \qquad 2.45$$

which relates the rate of advection to the rate of diffusion.

Finally, for evaporative cooling systems, the transport of water vapor within the air stream is governed by the species conservation equation. Assuming a binary mixture and Fickian diffusion

$$\underline{v} \cdot \nabla \rho_v = D_{va}\, \nabla^2 \rho_v \qquad 2.46$$

where ρ_v is the vapor mass partial density and D_{va} is the binary diffusion coefficient of water vapor in air. To render this equation dimensionless, a dimensionless vapor mass partial density ρ_v^* is defined based on a reference vapor mass partial density $\rho_{v,c}$ and a characteristic constant vapor mass partial density difference $\Delta\rho_{v,c}$

$$\rho_v^* = \frac{\rho_v - \rho_{v,c}}{\Delta\rho_{v,c}} \qquad 2.47$$

Substituting dimensionless variables into equation 2.46 yields

$$\underline{v}^* \cdot \nabla^* \rho_v^* = \frac{D_{va}}{v_c\, L_c}\, \nabla^{*2} \rho_v^* \qquad 2.48$$

Analogously to the energy equation, forcing the appearance of the Reynolds number in the diffusion term leads to

$$\frac{D_{va}}{v_c\, L_c} = \frac{\mu}{\rho\, v_c\, L_c} \frac{\rho\, D_{va}}{\mu} = \frac{1}{Re\, Sc} \qquad 2.49$$

The emerging parameter is the Schmidt number (Sc), which defines the ratio of momentum diffusivity to mass diffusivity

$$Sc = \frac{\mu}{\rho\, D_{va}} = \frac{\nu}{D_{va}} \qquad 2.50$$

The relationship between thermal and mass diffusivity is further described by the Lewis number (Le), defined as the ratio of the Schmidt number to the Prandtl number

$$Le = \frac{Sc}{Pr} = \frac{\alpha}{D_{va}} \qquad 2.51$$

This is a property that is fundamental to the analogy between heat and mass transfer in psychrometric processes.

2.10. Mean velocity in internal flows

In internal flows, viscous effects and wall friction lead to the development of a non-uniform velocity profile across the duct cross-section. To simplify the thermodynamic analysis, a mean velocity $\bar{v}$ is defined, allowing the mass flow rate to be expressed in terms of a bulk averaged value rather than local variations.

The mass flow rate $\dot{m}$, is determined by integrating the local mass flux over the cross-sectional area A_c

$$\dot{m} = \int_{A_c} \rho \, v \, dA \qquad 2.52$$

where v is the local velocity, ρ is the local fluid density, and dA is the differential surface element.

By defining a mean velocity $\bar{v}$, the mass flow rate can typically be expressed as

$$\dot{m} = \rho \, \bar{v} \, A_c \qquad 2.53$$

Physically, $\bar{v}$ represents the equivalent uniform velocity that, if applied across the entire cross-sectional area, would produce the same mass flow rate as the actual non-uniform velocity profile. Assuming the fluid density ρ is uniform across the cross-section, the comparison of equations 2.52 and 2.53 yields

$$\bar{v} = \frac{1}{\rho \, A_c} \int_{A_c} \rho \, v \, dA \qquad 2.54$$

This definition provides a single representative velocity that simplifies further calculations.

2.11. Heat and mass transfer in internal flow

In internal flows where a temperature difference exists between the fluid and the walls, a temperature profile develops across the cross-section, resulting in a non-uniform temperature distribution. To simplify heat transfer analysis, the bulk temperature T_b is introduced. It is defined as the temperature that would yield the same total enthalpy flow as the actual temperature distribution.

The total enthalpy flow rate $\dot{Q}$ across a cross-sectional area A_c is given by the integral of the local enthalpy flux

$$\dot{Q} = \int_{A_c} \rho \, v \, c_p \, T \, dA \qquad 2.55$$

In this equation, c_p is the specific heat at constant pressure, T is the temperature, ρ is the density, v is the velocity and dA is the differential surface element.

By using the bulk temperature, the total enthalpy flow rate can be expressed in a simplified form, treating both the temperature and the velocity as uniform across the entire cross-section

$$\dot{Q} = \dot{m} \, c_p \, T_b \qquad 2.56$$

This approach allows the complex distribution of local temperatures and velocities to be represented by single, average values for the purpose of heat transfer calculations.

Combining equations 2.55 and 2.56 gives the bulk temperature

$$T_b = \frac{1}{\dot{m} \, c_p} \int_{A_c} \rho \, v \, c_p \, T \, dA \qquad 2.57$$

Heat conduction in a fluid is described by Fourier's law

$$\dot{Q}'' = -k \, \nabla T \qquad 2.58$$

where $\dot{Q}''$ is the heat flux, k is the thermal conductivity, and ∇T is the temperature gradient. Under the assumption of one-dimensional heat transfer normal to a wall, this reduces to

$$\dot{Q}'' = -k \, \frac{\partial T}{\partial y} \qquad 2.59$$

Newton's law of cooling expresses the convective heat flux at a surface boundary

$$\dot{Q}'' = h_c\,(T_w - T_b) \qquad 2.60$$

where h_c is the convection heat transfer coefficient and T_w is the wall temperature. In internal flows, the convective heat flux at the wall must equal the conductive flux given by Fourier's law at the wall, due to the no-slip condition, which assumes the fluid in contact with the wall is stationary. Neglecting axial conduction and equating relations 2.59, evaluated at the wall, and 2.60 gives

$$-k\left.\frac{\partial T}{\partial y}\right|_{y=0} = h_c\,(T_w - T_b) \qquad 2.61$$

To derive the dimensionless heat transfer coefficient, it is necessary to normalize the variables. While the general solution of the energy equation (discussed in Section 2.9) employs fixed reference scales, the definition of the local heat transfer coefficient relies on the local driving force $(T_w - T_b)$, which varies along the duct. Recalling the dimensionless wall-normal coordinate

$$y^* = \frac{y}{L_c} \qquad 2.62$$

where L_c is the characteristic length (hydraulic diameter in internal flows), and the dimensionless temperature

$$T^* = \frac{T - T_w}{T_b - T_w} \qquad 2.63$$

equation 2.61 can be rewritten in dimensionless form

$$-\left.\frac{\partial\left(\frac{T}{T_w-T_b}\right)}{\partial\left(\frac{y}{L_c}\right)}\right|_{\frac{y}{L_c}=0}\frac{1}{L_c}=\frac{h_c}{k} \tag{2.64}$$

By adding and subtracting the wall temperature T_w inside the partial derivative, the result remains unchanged, since the derivative of T_w in the wall-normal direction is zero

$$-\left.\frac{\partial\left(\frac{T-T_w+T_w}{T_w-T_b}\right)}{\partial\left(\frac{y}{L_c}\right)}\right|_{\frac{y}{L_c}=0}\frac{1}{L_c}=\frac{h_c}{k} \tag{2.65}$$

From this, the derivative can be separated as

$$\left.\frac{\partial\left(\frac{T_w}{T_b-T_w}\right)}{\partial\left(\frac{y}{L_c}\right)}\right|_{\frac{y}{L_c}=0}+\left.\frac{\partial\left(\frac{T-T_w}{T_b-T_w}\right)}{\partial\left(\frac{y}{L_c}\right)}\right|_{\frac{y}{L_c}=0}=\left.\frac{\partial\left(\frac{T-T_w}{T_b-T_w}\right)}{\partial\left(\frac{y}{L_c}\right)}\right|_{\frac{y}{L_c}=0}=\frac{h_c\,L_c}{k} \tag{2.66}$$

This leads to the definition of the Nusselt number, which expresses the dimensionless temperature gradient at the wall and provides a measure of the convective heat transfer at the surface

$$Nu=\left.\frac{\partial\left(\frac{T-T_w}{T_b-T_w}\right)}{\partial\left(\frac{y}{L_c}\right)}\right|_{\frac{y}{L_c}=0}=\left.\frac{\partial T^*}{\partial y^*}\right|_{y^*=0}=\frac{h_c\,L_c}{k} \tag{2.67}$$

Several studies have been conducted to determine the Nusselt number for specific duct geometry and conditions [87]. For laminar flow in parallel-plate channels, analytical solutions for the asymptotic fully developed region include:

Constant and uniform wall temperature

$$Nu = 7.54070087 \tag{2.68}$$

Constant and uniform wall heat flux

$$Nu = 8.2352941 \tag{2.69}$$

One adiabatic wall, one constant temperature wall

$$Nu = 4.861 \tag{2.70}$$

One adiabatic wall, one constant heat flux wall

$$Nu = 5.385 \tag{2.71}$$

However, in the thermal entrance region where the boundary layer is developing, the Nusselt number is not constant. For a hydrodynamically fully developed but thermally developing flow, the solution for constant wall heat flux is given by the series expansion

$$Nu = \frac{1}{\frac{17}{140} + \frac{1}{4}\sum_{n=1}^{\infty}\left[C_n\, Y_n(1)\, e^{-\left(\frac{32}{3}\beta_n^2\, x^*\right)}\right]} \tag{2.72}$$

Whereas for a wall heat flux varying exponentially in the axial direction, the solution is

$$Nu = \frac{3}{8}\frac{1}{\sum_{n=1}^{\infty}\left\{\frac{-C_n\, Y_n(1)\, \beta_n^2}{\frac{32}{3}\beta_n^2 + m}\left[1 - e^{-\left(\frac{32}{3}\beta_n^2 + m\right)x^*}\right]\right\}} \tag{2.73}$$

where m is a parameter describing the exponential variation of the wall heat flux along the axial direction. In these equations, the evolution of the Nusselt number is described as a function of the dimensionless axial coordinate x^* defined as

$$x^* = \frac{x}{D_h\, Pe} = \frac{x}{D_h\, Re\, Pr} = x\, \frac{k}{D_h^2\, \rho\, \bar{v}\, c_p} \qquad 2.74$$

In equations 2.72 and 2.73, β_n, Y_n and C_n represent the eigenvalues, eigenfunctions, and constants of the Sturm-Liouville problem, respectively. The values for the first ten modes ($n = 1, \ldots, 10$) are reported in Table 2.1.

Table 2.1. First ten eigenvalues and constants for the solution of the thermal entry problem with constant wall heat flux.

n	β_n	$-C_n\, Y_n(1)$
1	4.287224	0.2222280
2	8.30372	0.0725316
3	12.3106	0.0373691
4	16.3145	0.0232829
5	20.3171	0.0161112
6	24.3189	0.0119190
7	28.3203	0.0092342
8	32.3214	0.0074013
9	36.3223	0.0060881
10	40.3231	0.0051116

For higher order modes, the following asymptotic approximations provide high accuracy

$$\beta_n = 4\, n + \frac{1}{3} \qquad 2.75$$

$$C_n\, Y_n(1) = -2.401006045\, {\beta_n}^{-5/3} \qquad 2.76$$

A comparison between the first ten tabulated values and those derived from the aforementioned formulas is presented below. Figure 2.1-A compares the β_n values from Table 2.1 with those obtained via equation 2.75, while Figure 2.1-B depicts the percentage error between the two formulations. It is observed that for the first index

n, the error is below 1.1 %; subsequently, the error decays exponentially, dropping below 0.1 % at the fifth index and continuing to decrease for higher values.

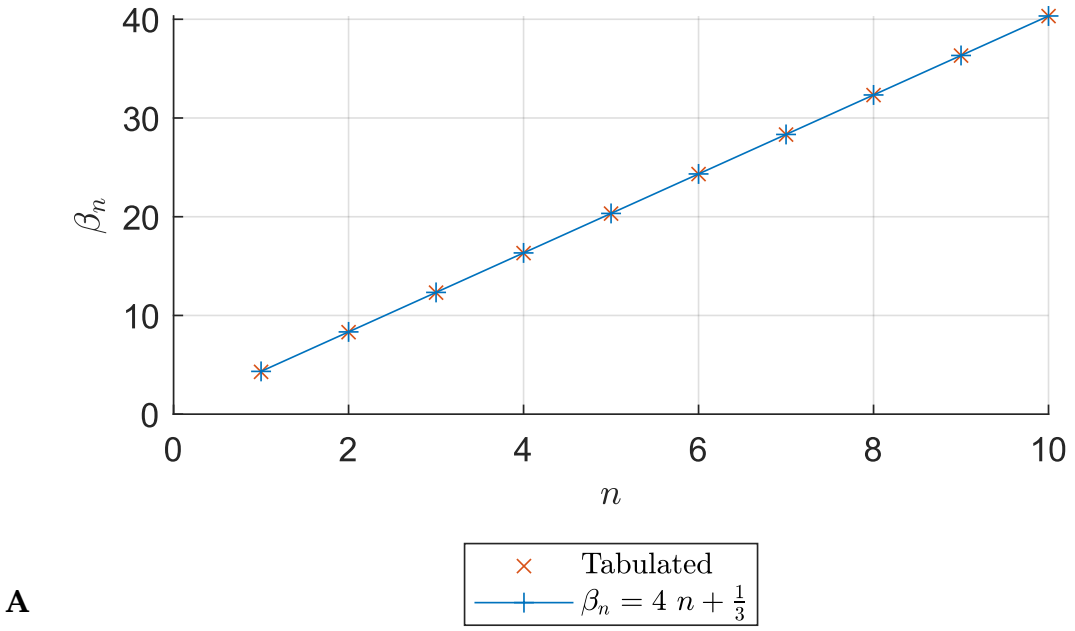

A

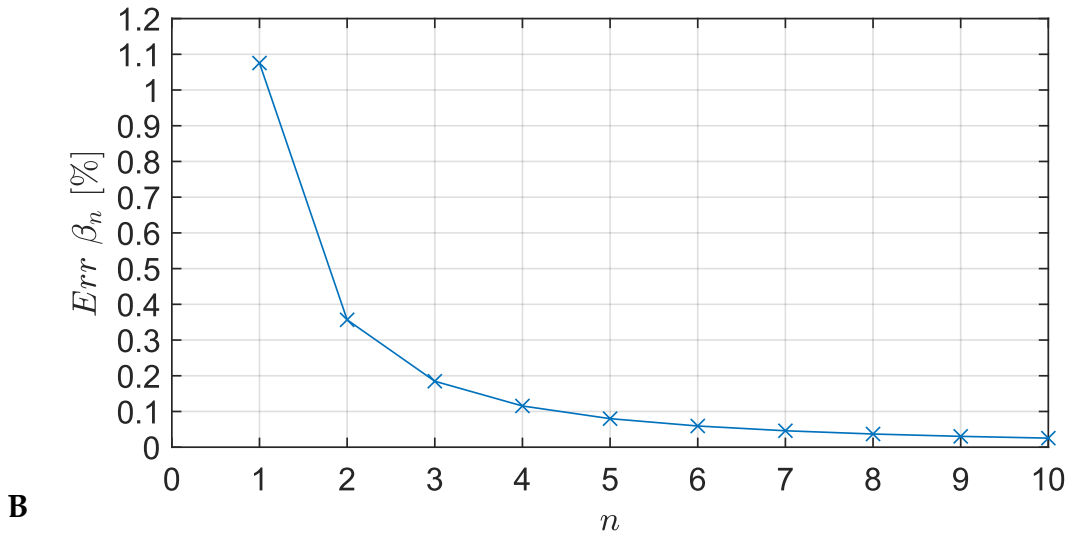

B

Figure 2.1. Comparison between tabulated values and those calculated using Eq. 2.75 for the parameter β_n (A) and percentage error between the two formulations (B) for the first ten indices.

Similarly, the comparison between the values in Table 2.1 and those obtained via equation 2.76 for the parameters $C_n\ Y_n(1)$ is illustrated in Figure 2.2-A. Figure 2.2-B

displays the relative percentage error: although the error exceeds 6 % for the first index, it exhibits a similar exponential decay, reaching 1 % at the tenth index.

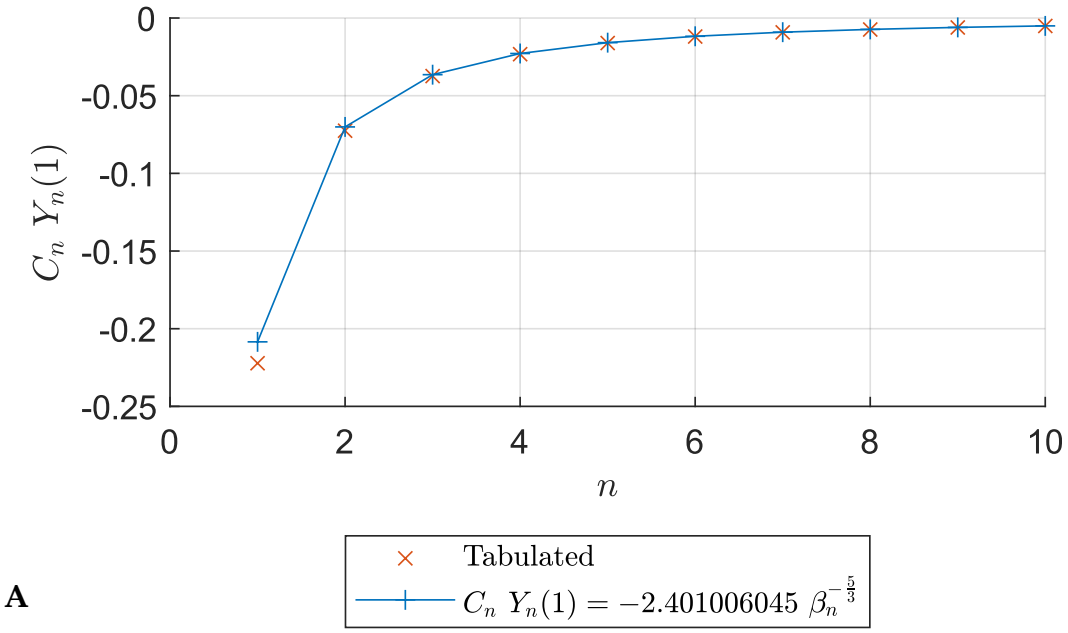

A

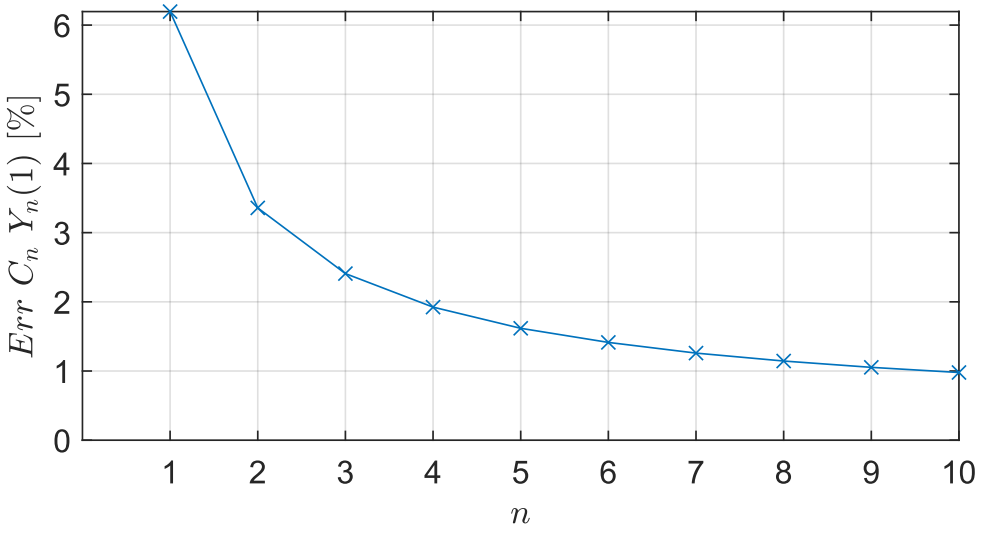

B

Figure 2.2. Comparison between tabulated values and those calculated using Eq. 2.76 for the parameter $C_n\ Y_n(1)$ (A) and percentage error between the two formulations (B) for the first ten indices.

The series expansions in equations 2.72 and 2.73 exhibit slow convergence, necessitating a high number of terms to achieve accurate results. The Nusselt number results for these two cases are presented below. The solutions were evaluated

considering truncation numbers of 10^1, 10^3, 10^5 and 10^7 terms. Figure 2.3 displays a dashed line representing the asymptotic value for fully developed flow with constant heat flux (Eq. 2.69), alongside two solid curves corresponding to Eq. 2.72 (black) and Eq. 2.73 (blue). It is evident from Figure 2.3-A that, with only 10 terms, Eq. 2.73 yields values that deviate significantly from Eq. 2.72 at low dimensionless axial coordinates, x_{th}^*. Increasing the number of terms to 10^3 (Figure 2.3-B) reduces the discrepancy, although significant differences persist. Further increasing the truncation number leads to a progressive convergence of the two curves. It should be noted that the blue curve actually depicts a family of curves for different coefficients m, which coalesce at low x_{th}^* values. Figure 2.4 details the behavior of the curves near the fully developed region, within the interval $10^{-3} \leq x_{th}^* \leq 2 \times 10^{-1}$. In this range, the curves associated with different m values become distinguishable as the family of curves diverges. Consistent with previous observations, using only the first ten terms (Figure 2.4-A) results in variable heat flux curves that are notably inaccurate, appearing consistently higher than the constant flux curve for all considered m coefficients. As the number of terms increases, the variable flux curves gradually settle to their correct positions: below the constant flux line for negative m values and above it for positive m values. This behavior confirms the consistency of the two formulations, as the constant heat flux condition represents a special case of the exponential flux where $m = 0$.

To enhance the generality of the Nusselt number calculation, a discrete wall heat flux $q_w(x)$ defined through a series of linear segments is now considered. Adopting the analytical framework established by Cess and Shaffer [88], and starting from the general superposition integral for arbitrary heat flux variations derived via the method of Siegel et al. [89], the wall temperature distribution is given by

$$T_w(x^*) - T_0 = \frac{1}{k}\int_0^x \left[\frac{4}{Pe} - \frac{8}{3}\sum_{n=1}^{\infty} C_n\, Y_n(1)\, \frac{\beta_n^2}{Pe}\, e^{-\frac{8}{3}\frac{\beta_n^2}{Pe}\frac{(x-x')}{a}}\right] q_w(x')\, dx' \qquad 2.77$$

where the parameter a identifies the channel half-height. The longitudinal coordinate is non-dimensionalized using the definition in equation 2.74. Considering the hydraulic diameter expressed in terms of the channel half-height

$$x^* = \frac{x}{Pe\, D_h} = \frac{x}{Pe\, 4\, a} \qquad 2.78$$

which implies

$$x = Pe\, 4\, a\, x^* \qquad 2.79$$

$$x' = Pe\, 4\, a\, x^{*\prime} \qquad 2.80$$

and the differential transforms as

$$dx' = Pe\, 4\, a\, dx^{*\prime} \qquad 2.81$$

Substituting the relationships 2.79, 2.80 and 2.81 into equation 2.77 yields the transformed integral equation

$$T_w(x^*) - T_0 = \frac{a}{k}\int_0^{x^*} \left[16 - \frac{32}{3}\sum_{n=1}^{\infty} C_n\, Y_n(1)\, \beta_n^2\, e^{-\frac{32}{3}\beta_n^2 (x^* - x^{*\prime})}\right] q_w(x^{*\prime})\, dx^{*\prime} \qquad 2.82$$

Separating the integral into two components, factoring out the constant terms, and moving the integral operator inside the summation, leads to

A

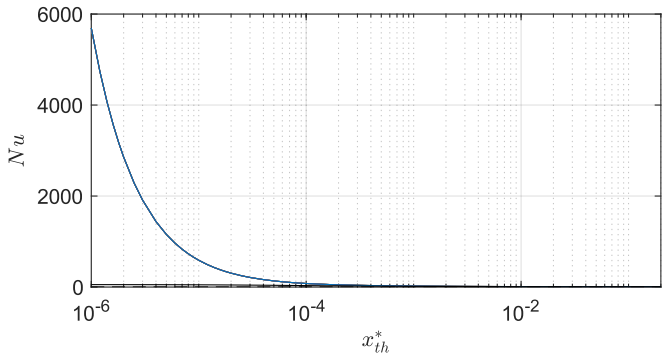

B

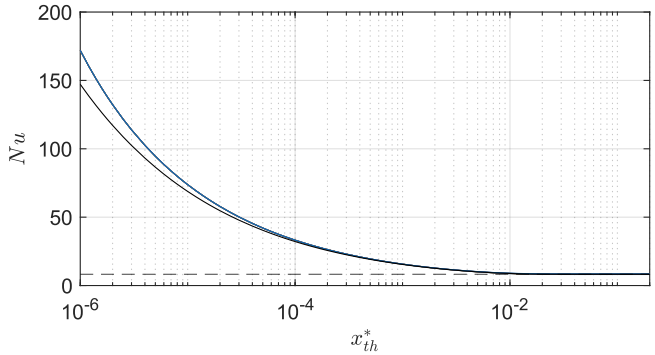

C

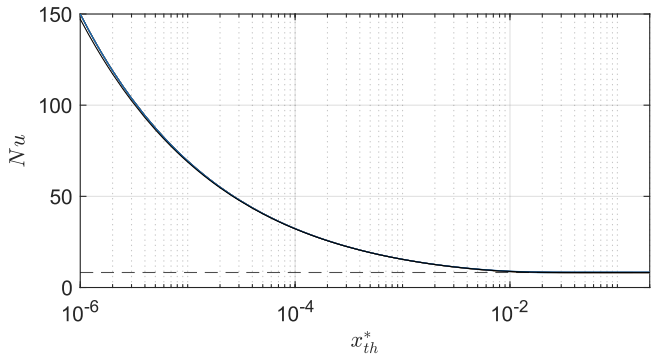

D

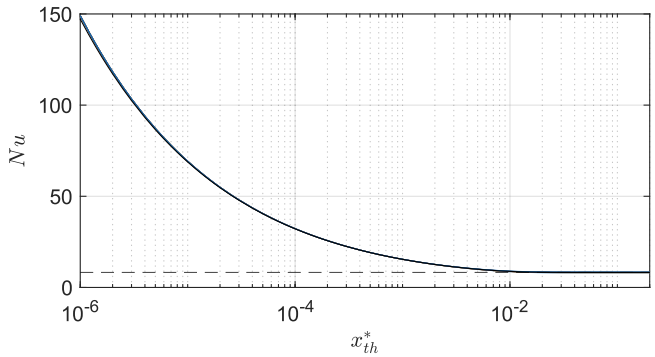

Figure 2.3. Nusselt number profiles in parallel-plate channels under exponentially varying wall heat flux conditions, calculated using 10^1 *(A),* 10^3 *(B),* 10^5 *(C) and* 10^7 *(D) series truncation terms.*

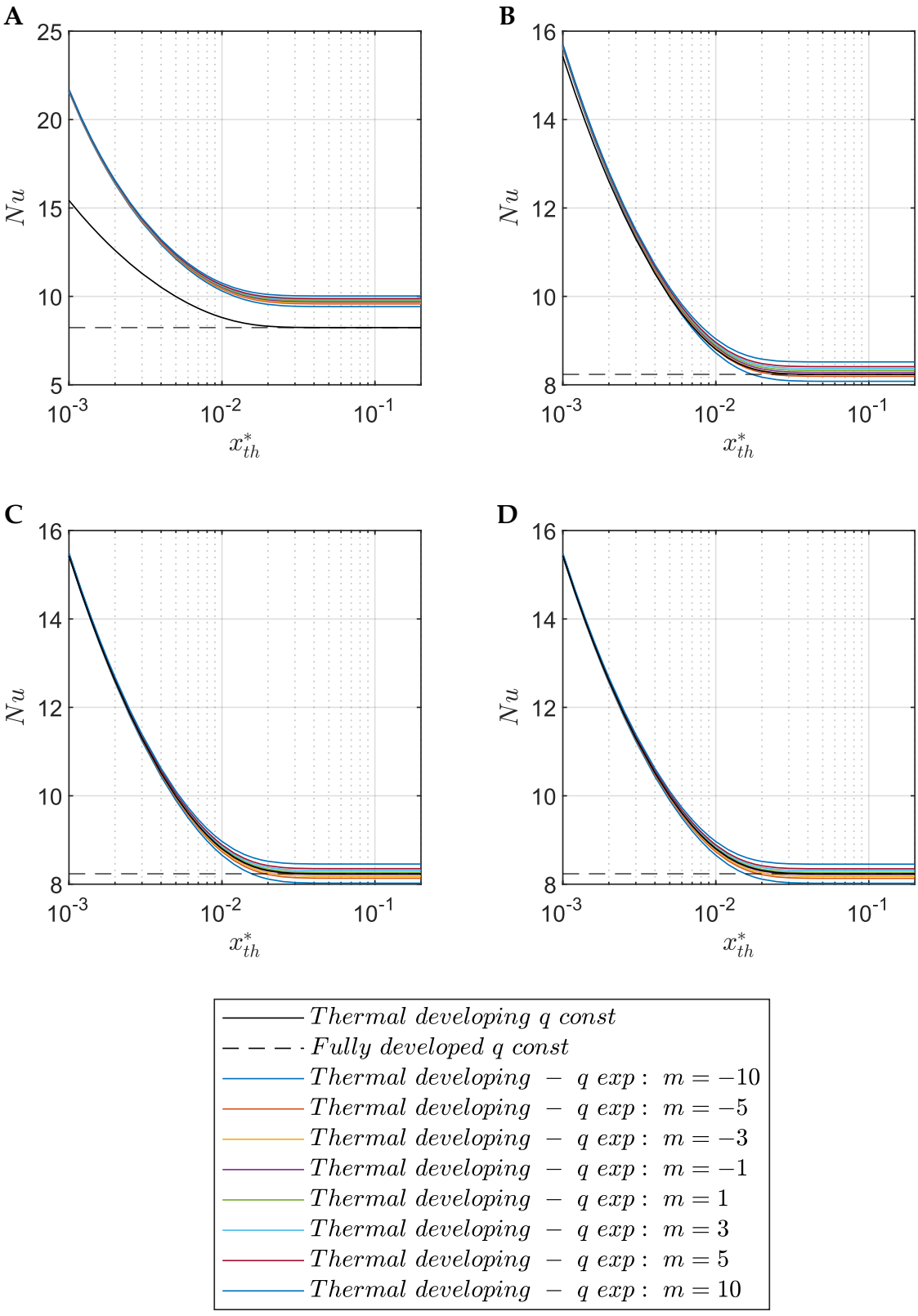

Figure 2.4. Detailed view of the Nusselt number near the fully developed flow region for parallel-plate channels with exponentially varying wall heat flux, for different values of the exponential coefficient m, calculated using 10^1 *(A),* 10^3 *(B),* 10^5 *(C), and* 10^7 *(D) series terms.*

$$T_w(x^*) - T_0 = \frac{16\,a}{k}\int_0^{x^*} q_w(x^*)\,dx^{*\prime} - \frac{32\,a}{3\,k}\sum_{n=1}^{\infty}\left[C_n\,Y_n(1)\,\beta_n^2\int_0^{x^*} e^{-\frac{32}{3}\beta_n^2\,(x^*-x^{*\prime})}\,q_w(x^{*\prime})\,dx^{*\prime}\right] \quad 2.83$$

Subsequently, performing an enthalpy balance on the considered duct section allows the bulk temperature rise to be expressed as

$$T_b(x^*) - T_0 = \frac{\int_0^{x'} q_w(x')\,2\,W\,dx'}{\dot{m}\,c_p} = \frac{\int_0^{x'} q_w(x')\,2\,W\,dx'}{\rho\,\bar{v}\,2\,a\,W\,c_p} \quad 2.84$$

where W represents the depth of the exchange surface. Introducing the dimensionless coordinate and applying appropriate simplifications, this relationship becomes

$$T_b(x^*) - T_0 = \frac{4\,Pe\int_0^{x^{*\prime}} q_w(x^{*\prime})\,dx^{*\prime}}{\rho\,\bar{v}\,c_p} \quad 2.85$$

Substituting the definition of the Péclet number yields

$$T_b(x^*) - T_0 = \frac{16\,a}{k}\int_0^{x^{*\prime}} q_w(x^{*\prime})\,dx^{*\prime} \quad 2.86$$

Subtracting equation 2.86 from equation 2.83 results in the cancellation of the first integral term, leading to the expression for the local temperature difference

$$T_w(x^*) - T_b(x^*) = -\frac{32\,a}{3\,k}\sum_{n=1}^{\infty}\left[C_n\,Y_n(1)\,\beta_n^2\int_0^{x^*} e^{-\frac{32}{3}\beta_n^2\,(x^*-x^{*\prime})}\,q_w(x^{*\prime})\,dx^{*\prime}\right] \quad 2.87$$

The heat flux must now be considered as a function of the dimensionless coordinate $q_w(x^*)$ Let x_i^* be the dimensionless coordinate of the i-th node, where $i = 1,2,\ldots,N$. Within each interval $x_{i-1}^* \le x^{*\prime} \le x_i^*$, the heat flux is expressed as

$$q_w(x^{*\prime}) = q_{i-1} + m_i\,(x^{*\prime} - x^*_{i-1}) \qquad 2.88$$

where q_{i-1} is the known heat flux at the previous node, and m_i is the slope of the linear segment, defined as

$$m_i = \frac{q_i - q_{i-1}}{x^*_i - x^*_{i-1}} \qquad 2.89$$

To evaluate the convolution integral $I_n(x^*_i)$ at the current node x^*_i, the integration domain is partitioned into the history up to the previous node and the contribution of the current segment

$$I_n(x^*_i) = \int_0^{x^*_{i-1}} e^{-\frac{32}{3}\beta_n^2\,(x^*_i - x^{*\prime})}\, q_w(x^{*\prime})\, dx^{*\prime} + \int_{x^*_{i-1}}^{x^*_i} e^{-\frac{32}{3}\beta_n^2\,(x^*_i - x^{*\prime})}\, q_w(x^{*\prime})\, dx^{*\prime} \qquad 2.90$$

Defining the current step length as

$$\Delta x^*_i = x^*_i - x^*_{i-1} \qquad 2.91$$

the exponent in the first integral of equation 2.90 can be decomposed as

$$e^{-\frac{32}{3}\beta_n^2\,(x^*_i - x^{*\prime})} = e^{-\frac{32}{3}\beta_n^2\,(x^*_i - x^*_{i-1} + x^*_{i-1} - x^{*\prime})} = e^{-\frac{32}{3}\beta_n^2\,\Delta x^*_i}\; e^{-\frac{32}{3}\beta_n^2\,(x^*_{i-1} - x^{*\prime})} \qquad 2.92$$

Consequently, the decay term $e^{-\frac{32}{3}\beta_n^2\,\Delta x^*_i}$ is constant with respect to the integration variable $x^{*\prime}$ and can be factored out. Recognizing that the remaining integral corresponds exactly to the value calculated at the previous node $I_n(x^*_{i-1})$, the total integral can be expressed recursively

$$I_n(x^*_i) = I_n(x^*_{i-1})\, e^{-\frac{32}{3}\beta_n^2\,\Delta x^*_i} + \Delta I_{n,i} \qquad 2.93$$

The term $\Delta I_{n,i}$ represents the contribution of the current linear segment.

Introducing the local variable

$$\varepsilon = x^{*\prime} - x_{i-1}^{*} \tag{2.94}$$

and substituting equation 2.88 into the second integral of equation 2.90, leads to

$$\Delta I_{n,i} = \int_0^{\Delta x_i^*} e^{-\frac{32}{3}\beta_n^2 (\Delta x_i^* - \varepsilon)} \, (q_{i-1} + m_i \, \varepsilon) \, d\varepsilon \tag{2.95}$$

Factoring out the exponential term independent of the integration variable and splitting the integral into two parts yields

$$\Delta I_{n,i} = e^{-\frac{32}{3}\beta_n^2 \Delta x_i^*} \left(q_{i-1} \int_0^{\Delta x_i^*} e^{\frac{32}{3}\beta_n^2 \varepsilon} \, d\varepsilon + m_i \int_0^{\Delta x_i^*} \varepsilon \, e^{\frac{32}{3}\beta_n^2 \varepsilon} \, d\varepsilon \right) \tag{2.96}$$

The first elementary integral yields

$$\int_0^{\Delta x_i^*} e^{\frac{32}{3}\beta_n^2 \varepsilon} \, d\varepsilon = \frac{1}{\frac{32}{3}\beta_n^2} \left(e^{\frac{32}{3}\beta_n^2 \Delta x_i^*} - 1 \right) \tag{2.97}$$

The second integral is evaluated using the integration by parts rule

$$\int A \, dB = A \, B - \int B \, dA \tag{2.98}$$

Setting

$$A = \varepsilon \tag{2.99}$$

implies

$$dA = d\varepsilon \tag{2.100}$$

and considering

$$dB = e^{\frac{32}{3}\beta_n^2\,\varepsilon}\,d\varepsilon \tag{2.101}$$

yields

$$B = \frac{e^{\frac{32}{3}\beta_n^2\,\varepsilon}}{\frac{32}{3}\,\beta_n^2} \tag{2.102}$$

Substituting these terms into equation 2.98 leads to

$$\int_0^{\Delta x_i^*} \varepsilon\, e^{\frac{32}{3}\beta_n^2\,\varepsilon}\,d\varepsilon = \left[\varepsilon\,\frac{e^{\frac{32}{3}\beta_n^2\,\varepsilon}}{\frac{32}{3}\,\beta_n^2}\right]_0^{\Delta x_i^*} - \int_0^{\Delta x_i^*} \frac{e^{\frac{32}{3}\beta_n^2\,\varepsilon}}{\frac{32}{3}\,\beta_n^2}\,d\varepsilon \tag{2.103}$$

which, upon evaluation, results in

$$\int_0^{\Delta x_i^*} \varepsilon\, e^{\frac{32}{3}\beta_n^2\,\varepsilon}\,d\varepsilon = \frac{\Delta x_i^*\, e^{\frac{32}{3}\beta_n^2\,\Delta x_i^*}}{\frac{32}{3}\,\beta_n^2} - \frac{e^{\frac{32}{3}\beta_n^2\,\Delta x_i^*} - 1}{\left(\frac{32}{3}\,\beta_n^2\right)^2} \tag{2.104}$$

Substituting the results 2.97 and 2.104 into relation 2.96 gives

$$\Delta I_{n,i} = e^{-\frac{32}{3}\beta_n^2\,\Delta x_i^*}\left\{q_{i-1}\,\frac{e^{\frac{32}{3}\beta_n^2\,\Delta x_i^*} - 1}{\frac{32}{3}\,\beta_n^2} + m_i\left[\frac{\Delta x_i^*\, e^{\frac{32}{3}\beta_n^2\,\Delta x_i^*}}{\frac{32}{3}\,\beta_n^2} - \frac{e^{\frac{32}{3}\beta_n^2\,\Delta x_i^*} - 1}{\left(\frac{32}{3}\,\beta_n^2\right)^2}\right]\right\} \tag{2.105}$$

Rearranging the terms, the closed-form solution for the step update is

$$\Delta I_{n,i} = q_{i-1}\,\frac{1-e^{-\frac{32}{3}\beta_n^2\,\Delta x_i^*}}{\frac{32}{3}\,\beta_n^2} + m_i\left[\frac{\Delta x_i^*}{\frac{32}{3}\,\beta_n^2} - \frac{1-e^{-\frac{32}{3}\beta_n^2\,\Delta x_i^*}}{\left(\frac{32}{3}\,\beta_n^2\right)^2}\right] \qquad 2.106$$

Once calculated, the term $\Delta I_{n,i}(x_i^*)$ can be substituted into equation 2.93 to update the total integral $I_n(x_i^*)$. The wall temperature expression (equation 2.87) then becomes

$$T_w(x_i^*) - T_b(x_i^*) = -\frac{32\,a}{3\,k}\sum_{n=1}^{\infty}[C_n\,Y_n(1)\,\beta_n^2\,I_n(x_i^*)] \qquad 2.107$$

At this point, the definition of the Nusselt number (equation 2.67) is utilized, substituting the convective coefficient with the ratio of the heat flux per unit area to the temperature difference. The Nusselt number is thus expressed as

$$Nu(x_i^*) = \frac{q_w(x_i^*)\,4\,a}{k\,[T_w(x_i^*) - T_b(x_i^*)]} \qquad 2.108$$

Finally, substituting the temperature difference between the wall and the bulk from equation 2.107 into the Nusselt number definition

$$Nu(x_i^*) = \frac{3}{8}\,\frac{q_w(x_i^*)}{\sum_{n=1}^{\infty}\left[-C_n\,Y_n(1)\,\beta_n^2\,\Delta I_{n,i}(x_i^*)\right]} \qquad 2.109$$

This recursive formulation allows for the exact calculation of the Nusselt number for an arbitrarily complex heat flux profile approximated by linear segments, without requiring global curve fitting.

A similar approach can be used to describe the transport of a chemical species in a mixture. In internal flows with mass transfer due to evaporation of a liquid film at the wall, a concentration profile develops for the species undergoing evaporation.

Referring to equation 2.52, the total mass flow rate of species i across a cross-sectional area A_c is obtained by integrating the local mass flux

$$\dot{m}_v = \int_{A_c} v\,\rho_v\,dA \qquad 2.110$$

where $\dot{m}_v$ is the total mass flow rate of vapor, v is the velocity, ρ_v is the partial density of vapor and dA is the differential surface element.

Analogous to the bulk temperature in heat transfer, a bulk partial density of vapor, $\rho_{v,b}$, can be introduced. The mass flow rate can then be expressed as

$$\dot{m}_v = \dot{V}\,\rho_{v,b} \qquad 2.111$$

where $\dot{V}$ is the volumetric flow rate of the mixture. Equating equations 2.110 and 2.111, defines the bulk density

$$\rho_{v,b} = \frac{1}{\dot{V}} \int_{A_c} v\,\rho_v\,dA \qquad 2.112$$

In the context of diffusion, the analog of Fourier's law is Fick's law. For mass transfer in a binary mixture, Fick's postulate is written as

$$\dot{m}_v'' = -D_{va}\,\nabla\rho_v \qquad 2.113$$

where $\dot{m}_v''$ is the mass flux of vapor, D_{va} is the diffusion coefficient of vapor in air, and $\nabla\rho_v$ is the gradient of the partial density of the vapor.

For one-dimensional mass transfer normal to the wall, this reduces to

$$\dot{m}_v'' = -D_{va}\,\frac{\partial\rho_v}{\partial y} \qquad 2.114$$

By analogy with Newton's law of cooling, the mass transfer rate from a wall to the fluid can be expressed using a mass transfer coefficient

$$\dot{m}_v'' = h_m \left(\rho_{v,w} - \rho_{v,b}\right) \qquad 2.115$$

where h_m is the mass transfer coefficient, $\rho_{v,w}$ is the density of vapor at the wall, and $\rho_{v,b}$ is the bulk density of species i in the fluid.

Equating equations 2.114, evaluated at the wall, and 2.115 gives

$$-D_{va} \left.\frac{\partial \rho_v}{\partial y}\right|_{y=0} = h_m \left(\rho_{v,w} - \rho_{v,b}\right) \qquad 2.116$$

Non-dimensionalizing this relation following the same procedure used for heat transfer yields the Sherwood number, the mass transfer analog of the Nusselt number

$$Sh = \left.\frac{\partial \left(\frac{\rho_v - \rho_{v,w}}{\rho_{v,b} - \rho_{v,w}}\right)}{\partial \left(\frac{y}{L_c}\right)}\right|_{\frac{y}{L_c}=0} = \left.\frac{\partial \rho_v^*}{\partial y^*}\right|_{y^*=0} = \frac{h_m L_c}{D_{va}} \qquad 2.117$$

This dimensionless number expresses the gradient of the normalized species concentration at the wall and provides a measure of convective mass transfer.

2.12. Thermal resistance and overall heat transfer coefficient

In many engineering applications, such as heat exchangers, heat transfer occurs across a solid medium separating two fluids at different temperatures. This process typically involves a series of mechanisms: convection from the hot fluid to the wall surface, conduction through the wall layers, and convection from the opposite wall surface to the cold fluid.

To analyze such composite systems, it is convenient to utilize the electrical analogy, where the heat transfer rate $\dot{Q}$ is viewed as a current driven by a temperature difference

ΔT (potential) across a network of thermal resistances R_{th}. The thermal resistance for convective heat transfer at a surface is defined as

$$R_{conv} = \frac{1}{h_c\, A} \qquad 2.118$$

where A is the heat transfer area. Similarly, for one-dimensional conduction through a plane wall of thickness s and thermal conductivity k, the thermal resistance is

$$R_{cond} = \frac{s}{k\, A} \qquad 2.119$$

Since these resistances occur in series, the total resistance R_{tot} is the sum of the individual contributions. The total heat transfer rate can thus be expressed as

$$\dot{Q} = \frac{\Delta T_{tot}}{R_{tot}} = U\, A\, \Delta T_{tot} \qquad 2.120$$

where U is defined as the overall heat transfer coefficient. This parameter combines the effects of convection and conduction into a single value. For a system consisting of a multi-layered wall separating two fluids, U is given by

$$U = \left(\frac{1}{h_{c,1}} + \sum_{j=1}^{N} \frac{s_j}{k_j} + \frac{1}{h_{c,2}} \right)^{-1} \qquad 2.121$$

In this expression, indices 1 and 2 refer to the fluid domains on the two opposite sides of the separating wall, with $h_{c,1}$ and $h_{c,2}$ representing their respective convective heat transfer coefficients. The summation term accounts for the total conductive resistance of the solid medium; the index j iterates through the N distinct layers constituting the wall (e.g., structural material, coating, fouling), where s_j denotes the thickness and k_j the thermal conductivity of the j-th layer.

This formulation allows the complex heat transfer process through composite media to be calculated using the bulk temperatures of the fluids and a single global coefficient.

2.13. Lewis's experiment

Parameters		
$\dot{Q}$	W	*Energy flow rate*
h	$W/(m^2\ K)$ $kg_v/(s\ m^2\ Pa)$ $kg_{da}/(s\ m^2)$	*Exchange coefficient*
i	J/kg_{da}	*Specific enthalpy of humid air*
i_{lv}	J/kg	*Latent specific heat capacity of evaporation*
$\dot{m}$	kg/s	*Mass flow rate*
p	Pa	*Pressure*
T	K	*Temperature*

Subscripts	
b	*Bulk*
c	*Convective*
da	*Dry air*
e	*Evaporated*
f	*Feed*
i	*Interface*
m	*Mass*
p	*Referred to partial pressure*
s	*Sensible*
v	*Vapor*
ω	*Referred to specific humidity*

Lewis, in 1922 [90], analyzed the steady flow of unsaturated moist air inside a long thermally insulated tunnel. At the bottom of the tunnel, a porous absorbent material is continuously wetted with water supplied at the temperature of the exposed surface of

the pad. No longitudinal motion of the liquid film occurs, and the air velocity is sufficiently low that frictional heating can be neglected.

As shown in Figure 2.5 an infinitesimal control volume of the duct is considered. During its passage through the tunnel, the unsaturated air absorbs vapor through evaporation from the liquid film. Since the duct is insulated, all energy exchanges must occur exclusively between the air stream and the liquid film. Evaporation removes latent heat from the liquid surface, which must be supplied by the air flow. As a result, the air stream is cooled. If the tunnel is sufficiently long, thermal and hygrometric equilibrium is eventually reached between the air and the wetted surface.

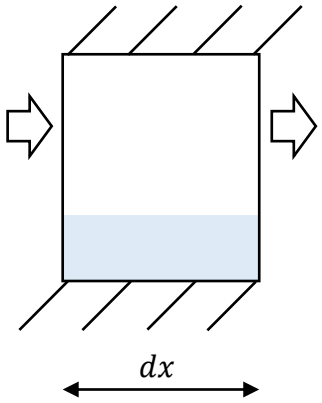

Figure 2.5. Schematic representation of an infinitesimal control volume in a wet-walled duct thermally insulated from the surroundings.

Under steady-state conditions, the thermodynamic properties of the air stream (temperature, relative humidity, and vapor partial pressure) vary along the longitudinal direction but remain constant in time at any fixed position. A local analysis of the interface between the air and the liquid film in an infinitesimal duct section is presented in Figure 2.6.

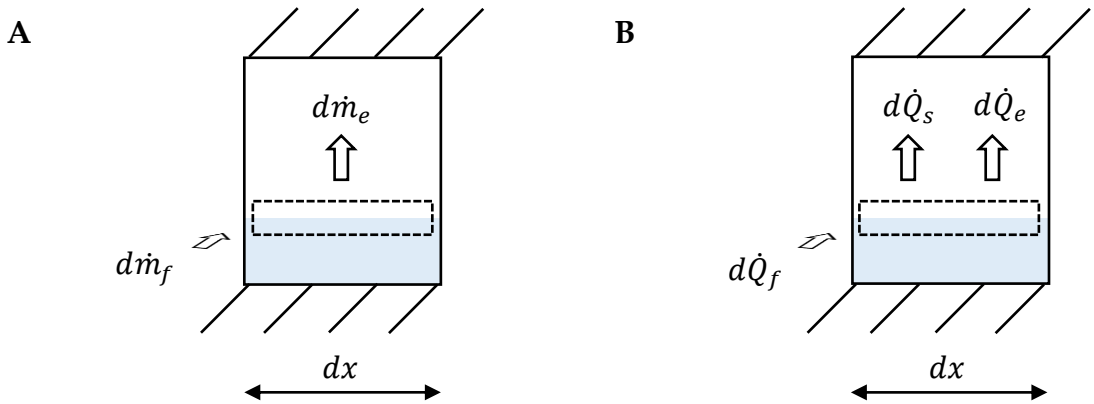

Figure 2.6. Local analysis at the air-water interface under adiabatic conditions: (A) Mass balance; (B) Energy balance.

To sustain steady evaporation, the evaporated water mass flow rate $\dot{m}_e$ must be replenished by a feed liquid flow rate $\dot{m}_f$ into the film

$$d\dot{m}_e = d\dot{m}_f \qquad 2.122$$

The interface must also satisfy an energy balance. Since the duct is thermally insulated from the surroundings, the only contributions are:

- the sensible heat exchanged between the bulk air and the liquid interface;
- the energy carried away by the evaporated vapor;
- the energy carried into the film by the feed liquid.

The sensible heat transferred locally between the film and the airflow $d\dot{Q}_s$ can be written using Newton's law of cooling (eq. 2.60)

$$d\dot{Q}_s = h_c\,(T_i - T_b)\,dA \qquad 2.123$$

where h_c is the convective heat transfer coefficient, T_i is the interface temperature, T_b is the bulk air temperature, and dA is the infinitesimal wall area.

Based on previous observations that relate evaporation to the gradient of vapor partial pressure between the interface and the air [13], the local evaporated mass flow rate

$d\dot{m}_e$ can be expressed, in analogy with Newton's law of cooling, by introducing a mass transfer coefficient defined with respect to vapor partial pressure differences.

$$d\dot{m}_e = h_{m,p}\left(p_{v,i} - p_{v,b}\right) dA \qquad 2.124$$

where $h_{m,p}$ is the convective mass transfer coefficient based on vapor partial pressure differences, $p_{v,i}$ is the interface vapor partial pressure, $p_{v,b}$ is the bulk vapor partial pressure, and dA is, again, the infinitesimal wall area.

At the interface, a phase change process occurs at a defined temperature. The energy flux associated with the vapor leaving the interface can therefore be expressed as the product of the evaporated mass flow rate and the specific enthalpy of the vapor

$$d\dot{Q}_e = d\dot{m}_e \left[i_{lv}(T_0) + c_{p,v}\,(T_i - T_0)\right] \qquad 2.125$$

Similarly, assuming incompressibility, the energy supplied by the feed liquid $d\dot{Q}_f$ is

$$d\dot{Q}_f = d\dot{m}_f\, c_f\,(T_i - T_0) \qquad 2.126$$

with c_f being the specific heat of the feed liquid.

With reference to Figure 2.6-B, the energy balance at the interface can be written as

$$d\dot{Q}_s + d\dot{Q}_e = d\dot{Q}_f \qquad 2.127$$

Expanding the terms using the flux definitions (equations 2.123, 2.125 and 2.126), the balance becomes

$$h_c\,(T_i - T_b)\,dA + d\dot{m}_e \left[i_{lv}(T_0) + c_{p,v}\,(T_i - T_0)\right] = d\dot{m}_f\, c_f\,(T_i - T_0) \qquad 2.128$$

Using the mass balance 2.122, this reduces to

$$h_c\,(T_i - T_b)\,dA + d\dot{m}_e\left\{i_{lv}(T_0) + c_{p,v}\,(T_i - T_0) - c_f\,(T_i - T_0)\right\} = 0 \qquad 2.129$$

Since the enthalpy difference between vapor and liquid at the same temperature equals the latent heat of vaporization, the balance simplifies to

$$h_c\,(T_i - T_b)\,dA = -d\dot{m}_e\,i_{lv}(T_i) \qquad 2.130$$

This relation indicates that the sensible heat flow, as defined, must be negative. In steady state, this requires the interface temperature to be lower than the bulk air temperature.

Substituting equation 2.124 into equation 2.130 yields

$$h_c\,(T_i - T_b)\,dA = -i_{lv}(T_i)\,h_{m,p}\left(p_{v,i} - p_{v,b}\right)dA \qquad 2.131$$

or equivalently

$$T_b - T_i = \frac{h_{m,p}\,i_{lv}}{h_c}\left(p_{v,i} - p_{v,b}\right) \qquad 2.132$$

Using the definition of specific humidity for an ideal gas mixture (eq. 2.26), the vapor partial pressure can be expressed as

$$p_v = p\,\frac{\frac{\omega}{M_v}}{\frac{\omega}{M_v} + \frac{1}{M_{da}}} \qquad 2.133$$

Applying this to both bulk vapor partial pressure $p_{v,b}$ and interface vapor partial pressure $p_{v,i}$ transforms equation 2.132 into

$$T_b - T_i = \frac{h_{m,p}\, i_{lv}}{h_c}\, p \left(\frac{\frac{\omega_i}{M_v}}{\frac{\omega_i}{M_v} + \frac{1}{M_{da}}} - \frac{\frac{\omega_b}{M_v}}{\frac{\omega_b}{M_v} + \frac{1}{M_{da}}} \right) \qquad 2.134$$

For low humidity levels, the terms ω_i/M_v and ω_b/M_v are negligible compared to $1/M_{da}$, leading to the approximation

$$T_b - T_i = \frac{h_{m,p}\, i_{lv}}{h_c}\, p\, \frac{M_{da}}{M_v}\, (\omega_i - \omega_b) \qquad 2.135$$

To preserve the form of equation 2.132, a mass transfer coefficient based on specific humidity $h_{m,\omega}$ can be defined as

$$h_{m,\omega} = \frac{M_{da}}{M_v}\, p\, h_{m,p} \qquad 2.136$$

so that equation 2.135 becomes

$$T_b - T_i = \frac{h_{m,\omega}\, i_{lv}}{h_c}\, (\omega_i - \omega_b) \qquad 2.137$$

Proceeding with the analysis of the airflow, and with reference to Figure 2.7, the flow of dry air remains constant along the duct, while the vapor flow increases as the evaporated mass enters the stream.

Within the control volume, the increase in vapor mass flow is therefore equal to the evaporated mass

$$d\dot{m}_v = d\dot{m}_e \qquad 2.138$$

The variation in the energy of the airflow can be expressed as

$$\dot{m}_{da}\, di_u = d\dot{Q}_s + d\dot{Q}_e \qquad 2.139$$

The specific enthalpy of moist air i_u, as shown in equation 2.32, is

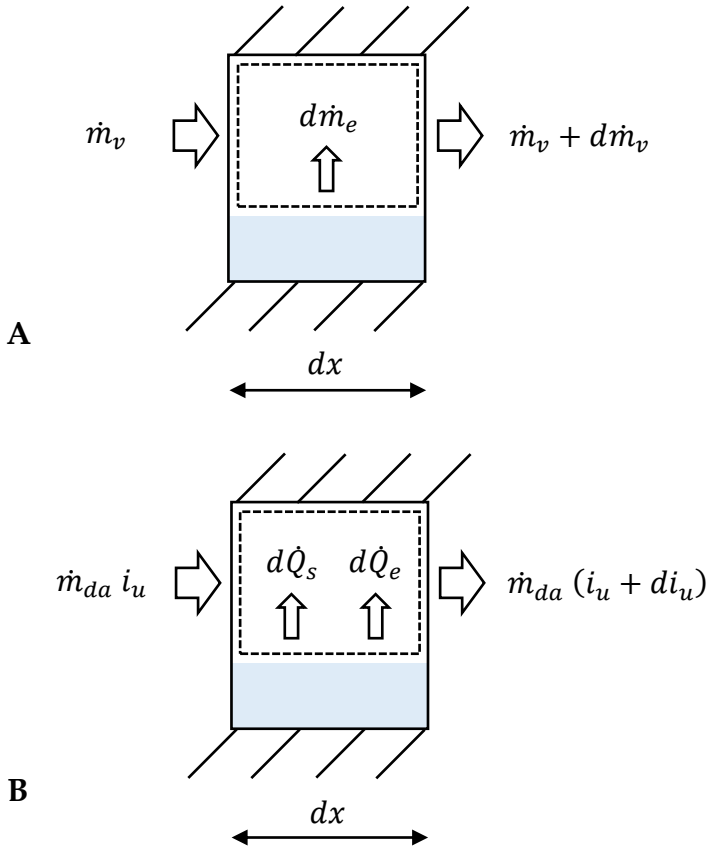

Figure 2.7. Control volume applied to the air stream for the longitudinal balance along the adiabatic duct.

$$i_u = c_{p,da}\,(T_b - T_0) + \omega_b\left[i_{lv}(T_0) + c_{p,v}\,(T_b - T_0)\right] \qquad 2.140$$

For a perfect gas mixture with constant specific heat capacity, the differential is given by

$$di_u = \frac{\partial i_u}{\partial T_b}\,dT_b + \frac{\partial i_u}{\partial \omega_b}\,d\omega_b \qquad 2.141$$

this reduces to

$$di_u = c_{p,da}\,dT_b + d\omega_b\left[i_{lv}(T_0) + c_{p,v}\,(T_b - T_0)\right] + \omega_b\,c_{p,v}\,dT_b \qquad 2.142$$

Substituting this expression into equation 2.139 and expanding the sensible and evaporative energy fluxes, yields

$$\dot{m}_{da}\left\{c_{p,da}\,dT_b + d\omega_b\left[i_{lv}(T_0) + c_{p,v}\,(T_b - T_0)\right] + \omega_b\,c_{p,v}\,dT_b\right\} = h_c\,(T_i - T_b)\,dA + d\dot{m}_e\left[i_{lv}(T_0) + c_{p,v}\,(T_i - T_0)\right] \quad 2.143$$

Here, the term involving the specific heat of moist air per unit mass of dry air $c_{p,u}$ (as defined in 2.33), becomes apparent. In addition, the variation in specific humidity can be related to the evaporated mass flow, giving

$$\dot{m}_{da}\,c_{p,u}\,dT_b + d\dot{m}_e\left[i_{lv}(T_0) + c_{p,v}\,(T_b - T_0)\right] = h_c\,(T_i - T_b)\,dA + d\dot{m}_e\left[i_{lv}(T_0) + c_{p,v}\,(T_i - T_0)\right] \quad 2.144$$

At this stage, the terms involving the evaporated mass can be combined

$$\dot{m}_{da}\,c_{p,u}\,dT_b + d\dot{m}_e\,c_{p,v}\,(T_b - T_i) = h_c\,(T_i - T_b)\,dA \quad 2.145$$

Using the equality derived previously in equation 2.130, the sensible heat transfer term can be replaced, yielding

$$\dot{m}_{da}\,c_{p,u}\,dT_b + d\dot{m}_e\,c_{p,v}\,(T_b - T_i) = -i_{lv}(T_i)\,d\dot{m}_e \quad 2.146$$

This balance shows that the reduction in the bulk air temperature is not only associated with the latent heat of evaporation, but also with an additional contribution related to the difference between the bulk and interface temperatures. However, this contribution is generally small. Lewis therefore neglects it, obtaining

$$-c_{p,u}\,dT_b = i_{lv}(T_i)\,d\omega_b \quad 2.147$$

For a sufficiently long duct, the air stream eventually reaches equilibrium with the liquid film, with bulk temperature and humidity achieving steady values. Integrating equation 2.147 between the initial bulk conditions ($T_{b,1}$,$\omega_{b,1}$) and the equilibrium values ($T_{b,2}$, $\omega_{b,2}$) gives

$$-\int_{T_{b,1}}^{T_{b,2}} c_{p,u}\, dT_b = \int_{\omega_{b,1}}^{\omega_{b,2}} i_{lv}(T_i)\, d\omega_b \qquad 2.148$$

Although both the specific heat of moist air and the latent heat of evaporation vary, neglecting these variations simplifies the relation to

$$-c_{p,u}\left(T_{b,2} - T_{b,1}\right) = i_{lv}\left(\omega_{b,2} - \omega_{b,1}\right) \qquad 2.149$$

which can be rearranged in the same form as equation 2.137

$$T_{b,1} - T_{b,2} = \frac{i_{lv}}{c_{p,u}}\left(\omega_{b,2} - \omega_{b,1}\right) \qquad 2.150$$

Equations 2.137 and 2.150 thus provide two relations of identical form that describe the evaporation process in an adiabatic duct. Lewis concluded that, under the stated assumptions, these relations must be equal. It is concluded that

$$T_{b,2} = T_i \qquad 2.151$$

$$\omega_{b,2} = \omega_i \qquad 2.152$$

$$\frac{h_c}{h_{m,\omega}} = c_{p,u} \qquad 2.153$$

In conclusion, Lewis's analysis provides an elegant framework for describing the evaporative cooling of air in an adiabatic duct. However, certain conceptual inconsistencies emerge upon closer examination. In Lewis's original derivation, ambiguity arises from the notation used for bulk conditions, which often fails to distinguish between the fixed inlet values and the variables evolving locally along the flow coordinate (in this chapter denoted as $T_{b,1}$, T_b, $\omega_{b,2}$, ω_b). This obscures the fundamental difference between local and global balances. The direct comparison between a strictly local relation (eq. 2.137) and an integrated balance extending from the inlet to equilibrium conditions (eq. 2.150) imposes a mathematical equivalence that

is not rigorously justified without priori assumptions. A critical limitation lies in the treatment of the interface temperature T_i. In Lewis's formulation, T_i is implicitly treated as a constant parameter corresponding to the equilibrium value throughout the integration process. Conversely, a fully local analysis would require T_i to vary progressively along the duct to satisfy the coupled mass and energy balances at every cross-section.

Furthermore, it must be emphasized that the psychrometric treatment and the underlying assumptions of the Lewis relation are valid under conditions sufficiently far from saturation. In this regime, the moist air mixture can be safely modeled using the ideal gas law. Near the saturation limit, the non-ideal behavior of the water vapor phase and the associated thermophysical coupling may introduce deviations that are not captured by this simplified local balance.

Despite these limitations, Lewis's approach remains a cornerstone of psychrometry. Its assumptions and simplifications must be acknowledged, particularly when extending the conclusions to more general configurations or when interpreting the physical validity of the derived relations.

2.14. Numerical integration of ordinary differential equations

Ordinary differential equations (ODEs) play a central role in the modeling of physical, chemical, biological, and economic phenomena. In many engineering applications, including the analysis of heat and mass transfer in evaporative cooling systems, these equations do not admit a closed-form analytical solution, thus necessitating the use of numerical approximation techniques [91].

Among the available strategies, numerical integration methods aim to approximate the continuous solution by computing values at discrete grid nodes. The underlying

concept is that the derivative of a function can be expressed as the limit of incremental ratios, which can be approximated using finite difference formulas. This approach enables the transformation of a continuous problem into a discrete one that can be solved iteratively.

The canonical form of a Cauchy problem (or Initial Value Problem) is defined as

$$\frac{du}{dx} = f(u, x)$$
$$u(x_0) = u_0 \qquad 2.154$$

where, u(x) is the unknown function depending on x, $f(u, x)$ is a known, sufficiently regular function that defines the differential equation, x_0 is the initial condition in the domain of interest and u_0 denotes the initial value of the unknown function.

Discretization consists in replacing the continuous domain with a grid made of equally spaced nodes

$$x_n = x_0 + n\,h, n = 0,1,2, \ldots \qquad 2.155$$

where h is the step size. The objective is to construct a sequence $\{u_n\}$ such that

$$u_n \cong u(x_n) \qquad 2.156$$

A fundamental approach is the explicit Euler method, which approximates the solution at the next step using a first-order Taylor expansion

$$u_{n+1} = u_n + h\,f(u_n, x_n) \qquad 2.157$$

Although simple and intuitive, this method exhibits a local truncation error of order $0(h^2)$ and a global error of order $0(h)$. As a result, it is often inaccurate and unstable when applied to real-world problems.

To improve accuracy and stability, higher-order methods are employed, among which the Runge-Kutta family is particularly prominent. The fourth-order Runge-Kutta method (RK4) is one of the most widely used and valued schemes for the numerical integration of ODEs. It provides an excellent compromise between computational complexity and accuracy, delivering global errors of order $0(h^4)$

The core principle of RK4 is to combine multiple evaluations of the function $f(u, x)$ within each interval $[x_n, x_{n+1}]$. By constructing a weighted average of these slopes, accounting for the initial point, two intermediate midpoints, and the final point, the method achieves a high-accuracy estimate of the increment.

The iterative formula is

$$u_{n+1} = u_n + \frac{h}{6}\,(K_1 + 2\,K_2 + 2\,K_3 + K_4) \qquad 2.158$$

with the incremental coefficients K_i defined as

$$K_1 = f(u_n, x_n) \qquad 2.159$$

$$K_2 = f\left(u_n + \frac{1}{2}\,K_1\,h, x_n + \frac{h}{2}\right) \qquad 2.160$$

$$K_3 = f\left(u_n + \frac{1}{2}\,K_2\,h, x_n + \frac{h}{2}\right) \qquad 2.161$$

$$K_4 = f(u_n + K_3\,h, x_n + h) \qquad 2.162$$

The weighted average $\frac{1}{6}\,(K_1 + 2\,K_2 + 2\,K_3 + K_4)$ yields a value that approximates the mean slope across the step, thereby reducing the discretization error.

RK4 belongs to the class of single-step methods and ensures a local truncation error of order $0(h^5)$. Consequently, the accumulated global error is of order $0(h^4)$. This level of accuracy makes RK4 considerably superior to elementary methods such as Euler's method, while retaining a moderate computational cost, since it requires four

evaluations of the function $f(u, x)$ per step. Regarding stability, RK4 is conditionally stable: both accuracy and stability depend on the choice of step size h which must be sufficiently small in relation to the problem under study.

In the context of this thesis, the RK4 method will be the primary tool used to solve the coupled differential equations governing the heat and mass transfer along the evaporative cooling channels, allowing for the precise determination of temperature and humidity profiles.

3. M-cycle numerical 1D model

Parameters

A	m^2	*Area*
c	$W/(kg\ K)$	*Specific heat capacity for incompressible substances*
c_p	$W/(kg\ K)$	*Specific heat capacity at constant pressure*
h	m	*Discretization cell step size*
h_c	$W/(m^2\ K)$	*Convective heat transfer coefficient*
h_m	$kg_{da}/(s\ m^2)$	*Mass transfer coefficient*
i	J/kg_{da}	*Specific enthalpy of humid air*
i_{lv}	J/kg	*Specific latent heat of vaporization*
k	$W/(m\ K)$	*Thermal conductivity*
L	m	*HMX length*
Le_f	$-$	*Lewis factor*
M	kg/mol	*Molar mass*
$\dot{m}$	kg/s	*Mass flow rate*
p	Pa	*Pressure*
$\dot{Q}$	W	*Enthalpy flow rate*
r_m	$-$	*Mass recirculation ratio*
R	$J/(mol\ K)$	*Ideal gas constant*
s	m	*Thickness*
T	K	*Temperature*
U	$W/(m^2\ K)$	*Global heat transfer coefficient*
V	m^3	*Volume*
$\dot{V}$	m^3/s	*Volume flow rate*
W	m	*HMX width*
x	m	*Longitudinal coordinate*
Δ		*Difference*
ε	$-$	*Effectiveness*
ρ	kg_v/m^3	*Mass vapor partial density*
ω	kg_v/kg_{da}	*Specific humidity*
CC	W	*Cooling Capacity*

SCC	J/kg	*Specific Cooling Capacity*
VCC	W/m^3	*Volumetric Cooling Capacity*
$VICC$	W/m^3	*Volumetric Indoor Cooling Capacity*

Subscripts

da	*Dry air*	v	*Vapor*
u	*Humid air*	e	*Evaporated*
f	*Feed*	sat	*Saturation*
d	*Dry channel*	i	*Interface*
w	*Wet channel*	0	*Reference*
s	*Sensible*	l	*Latent*
in	*Inlet*	out	*Outlet*
$indoor$	*Cooled environment*	HMX	*Heat and mass exchanger*
wb	*Wet-bulb*	dp	*Dew-point*

This chapter presents an iterative numerical model for analyzing an indirect counterflow heat and mass exchanger (HMX) operating under steady-state conditions. The model is one-dimensional (1D) and is based on the discretization of the HMX along the longitudinal direction (Figure 3.1-A). For each discrete element, heat and mass transfer processes are evaluated by distinguishing three regions: the dry channel bulk, the liquid film interface and the wet channel bulk (Figure 3.1-B).

In the following analysis, a one-dimensional reference system is adopted, with the x-axis oriented from the dry channel inlet to its outlet, as shown in Figure 3.1-A. After presenting the model, the governing equations will be developed for a parallel-channel geometry.

With reference to Figure 3.2, the air–liquid interface area A is defined as the product of the depth of the exchange surface W and its longitudinal extension L. To enable numerical calculations, an infinitesimal surface element dA is introduced. For a single

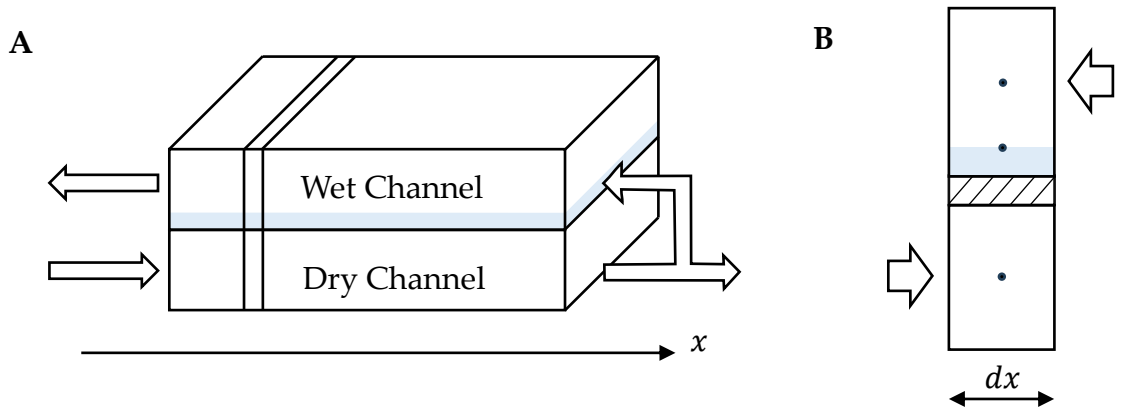

Figure 3.1. HMX discretization (A) and infinitesimal control volume with the evaluation points (B).

discretized cell, this infinitesimal area corresponds to the product of the channel depth W and an infinitesimal increment along the longitudinal coordinate dx

$$dA = W\ dx \tag{3.1}$$

This discretization framework forms the basis of the numerical model, enabling the systematic application of conservation equations to each control volume.

To simplify the one-dimensional problem, the following assumptions are typically adopted:

1. The channel height is small compared to its width, so the flow can be considered one-dimensional;
2. The cooler is perfectly insulated from the surroundings;
3. The flow is in steady-state regime;
4. The fluids are treated as ideal gases;
5. Longitudinal heat conduction and mass diffusion are negligible;
6. Radiative heat transfer is neglected.

Since the objective is to analyze the behavior of an indirect evaporative heat exchanger, it is necessary to account for the energy exchanges between the interacting fluids, which involve both sensible heat transfer and mass transfer.

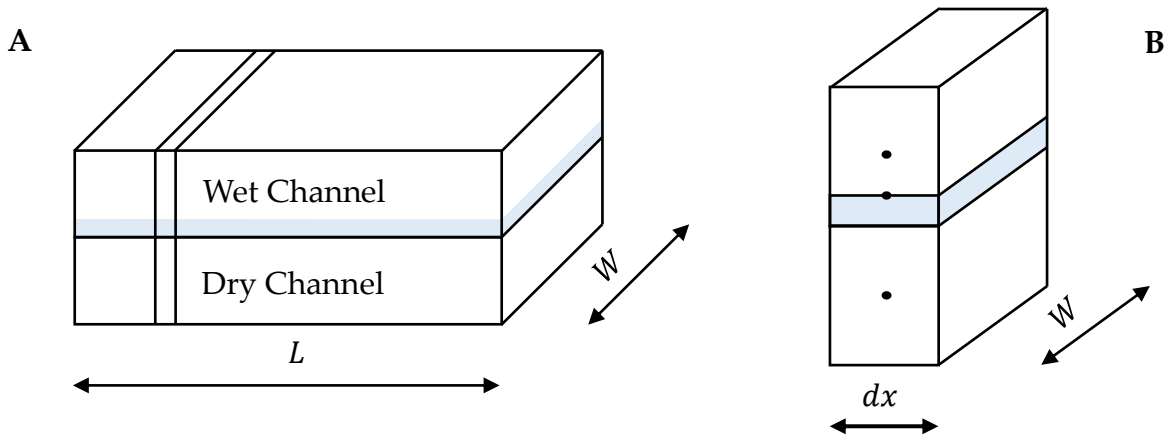

Figure 3.2. Geometric parameters defining the exchange area for the HMX (A) and for a discretized cell (B).

3.1. Dry channel analysis

In the dry channel, energy exchange occurs only through the sensible heat transfer between the airflow and the heat exchange surface, as no mass transfer takes place. This heat exchange is driven by the temperature difference between the dry channel airflow and the exchange wall.

In the wet channel, energy is exchanged between the airflow and the liquid film through two distinct mechanisms. The first is sensible heat transfer, occurring due to the temperature difference between the air-liquid interface and the wet channel airflow. The second is the energy associated with the evaporated mass of the liquid film that enters the wet channel flow. This phenomenon also leads to an increase in the vapor content in the airflow due to mass transfer from the liquid film.

The transfer of energy through these mechanisms is hindered by different resistances. Considering the mechanisms described for both channels, along with the presence of the impermeable wall that separates them and the thin stationary liquid film, various resistances associated with the different energy transfer phenomena can be identified. As illustrated in Figure 3.3, these include convective resistance within the dry channel, conductive resistance through the exchange wall, thermal resistance of the liquid film

on the wet side of the wall, and, finally, both convective and mass transfer resistances in the wet channel.

In the dry channel, the total mass flow rate remains constant along its entire length. Consequently, within a control volume, there are no variations in the mass flow rate of either dry air $\dot{m}_{da,d}$ or water vapor $\dot{m}_{v,d}$ (Figure 3.4-A). Since the fluid exchanges energy with the wall, its enthalpy power $\dot{Q}_d$ varies along with the longitudinal coordinate.

Given that the dry air mass flow rate is constant, it can be used to express the change in enthalpy power $d\dot{Q}_d$ along the channel, in terms of the specific enthalpy of the humid air mixture i_d, as defined by equation 2.32 (Figure 3.4-B). This leads to the expression

$$d\dot{Q}_d = \dot{m}_{da,d}\, di_d \qquad 3.2$$

where $\dot{m}_{da,d}$ represents the dry air mass flow rate in the dry channel, and di_d is the variation in the specific enthalpy of the humid air mixture in the dry channel.

The sensible heat flux transferred through the exchange wall is denoted as $d\dot{Q}_{sd}$. This value is considered positive here when heat is transferred from the dry channel fluid to the wall, as illustrated in Figure 3.4-B.

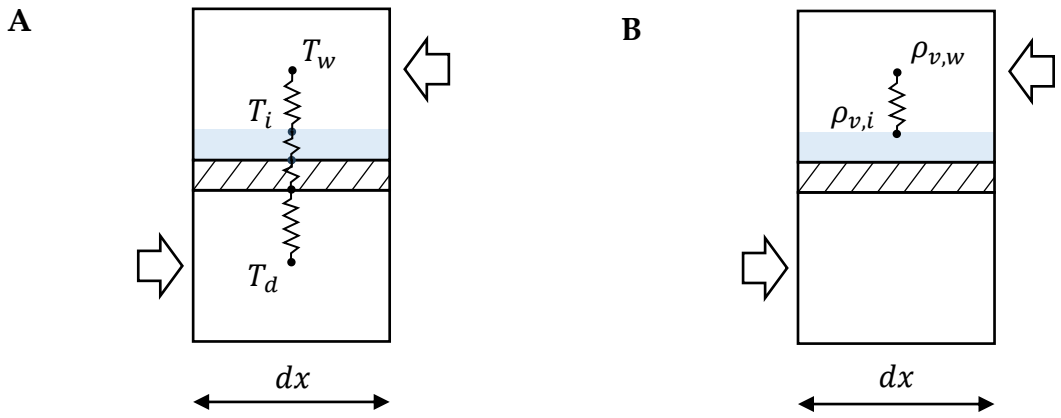

Figure 3.3 Thermal resistances (A) and mass transfer resistance (B) for the infinitesimal element.

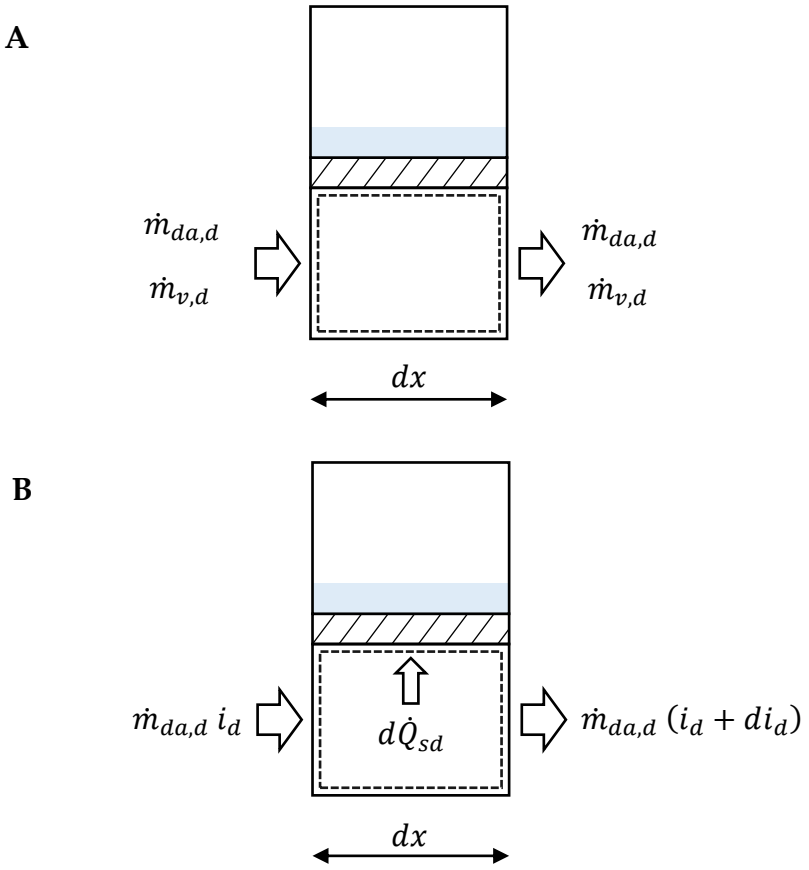

Figure 3.4. Dry channel control volume. Mass balance (A) and energy balance (B).

Since the exchanger is assumed to be thermally insulated from the external environment, the sensible heat flux transferred through the exchange wall must exactly correspond to the variation in enthalpy power of the dry channel fluid, as expressed by equation 3.2.

According to the adopted convention, a positive heat flux implies a reduction in the enthalpy power of the dry channel fluid along its flow direction. Therefore, the relationship between the sensible heat flux transferred through the exchange wall and the variation in enthalpy power of the fluid is given by

$$d\dot{Q}_d = -d\dot{Q}_{sd} \qquad 3.3$$

By combining equations 3.2 and 3.3, we obtain

$$\dot{m}_{da,d}\, di_d = -d\dot{Q}_{sd} \qquad 3.4$$

This equation shows that the change in enthalpy of the dry channel airflow is entirely determined by the sensible heat transferred through the exchange wall.

3.2. Wet channel analysis

In the wet channel, the evaporation of the liquid film on the wall increases the vapor content $\dot{m}_{v,w}$ along the flow direction while the dry air mass flow rate $\dot{m}_{da,w}$ remains constant (Figure 3.5-A). As a result, the enthalpy power of the fluid $\dot{Q}_w$ varies along the longitudinal coordinate due to both sensible power transfer between the fluid and the liquid film $\dot{Q}_{sw}$, and the energy associated with liquid evaporation $\dot{Q}_{ew}$. Since the dry air mass flow rate is constant, it can be used to express the variation in enthalpy power of the wet channel fluid $d\dot{Q}_w$ along the longitudinal direction through the specific enthalpy of the humid air mixture i_w, as defined by equation 2.32 (Figure 3.5-B). This leads to the expression

$$d\dot{Q}_w = \dot{m}_{da,w}\, di_w \qquad 3.5$$

where $\dot{m}_{da,w}$ represents the dry air mass flow rate in the wet channel, and di_w is the variation in the specific enthalpy of the humid air mixture in the wet channel.

Energy fluxes directed from the liquid film to the wet channel fluid are considered positive here, as shown in Figure 3.5-B.

Again, since the exchanger is assumed to be thermally insulated from the external environment, the variation in enthalpy power of the wet channel fluid, as expressed by equation 3.5, corresponds to the power exchanged with the liquid film. According to the adopted convention, a positive energy transfer between the airflow and the liquid film results in an increase in the enthalpy power of the wet channel fluid along the flow direction. However, since the wet channel operates in counterflow (the fluid

moves in the negative x-direction), a positive energy gain corresponds to a negative gradient in the spatial reference frame. Consequently, the following relationship is obtained

$$d\dot{Q}_w = -\left(d\dot{Q}_{sw} + d\dot{Q}_{ew}\right) \qquad 3.6$$

By combining equations 3.5 and 3.6, the equation yields

$$\dot{m}_{da,w}\, di_w = -\left(d\dot{Q}_{sw} + d\dot{Q}_{ew}\right) \qquad 3.7$$

This equation highlights that the energy gained by the airflow in the wet channel comes from both sensible heat transfer with the liquid film and the enthalpy carried by the vapor added to the flow through evaporation.

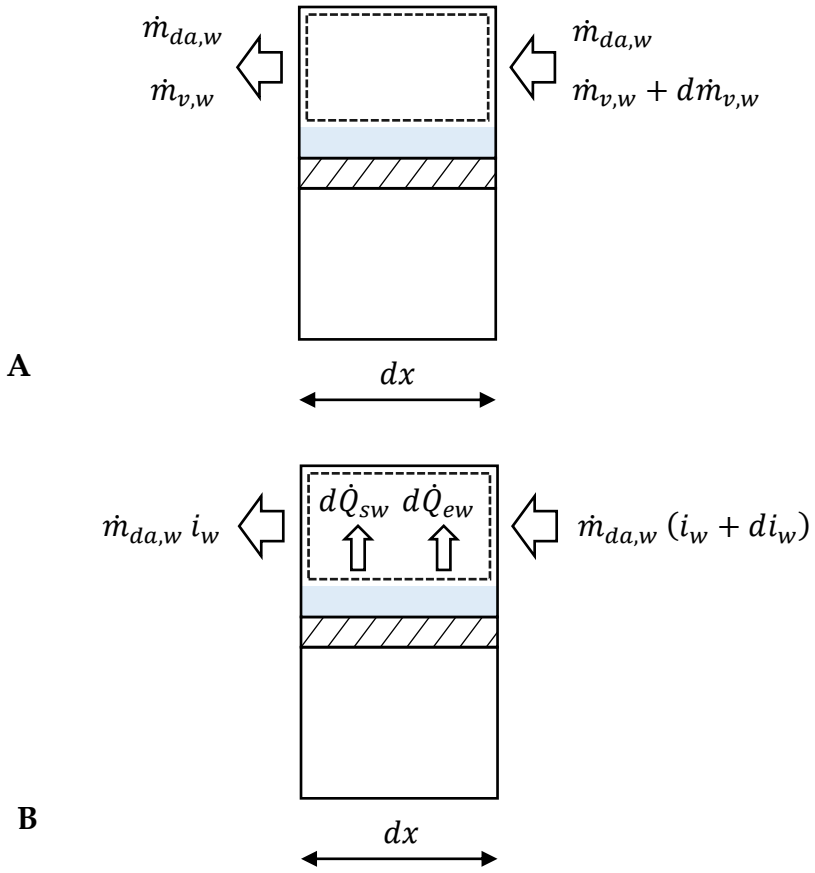

Figure 3.5. Wet channel control volume. Mass balance (A) and energy balance (B).

3.3. Film channel analysis

Regarding the analysis of the liquid film, assuming steady-state conditions and a static fluid, i.e., no mass flow in the longitudinal direction, the mass balance, with reference to Figure 3.6-A, is given by the equation

$$d\dot{m}_e = d\dot{m}_f \tag{3.8}$$

where $d\dot{m}_e$ represents the amount of liquid evaporated within the control volume, while $d\dot{m}_f$ is the amount of liquid that must be supplied to ensure that the mass of water in the film remains constant over time.

The energy balance of the liquid film, with reference to Figure 3.6-B, is expressed as

$$d\dot{Q}_{sd} + d\dot{Q}_f = d\dot{Q}_{sw} + d\dot{Q}_{ew} \tag{3.9}$$

According to the conventions adopted here, the term $d\dot{Q}_{sd}$ represents the energy transferred from the dry channel to the film and is therefore regarded as an energy gain. $d\dot{Q}_f$ denotes an additional energy gain, as it corresponds to the enthalpy carried by the feed liquid reintroduced into the film. $d\dot{Q}_{sw}$ accounts for the sensible energy exchanged from the film to the wetted channel due to temperature difference and is thus treated as an energy loss. Finally, $d\dot{Q}_{ew}$ represents another energy loss, associated with the enthalpy of the vapor leaving the film during evaporation.

When all these energy fluxes are balanced, the system operates under steady-state conditions, with no net accumulation of energy within the liquid film.

By substituting equations 3.3 and 3.6 into equation 3.9, the energy balance equation between the two channels is obtained

$$-d\dot{Q}_d + d\dot{Q}_f = -d\dot{Q}_w \tag{3.10}$$

Substituting equations 3.2 and 3.5 into this relation leads to

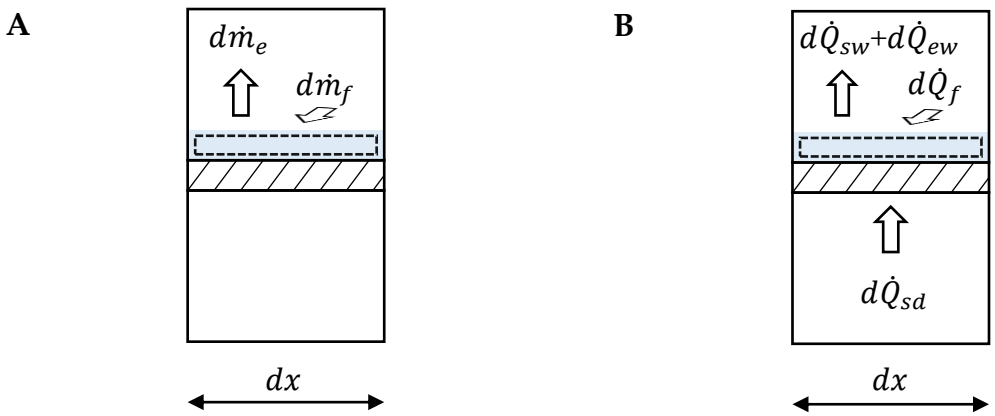

Figure 3.6. Liquid film control volume. Mass balance (A) and energy balance (B).

$$-\dot{m}_{da,d}\, di_d + d\dot{Q}_f = -\dot{m}_{da,w}\, di_w \qquad 3.11$$

This equation shows that, at steady state, the net energy exchanged between the dry and wet channels is balanced by the energy carried by the feed liquid into the film.

3.4. Sensible heat transfer

In the dry channel control volume (Figure 3.4), sensible energy is transferred from the air through the separating wall. Referring to the thermal resistances in Figure 3.3, only sensible energy transfer occurs from the dry channel air to the air-water interface in the wet channel, assuming a stationary liquid film. The process between these two points involves convective energy transfer within the fluid of the dry channel, conductive transfer through the separating wall, and conductive transfer through the stationary liquid film. It is worth noting that radiative exchange between the walls is omitted from this balance; given the compact design and the thermal levels involved, the radiative contribution is considered secondary compared to the high-intensity convective and evaporative phenomena occurring at the interface.

According to the definition of the overall heat transfer coefficient in equation 2.120, the heat transfer rate from the dry channel to the air-water interface can be expressed as

$$d\dot{Q}_{sd} = U_{i\leftarrow d}\,(T_d - T_i)\,dA \qquad 3.12$$

where T_d is the bulk temperature of the fluid in the dry channel, T_i is the temperature at the air-water interface, dA is the infinitesimal heat exchange surface, and $U_{i\leftarrow d}$ is the global heat transfer coefficient from the airflow in the dry channel to the air-water interface. Based on the series resistance model (eq. 2.121), $U_{i\leftarrow d}$ is calculated as.

$$U_{i\leftarrow d} = \left(\frac{1}{h_{c,d}} + \sum_{j=1}^{N_{layer}} \frac{s_{w,j}}{k_{w,j}}\right)^{-1} \qquad 3.13$$

where $s_{w,\mathrm{j}}$ and $k_{w,\mathrm{j}}$ represent the thickness and the thermal conductivity of the j-th layer of the exchange wall, respectively, while $h_{c,d}$ denotes the convective heat transfer coefficient of the dry channel.

Considering the control volume in the wet channel, as shown in Figure 3.5, a portion of the energy exchanged between the wet channel fluid and the air-water interface occurs via sensible heat transfer. With reference to the thermal resistance in Figure 3.3, this transfer takes place via convective exchange between the air in the wet channel and the air-water interface, which can be described by Newton's law of cooling (2.60)

$$d\dot{Q}_{sw} = h_{c,w}\,(T_i - T_w)\,dA \qquad 3.14$$

where $h_{c,w}$ is the convective heat transfer coefficient in the wet channel, and T_w is the bulk temperature of the fluid in the wet channel.

3.5. Latent heat transfer

Considering the control volume in the wet channel shown in Figure 3.5, a portion of the energy exchanged between the wet channel fluid and the air-water interface occurs as latent heat transfer. This corresponds to the evaporated liquid mass $\dot{m}_e$ and

represents the energy associated with evaporation. It is therefore calculated using the specific enthalpy of saturated vapor at the interface temperature $i_{v,i}$

$$d\dot{Q}_{ew} = d\dot{m}_e \, i_{vi} \qquad 3.15$$

The infinitesimal mass flow rate of evaporated mass corresponds to the variation in the total amount of vapor in the section. Evaporation increases the vapor content of the flow, but since the humid air in the wet channel flows in the opposite direction to the x-axis, a positive evaporation rate corresponds to a negative gradient of the vapor mass flow rate in the spatial domain

$$d\dot{m}_{v,w} = -d\dot{m}_e \qquad 3.16$$

Dividing both terms by the dry air mass flow rate $\dot{m}_{da,w}$ gives a relation for the change in specific humidity across the section

$$d\omega_w = \frac{d\dot{m}_{v,w}}{\dot{m}_{da,w}} = -\frac{d\dot{m}_e}{\dot{m}_{da,w}} \qquad 3.17$$

With this relation, the change in specific humidity is directly related to the evaporated mass flow, following the conventions adopted in this study.

3.6. Feed liquid energy

The energy contribution from the feed liquid $d\dot{Q}_f$ identified in equation 3.11 via the film energy balance (Figure 3.6-B), can be calculated as

$$d\dot{Q}_f = d\dot{m}_f \, i_f \qquad 3.18$$

where $d\dot{m}_f$ represents the mass of the reintroduced liquid, and i_f is its specific enthalpy. According to the film mass balance derived in equation 3.8, the supply water mass is equal to the evaporated water mass $d\dot{m}_e$. Assuming that water behaves as an incompressible fluid, the specific enthalpy can be expressed as

$$d\dot{Q}_f = d\dot{m}_f \, c_f \, (T_f - T_0) \qquad 3.19$$

where c_f is the specific heat capacity of the feed liquid, and T_f is its temperature.

By incorporating equations 3.8 and 3.16, equation 3.19 can be rewritten in as

$$d\dot{Q}_f = -\dot{m}_{da,w} \, d\omega_w \, c_f \, (T_f - T_0) \qquad 3.20$$

This expression shows that the energy supplied by the feed liquid is directly related to the variation in specific humidity within the wet channel, according to the adopted conventions.

3.7. Perfect gas in dry channel

In the dry channel there is no mass variation for either dry air or water vapor. In this condition, under the assumption of a perfect gas mixture, the enthalpy of humid air depends only on the fluid temperature. Consequently, the energy contained in the mixture, as defined in equation 3.4, can be determined using the following relation

$$\dot{m}_{da,d} \, di_d = \dot{m}_{da,d} \, c_{p,ud} \, dT_d \qquad 3.21$$

where $\dot{m}_{da,d}$ represents the mass flow rate of dry air in the dry channel, $c_{p,ud}$ denotes the specific heat capacity of the humid air mixture, calculated according to equation 2.33, and dT_d represents the temperature change of the mixture within the control volume.

By applying the energy balance equation for the dry channel 3.3 and substituting equations 3.21 and 3.12, the following expression is obtained

$$\dot{m}_{da,d} \, c_{p,ud} \, dT_d = -U_{i \leftarrow d} \, (T_d - T_i) \, dA \qquad 3.22$$

This equation represents the governing relation for energy exchange in the dry channel, considering the flow as a perfect gas mixture.

3.8. Hasan model

In the model proposed by Hasan [92], the mass transfer coefficient is correlated to the difference in specific humidity between the air–water interface and the bulk flow. This approach follows the formulation of Lewis [90], already presented in section 2.13. The evaporated mass flow rate is therefore calculated as

$$d\dot{m}_e = h_{m,w}\,(\omega_i - \omega_w)\,dA \qquad 3.23$$

Multiplying and dividing the left-hand side by the dry air mass flow rate in the wet channel $\dot{m}_{da,w}$ and applying relation 3.17, this expression can be rewritten as

$$\dot{m}_{da,w}\,d\omega_w = -h_{m,w}\,(\omega_i - \omega_w)\,dA \qquad 3.24$$

The enthalpy flux associated with evaporation is expressed using the latent heat of vaporization

$$d\dot{Q}_{ew} = i_{lv}\,d\dot{m}_e \qquad 3.25$$

The energy balance of the liquid film, which governs the coupling between the two airflows, is given by

$$d\dot{Q}_d = d\dot{Q}_w \qquad 3.26$$

By combining equations 3.8 and 3.16, this balance yields

$$\dot{m}_{da,d}\,c_{p,ud}\,dT_d = \dot{m}_{da,w}\,di_w \qquad 3.27$$

Furthermore, inserting into relation 3.7 the sensible heat transfer term from equation 3.14 and the evaporative contribution from equations 3.23 and 3.25, the following expression is obtained

$$\dot{m}_{da,w}\, di_w = -\left[h_{c,w}\,(T_i - T_w)\, dA + i_{lv}\, h_{m,w}\,(\omega_i - \omega_w)\, dA\right] \qquad 3.28$$

The specific enthalpy of humid air, as defined in equation 2.32, can be written as

$$i = c_{p,da}\,(T - T_0) + \omega\left[i_{lv} + c_{p,v}\,(T - T_0)\right] \qquad 3.29$$

which can be expanded as

$$i = c_{p,da}\,(T - T_0) + \omega\, c_{p,v}\,(T - T_0) + \omega\, i_{lv} \qquad 3.30$$

Introducing the specific heat capacity of humid air $c_{p,u}$, as defined in equation 2.33, this relation can be rewritten as

$$i = c_{p,u}\,(T - T_0) + \omega\, i_{lv} \qquad 3.31$$

The air temperature can then be expressed as

$$T = T_0 + \frac{i - \omega\, i_{lv}}{c_{p,u}} \qquad 3.32$$

By applying this expression both to the bulk temperature of the wet channel and to the film temperature, and setting $T_0 = 0$, equation 3.28 becomes

$$\dot{m}_{da,w}\, di_w = -\left[h_{c,w}\left(\frac{i_i - \omega_i\, i_{lv}}{c_{p,u,i}} - \frac{i_w - \omega_w\, i_{lv}}{c_{p,u,w}}\right) dA + i_{lv}\, h_{m,w}\,(\omega_i - \omega_w)\, dA\right] \qquad 3.33$$

Neglecting variations in the humid air specific heat between interface and bulk, and expanding the right-hand side, yields

$$\dot{m}_{da,w}\, di_w = -\left[\frac{h_{c,w}}{c_{p,u}}\,(i_i - i_w)\, dA - \frac{h_{c,w}}{c_{p,u}}\, i_{lv}\,(\omega_i - \omega_w)\, dA \right.$$
$$\left. + i_{lv}\, h_{m,w}\,(\omega_i - \omega_w)\, dA\right] \qquad 3.34$$

Multiplying and dividing the second term by $h_{m,w}$, the humidity-related terms can be grouped as

$$\dot{m}_{da,w}\, di_w = -\left[\frac{h_{c,w}}{c_{p,u}}\,(i_i - i_w)\, dA \right.$$
$$\left. + i_{lv}\, h_{m,w}\left(1 - \frac{h_{c,w}}{c_{p,u}\, h_{m,w}}\right)(\omega_i - \omega_w)\, dA\right] \qquad 3.35$$

At this point, the term containing the ratio of transfer coefficients is recognized as the Lewis factor 2.153

$$Le_f = \frac{h_{c,w}}{c_{p,u}\, h_{m,w}} \qquad 3.36$$

By imposing the unitary Lewis factor, as suggested by Lewis [90] and derived in chapter 2.13, one obtains

$$Le_f = \frac{h_{c,w}}{c_{p,u}\, h_{m,w}} = 1 \Rightarrow h_{m,w} = \frac{h_{c,w}}{c_{p,u}} \qquad 3.37$$

Thus, equation 3.35 simplifies to

$$\dot{m}_{da,w}\, di_w = -h_{m,w}\,(i_i - i_w)\, dA \qquad 3.38$$

This formulation demonstrates that energy transfer in the wet channel can be modeled as a process driven by the enthalpy difference between the air–water interface and the bulk flow, following the procedure first introduced by Merkel [93] in his study of evaporative cooling towers.

At this stage, the governing system of equations proposed by Hasan is composed of relations 3.22, 3.24, 3.38 and 3.26, which together form the local calculation model

$$\begin{aligned}
&\dot{m}_{da,d}\, c_{p,ud}\, dT_d = -U_{i\leftarrow d}\,(T_d - T_i)\, dA \\
&\dot{m}_{da,w}\, d\omega_w = -h_{m,w}\,(\omega_i - \omega_w)\, dA \\
&\dot{m}_{da,w}\, di_w = -h_{m,w}\,(i_i - i_w)\, dA \\
&\dot{m}_{da,d}\, c_{p,ud}\, dT_d = \dot{m}_{da,w}\, di_w
\end{aligned} \qquad 3.39$$

In this system, the interface humidity ratio ω_i and the interface specific enthalpy i_i are functions of the interface temperature T_i. Under the assumption of saturation at the interface, the relative humidity is set equal to unity, and the specific humidity is therefore calculated from relation 2.28

$$\omega_i = \frac{M_v}{M_{da}}\,\frac{p_{v,sat}(T_i)}{p - p_{v,sat}(T_i)} \qquad 3.40$$

while the specific enthalpy at the interface, following equation 2.32, is given by

$$i_i = c_{p,da}\,(T_i - T_0) + \omega_i\left[i_{lv} + c_{p,v}\,(T_i - T_0)\right] \qquad 3.41$$

For a parallel-plate heat exchanger, the infinitesimal exchange area can be calculated using relation 3.1, and the complete system of equations can thus be written as

$$\begin{aligned}
&\dot{m}_{da,d}\, c_{p,ud}\, dT_d = -U_{i\leftarrow d}\,(T_d - T_i)\, W\, dx \\
&\dot{m}_{da,w}\, d\omega_w = -h_{m,w}\,(\omega_i - \omega_w)\, W\, dx \\
&\dot{m}_{da,w}\, di_w = -h_{m,w}\,(i_i - i_w)\, W\, dx \\
&\dot{m}_{da,d}\, c_{p,ud}\, dT_d = \dot{m}_{da,w}\, di_w
\end{aligned} \qquad 3.42$$

Dividing the governing equations by dx yields the local differential form used for spatial discretization

$$\dot{m}_{da,d}\, c_{p,ud}\, \frac{dT_d}{dx} = -U_{i\leftarrow d}\, (T_d - T_i)\, W$$

$$\dot{m}_{da,w}\, \frac{d\omega_w}{dx} = -h_{m,w}\, (\omega_i - \omega_w)\, W$$

$$\dot{m}_{da,w}\, \frac{di_w}{dx} = -h_{m,w}\, (i_i - i_w)\, W$$

$$\dot{m}_{da,d}\, c_{p,ud}\, \frac{dT_d}{dx} = \dot{m}_{da,w}\, \frac{di_w}{dx}$$

3.43

In the first three equations, the unknown fields T_d, ω_w, i_w appear both in their algebraic form and as differential terms. The first three equations are ordinary differential equations (ODEs) in space and are well suited for solution via finite-difference or explicit ODE integration schemes. By isolating the derivatives, the system can be written in the standard ODE form

$$\frac{dT_d}{dx} = -\frac{U_{i\leftarrow d}\, (T_d - T_i)\, W}{\dot{m}_{da,d}\, c_{p,ud}} = f_1(T_d, T_i) \qquad 3.44$$

$$\frac{d\omega_w}{dx} = -\frac{h_{m,w}\, (\omega_i - \omega_w)\, W}{\dot{m}_{da,w}} = f_2(\omega_w, T_i) \qquad 3.45$$

$$\frac{di_w}{dx} = -\frac{h_{m,w}\, (i_i - i_w)\, W}{\dot{m}_{da,w}} = f_3(i_w, T_i) \qquad 3.46$$

Using finite-difference or ODE integrators provides approximations of the solution at the discretization nodes. If the classical fourth-order Runge–Kutta (RK4) method is adopted (see Chapter 2.14), the RK4 equations for the three dependent variables are given by

$$T_{d,n+1} \cong T_{d,n} + \frac{h}{6}\left(K_{f_1,1} + 2\,K_{f_1,2} + 2\,K_{f_1,3} + K_{f_1,4}\right) \quad 3.47$$

$$\omega_{w,n+1} \cong \omega_{w,n} + \frac{h}{6}\left(K_{f_2,1} + 2\,K_{f_2,2} + 2\,K_{f_2,3} + K_{f_2,4}\right) \quad 3.48$$

$$i_{w,n+1} \cong i_{w,n} + \frac{h}{6}\left(K_{f_3,1} + 2\,K_{f_3,2} + 2\,K_{f_3,3} + K_{f_3,4}\right) \quad 3.49$$

where h represents the discretization step and each $K_{f_j,k}$ denotes the usual RK4 stage evaluation of the function f_j at the appropriate intermediate point.

Assuming a sufficiently small step size h so that finite increments approximate the corresponding derivatives, the fourth equation, representing the global energy coupling between the two channels, can be expressed in discretized difference form as

$$\dot{m}_{da,d}\, c_{p,ud}\left(T_{d,n+1} - T_{d,n}\right) = \dot{m}_{da,w}\left(i_{w,n+1} - i_{w,n}\right) \quad 3.50$$

Because the wet-channel flow is countercurrent with respect to both the dry-channel flow and the exchanger longitudinal axis, the solution is advanced in the wet channel from node $n+1$ to node n. Consequently, the marching system is arranged to compute the unknowns at node n from values known at node $n+1$. Written accordingly, the discrete update system becomes

$$\begin{aligned}
T_{d,n+1} &\cong T_{d,n} + \frac{h}{6}\left(K_{f_1,1} + 2\,K_{f_1,2} + 2\,K_{f_1,3} + K_{f_1,4}\right) \\
\omega_{w,n} &\cong \omega_{w,n+1} - \frac{h}{6}\left(K_{f_2,1} + 2\,K_{f_2,2} + 2\,K_{f_2,3} + K_{f_2,4}\right) \\
i_{w,n} &\cong i_{w,n+1} - \frac{h}{6}\left(K_{f_3,1} + 2\,K_{f_3,2} + 2\,K_{f_3,3} + K_{f_3,4}\right) \\
\dot{m}_{da,d}\, c_{p,ud}\left(T_{d,n+1} - T_{d,n}\right) &= \dot{m}_{da,w}\left(i_{w,n+1} - i_{w,n}\right)
\end{aligned} \quad 3.51$$

In this discrete system the unknowns to be solved at each step are $T_{d,n+1}$, $\omega_{w,n}$, $i_{w,n}$ and T_i. The starting values for the step are $T_{d,n}$, $\omega_{w,n+1}$, $i_{w,n+1}$. Note that T_i is implicitly

present in all RK4 stage coefficients $K_{f_{j,k}}$, since the functions f_1, f_2 and f_3 depend explicitly on the interface state.

Rewriting the four discrete relations in residual form yields a nonlinear system of four equations in four unknowns

$$\begin{aligned} &F_1(T_{d,n+1}, T_i) = 0 \\ &F_2(\omega_{w,n}, T_i) = 0 \\ &F_3(i_{w,n}, T_i) = 0 \\ &F_4(T_{d,n+1}, i_{w,n}) = 0 \end{aligned} \qquad 3.52$$

This nonlinear algebraic system is solved at each spatial step using the Newton–Raphson method (or another suitable multidimensional solver), iterating until the residuals fall below the prescribed convergence tolerance.

In Hasan's formulation, the mass transfer coefficient $h_{m,w}$ is applied to the specific humidity gradient, effectively treating it as Lewis in his 1922 work. However, Lewis' demonstration holds strictly for direct evaporative processes, based on the use of equation 2.146 derived from relation 2.130, which in turn assumes no additional energy inputs to the flow (as obtained from energy balance 2.127). In the context of indirect evaporative channels, this fundamental assumption is violated due to the sensible heat transferred from the dry channel through the wall; therefore, the direct extension of Lewis's conclusions to this configuration is not theoretically rigorously justified.

A second critical issue concerns the formulation of the energy balances. In the wet channel, the humid air flow receives vapor at a given temperature, bringing with it an enthalpy contribution associated with the vapor. Multiplying the evaporated mass flow solely by the latent heat of vaporization, as in equation 3.25, neglects the sensible energy carried by the vapor, resulting in an underestimation of the enthalpy change in

the wet channel. Furthermore, the energy balance of the liquid film in equation 3.26 omits the energy input from the reintroduced feed liquid. This also results in a systematic energy deficit in the model.

3.9. Proposed Model

In the proposed model, the evaporated water mass flow rate is driven by the difference between the vapor partial density at the interface and that in the bulk flow, as expressed in equation 2.115. This relation can be written as

$$d\dot{m}_e = h_{m,w}\left(\rho_{v,i} - \rho_{v,w}\right) dA \qquad 3.53$$

For perfect gases, the vapor partial density at the interface $\rho_{v,i}$ can be obtained from equation 2.13 and expressed in terms of pressure and temperature at the interface as

$$\rho_{v,i} = \frac{p_{v,i}\, M_v}{R\, T_i} \qquad 3.54$$

Assuming saturation conditions at the interface, this becomes

$$\rho_{v,i} = \frac{p_{v,sat}(T_i)\, M_v}{R\, T_i} \qquad 3.55$$

The bulk vapor partial density $\rho_{v,w}$ can be calculated using equation 2.111, which relates the total vapor mass flow rate across the section $\dot{m}_{v,w}$ to the total volumetric flow rate $\dot{V}_w$

$$\rho_{v,w} = \frac{\dot{m}_{v,w}}{\dot{V}_w} \qquad 3.56$$

Substituting equations 3.55 and 3.56 into equation 3.53, the evaporated mass flow rate becomes

$$d\dot{m}_e = h_{m,w} \left[\frac{p_{v,sat}(T_i)\, M_v}{R\, T_i} - \frac{\dot{m}_{v,w}}{\dot{V}_w} \right] dA \qquad 3.57$$

Dividing both sides of this equation by the total dry air mass flow rate $\dot{m}_{da,w}$ and applying equation 3.17, which relates the evaporated mass flow to the variation of specific humidity in the wet channel, yields

$$d\omega_w = -h_{m,w} \left[\frac{p_{v,sat}(T_i)\, M_v}{R\, T_i\, \dot{m}_{da,w}} - \frac{\omega_w}{\dot{V}_w} \right] dA \qquad 3.58$$

With this relationship established for the variation of total humidity in the wet channel, the energy associated with the evaporated vapor mass flow rate can now be determined using equations 3.15 and 3.17.

$$d\dot{Q}_{ew} = -\dot{m}_{da,w}\, d\omega_w\, i_{vi} \qquad 3.59$$

Here, i_{vi} is the specific enthalpy of the vapor evaluated at the evaporation temperature, i.e. the interface temperature. Assuming ideal gas behavior for the vapor, it can be written as

$$i_{vi} = i_{lv0} + c_{p,v}\,(T_i - T_0) \qquad 3.60$$

where i_{lv0} represents the latent heat of evaporation of water evaluated at the reference temperature T_0. Substituting into equation 3.59 gives the evaporation enthalpy flux

$$d\dot{Q}_{ew} = -\dot{m}_{da,w}\, d\omega_w \left[i_{lv0} + c_{p,v}\,(T_i - T_0) \right] \qquad 3.61$$

Along the wet channel, the enthalpy of humid air varies due to changes in both fluid temperature and vapor content, which affect the specific humidity of the flow. Differentiating the specific enthalpy of humid air (eq 2.32) for a perfect gas mixture with constant specific heat capacity leads to

$$di_w = \frac{\partial i_w}{\partial T_w}\, dT_w + \frac{\partial i_w}{\partial \omega_w}\, d\omega_w \tag{3.62}$$

which expands to

$$di_w = \left(c_{p,a} + \omega_w\, c_{p,v}\right) dT_w + \left[i_{lv0} + c_{p,v}\,(T_w - T_0)\right] d\omega_w \tag{3.63}$$

Multiplying by the dry air mass flow rate in the wet channel gives

$$\begin{aligned} \dot{m}_{da,w}\, di_w = {} & \dot{m}_{da,w}\left(c_{p,a} + \omega_w\, c_{p,v}\right) dT_w \\ & + \dot{m}_{da,w}\, d\omega_w \left[i_{lv0} + c_{p,v}\,(T_w - T_0)\right] \end{aligned} \tag{3.64}$$

From equation 3.7, this must equal the negative of the sum of the sensible heat flux and the enthalpy flux of evaporated vapor. Noting that the last term of equation 3.64 is similar to equation 3.61, except for the sign and the use of the bulk temperature of the wet channel T_w instead of the interface temperature T_i. By adding and subtracting the interface temperature in the last term of equation 3.64 gives

$$\begin{aligned} & \dot{m}_{da,w}\, d\omega_w \left[i_{lv0} + c_{p,v}\,(T_w + T_i - T_i - T_0)\right] \\ & \qquad = \dot{m}_{da,w}\, d\omega_w \left[i_{lv0} + c_{p,v}\,(T_i - T_0)\right] \\ & \qquad + \dot{m}_{da,w}\, d\omega_w\, c_{p,v}\,(T_w - T_i) \end{aligned} \tag{3.65}$$

Thus, equation 3.64 becomes

$$\begin{aligned} \dot{m}_{da,w}\, di_w = {} & \dot{m}_{da,w}\left(c_{p,a} + \omega_w\, c_{p,v}\right) dT_w + \dot{m}_{da,w}\, d\omega_w \left[i_{lv0} + c_{p,v}\,(T_i - T_0)\right] \\ & + \dot{m}_{da,w}\, d\omega_w\, c_{p,v}\,(T_w - T_i) \end{aligned} \tag{3.66}$$

Equating to equation 3.7 gives

$$\dot{m}_{da,w}\left(c_{p,a}+\omega_w\,c_{p,v}\right)dT_w+\dot{m}_{da,w}\,d\omega_w\left[i_{lv0}+c_{p,v}\,(T_i-T_0)\right]$$
$$+\dot{m}_{da,w}\,d\omega_w\,c_{p,v}\,(T_w-T_i)=-\left(d\dot{Q}_{sw}+d\dot{Q}_{ew}\right) \qquad 3.67$$

Substituting the contribution of the enthalpy flux just obtained as in equation 3.61, the following expression is obtained

$$\dot{m}_{da,w}\left(c_{p,a}+\omega_w\,c_{p,v}\right)dT_w+\dot{m}_{da,w}\,d\omega_w\,c_{p,v}\,(T_w-T_i)-d\dot{Q}_{ew}$$
$$=-\left(d\dot{Q}_{sw}+d\dot{Q}_{ew}\right) \qquad 3.68$$

Simplifying leaves only the sensible contribution

$$\dot{m}_{da,w}\left(c_{p,a}+\omega_w\,c_{p,v}\right)dT_w+\dot{m}_{da,w}\,d\omega_w\,c_{p,v}\,(T_w-T_i)=-d\dot{Q}_{sw} \qquad 3.69$$

Using equation 3.14 for sensible heat flux yields

$$\dot{m}_{da,w}\left(c_{p,a}+\omega_w\,c_{p,v}\right)dT_w+\dot{m}_{da,w}\,d\omega_w\,c_{p,v}\,(T_w-T_i)$$
$$=-h_{s,w}\,(T_i-T_w)\,dA \qquad 3.70$$

Rearranging explicitly for the wet channel temperature differential

$$dT_w=-\frac{h_{c,w}\,(T_i-T_w)\,dA+\dot{m}_{da,w}\,d\omega_w\,c_{p,v}\,(T_w-T_i)}{\dot{m}_{da,w}\left(c_{p,a}+\omega_w\,c_{p,v}\right)} \qquad 3.71$$

For the wet channel energy balance, starting from equation 3.7 and substituting energy fluxes from equations 3.14 and 3.59, the following expression is derived

$$\dot{m}_{da,w}\,di_w=-h_{c,w}\,(T_i-T_w)\,dA+\dot{m}_{da,w}\,d\omega_w\left[i_{lv0}+c_{p,v}\,(T_i-T_0)\right] \qquad 3.72$$

To formulate the energy balance of the liquid film introduced in equation 3.9, the previously derived relations are reused. The contribution of the dry channel is obtained by combining equations 3.4 and 3.21, while the contribution of the wet channel results from combining equations 3.7 and 3.72. For the feed liquid of the

system, equation 3.20 is applied. Substituting these expressions, the energy balance of the liquid film can be written as

$$-\dot{m}_{da,d}\, c_{p,ud}\, dT_d - \dot{m}_{da,w}\, d\omega_w\, c_f\, (T_f - T_0) = h_{c,w}\, (T_i - T_w)\, dA - \dot{m}_{da,w}\, d\omega_w \left[i_{lv0} + c_{p,v}\, (T_i - T_0)\right] \quad 3.73$$

Thus, the governing system of equations for the evaporative heat exchanger in this model consists of equations 3.22, 3.58, 3.71 and 3.73

$$m_{da,d}\, c_{p,ud}\, dT_d = -U_{i\leftarrow d}\, (T_d - T_i)\, dA$$

$$d\omega_w = -h_{m,w} \left[\frac{p_{v,sat}(T_i)\, M_v}{R\, T_i\, \dot{m}_{da,w}} - \frac{\omega_w}{\dot{V}_w}\right] dA$$

$$dT_w = -\frac{h_{c,w}\, (T_i - T_w)\, dA + \dot{m}_{da,w}\, d\omega_w\, c_{p,v}\, (T_w - T_i)}{\dot{m}_{da,w}\left(c_{p,a} + \omega_w\, c_{p,v}\right)} \quad 3.74$$

$$-\dot{m}_{da,d}\, c_{p,ud}\, dT_d - \dot{m}_{da,w}\, d\omega_w\, c_f\, (T_f - T_0) = h_{c,w}\, (T_i - T_w)\, dA - \dot{m}_{da,w}\, d\omega_w \left[i_{lv0} + c_{p,v}\, (T_i - T_0)\right]$$

Assuming that the feed liquid temperature coincides with the interface temperature ($T_f = T_i$), the set of unknowns is:

- Bulk temperature of the dry channel and its derivative (T_d, dT_d);
- Bulk temperature of the wet channel and its derivative (T_w, dT_w);
- Bulk specific humidity of the wet channel and its derivative (ω_w, $d\omega_w$);
- Interface temperature (T_i).

Using the infinitesimal area relation for parallel-plate channels (equation 3.1), the equations can be rewritten in terms of longitudinal derivatives

$$\frac{dT_d}{dx} = -\frac{U_{i\leftarrow d}\,(T_d - T_i)\,W}{m_{da,d}\,c_{p,ud}}$$

$$\frac{d\omega_w}{dx} = -h_{m,w}\left[\frac{p_{v,sat}(T_i)\,M_v}{R\,T_i\,\dot{m}_{da,w}} - \frac{\omega_w}{\dot{V}_w}\right] W$$

$$\frac{dT_w}{dx} = -\frac{h_{c,w}\,(T_i - T_w)\,W + \dot{m}_{da,w}\,\frac{d\omega_w}{dx}\,c_{p,v}\,(T_w - T_i)}{\dot{m}_{da,w}\left(c_{p,a} + \omega_w\,c_{p,v}\right)} \qquad 3.75$$

$$-\dot{m}_{da,d}\,c_{p,ud}\,\frac{dT_d}{dx} - \dot{m}_{da,w}\,\frac{d\omega_w}{dx}\,c_f\,(T_i - T_0)$$

$$= h_{c,w}\,(T_i - T_w)\,W - \dot{m}_{da,w}\,\frac{d\omega_w}{dx}\left[i_{lv0} + c_{p,v}\,(T_i - T_0)\right]$$

In the first two equations, the derivative of the unknown variable can be expressed as an explicit function of the variable itself. These equations can thus be advanced numerically using finite-difference ODE integrators. Defining

$$\frac{dT_d}{dx} = -\frac{U_{i\leftarrow d}\,(T_d - T_i)\,W}{\dot{m}_{da,d}\,c_{p,ud}} = f_1(T_d, T_i) \qquad 3.76$$

$$\frac{d\omega_w}{dx} = -h_{m,w}\left[\frac{p_{v,sat}(T_i)\,M_v}{R\,T_i\,\dot{m}_{da,w}} - \frac{\omega_w}{\dot{V}_w}\right] W = f_2(\omega_w, T_i) \qquad 3.77$$

Using finite-difference schemes, approximations of the solution are obtained at the discretization nodes. With the classical fourth-order Runge–Kutta method (RK4, see Chapter 2.14), the integration of the first two equations yields

$$T_{d,n+1} \cong T_{d,n} + \frac{h}{6}\left(K_{f_1,1} + 2\,K_{f_1,2} + 2\,K_{f_1,3} + K_{f_1,4}\right) \qquad 3.78$$

$$\omega_{w,n+1} \cong \omega_{w,n} + \frac{h}{6}\left(K_{f_2,1} + 2\,K_{f_2,2} + 2\,K_{f_2,3} + K_{f_2,4}\right) \qquad 3.79$$

By substituting the second equation of the system 3.75, which expresses the variation of the wet-channel specific humidity, into the last two equations of the system, the following relations are obtained

$$\frac{dT_w}{dx}$$

$$= -\frac{h_{c,w}\,(T_i - T_w)\,W - \dot{m}_{da,w}\,h_{m,w}\left[\frac{p_{v,sat}(T_i)\,M_v}{R\,T_i\,\dot{m}_{da,w}} - \frac{\omega_w}{\dot{V}_w}\right] W\,c_{p,v}\,(T_w - T_i)}{\dot{m}_{da,w}\left(c_{p,a} + \omega_w\,c_{p,v}\right)} \qquad 3.80$$

$$-\dot{m}_{da,d}\,c_{p,ud}\,\frac{dT_d}{dx}$$

$$= h_{c,w}\,(T_i - T_w)\,W$$

$$+ \dot{m}_{da,w}\,h_{m,w}\left[\frac{p_{v,sat}(T_i)\,M_v}{R\,T_i\,\dot{m}_{da,w}} - \frac{\omega_w}{\dot{V}_w}\right] W\left[i_{lv0}\right. \qquad 3.81$$

$$\left. + \left(c_{p,v} - c_f\right)(T_i - T_0)\right]$$

In these two expressions, the wet-channel specific humidity ω_w appears multiple times. To simplify the formulation, an additional approximation is introduced by exploiting the equivalence between the derivative of the unknown variable and the corresponding function definition. From equation 3.77 it can be written

$$\frac{d\omega_w}{dx} = f_2(\omega_w, T_i) \cong \frac{\omega_{w,n+1} - \omega_{w,n}}{h} \qquad 3.82$$

which leads to an explicit approximated expression for the bulk specific humidity ω_w

$$\omega_w \cong \dot{V}_w\left[\frac{\omega_{w,n+1} - \omega_{w,n}}{h\,h_{m,w}\,W} + \frac{p_{v,sat}(T_i)\,M_v}{R\,T_i\,\dot{m}_{da,w}}\right] \qquad 3.83$$

Equation 3.80, which includes both the wet-channel bulk temperature T_w and its derivative, can then be reformulated for numerical integration by observing its dependence on the additional unknowns ω_w and T_i.

$$\frac{dT_w}{dx} = f_3(T_w, \omega_w, T_i) \qquad 3.84$$

Applying the fourth-order Runge–Kutta method again, the evolution of the wet-channel bulk temperature is approximated by

$$T_{w,n+1} \cong T_{w,n} + \frac{h}{6}\left(K_{f_3,1} + 2\,K_{f_3,2} + 2\,K_{f_3,3} + K_{f_3,4}\right) \qquad 3.85$$

In equation 3.81, the unknown variables T_w, ω_w and T_i appear once again. The bulk wet-channel temperature T_w remains undetermined. Proceeding in the same manner as for the bulk humidity of the wet channel, an approximation for this quantity can also be obtained. Starting from equations 3.80 and 3.84 it can be written

$$\frac{dT_w}{dx} = f_3(T_w, \omega_w, T_i) \cong \frac{T_{w,n+1} - T_{w,n}}{h} \qquad 3.86$$

from which

$$T_w \cong T_i + \frac{\left(T_{w,n+1} - T_{w,n}\right)\dot{m}_{da,w}\left(c_{p,a} + \omega_w\, c_{p,v}\right)}{h\,W\left\{h_{c,w} + \dot{m}_{da,w}\,h_{m,w}\left[\frac{p_{v,sat}(T_i)\,M_v}{R\,T_i\,\dot{m}_{da,w}} - \frac{\omega_w}{\dot{V}_w}\right]c_{p,v}\right\}} \qquad 3.87$$

Approximate relations have thus been obtained for both the specific humidity and the bulk temperature of the wet channel. In order to complete the set of governing equations, the energy balance for the dry-channel film (eq 3.81) is considered. This relation contains the derivative of the bulk dry-channel temperature T_{d} with respect to the streamwise coordinate x. By using a discretized difference form for the derivative

$$
\begin{aligned}
-\dot{m}_{da,d}\, c_{p,ud}\, \frac{T_{d,n+1} - T_{d,n}}{h} & \\
&= h_{c,w}\, (T_i - T_w)\, W \\
&+ \dot{m}_{da,w}\, h_{m,w} \left[\frac{p_{v,sat}(T_i)\, M_v}{R\, T_i\, \dot{m}_{da,w}} - \frac{\omega_w}{\dot{V}_w}\right] W \left[i_{lv0}\right. \\
&+ \left.\left(c_{p,v} - c_f\right)\, (T_i - T_0)\right]
\end{aligned}
\qquad 3.88
$$

Rearranging the above relation provides an explicit update for the bulk dry-channel temperature at the next node

$$
\begin{aligned}
T_{d,n+1} = T_{d,n} - \frac{h}{\dot{m}_{da,d}\, c_{p,ud}} \Bigg\{ & h_{c,w}\, (T_i - T_w)\, W \\
&+ \dot{m}_{da,w}\, h_{m,w} \left[\frac{p_{v,sat}(T_i)\, M_v}{R\, T_i\, \dot{m}_{da,w}} - \frac{\omega_w}{\dot{V}_w}\right] W \left[i_{lv0}\right. \\
&+ \left.\left(c_{p,v} - c_f\right)\, (T_i - T_0)\right] \Bigg\}
\end{aligned}
\qquad 3.89
$$

At this stage, the set of governing relations available for advancing the solution with the RK4 finite-difference method includes equations 3.78, 3.79, 3.83, 3.85, 3.87 and 3.89. The unknowns to be determined at each integration step are $T_{d,n+1}$, $\omega_{w,n}$, ω_w, $T_{w,n}$, T_w and T_i.

It must also be recalled that the flow in the wet channel develops in the direction opposite to the longitudinal coordinate x. Consequently, when applying the Runge–Kutta updates (equations 3.79 and 3.85) , the variables must be explicitly evaluated at node n rather than at node $n + 1$.

$$T_{d,n+1} \cong T_{d,n} + \frac{h}{6}\left(K_{f_1,1} + 2\,K_{f_1,2} + 2\,K_{f_1,3} + K_{f_1,4}\right)$$

$$\omega_{w,n} \cong \omega_{w,n+1} - \frac{h}{6}\left(K_{f_2,1} + 2\,K_{f_2,2} + 2\,K_{f_2,3} + K_{f_2,4}\right)$$

$$\omega_w \cong \dot{V}_w \left[\frac{\omega_{w,n+1} - \omega_{w,n}}{h\,h_{m,w}\,W} + \frac{p_{v,sat}(T_i)\,M_v}{R\,T_i\,\dot{m}_{da,w}}\right]$$

$$T_{w,n} \cong T_{w,n+1} - \frac{h}{6}\left(K_{f_3,1} + 2\,K_{f_3,2} + 2\,K_{f_3,3} + K_{f_3,4}\right)$$

$$T_w \cong T_i + \frac{\left(T_{w,n+1} - T_{w,n}\right)\dot{m}_{da,w}\left(c_{p,a} + \omega_w\,c_{p,v}\right)}{h\,W\left\{h_{c,w} + \dot{m}_{da,w}\,h_{m,w}\left[\frac{p_{v,sat}(T_i)\,M_v}{R\,T_i\,\dot{m}_{da,w}} - \frac{\omega_w}{\dot{V}_w}\right]c_{p,v}\right\}} \qquad 3.90$$

$$T_{d,n+1} = T_{d,n} - \frac{h}{\dot{m}_{da,d}\,c_{p,ud}}\left\{h_{c,w}\left(T_i - T_w\right)W + \dot{m}_{da,w}\,h_{m,w}\left[\frac{p_{v,sat}(T_i)\,M_v}{R\,T_i\,\dot{m}_{da,w}} - \frac{\omega_w}{\dot{V}_w}\right]W\left[i_{lv0} + \left(c_{p,v} - c_f\right)\left(T_i - T_0\right)\right]\right\}$$

This system provides the complete framework required to resolve the model at each integration step. Rewriting the system in residual form yields a nonlinear system of six equations in six unknowns

$$F_1(T_{d,n+1}, T_i) = 0$$

$$F_2(\omega_{w,n}, T_i) = 0$$

$$F_3(\omega_w, \omega_{w,n}, T_i) = 0$$

$$F_4(T_{w,n+1}, T_i) = 0$$

$$F_5(T_w, T_{w,n+1}, \omega_w, T_i) = 0$$

$$F_6(T_{d,n+1}, T_w, \omega_w, T_i) = 0$$

3.91

The system can now be solved at each discretization step by applying a Newton–Raphson procedure, which iteratively converges to the set of unknowns that satisfies all governing relations simultaneously.

3.10. Performance indicators for evaporative HMX

Once the governing physical models have been defined and the numerical solution procedure has been completed, the resulting temperature, humidity, and mass flow rate fields can be post-processed to derive a set of synthetic indicators suitable for characterizing the performance of an M-cycle device. These indicators enable a quantitative assessment of system behavior for a given geometric configuration and specified inlet air conditions, allowing consistent comparisons across different operating scenarios and design solutions. In the following, the main performance indicators employed in this work are introduced.

A first and direct measure of the thermal performance of the system is the temperature drop achieved by the dry channel air, defined as

$$\Delta T_d = T_{d,in} - T_{d,out} \qquad 3.92$$

where $T_{d,in}$ and $T_{d,out}$ are the inlet and outlet temperatures of the dry channel air, respectively.

This parameter provides an immediate and physically intuitive quantification of the cooling effect produced by the exchanger. Unlike normalized performance indicators, the temperature drop directly reflects the absolute reduction in air temperature and is therefore particularly useful for evaluating the practical cooling capability of the system under different operating conditions.

The thermal performance of evaporative cooling systems is traditionally evaluated through effectiveness metrics, which quantify the degree to which the outlet air temperature approaches the thermodynamic limit imposed by the inlet air conditions. For conventional evaporative cooling systems, the minimum achievable air temperature is bounded by the wet-bulb temperature (ε_{wb}) of the inlet air. Accordingly, system performance is commonly expressed through wet-bulb effectiveness, defined as

$$\varepsilon_{wb} = \frac{T_{d,in} - T_{d,out}}{T_{d,in} - T_{wb,in}} \qquad 3.93$$

where $T_{wb,in}$ is the inlet wet-bulb temperature. This metric provides a normalized measure of the cooling performance relative to the maximum theoretical cooling potential attainable in single-stage evaporative systems.

The development of regenerative M-cycle configurations enables air cooling beyond the wet-bulb temperature limit. In such systems, the ultimate thermodynamic constraint is represented by the dew-point temperature of the inlet air. Consequently, the most appropriate indicator of thermal performance for an M-cycle device is the dew-point effectiveness (ε_{dp}), defined as

$$\varepsilon_{dp} = \frac{T_{d,in} - T_{d,out}}{T_{d,in} - T_{dp,in}} \qquad 3.94$$

where $T_{dp,in}$ is the inlet air dew-point temperature. The dew-point effectiveness quantifies the extent to which the regenerative cooling process exploits the available

thermodynamic potential and approaches the theoretical lower temperature bound associated with the dew point. Nevertheless, wet-bulb effectiveness remains widely employed in the analysis of M-cycle systems, as it enables direct comparison with conventional evaporative cooling technologies and provides an immediate indication of the extent to which the wet-bulb temperature limit is exceeded.

While effectiveness metrics describe the quality of the cooling process, they do not provide information on the amount of cooling delivered by the system. To address this limitation, the Cooling Capacity (CC) is introduced as a measure of the useful cooling power associated with the temperature reduction of the product air stream in the dry channel. In indirect evaporative cooling systems, no moisture exchange occurs in the dry channel. The process can be described through a sensible energy balance. Under the assumption of constant thermophysical properties of the humid air mixture, the Cooling Capacity is defined as

$$CC = \dot{m}_{da,d}\,(1 - r_m)\,c_{p,u}\,\Delta T_d \qquad 3.95$$

where $\dot{m}_{da,d}$ is the dry air inlet mass flow rate, which remains constant along the dry channel, r_m is the recirculation ratio and $c_{p,u}$ is the specific heat capacity of humid air, as defined in equation 2.33. The term $(1 - r_m)$ represents the fraction of the inlet air stream delivered as product air. This expression directly links the Cooling Capacity to both the thermodynamic outcome of the regenerative process and the useful airflow rate supplied by the system.

Based on the total Cooling Capacity, additional normalized performance indicators can be defined to enable comparisons across different operating conditions and system sizes.

The Specific Cooling Capacity (SCC) is obtained by normalizing the Cooling Capacity with respect to the inlet air mass flow rate

$$SCC = \frac{CC}{\dot{m}_{da,d}} = (1 - r_m)\, c_{p,u}\, \Delta T_d \qquad 3.96$$

This parameter represents the cooling power delivered per unit mass flow rate of inlet air and provides a measure of the thermodynamic performance of the system independently of its scale.

The Volumetric Cooling Capacity (VCC) is defined by normalizing the Cooling Capacity with respect to the volume of the HMX

$$VCC = \frac{CC}{V_{HMX}} \qquad 3.97$$

where V_{HMX} is the volume of the HMX. This indicator quantifies the cooling power per unit volume and is particularly relevant for evaluating the compactness of the system and comparing the performance of exchangers with different sizes.

Despite the usefulness of the previously introduced indicators, performance metrics based solely on the air-side temperature drop across the exchanger are not sufficient to fully characterize the actual cooling effect delivered to the conditioned environment. In particular, the Volumetric Cooling Capacity quantifies the cooling power generated within the exchanger volume but does not explicitly account for the interaction between the supply air conditions and the indoor thermal requirements.

To address this limitation, an additional performance indicator, referred to as the Volumetric Indoor Cooling Capacity ($VICC$), is introduced. This parameter represents the effective cooling power delivered to the conditioned space per unit volume of the HMX. The $VICC$ is defined based on the temperature difference between the indoor temperature and the supply air temperature delivered by the M-cycle unit, and is defined as

$$VICC = \frac{\dot{m}_{da,d}\,(1 - r_m)\,c_{p,u}\left(T_{indoor} - T_{d,out}\right)}{V_{HMX}} \qquad 3.98$$

where T_{indoor} is the indoor air temperature. This formulation explicitly links the system performance to the actual cooling demand of the conditioned space. Unlike VCC, which is based solely on the temperature drop across the exchanger, the $VICC$ accounts for the ability of the system to reduce the indoor cooling load.

This indicator is particularly useful when evaluating the practical performance of the system in real operating conditions, as it provides a more representative measure of the cooling contribution to the indoor environment.

The operation of the M-cycle system should not be evaluated solely in terms of cooling power; the associated water consumption required to achieve such performance must also be considered. Accordingly, an additional key performance indicator is the total water consumption, defined as the mass flow rate of evaporated water in the wet channel

$$\dot{m}_{e,HMX} = \dot{m}_{da,d}\left(\omega_{w,out} - \omega_{w,in}\right) \qquad 3.99$$

This quantity provides a direct measure of the water resources required to sustain the evaporative cooling process. Water consumption plays a central role in evaluating the operational sustainability of M-cycle systems, particularly under humid climatic conditions or in applications where water availability represents a critical design constraint.

However, similarly to the CC, the total water consumption does not account for the physical size of the device. To enable a consistent comparison between systems of different scales, a normalized performance indicator can be introduced by relating the water consumption to the volume of the heat and mass exchanger.

The Volumetric Water Consumption (VWC) is therefore defined as

$$VWC = \frac{\dot{m}_{e,HMX}}{V_{HMX}} \qquad 3.100$$

This parameter represents the water consumption per unit volume of the exchanger and provides a compactness-oriented metric complementary to the VCC and $VICC$.

The introduced set of performance indicators provides a comprehensive assessment of the trade-offs between thermal performance, resource intensity and operating conditions in M-cycle devices.

4. Algorithm description

The computational algorithm of the M-cycle heat exchanger has been implemented in MATLAB using a nested iterative structure that reflects the different evolution of the flows in the two channels. The numerical formulation is based on a one-dimensional discretization along the longitudinal direction of the exchanger: the total length is divided into N cells of length h. Consequently, the domain is defined by $N + 1$ nodes, representing the interfaces between adjacent cells. At each node the relevant thermodynamic variables are defined.

The peculiarity of the problem lies in the opposite directions of the two flows. In the dry channel, which represents the primary flow, the solution proceeds from the inlet to the outlet: the inlet conditions are known, and for each cell n, the input values are directly provided by the output of the previous cell $n - 1$. The computation therefore advances sequentially in the positive x-direction until the thermodynamic state at the channel outlet is determined.

The wet channel, on the other hand, operates in counterflow and does not have known inlet conditions a priori. For this reason, the algorithm adopts an iterative procedure. During the first iteration, the inlet conditions of the wet channel are initialized with guess values for each step. From the second iteration onwards, the structure of the code imposes that the inlet conditions of the wet channel at each step are determined from the outlet conditions of the subsequent step, which, due to the counterflow configuration, corresponds to a higher longitudinal coordinate, as obtained in the previous iteration.

The overall solution is therefore organized into two nested loops. The inner loop scans through all the discretization cells, solving mass and energy balances by evaluating the convective heat and mass transfer coefficients. The outer loop iteratively updates the inlet conditions of each wet-channel step on the basis of the outlet values obtained

at the previous iteration, until the prescribed convergence criteria, defined by the tolerance vector, are satisfied.

In this scheme, the dry channel evolves in the direct sense with explicit propagation of inlet conditions, whereas the wet channel evolves in the opposite sense with iterative propagation based on the results of previous iterations. Convergence of the procedure ensures consistency between the two counterflowing streams and allows reconstruction of the complete thermohygrometric field in the exchanger.

4.1. Input data structure

Before the calculation begins, the algorithm defines two MATLAB struct variables, named inputs and setup, whose purpose is to clearly separate the physical–geometrical parameters of the problem from the numerical settings related to the solution procedure. This design choice keeps the solver code clean and modular, and facilitates automatic initialization of different simulation scenarios, also through external scripts.

The inputs structure collects the descriptive data of the physical system. It stores the geometric parameters of the exchanger, the thermohygrometric properties of the inlet air stream, and the mass fraction of recirculated flow feeding the wet channel.

The setup structure, instead, serves an exclusively numerical function. It contains the algorithm control parameters, such as the maximum number of iterations, the convergence tolerances for the main state variables, the maximum number of Newton–Raphson sub-iterations, and a set of logical flags that allow optional computational settings.

4.2. Variable initialization

The first stage of the code is dedicated to loading the problem parameters from the inputs and setup structures, followed by the calculation of derived geometrical and

physical quantities. In this phase, quantities such as the channel cross-sectional areas, the equivalent hydraulic diameters, the number and extent of exchange surfaces, as well as the moist-air properties at the inlet—recalculated from the assigned thermophysical conditions—are determined.

Subsequently, a one-dimensional discretization is performed along the exchanger length. The channel is divided into N computational cells of step size h (Figure 4.1). For each node, spatial coordinates are defined, and for each cell, the associated exchange areas are calculated. In this way, the exchanger is represented as a sequence of elementary subsystems, within which local mass and energy balances can be applied. This discretization forms the basis of the iterative procedure, as it allows the global problem to be handled as a sequential coupling of finite cells, each characterized by well-defined geometry and exchange conditions.

4.3. Matrix allocation

Once the number of discretization cells, and therefore the total number of nodes, is established, the algorithm initializes the variables required to store the input and output values for each cell of the exchanger. For computational efficiency, all thermodynamic variables of interest are pre-allocated in matrices of maximum size equal to the product of the number of nodes N and the maximum number of iterations.

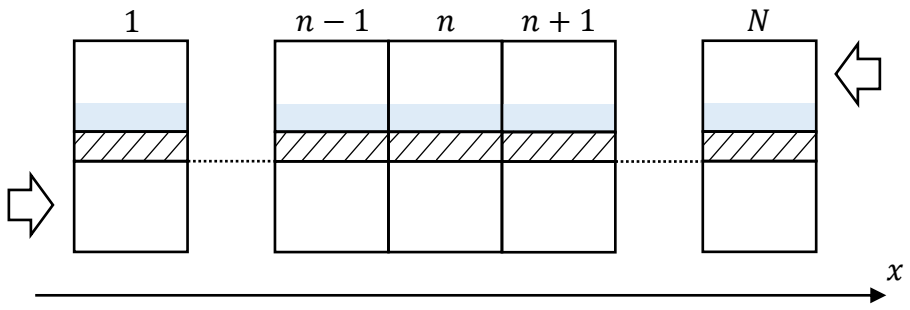

Figure 4.1. Computational cells of the heat exchanger.

This implementation choice serves three main purposes:

1) to avoid dynamic memory reallocation during iteration;
2) to reduce execution times related to data structure management;
3) to ensure full storage of the iteration history, useful both for convergence monitoring and for post-processing analyses.

Once convergence is reached, unused portions of the matrices are discarded, thus reducing memory requirements for final storage and returning a structure that contains only the data corresponding to the converged solution. In this way, an optimal compromise is achieved between numerical efficiency, traceability of iterations, and compactness of the final output.

4.4. Main iterative loop

After the preliminary initialization phase, the algorithm enters the core of the solution procedure, organized in a while loop that continues until the convergence criteria are satisfied or, alternatively, until the maximum allowed number of iterations is reached.

Within this loop, the first iteration is distinguished from subsequent ones. At the beginning of the computation, the inlet state variables of the wet channel cannot be determined a priori, as they depend on the recirculated flow from the dry channel. Similarly, the inlet conditions for all wet-channel cells cannot be specified, since they also depend on the channel inlet. To initiate the calculation, guess values are therefore assigned, generally uniform along the domain (Figure 4.2-A)

$$\Phi^{(1)}_{wet,input,n} = \Phi_{guess}, \forall n \in [1, N] \qquad 4.1$$

where Φ indicates a generic wet-channel state variable and n the cell index.

From the second iteration onwards, the wet-channel inlet values for each computational cell are reconstructed using the output results of the previous iteration

(Figure 4.2-B). Since the wet flow is countercurrent (flowing from node $n+1$ to node n), the inlet of cell n corresponds to the outlet of the downstream cell $n+1$. Denoting i as the current iteration index, the update rule is

$$\Phi_{wet,input,n}^{(i)} = \Phi_{wet,output,n+1}^{(i-1)}, n = 1, \dots, N-1, i \geq 2 \quad 4.2$$

The input conditions for the last cell N (entering at node $N+1$) are updated from the dry-channel outlet at the previous iteration, corresponding to the recirculation point

$$\Phi_{wet,input,N}^{(i)} = \Phi_{dry,n+1}^{(i-1)} \quad 4.3$$

The dry-channel variables, in contrast, do not require guess values, since for each iteration the input of a cell always depends on the output of the previous cell at the same iteration

$$\Phi_{dry,input,n}^{(i)} = f\left(\Phi_{dry,output,n-1}^{(i)}\right) \quad 4.4$$

where the function f accounts for possible correlations between dry-channel outputs and wet-channel inlets.

Moreover, the inlet condition of the first dry-channel cell is always equal to the prescribed exchanger inlet condition, which is the only known boundary condition of the problem. Consequently, at each iteration, only the input vectors for the wet-channel variables must be constructed.

Once these input vectors are built for all cells, the calculation proceeds cell by cell in sequential order from the first to the last.

4.5. Local cell resolution

With the wet-channel input vectors defined for the current iteration, the code executes a *for* loop over the N discretization nodes. For each cell, the local mass and energy balances are solved.

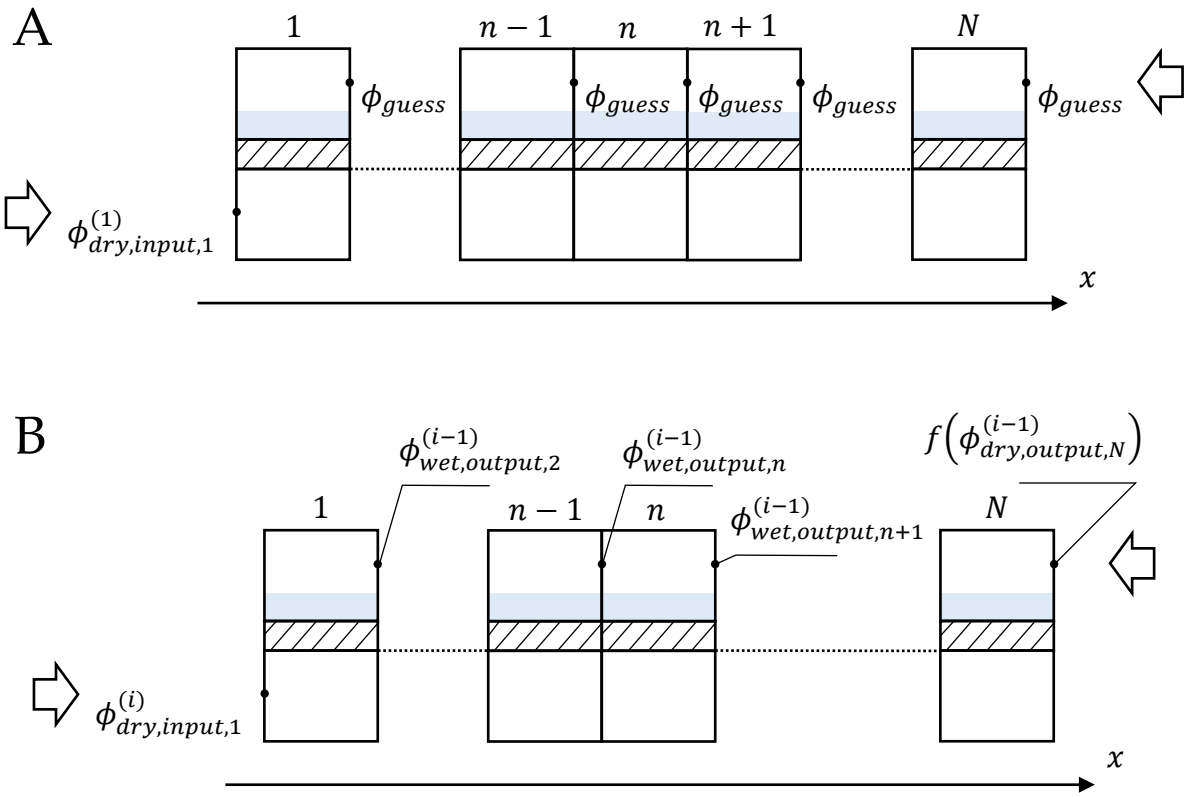

Figure 4.2. Input parameters for each computational cell at the first iteration (A) and at subsequent iterations (B).

At each step of the loop, the input parameters associated with the current cell are retrieved from the input vectors. The detailed execution of the cell calculations is then delegated to an external function, called at each step. This modular structure ensures code flexibility and maintainability: possible modifications to the exchange models or constitutive relations can be implemented separately without altering the overall structure of the solver.

As already mentioned, the dry-channel cell outputs are used directly as inputs for the next cell, while the wet-channel cell inputs are reconstructed from the dedicated input vectors defined at the beginning of the iteration.

Figure 4.3 illustrates the input and output variables for the dry and wet channels during program execution.

First iteration

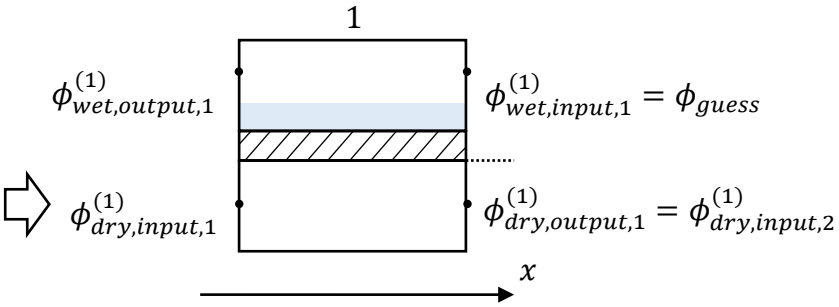

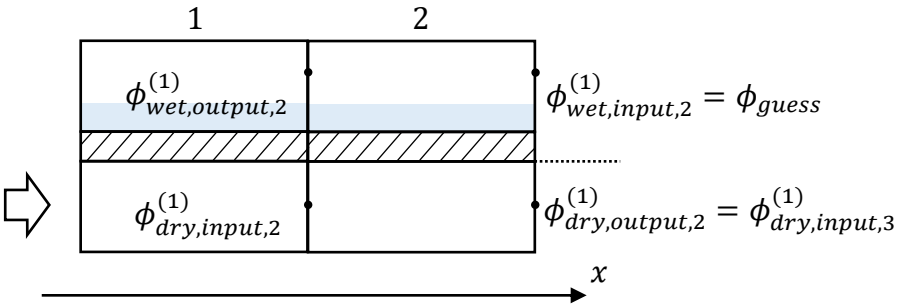

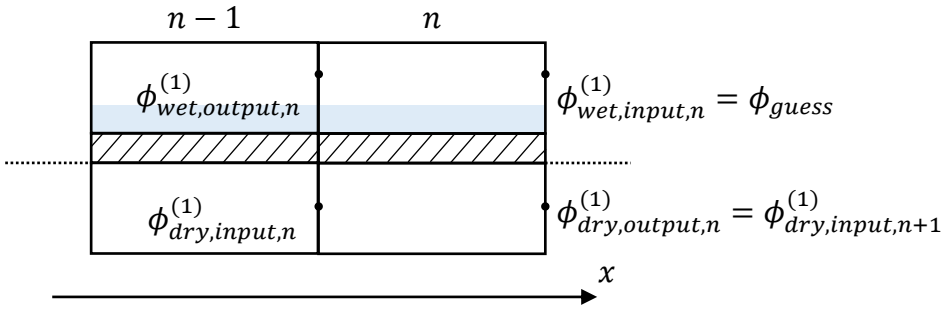

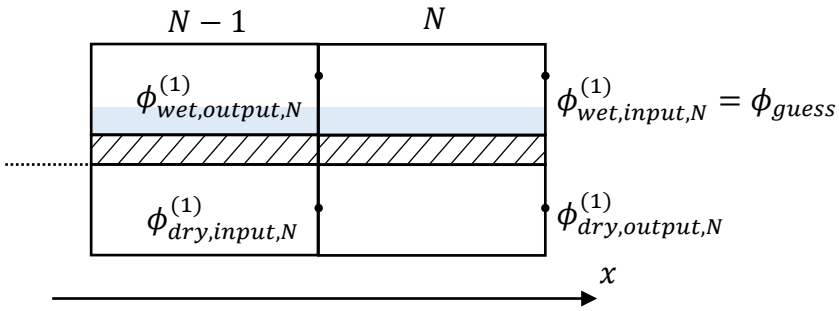

Subsequent iterations

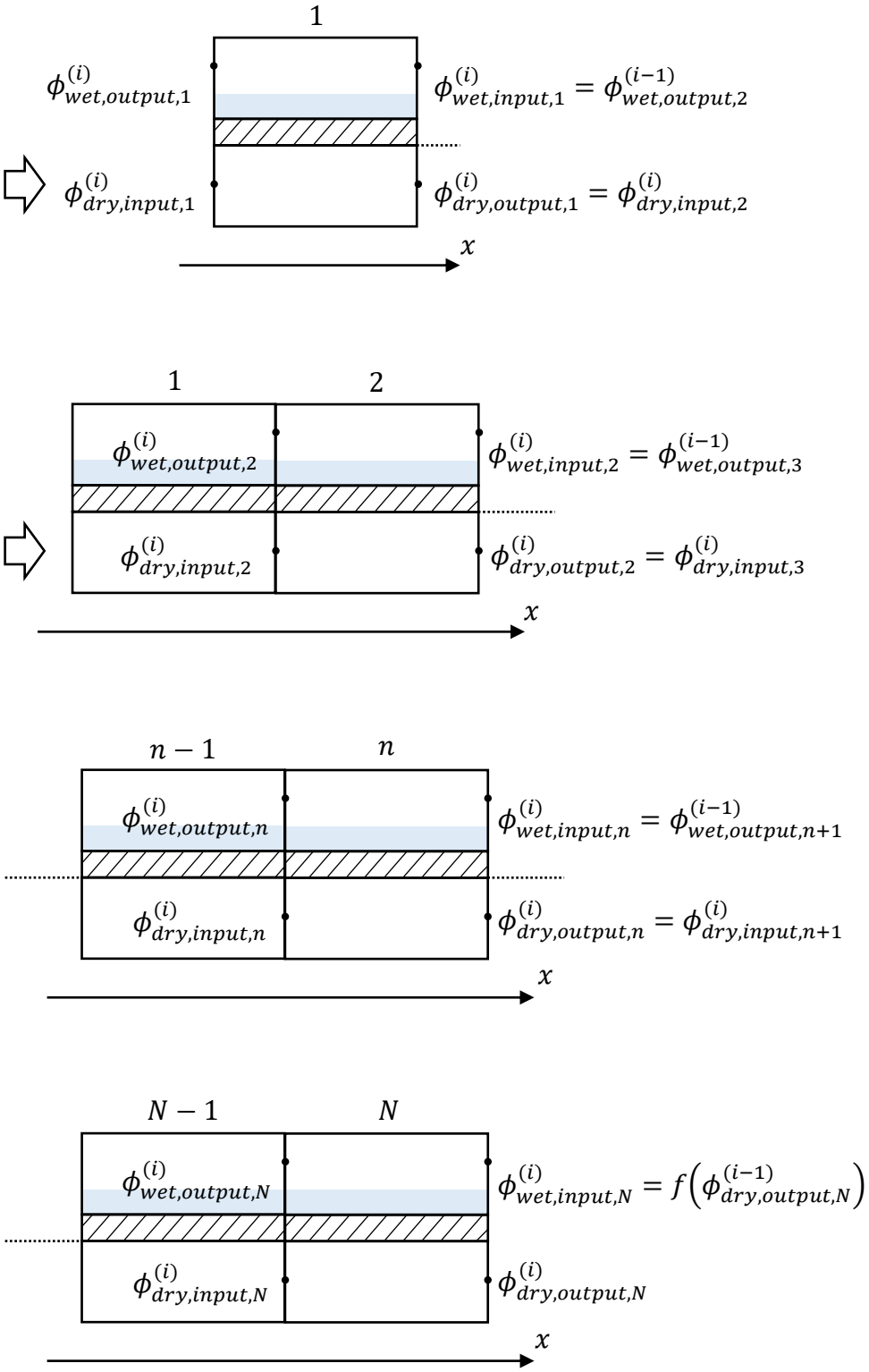

Figure 4.3. Input and output variables for the computational cells during the calculation procedure.

4.6. Boundary inlet conditions

The boundary conditions at the dry channel inlet are derived from experimentally measurable quantities. Typically, the available measurements include the total volumetric flow rate $\dot{V}_{tot}$ (measured via a flowmeter), the fluid temperature T (thermometer), the relative humidity φ (hygrometer), and the total static pressure p (manometer). From these measurements, the thermodynamic state of the mixture is fully determined. Once partial quantities are known, the equivalent molar mass of the mixture M can be derived from the equation of state

$$M = \frac{(\dot{m}_{da} + \dot{m}_v)\, R\, T}{p\, \dot{V}} \qquad 4.5$$

To analyze the exchanger performance as a function of operating conditions, the recirculation ratio (or working air fraction) is typically imposed as an input parameter. This allows the cycle to be studied under controlled boundary conditions, independent of the specific geometric features that physically divert the flow. The inlet conditions of the wet channel are physically coupled to the outlet conditions of the dry channel. In an M-cycle configuration, a portion of the product air is diverted to become the working fluid. Once the recirculation ratio r is defined, the component mass flow rates entering the wet channel are determined as a fraction of the dry channel flow

$$\dot{m}_{wet,in} = r_m\, \dot{m}_{dry,out} \qquad 4.6$$

Since the diversion occurs ideally without heat loss or phase change, the thermodynamic state of the fluid entering the wet channel is identical to that leaving the dry channel. Therefore, the inlet temperature is approximated as

$$T_{wet,in} \approx T_{dry,out} \tag{4.7}$$

Regarding pressure, the fluid undergoes a pressure drop Δp_r due to the U-turn or diversion geometry required to enter the counterflow channels. Consequently, the inlet pressure of the wet channel is given by

$$p_{wet,in} = p_{dry,out} - \Delta p_r \tag{4.8}$$

where Δp_r represents the concentrated pressure loss coefficient associated with the recirculation geometry.

5. Neural network for system performance mapping

Numerical models, while highly precise due to their foundation in fundamental physical relationships, are inherently characterized by high computational costs and significant execution times. These constraints render them practically unusable for dynamic system simulations, which typically mandate the repetitive execution of the model for every single time-step over extended periods (e.g., annual energy analysis). The iterative solution of governing differential equations, although necessary for understanding the detailed thermodynamic behavior, becomes a bottleneck when the component performance must be evaluated hundreds of thousands of times under continuously varying boundary conditions. To bridge the gap between accurate physical modeling and the requirement for computational efficiency in dynamic simulations, an Artificial Neural Network (ANN) approach was adopted. Artificial Neural Networks are widely recognized in thermal engineering as powerful tools for creating "surrogate models" or "metamodels": they act as universal approximators capable of mapping complex, non-linear input-output relationships without requiring the explicit solution of the governing differential equations during runtime [94]. The objective of this phase is to synthesize the extensive dataset generated by the numerical model into a compact, mathematical function. This function serves as a black-box interpolator, enabling the prediction of the HMX performance (outlet temperatures and water consumption) for any set of intermediate operating conditions within the explored domain. This approach ensures that the dynamic analysis benefits from the accuracy of the physical model while achieving instantaneous calculation speeds.

5.1. Network design and hyperparameter selection

The development of an ANN for regression tasks is not a deterministic process but rather a heuristic one, involving a trade-off between model complexity, training speed, and generalization capability [95], [96]. The design phase requires the definition of

specific structural and algorithmic variables, referred to in machine learning literature as "hyperparameters". Unlike the internal model parameters (such as weights and biases) which are learned automatically during the training process, hyperparameters are configuration settings that must be defined a priori to control the learning process and the structure of the network itself. These include the number of hidden layers (depth), the number of neurons per layer (width), the type of activation functions, and the specific training algorithm employed [94], [95], [96]. The selection of appropriate hyperparameters is critical: a network that is too simple (high bias) may fail to capture the non-linear trends of the thermodynamic process (underfitting), whereas a network that is excessively complex (high variance) may memorize the noise in the training data, failing to generalize to new, unseen operating points (overfitting).

5.2. Network topology: depth vs. width

The first critical decision concerns the network topology, specifically the number of hidden layers (depth) and the number of neurons per layer (width).

Shallow Networks (Single Hidden Layer): According to the Universal Approximation Theorem, a single hidden layer with enough neurons can approximate any continuous function [97]. However, for complex non-linear problems like evaporative cooling, a single layer might require an exponentially large number of neurons, which can be computationally infeasible and may fail to generalize correctly [98].

Deep Networks (Multiple Hidden Layers): Adding more layers allows the network to learn hierarchical features, where complex concepts are defined in terms of simpler ones [98]. Empirical results suggest that deep architectures can model complex non-linearities more efficiently, often requiring fewer total neurons compared to shallow networks to achieve the same accuracy [98], [99].

5.3. Activation functions

The selection of the activation function is a pivotal step in network design, as it dictates how the weighted sum of inputs is transformed into an output, effectively injecting the necessary non-linearity into the model to capture complex physical relationships [95]. In the current landscape of deep learning, particularly for image processing and computer vision, the Rectified Linear Unit (ReLU) has gained immense popularity due to its computational efficiency and speed [98]. However, ReLU presents significant limitations when applied to regression tasks involving continuous physical phenomena. Specifically, it is non-differentiable at the origin and prone to the so-called "dying ReLU" problem, where neurons become inactive and stop learning. These characteristics make it less suitable for modeling the smooth, continuous gradients typical of thermodynamic systems. Among the smooth, "S-shaped" non-linear functions, the Logistic Sigmoid has been historically common. Nevertheless, it maps inputs to a strictly positive (0, 1) range and is known to suffer from the "vanishing gradient" problem, which can severely hamper the training speed and convergence in deeper architectures [100]. In contrast, the Hyperbolic Tangent (Tanh) function maps inputs to a symmetric (-1, 1) range. Its zero-centered nature typically results in faster convergence rates compared to the standard sigmoid, as it allows for a more balanced weight update, avoiding the 'zig-zagging' behavior of gradient descent typical of non-zero mean inputs [95], [101].

5.4. Optimization strategy for the training algorithm

The training phase of an Artificial Neural Network is fundamentally an unconstrained optimization problem, where the objective is to iteratively adjust the network's internal parameters (weights and biases) to minimize a specific cost function, typically the Mean Squared Error (MSE) between the predicted outputs and the target values [102].

The choice of the optimization algorithm directly influences the convergence speed, the computational resources required, and the final accuracy of the model.

The standard approach for training feed-forward networks relies on Gradient Descent (GD) algorithms utilizing the backpropagation technique. As a first-order optimization method, GD updates the weights by moving in the direction of the negative gradient of the performance function. While robust and easy to implement, standard GD is known to suffer from slow convergence rates, particularly in function approximation tasks where the error surface may contain long, narrow valleys. Furthermore, its performance is highly sensitive to the choice of the learning rate: a value that is too low results in excessive training times, while a value that is too high can lead to unstable oscillatory behavior [95]. To address generalization issues, Bayesian Regularization (BR) offers a probabilistic approach. Instead of minimizing the error alone, BR minimizes a linear combination of squared errors and weights, effectively penalizing overly complex models (a process akin to Occam's razor). This makes it excellent for small or noisy datasets, as it inherently prevents overfitting without the need for a separate validation set [103]. However, the computational cost of BR is high, as it requires the calculation of the Hessian matrix at each iteration, making it slower and memory-intensive for larger datasets or more complex architectures. The Levenberg-Marquardt (LM) algorithm represents a sophisticated second-order optimization method designed to overcome the limitations of the previous approaches. It operates as a hybrid technique that interpolates between the Gauss-Newton algorithm (which provides quadratic convergence speed near the minimum) and the method of gradient descent (which guarantees stability when far from the solution) [104]. By dynamically adjusting a damping parameter, the LM algorithm shifts from gradient descent-like behavior in the early stages of training to Gauss-Newton-like behavior as the solution approaches the optimum.

5.5. Data pre-processing normalization

Data pre-processing is a prerequisite for effective machine learning, as Neural Networks are inherently sensitive to the scale and distribution of the input data [96]. The dataset generated for the HMX exhibits significant heterogeneity in the magnitude of its features. Feeding raw data with such disparate orders of magnitude into the network would be detrimental to the training process. During backpropagation, input variables with larger magnitudes would yield larger gradients, causing their associated weights to dominate the learning updates. This creates an ill-conditioned error surface (elongated rather than spherical), which forces the optimization algorithm to take infinitesimally small steps, leading to poor convergence rates or trapping the solution in local minima [101]. Furthermore, considering the use of the Hyperbolic Tangent (tansig) activation function in the hidden layers, large input values would push the neurons into their saturation regions (the asymptotic "flat" parts of the curve). In these regions, the derivative of the activation function approaches zero, effectively halting the weight updates. This phenomenon is known as the "vanishing gradient" problem [105].

5.6. Evaluation metrics for ANN regression

The evaluation of Artificial Neural Networks (ANNs) in regression problems requires a rigorous statistical characterization to quantify the agreement between predicted outputs and reference values. Relying on a single indicator is generally insufficient, since different metrics capture complementary aspects of model performance, including average error magnitude, sensitivity to outliers, and systematic bias.

Let y_i denote the i-th reference value, $\hat{y}_i$ the corresponding predicted value, and $\bar{y}$ the arithmetic mean of the reference dataset. The total number of samples is indicated as N. The prediction error (residual) is defined as

$$e_i = y_i - \hat{y}_i \quad 5.1$$

The Mean Absolute Error (MAE) quantifies the average magnitude of the prediction error without considering its sign

$$MAE = \frac{1}{N}\sum_{i=1}^{N}|e_i| \quad 5.2$$

This metric provides an intuitive measure of the typical deviation between predicted and reference values, expressed in the same units as the target variable.

The Root Mean Square Error ($RMSE$) is defined as

$$RMSE = \sqrt{\frac{1}{N}\sum_{i=1}^{N}e_i^2} \quad 5.3$$

Due to the quadratic penalization of errors, $RMSE$ is particularly sensitive to large deviations and outliers, providing a more conservative measure of model accuracy compared to MAE.

The Mean Absolute Percentage Error ($MAPE$) expresses the error in relative terms

$$MAPE = \frac{100}{N}\sum_{i=1}^{N}\left|\frac{y_i - \hat{y}_i}{y_i}\right| \quad 5.4$$

This metric becomes undefined when $y_i = 0$. Therefore, such cases must be excluded from the computation to avoid singularities.

The Coefficient of Variation of $RMSE$ ($CV(RMSE)$) is a normalized error metric defined as

$$CV(RMSE) = \frac{RMSE}{\bar{y}}\ 100 \qquad 5.5$$

This formulation enables dimensionless comparison of model accuracy across different systems or datasets with varying scales.

The Normalized Mean Bias Error ($NMBE$) quantifies the average systematic deviation between predictions and reference values

$$NMBE = \frac{\sum_{i=1}^{N}(y_i - \hat{y}_i)}{N\ \bar{y}}\ 100 \qquad 5.6$$

Unlike absolute metrics, the NMBE preserves the sign of the error, revealing whether the model exhibits a persistent tendency toward underestimation or overestimation

The coefficient of determination (R^2) measures the proportion of variance in the reference data explained by the model

$$R^2 = 1 - \frac{\sum_{i=1}^{N}(y_i - \hat{y}_i)^2}{\sum_{i=1}^{N}(y_i - \bar{y})^2} \qquad 5.7$$

Values of R^2 close to unity indicate a strong agreement between predicted and reference data.

Absolute error metrics such as MAE and $RMSE$ provide direct information on prediction accuracy in physical units. Normalized metrics such as $CV(RMSE)$ and $NMBE$ enable dimensionless evaluation and facilitate comparison across different systems and operating conditions. Finally, correlation-based indicators such as R^2 complement the analysis by quantifying the strength of linear agreement between predicted and reference values. Together, these metrics provide a comprehensive framework for evaluating the predictive performance, robustness, and reliability of ANN-based regression models.

6. Numerical results and performance output analysis

This chapter presents the numerical results derived from the application of the computational models described in the previous sections to characterize the thermo-hygrometric performance of the M-cycle HMX. The analysis begins with a validation of the consolidated Hasan model, evaluating its predictive accuracy against benchmark literature data and independent experimental findings. Subsequently, a comprehensive parametric study is conducted to map the system sensitivity to variations in the recirculation ratio and inlet air velocity, quantifying their combined impact on key performance indicators such as thermodynamic effectiveness, cooling capacity metrics, and water consumption. Finally, a critical comparison between the Hasan model and the formulation proposed in this research is presented, providing a more rigorous physical analysis of the local heat and mass transfer gradients and dimensionless transport parameters throughout the exchanger channels.

6.1. Benchmarking of the Hasan model

The computational model developed by Hasan [92], discussed in section 3.8, was implemented in MATLAB and validated using the input data reported in the original publication. The regenerative HMX geometry is defined by a channel length and width of 0.5 m. Both the dry and wet channels have a height of 3.5 mm, separated by a wall with a thickness of 1.5 mm. The numerical configuration simulates a single representative pair consisting of one dry channel and one wet channel. Consistent with the reference study, the Nusselt number for both channels was fixed at $Nu = 4.861$. As detailed in equation 2.70, this value corresponds to fully developed laminar flow in parallel-plate channels under the boundary condition of constant heat flux on one wall and an adiabatic condition on the opposite wall.

The initial airflow conditions are set to a dry-side inlet temperature of 30°C and an inlet specific humidity of 9 g_v/kg_{da}. The dry air inlet mass flow rate is 0.0014 kg/s. The working to inlet air ratio is fixed at 0.7. All parameters utilized for the model validation are summarized in Table 6.1.

Since the thermal conductivity of the channel wall (k_{wall}) was not explicitly specified in the original work, a sensitivity analysis was performed to assess the impact of this parameter on the results and to confirm the validity of the code. Two simulations were conducted using extreme values for the wall thermal conductivity, which are representative of common materials used in indirect evaporative coolers (see Table 6.2):

Table 6.1. Input parameters used for the computational model, based on the data reported by Hasan [92].

HMX geometric parameters			
Length	L	0.5	m
Width	W	0.5	m
Dry channel height	s_d	3.5	mm
Wet channel height	s_w	3.5	mm
Wall thickness	s_{wall}	1.5	mm
Number of dry channels	N_d	1	
Number of wet channels	N_w	1	
Air Flow and Operating Conditions			
Dry inlet temperature	$T_{d,i}$	30	°C
Dry inlet specific humidity	$\omega_{d,i}$	9	g_v/kg_a
Dry inlet mass flow rate	$\dot{m}_{da,d}$	0.0014	kg/s
Working to inlet mass flow rate	r_m	0.7	
Exchange coefficients			
Dry channel Nusselt number	Nu_d	4.861	
Wet channel Nusselt number	Nu_w	4.861	
Wet channel Lewis number	Le_w	1	

- Polymer wall: $k_{wall} = 0.46\ W/(m\ K)$ (Low conductivity).
- Aluminum wall: $k_{wall} = 237\ W/(m\ K)$ (High conductivity).

The results presented below show that the deviations between the two cases are limited. This indicates that the numerical model reproduces the reference results with low sensitivity to the assumed wall material. In the following figures, solid lines represent the simulation with the polymer wall ($k_{wall} = 0.46\ W/(m\ K)$), while dashed lines refer to the aluminum wall ($k_{wall} = 237\ W/(m\ K)$).

Figure 6.1 compares the temperature profiles along the axial coordinate for the dry channel (red), the wet channel (blue), and the liquid film interface (magenta). The dry-channel temperature (T_d) decreases monotonically along the flow direction. Only minor differences are observed between the two wall conductivity cases. The exit temperature is approximately $17.3°C$ for the polymer case and $17.05°C$ for the aluminum case. The wet-channel temperature (T_w) exhibits a non-monotonic behavior. Upon entering the wet channel, the temperature initially decreases due to the evaporative cooling effect. As the flow progresses toward the outlet, the trend reverses, and the temperature begins to rise due to heat transfer from the adjacent dry channel.

Table 6.2. Common wall materials thermal properties

Material	***Reference temperature*** K	***Thermal conductivity*** $\frac{W}{m\ K}$	
Aluminum (Pure)	300	237	*[106]*
Polyethylene low density		0.33	*[107]*
Polyethylene high density		$0.46 - 0.50$	*[107]*
Polyurethane coating		$0.17 - 0.21$	*[107]*
Polyurethane coating (highly filled)		$0.33 - 0.46$	*[107]*
Cotton	300	0.06	*[106]*

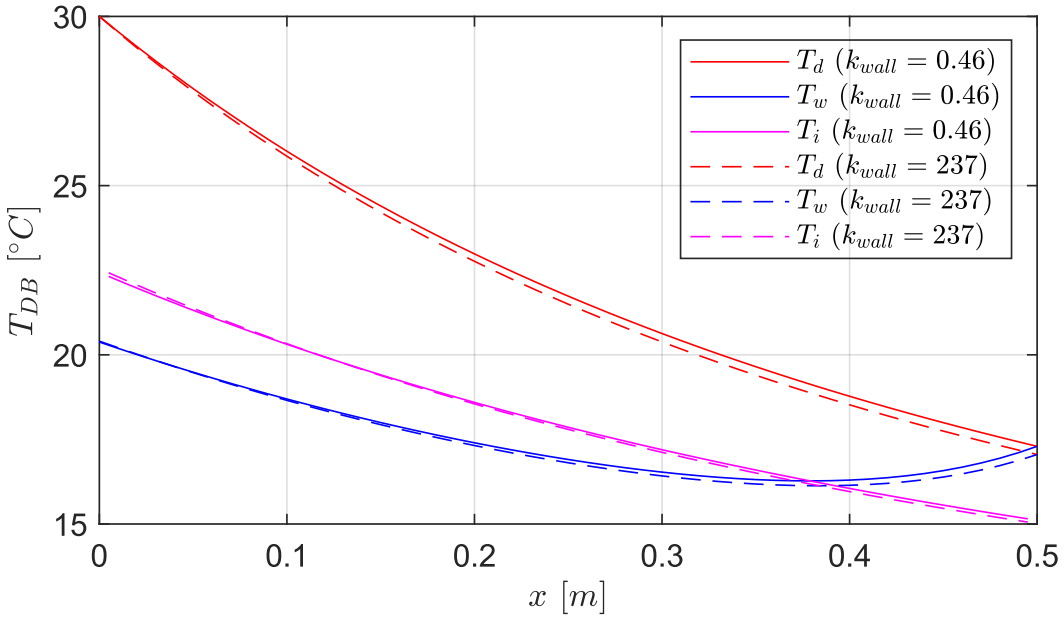

Figure 6.1. Comparison of temperature profiles for Hasan simulation with two different wall heat conductivity.

Conversely, the interface temperature (T_i) shows a continuous increasing trend along the entire length. Notably, in the initial portion of the wet channel, T_i is lower than the wet-channel temperature, whereas in the final section, it settles at an intermediate value between the dry and wet air temperatures.

Figure 6.2 illustrates the specific humidity (ω) trends. The dry-channel humidity (red lines) remains constant at the inlet value since no phase change occurs. In the wet channel (blue lines), the specific humidity increases along the flow direction due to evaporation. The interface specific humidity (magenta lines) also increases as a consequence of the rising interface temperature. The curves for the two conductivity cases overlap almost perfectly. The outlet specific humidity for the wet air is approximately 17 g_v/kg_{da} in both simulations. This indicates that the mass transfer driving force is not significantly affected by wall thermal properties.

Figure 6.3 displays the specific enthalpy profiles for the wet air (i_w) and the film interface (i_i). Both wet air enthalpy and interface enthalpy increase along the channel. This reflects the combined effect of latent heat transfer and the rise in temperature.

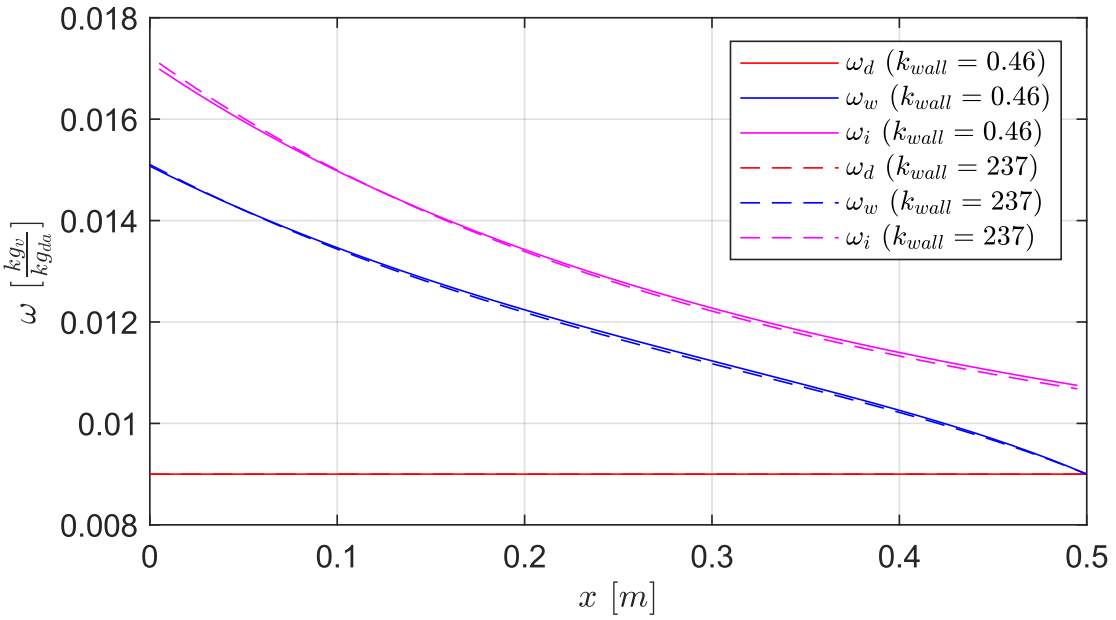

Figure 6.2. Comparison of specific humidity profiles for Hasan simulation with two different wall heat conductivity.

Comparison between the solid and dashed lines reveals a small discrepancy. For instance, the outlet wet air enthalpy is approximately 58.8 kJ/kg for the polymer case and approximately 58.9 kJ/kg for the aluminum case.

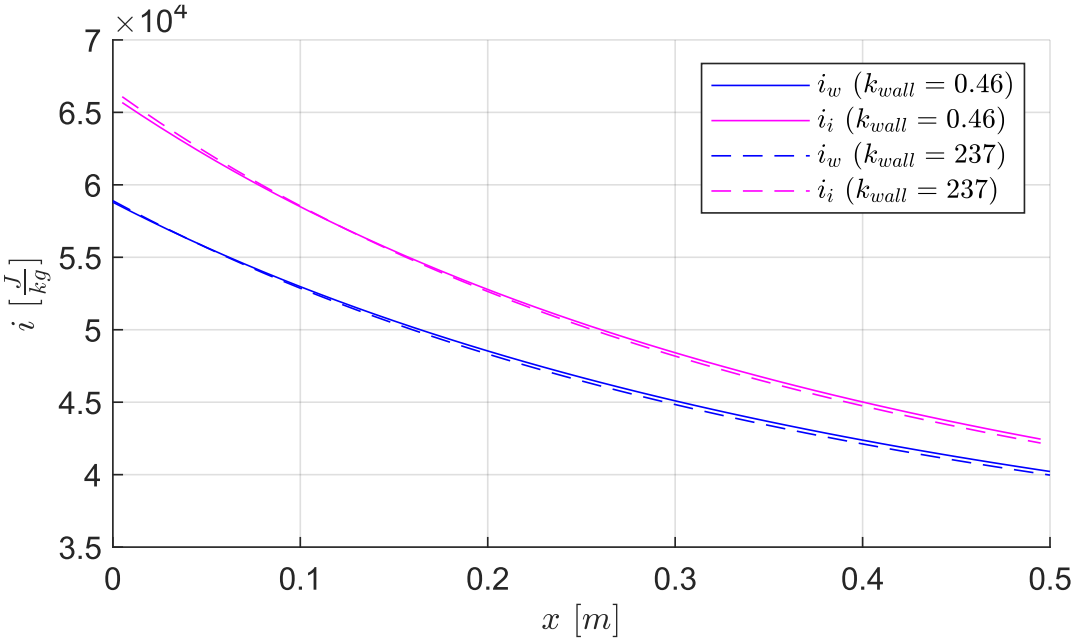

Figure 6.3. Comparison of wet channel specific enthalpy profiles for Hasan simulation with two different wall heat conductivity.

Figure 6.4 shows the relative humidity (φ) profile along the wet channel. The working air enters the wet channel and progressively approaches saturation as it flows toward the outlet. In the final section, relative humidity reaches values close to 100% in both scenarios. This indicates effective utilization of the evaporative potential.

Figure 6.5 presents the specific heat fluxes per unit area along the wet channel: total heat flux ($d\dot{Q}_w$), latent heat flux ($d\dot{Q}_l$), and sensible heat flux ($d\dot{Q}_s$). The latent heat flux remains positive and is the dominant contributor along the channel. Conversely, the sensible heat flux initially exhibits negative values near the wet channel inlet. This occurs because the liquid film temperature drops below the bulk wet air temperature, which causes the wet air stream to release sensible heat to the liquid film.

Further downstream, the sensible heat flux shifts to positive values and shows a steady growth, driven by the widening thermal gradient between the liquid film and the wet air stream.

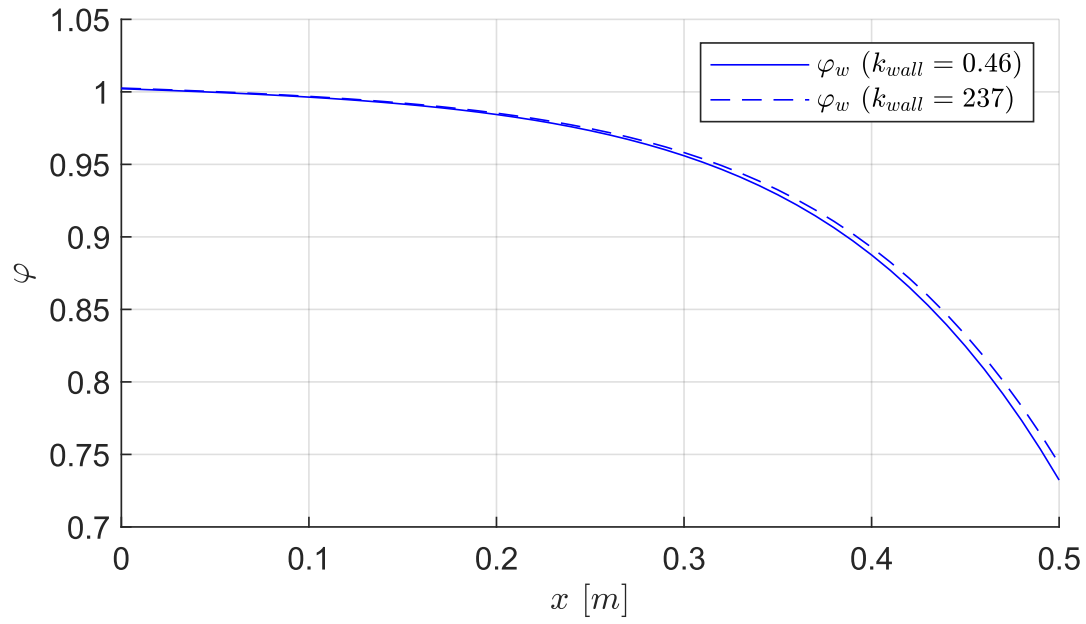

Figure 6.4. Comparison of wet channel relative humidity profiles for Hasan simulation with two different wall heat conductivity.

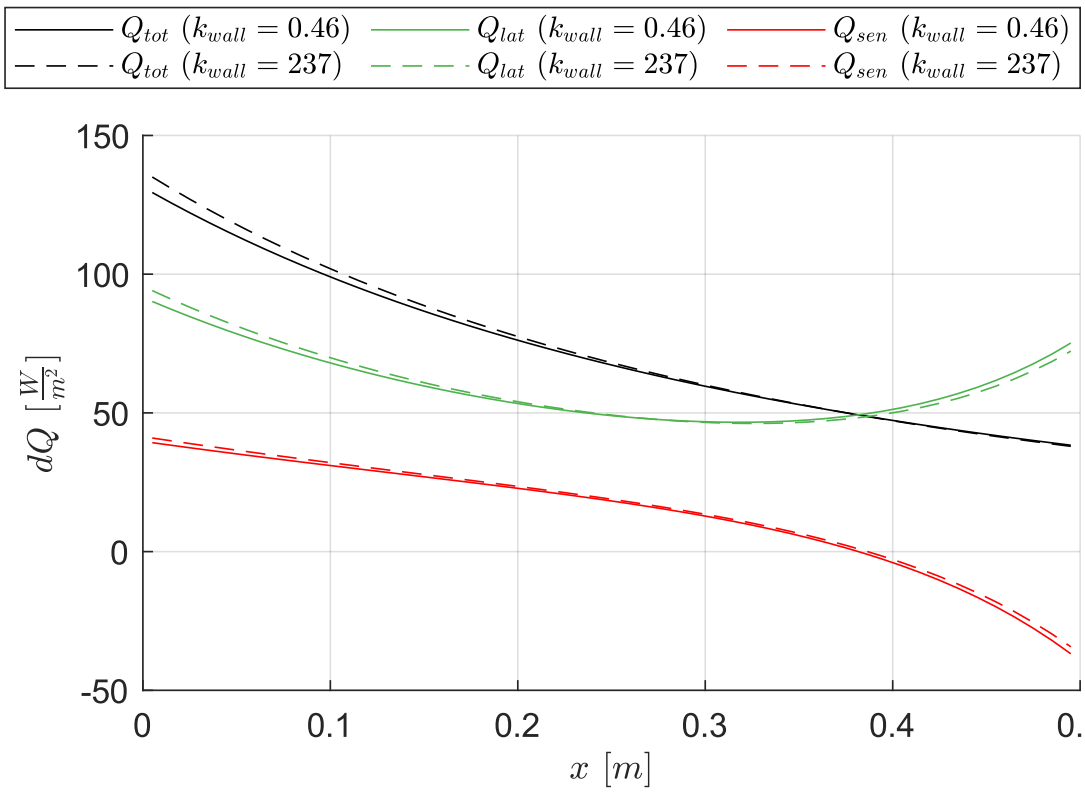

Figure 6.5. Comparison of specific heat fluxes per unit area profiles for Hasan simulation with two different wall heat conductivity.

Finally, Figure 6.6 introduces the profile of the specific evaporated water mass per unit area $d\dot{m}_e$. This is an original result not explicitly shown in Hasan's work. The profile is non-monotonic along the channel. At the wet channel inlet, the evaporation rate is high due to the large specific humidity difference between the unsaturated incoming air and the liquid film. The rate then decreases as the air accumulates moisture. In the final section of the channel, the evaporation rate increases again because of the rising liquid film temperature. This increase enhances the saturation humidity at the interface and the local mass transfer driving force.

The sensitivity analysis indicates that the wall thermal conductivity has a limited impact on the overall thermodynamic performance of the heat exchanger. This is reflected by the small deviations between the two simulations. All obtained profiles

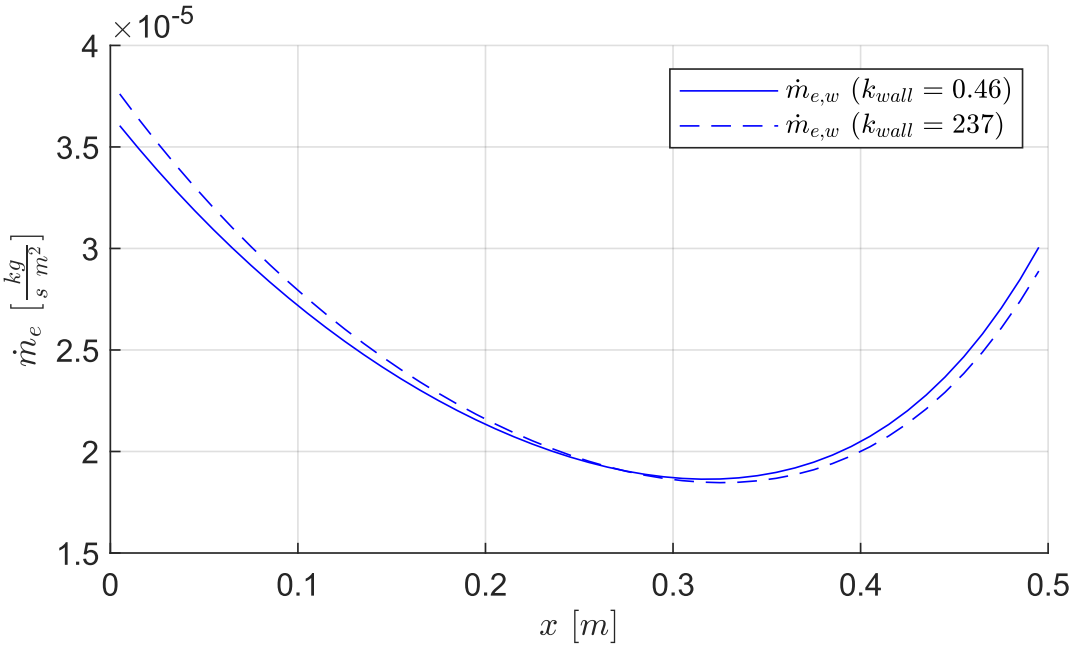

Figure 6.6. Comparison of evaporated water mass per unit area profiles for Hasan simulation with two different wall heat conductivity.

show good agreement with the reference data reported by Hasan, supporting the accuracy of the computational model.

The Hasan model has also been utilized in literature to verify the experimental results of Riangvilaikul and Kumar [108]. These findings were published by Fakhrabadi and Kowsary [109] and were obtained by applying the Nusselt value for fully developed laminar flow with a constant wall heat flux boundary condition (Equation 2.69) to both channels. Table 6.3 reports the geometric parameters of the heat exchanger used for the experimental analysis. The experimental tests consist of two series: the first maintains a constant inlet air velocity of 2.4 m/s while varying inlet temperature and humidity, whereas the second maintains a constant inlet temperature of 34 °C while varying flow velocity and humidity. In all tests, the working-to-inlet air ratio is fixed at 0.33. Figure 6.7 presents the results obtained with the model developed for this work, which reproduces the calculations performed by Fakhrabadi and Kowsary using Nusselt values for the constant wall heat flux condition. For comparison, results

obtained with Nusselt values for the constant wall temperature condition are also included.

The results obtained with Nusselt numbers for the constant heat flux boundary condition closely match the findings published by Fakhrabadi and Kowsary. As observed in Figure 6.7-A and consistent with their study, for cases with an inlet fluid velocity of 2.4 m/s, the Hasan model precision in determining the outlet temperature increases as the inlet humidity rises. For low-humidity cases, the lowest precision occurs as the inlet temperature increases, with the model overestimating the outlet temperatures. The percentage error regarding the dry-channel air temperature drop was calculated using the following relation

$$Err_{\Delta T} = \frac{\left|\Delta T_{d,sim} - \Delta T_{d,exp}\right|}{\Delta T_{d,exp}}\ 100 = \frac{\left|T_{d,o,exp} - T_{d,o,sim}\right|}{T_{d,i} - T_{d,o,exp}}\ 100 \qquad 6.1$$

where $\Delta T_{d,sim}$ and $\Delta T_{d,exp}$ represent the simulated and experimental air temperature drops, respectively, $T_{d,i}$ is the inlet dry-bulb temperature, while $T_{d,o,exp}$ and $T_{d,o,sim}$ denote the experimental and simulated outlet temperatures.

Among the cases tested at the specific humidity of 6.9 g_v/kg_{da}, the error ranges from 0.85% at 25 $°C$ to 7.43% at 45 $°C$. The results proposed here also illustrate the effect of employing the Nusselt number for the constant wall temperature boundary condition. In these cases, the predicted outlet temperatures are higher than the previous ones. This discrepancy increases as the inlet temperature rises and the inlet humidity decreases. Consequently, while results for high-humidity cases remain close to the experimental data, the percentage error reaches 9.7% for the case with an inlet temperature of 45 $°C$ and an inlet humidity of 6.9 g_v/kg_{da}.

Figure 6.7-B presents the same comparison with the second set of results provided by Riangvilaikul and Kumar. These data show the outlet temperatures for two inlet humidity levels at a fixed inlet temperature of 34 $°C$ for all cases. The variable being

modified is the inlet flow velocity. Although the experimental results are noisier than the previous sets, in general, the model highest precision is still associated with higher inlet humidity cases. Regarding the variation in inlet fluid velocity, the simulation with the constant wall heat flux Nusselt number overestimates the outlet temperature at high inlet velocities, while it underestimates it at low velocities.

Table 6.3. Geometric parameters of the Riangvilaikul and Kumar [108] experimental HMX.

HMX geometric parameters			
Length	L	1.2	m
Width	W	0.08	m
Dry channel height	s_d	5	mm
Wet channel height	s_w	5	mm
Wall thickness	s_{wall}	0.5	mm
Number of dry channels	N_d	4	
Number of wet channels	N_w	5	

The validation process demonstrates that the numerical model captures the thermodynamic behavior of the regenerative heat exchanger. The agreement between numerical and experimental data confirms the model reliability for the comprehensive parametric study and performance optimization presented in the following chapters.

6.2. System sensitivity analysis using the Hasan model

Following the numerical verification and benchmarking of the Hasan model against literature data, the model was utilized to perform a comprehensive parametric analysis. The objective was to investigate the thermal behavior of the indirect evaporative cooler under varying operating conditions. This section presents the results obtained by systematically varying the recirculation ratio and the inlet air mass flow rate, to quantify their impact on the cooling performance.

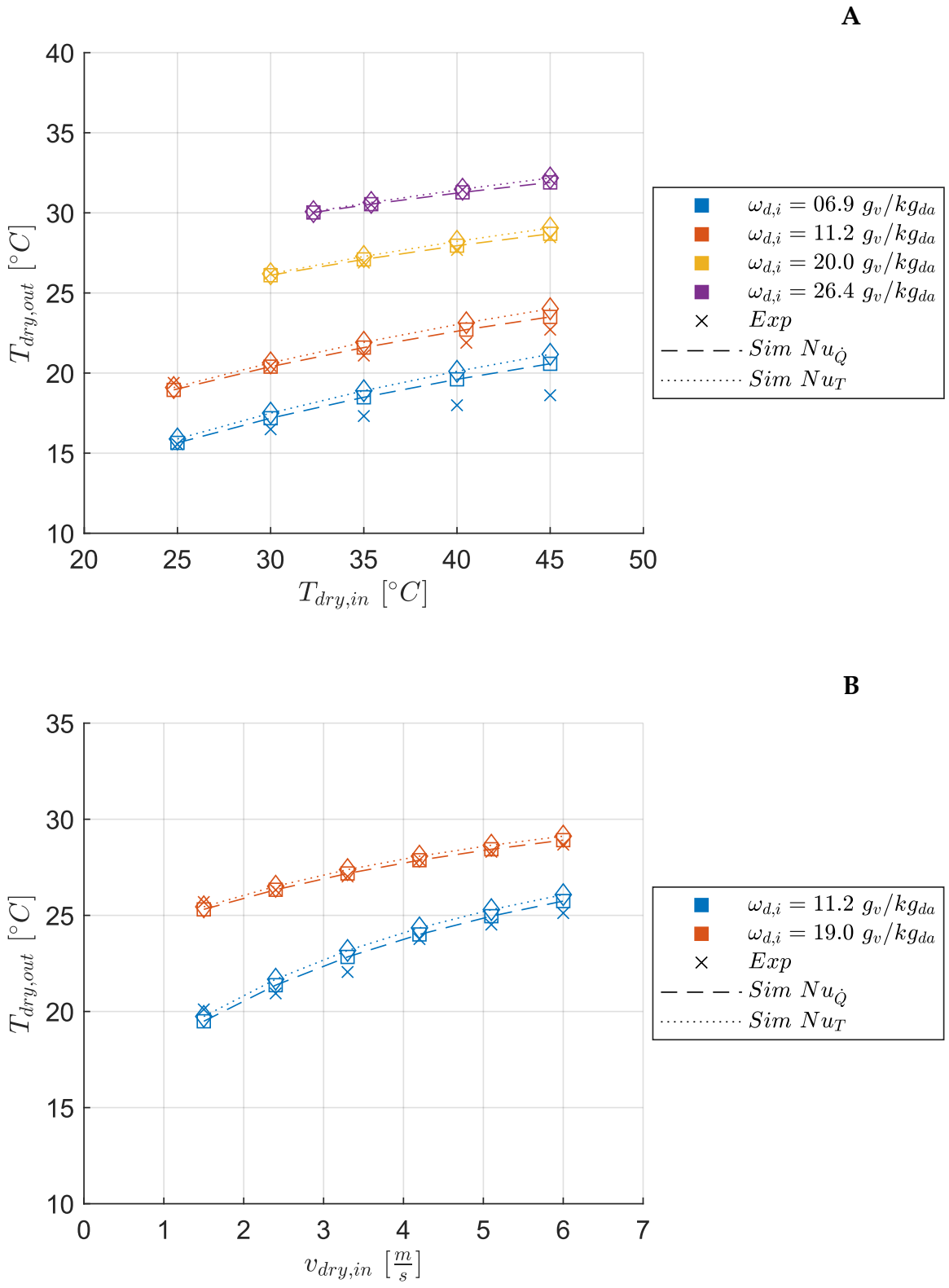

Figure 6.7. Comparison between experimental and simulation results for the Riangvilaikul and Kumar test cases. Variation of inlet temperature and humidity with $v_{d,i} = 2.4\ m/s$ and $r_m = 0.33$ (A); Variation of inlet air flow velocity and humidity with $T_{d,i} = 34\ °C$ and $r_m = 0.33$ (B).

Table 6.4. Summary of the inlet thermo-hygrometric conditions selected for the parametric analysis.

Cases		$T_{d,i}$ $°C$	$\omega_{d,i}$ g_v/kg_{da}
A	*Low temperature, low humidity*	25	6
B	*High temperature, low humidity*	40	6
C	*Moderate temperature, high humidity*	30	18
D	*High temperature, high humidity*	40	18

The analysis focuses on four distinct inlet air conditions, chosen to represent a range of different environmental scenarios and shown in Table 6.4.

The considered HMX geometry consists of a channel length of 0.2 m. The channel height is 2 mm for both the dry and wet channels. The channels are separated by an aluminum wall that is 0.5 mm thick. The assembly consists of 100 dry channels and 101 wet channels. All geometric parameters are detailed in Table 6.5. Constant thermophysical properties are assumed. The flow is fully developed in parallel-plate channels. Constant Nusselt numbers are used, corresponding to uniform wall heat flux conditions. A unit Lewis factor is also assumed.

The computational mesh size was selected as a compromise between computational speed and numerical accuracy. A mesh size of 1 cm was adopted for all simulations, with the exception of low-velocity and low-recirculation ratio cases ($v_{in} = 1.0\ m/s$ with $r_m = 0.1$ and 0.2; $v_{in} = 1.5\ m/s$ with $r_m = 0.1$ and 0.2) where a 0.5 cm mesh was used.

6.2.1. Effect of the recirculation ratio

The recirculation ratio (r_m), defined as the fraction of the inlet mass flow rate diverted to the wet channel, represents a critical control parameter for M-cycle heat exchangers. To assess its influence on the system's thermal profile and cooling effectiveness, simulation results are presented for recirculation ratios of 0.1, 0.3, and 0.5 across the

Table 6.5. Geometric input parameters used for the performance analysis.

HMX geometric parameters			
Length	L	0.2	m
Width	W	0.4	m
Dry channel height	s_d	2.0	mm
Wet channel height	s_w	2.0	mm
Wall thickness	s_{wall}	0.5	mm
Number of dry channels	N_d	100	
Number of wet channels	N_w	101	

four defined inlet conditions. The results are organized into four subplots (A–D), allowing for a comparative analysis between dry and humid operating environments. In the cases shown, the inlet velocity in the dry channel was fixed at $v_{d,i} = 1\ m/s$. Figure 6.8 illustrates the longitudinal temperature profiles for the dry channel (T_d, red line), wet channel (T_w, blue line), and liquid film interface (T_i, magenta line). Before examining the specific numerical values, it is instructive to analyze how the overall shape of the temperature profiles evolves as a function of the recirculation ratio. This evolution directly reflects the local distribution of the thermal driving force along the exchanger length.

A distinct change in the concavity of the dry channel temperature profile is evident across all cases. At high recirculation ($r_m = 0.5$), the profile exhibits a convex shape, characterized by a steep gradient near the inlet ($x = 0$) which gradually flattens towards the outlet. This reflects a high cooling effectiveness sustained by the specific thermal evolution of the wet channel. The working air flows in counter-current from the recirculation coordinate ($x = L$) toward the wet channel outlet ($x = 0$). Its temperature remains consistently lower than that of the dry channel, and the thermal gap between the two streams widens progressively toward the dry channel inlet. This persistent driving force is a direct consequence of the latent heat contribution.

Although the wet channel mass flow rate is lower than that of the dry channel, the energy absorbed by water evaporation limits its temperature rise. As a result, it remains smaller than the corresponding temperature drops in the dry channel. At low recirculation ($r_m = 0.1$), the concavity inverts. The curve is flatter near the inlet and steepens only towards the outlet ($x = L$). This behavior suggests that the cooling potential is suppressed in the initial portion of the exchanger due to the rapid thermal saturation of the wet channel stream. As a result, a significant fraction of the overall heat transfer is displaced toward the downstream region, close to the dry channel outlet. Furthermore, a characteristic behavior emerges in the wet channel temperature profile at low recirculation ratio ($r_m = 0.1$). As observed in the graphs, the wet channel temperature undergoes a sharp decrease immediately after entering the channel ($x = L$). This occurs because the diverted air enters at the dry outlet temperature and is rapidly cooled by evaporation at the interface. However, due to the low mass flow rate (and thus low thermal capacity), this temperature reduction cannot be sustained. The wet channel stream absorbs the sensible heat load from the dry channel. Consequently, its temperature rises again as it flows toward $x = 0$. This results in a pronounced local minimum in the wet channel temperature profile, a behavior consistently observed under low recirculation conditions.

In conditions characterized by low specific humidity ($\omega_{d,i} = 6\ g_v/kg_{da}$), the exchanger exhibits a strong positive response to increases in the working air fraction. Focusing on Figure 6.8-A ($T_{d,i} = 25\ °C$), the transition from $r_m = 0.1$ to $r_m = 0.5$ shifts the outlet temperature from approximately 21.1°C down to 9.3°C. The profile at $r_m = 0.1$ clearly shows the "recovery" phenomenon in the wet channel: the air enters at ~21°C, drops slightly, but exits the exchanger at ~25°C, fully thermally saturated. At $r_m = 0.5$, the wet channel air exits at ~19.7°C, maintaining a driving force along the entire length. This trend is amplified in Figure 6.8-B ($T_{d,i} = 40\ °C$). With $r_m = 0.1$, the dry channel air exits at 28.4°C. The wet channel temperature profile displays a

characteristic V-shaped distribution near the inlet ($x = L$): it enters at 28.4°C, drops to ~26°C due to flash evaporation, but is immediately overwhelmed by the heat flux, exiting the system at 39.6°C. This confirms that with 10% recirculation, the working fluid is unable to act as an effective heat sink for the hot primary stream. Conversely, with $r_m = 0.5$, the dry channel air is cooled to 10.1°C. These results demonstrate that, under low-humidity conditions (Cases A and B), the achievable cooling is primarily constrained by the thermal capacity of the wet channel stream rather than by psychrometric limitations. Consequently, increasing the recirculation ratio proves to be a highly effective strategy, yielding significant reductions in outlet temperature.

When transitioning to humid operating conditions, the governing mechanism shifts from a thermally limited to a mass-transfer-limited regime. In Figure 6.8-C, increasing r_m from 0.3 to 0.5 yields a marginal gain, reducing the outlet temperature from 23.9°C to 23.4°C. The wet channel air and interface temperatures converge closely, indicating that the evaporation process is inhibited by the high local humidity. Similarly, in Figure 6.8-D, the benefit of increasing recirculation ratio saturates. At $r_m = 0.5$, the outlet temperature is 23.5°C. It is worth noting the convergence of the results.

Despite a 10°C difference in inlet temperature between Case C and Case D, the outlet temperatures at $r_m = 0.5$ are nearly identical (23.4°C vs 23.5°C). This convergence confirms that, in humid environments, the system performance is predominantly governed by the inlet air dew-point temperature, with the sensible inlet temperature and further increases in recirculation playing a secondary role.

Figure 6.9 illustrates the longitudinal profiles of specific humidity for the dry channel (ω_d, red line), wet channel (ω_w, blue line), and the saturation specific humidity at the liquid film interface (ω_i, magenta line). Since the M-cycle operates as an indirect evaporative cooler, the primary air stream is physically separated from the wet interface. Consequently, the specific humidity in the dry channel (ω_d) remains constant along the entire length, resulting in a purely sensible cooling process.

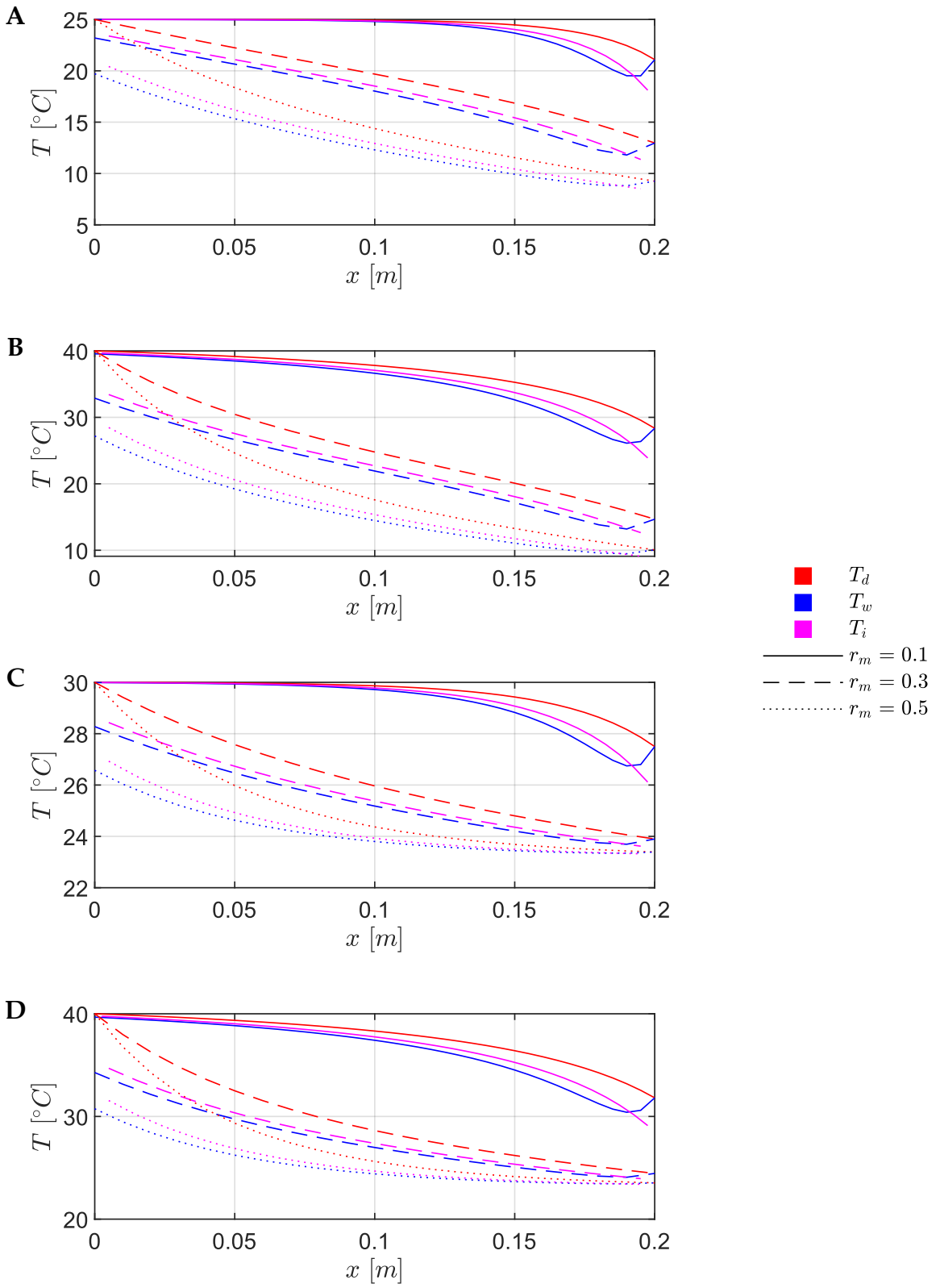

Figure 6.8. Temperature profiles of the dry channel, wet channel, and air-water interface at different recirculation ratios for $v_{d,i} = 1\ m/s$ and different inlet conditions: $T_{d,i} = 25\ °C, \omega_{d,i} = 6\ g_v/kg_{da}$ (A); $T_{d,i} = 40\ °C, \omega_{d,i} = 6\ g_v/kg_{da}$ (B); $T_{d,i} = 30\ °C, \omega_{d,i} = 18\ g_v/kg_{da}$ (C); $T_{d,i} = 40\ °C, \omega_{d,i} = 18\ g_v/kg_{da}$ (D).

Conversely, the wet channel is characterized by a continuous increase in humidity as the air flows from the inlet ($x = L$) to the outlet ($x = 0$), driven by the evaporation of the liquid film.

In the scenarios characterized by dry inlet air ($\omega_{d,i} = 6\ g_v/kg_{da}$), the system exhibits a high potential for mass transfer. The driving force for evaporation is the difference between the saturation humidity at the interface (ω_i) and the bulk humidity of the wet channel air (ω_w). Focusing on Figure 6.9-A ($T_{d,i} = 25\ °C$), the effect of the recirculation ratio is substantial. At low recirculation ($r_m = 0.1$), the specific humidity of the wet channel air rises steeply, increasing from the inlet value of 6 g_v/kg_{da} to an outlet value of approximately 20 g_v/kg_{da}. The profile shows that ω_w rapidly approaches ω_i (which remains nearly constant around 20 g_v/kg_{da} for a large portion of the duct). This indicates that the small mass of working air becomes saturated very quickly. As a result, the concentration gradient required for further evaporation is nullified in the initial part of the channel. At high recirculation ($r_m = 0.5$), the specific humidity increase is more gradual, reaching a maximum of only ~15 g_v/kg_{da} at the outlet. This is because the larger airflow dilutes the vapor, preventing the wet channel air from reaching saturation. In Figure 6.9-B ($T_{d,i} = 40\ °C$) under low recirculation conditions ($r_m = 0.1$), the limited heat sink capacity prevents significant cooling of the liquid film. Consequently, the high interface temperature maintains a high saturation humidity and promotes intense evaporation. This results in a sharp increase in the wet channel air specific humidity, which reaches approximately 47 g_v/kg_{da} at the outlet, effectively saturating the air at the high discharge temperature. Conversely, with $r_m = 0.5$, the wet channel air exits at approximately 24 g_v/kg_{da}. By maintaining the bulk humidity well below the saturation limit, the high recirculation ratio ensures a sustained driving force ($\omega_i - \omega_w$) along the entire length of the exchanger.

In humid conditions ($\omega_{d,i} = 18\ g_v/kg_{da}$), the mass transfer mechanism is constrained by the high inlet water vapor partial pressure. In Figure 6.9-C ($T_{d,i} = 30\ °C$), the profiles

for ω_w and ω_i exhibit a narrower separation gap compared to the dry cases. At low recirculation ($r_m = 0.1$), the specific humidity of the wet channel air increases due to the low mass flow rate, reaching an outlet value of approximately 27 g_v/kg_{da}. Increasing the recirculation to $r_m = 0.5$ results in a lower outlet humidity of approximately 22 g_v/kg_{da}, as the larger mass of working air dilutes the evaporated moisture. The interface saturation humidity ω_i follows a very similar trend, maintaining a minimal gap from ω_w. Similarly, in Figure 6.9-D ($T_{d,i} = 40\ °C$), despite the higher temperatures, the specific humidity growth is limited by the saturation constraint. At $r_m = 0.1$, the high interface temperature drives the outlet humidity up to approximately 48 g_v/kg_{da}, effectively saturating the small amount of working air at a very high temperature. At $r_m = 0.5$, the outlet humidity reaches a lower value of roughly 30 g_v/kg_{da}.

Finally, it is worth noting that the morphological evolution of humidity profiles mirrors the trends observed in the temperature analysis. At high recirculation ratio ($r_m = 0.5$), the humidity profiles display a convex shape, characterized by a continuous and distributed mass transfer along the entire channel length. Conversely, at low recirculation ratio ($r_m = 0.1$), the profiles exhibit a change in curvature.

To complete the analysis of the heat and mass transfer mechanisms, Figure 6.10 presents the local evaporation rate profiles along the channel length, which represent the local source term of the latent cooling power. A fundamental inversion in the evaporation profile behavior is observed across all inlet conditions when varying the recirculation ratio. This results in distinct locations where the cooling power is generated within the heat exchanger.

At low recirculation ($r_m = 0.1$), the evaporation rate exhibits a monotonically decreasing trend from the wet channel inlet ($x = L$) to the wet channel outlet ($x = 0$). Significant evaporation occurs at the wet channel entrance ($x = L$), where the fresh working air first enters the duct and interacts with the liquid film. Subsequently, the

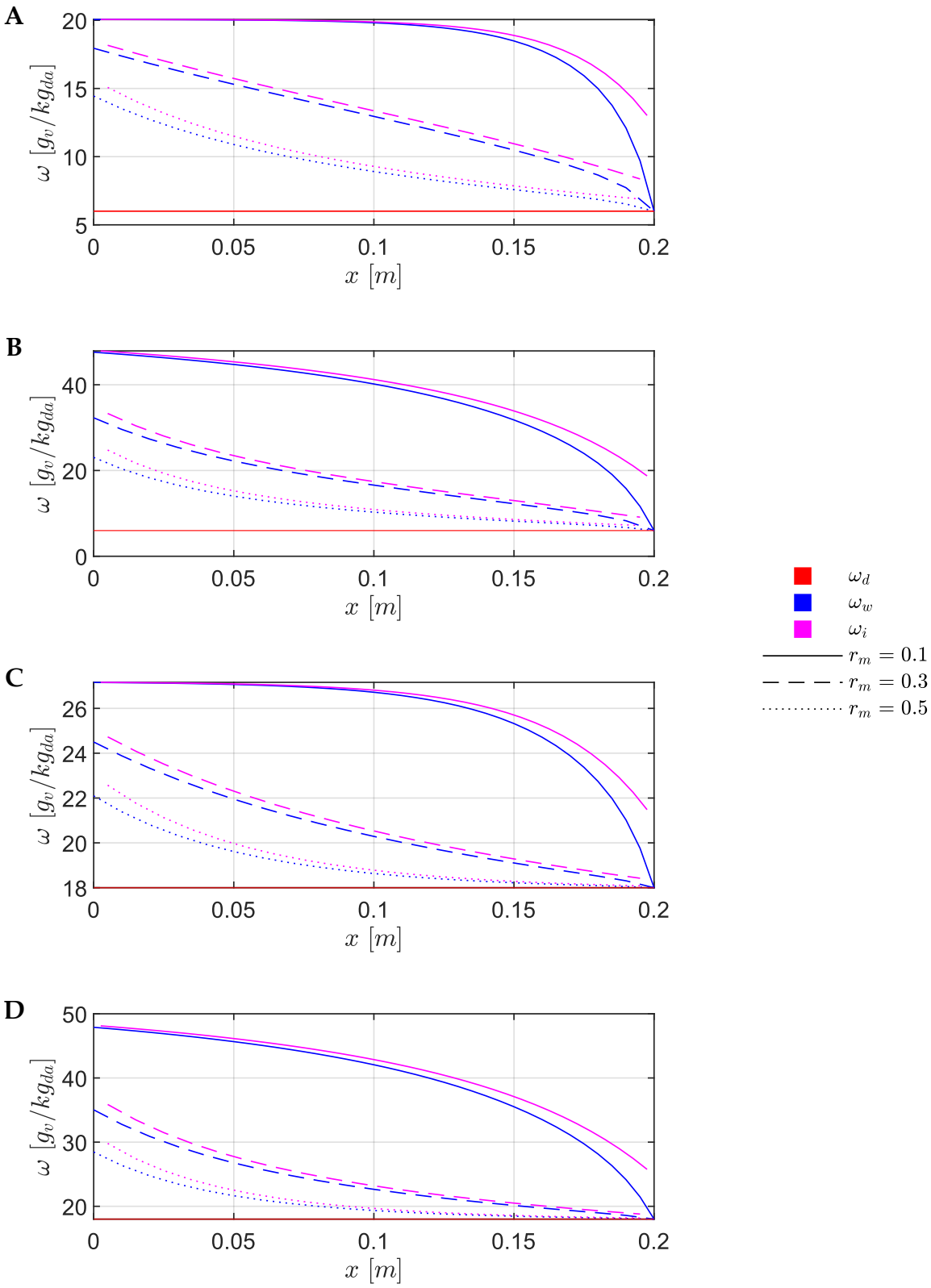

Figure 6.9. Specific humidity profiles of the dry channel, wet channel, and air-water interface at different recirculation ratios for $v_{d,i} = 1\ m/s$ and different inlet conditions: $T_{d,i} = 25\ °C, \omega_{d,i} = 6\ g_v/kg_{da}$ (A); $T_{d,i} = 40\ °C, \omega_{d,i} = 6\ g_v/kg_{da}$ (B); $T_{d,i} = 30\ °C, \omega_{d,i} = 18\ g_v/kg_{da}$ (C); $T_{d,i} = 40\ °C, \omega_{d,i} = 18\ g_v/kg_{da}$ (D).

evaporation rate declines sharply until it reaches practically null values. This is due to the small mass of working air reaching thermodynamic saturation shortly after entering the channel. As a result, a 'dead zone' is created in the region approaching the wet channel exit where no further latent heat is absorbed. As the recirculation ratio increases, the evaporation rate profile exhibits a more complex behavior where monotonicity is no longer guaranteed, as it becomes highly dependent on the specific inlet conditions. At intermediate recirculation levels ($r_m = 0.3$), the location of the maximum evaporation rate is not necessarily the wet channel inlet ($x = L$). Depending on the scenario, the peak may shift toward the wet-channel outlet ($x = 0$). Conversely, at high recirculation ratio ($r_m = 0.5$), the point of maximum evaporation consistently coincides with the wet channel exit ($x = 0$) across all investigated cases. A general trend observed across all analyzed cases is that an increase in the recirculation ratio consistently raises the local evaporation rates at the wet channel outlet ($x = 0$) while lowering the values at the wet-channel inlet ($x = L$). This behavior highlights that a higher wet channel mass flow rate prevents early thermodynamic saturation. As a result, the latent heat exchange shifts from a localized process near the recirculation point to a more distributed one, with peak intensity at the hottest section of the exchanger.

In Figure 6.10-A ($T_{d,i} = 25\ °C$), the case with $r_m = 0.5$ shows a peak evaporation rate of approximately 11 $g/(s\ m^2)$ at the wet channel outlet and a non-monotonic behavior. In contrast, the $r_m = 0.1$ case shows a value near zero over nearly half of the channel length, confirming the existence of a large inactive region. The impact of inlet temperature is evident in Figure 6.10-B ($T_{d,i} = 40\ °C$). The peak evaporation rate for $r_m = 0.5$ jumps to approximately 30 $g/(s\ m^2)$, nearly three times the value of Case A. This non-linear increase highlights how the vapor pressure curve amplifies the cooling potential in hot climates, if sufficient airflow is available to maintain a non-saturated wet channel stream.

In humid conditions, the evaporation rates are significantly suppressed. In Figure 6.10-C ($T_{d,i} = 30\ °C$), the peak evaporation rate for $r_m = 0.5$ is roughly 8 $g/(s\ m^2)$. Despite the inlet temperature being higher than in Case A, the evaporation rate is lower, confirming that the high ambient humidity reduces the mass transfer driving force and stifles the latent cooling process. Furthermore, in Figure 6.10-D ($T_{d,i} = 40\ °C$), the peak rate at $r_m = 0.5$ is approximately 23 $g/(s\ m^2)$. While significant, it is considerably lower than the dry equivalent (Case B). Moreover, for the low recirculation case ($r_m = 0.1$), the evaporation rate remains very low for most of the channel with high values only near the entrance ($x = L$).

These results demonstrate that increasing the recirculation ratio reduces the outlet temperature, thereby improving the dew-point effectiveness. However, this thermodynamic advantage comes at the cost of a reduced product flow rate, as a larger portion of the intake air is sacrificed to maintain the evaporative process.

6.2.2. Effect of inlet velocity

The inlet air velocity in the dry channel ($v_{d,i}$) represents another key operating parameter for M-cycle heat exchangers, as it governs both the processed airflow rate and the residence time available for heat and mass transfer. To assess its influence on the system thermal behavior and cooling effectiveness, simulation results are presented for inlet velocities of 1 m/s, 3 m/s, and 5 m/s across the four reference inlet conditions. The results are organized into four subplots (A–D), allowing for a direct comparison between dry and humid operating environments at different inlet temperatures. In all cases shown, the recirculation ratio is fixed at $r_m = 0.3$ to isolate the effect of inlet velocity while maintaining an intermediate extraction rate.

Figure 6.11 illustrates the longitudinal temperature profiles along the channel length for the dry channel (T_d, red line), wet channel (T_w, blue line), and liquid film interface

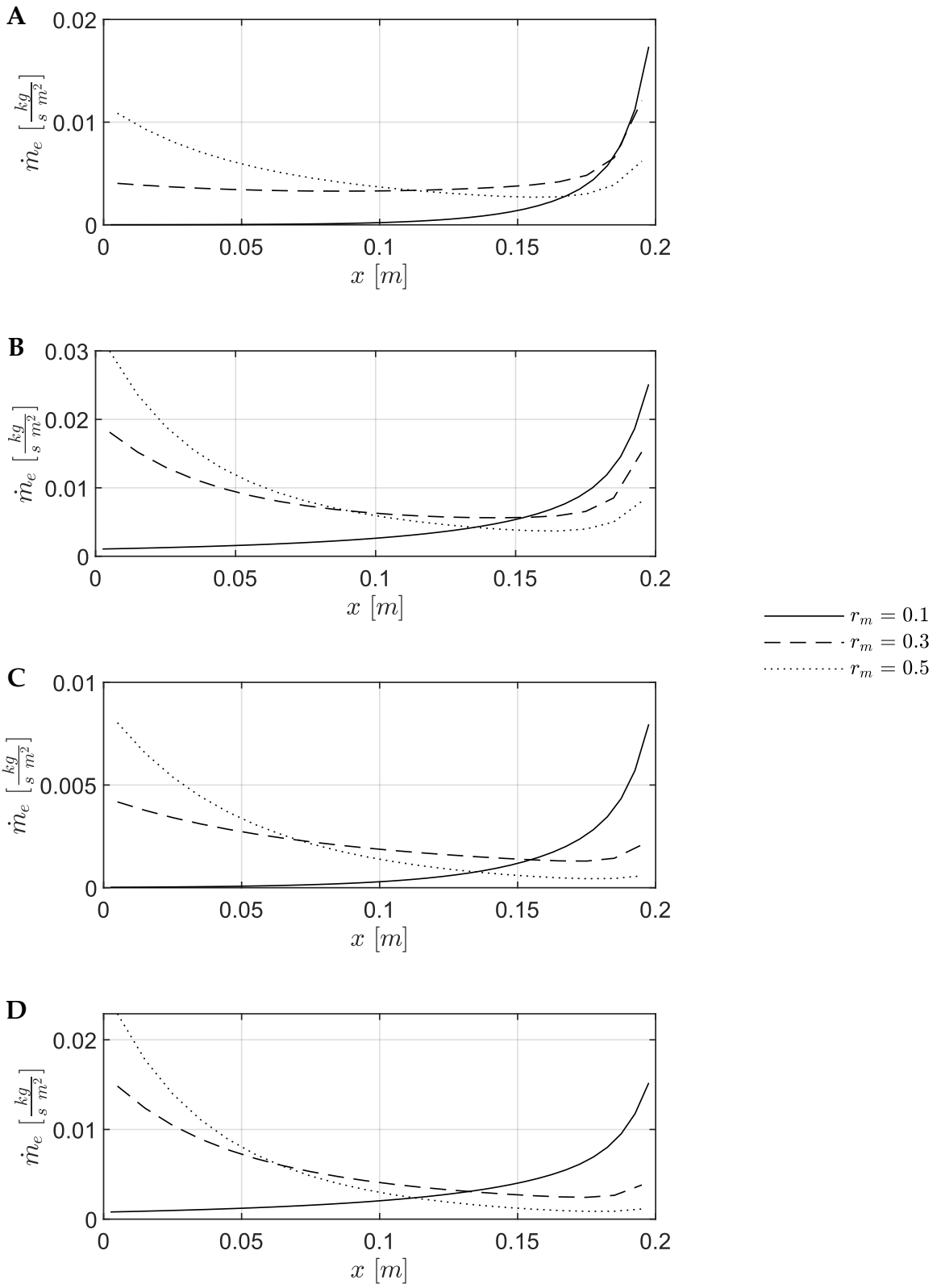

Figure 6.10. Local evaporation rate profiles along the wet channel at different recirculation ratios for $v_{d,i} = 1\ m/s$ *and different inlet conditions:* $T_{d,i} = 25\ °C, \omega_{d,i} = 6\ g_v/kg_{da}$ *(A);* $T_{d,i} = 40\ °C, \omega_{d,i} = 6\ g_v/kg_{da}$ *(B);* $T_{d,i} = 30\ °C, \omega_{d,i} = 18\ g_v/kg_{da}$ *(C);* $T_{d,i} = 40\ °C, \omega_{d,i} = 18\ g_v/kg_{da}$ *(D).*

(T_i, magenta line). The evolution of these profiles highlights how variations in inlet velocity modify the residence time and, consequently, the heat exchange mechanisms.

A consistent trend is observed across all operating conditions: increasing the inlet velocity leads to a degradation in cooling performance, as indicated by higher dry channel outlet temperatures ($T_{d,out}$). This behavior is directly related to the reduction in residence time. At low velocity, the air progresses slowly through the channel, allowing sufficient time for heat and mass transfer to occur. As the velocity increases, the air traverses the exchanger more rapidly and exits before the available cooling potential can be fully exploited. However, the system response is non-linear. The increase in outlet temperature between 1 m/s and 3 m/s is more pronounced than that observed between 3 m/s and 5 m/s, indicating that the influence of residence time on heat exchange efficiency diminishes as the flow rate increases.

In humid conditions (Figure 6.11-C,D), the dry channel temperature exhibits a predominantly convex profile at low velocity, approaching the dew-point limit along the channel. Conversely, under dry inlet conditions, the profiles display a more complex curvature. In Figure 6.11-B ($T_{d,i} = 40\ °C$), the profile is initially convex but undergoes a change in concavity in the downstream region. In Figure 6.11-A ($T_{d,i} = 25\ °C$), the initial portion of the profile appears nearly linear, followed by a more pronounced concave behavior in the second half of the exchanger.

The sensitivity to inlet velocity is particularly evident under dry and high-temperature conditions. In Figure 6.11-B ($T_{d,i} = 40\ °C$, low humidity), at $v_{d,i} = 1\ m/s$ the extended residence time allows the air to be cooled down to approximately 14.7 $°C$. Increasing the velocity to 3 m/s raises the outlet temperature to about 20.7 $°C$, while at 5 m/s it further increases to 24.6 $°C$. Overall, increasing the inlet velocity from 1 m/s to 5 m/s results in a performance penalty of approximately 10 $°C$. Although higher velocities may be attractive from a compactness standpoint, as they allow larger airflow rates per unit volume, they significantly reduce the dew-point effectiveness. A similar trend is

observed in Figure 6.11-A ($T_{d,i} = 25\ °C$), where the outlet temperature increases from 13 $°C$ at 1 m/s to 17.8 $°C$ at 5 m/s.

Under humid inlet conditions, the achievable cooling is inherently limited by the higher dew-point temperature; nevertheless, residence time remains a critical parameter. In the most severe case, Figure 6.11-D ($T_{d,i} = 40\ °C$, high humidity), the system struggles to provide significant cooling at high velocities. At 1 m/s, the outlet temperature reaches approximately 24.5 $°C$, whereas at 5 m/s it rises to 30.1 $°C$. Even in this constrained regime, the difference of about 5.6 $°C$ remains significant: at high velocity, the outlet temperature is only marginally lower than the ambient, while at low velocity a temperature reduction exceeding 15 $°C$ is achieved. In Figure 6.11-C ($T_{d,i} = 30\ °C$, high humidity) the performance range is narrower, with the outlet temperature increasing from 23.9 $°C$ at 1 m/s to 26.2 $°C$ at 5 m/s. In this case, the elevated humidity compresses the thermodynamic cooling potential, reducing the sensitivity of the system to velocity variations compared to dry-air conditions.

Beyond the dry channel analysis, a generally observed trend is observed also in the wet channel. While increasing the inlet velocity leads to higher dry channel outlet temperatures, the wet channel outlet temperature decreases slightly. As a result, the overall temperature rise within the wet channel becomes smaller as the velocity increases. Moreover, the location of temperature recovery in the wet channel, following the initial drop caused by intense evaporation near the inlet ($x = L$), progressively shifts downstream as the velocity increases. This behavior indicates that higher velocities delay the heat and mass transfer processes along the channel length.

These results confirm that inlet velocity plays a critical role in determining system performance. Low velocities favor high residence times, allowing the air temperature to approach the theoretical dew-point limit. Conversely, operation at high velocities is characterized by higher processed airflow rates but significantly reduced cooling effectiveness.

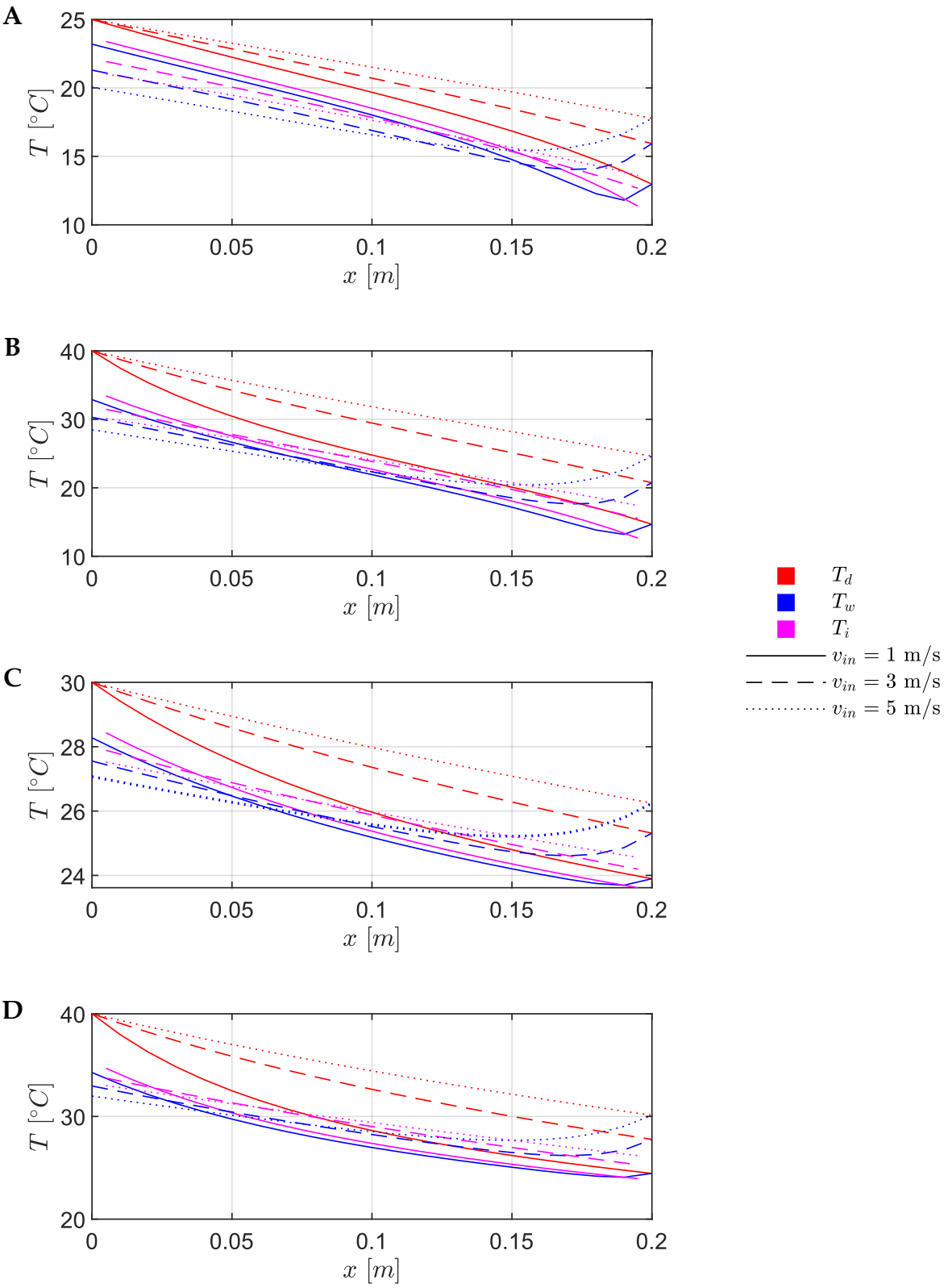

Figure 6.11. Temperature profiles of the dry channel, wet channel, and air-water interface at different inlet air velocities for $r_m = 0.3$ and different inlet conditions: $T_{d,i} = 25$ °C, $\omega_{d,i} = 6$ g_v/kg_{da} (A); $T_{d,i} = 40$ °C, $\omega_{d,i} = 6$ g_v/kg_{da} (B); $T_{d,i} = 30$ °C, $\omega_{d,i} = 18$ g_v/kg_{da} (C); $T_{d,i} = 40$ °C, $\omega_{d,i} = 18$ g_v/kg_{da} (D).

Figure 6.12 illustrates the longitudinal profiles of specific humidity in the wet channel (ω_w, blue line), together with the saturation humidity at the liquid film interface (ω_i, magenta line), for the three investigated inlet velocities. The specific humidity of the dry channel (ω_d, red line), remains constant along the channel in all configurations as a direct consequence of the indirect evaporative cooling process and is therefore not discussed further.

The effect of inlet velocity on the humidity evolution in the wet channel primarily reflects the dilution effect associated with higher air mass flow rates at a fixed recirculation ratio. The increase in airflow rate dominates the process, resulting in reduced specific humidity gains along the channel with increasing velocity.

This behavior is particularly evident under dry inlet conditions ($\omega_{d,i} = 6\ g_v/kg_{da}$), where the wet channel air operates far from saturation and can absorb significant amounts of moisture. In Figure 6.12-A ($T_{d,i} = 25\ °C$), the specific humidity increases from 6 to approximately 18 g_v/kg_{da} at an inlet velocity of 1 m/s, remaining close to the saturation value at the interface over a large portion of the channel length. When the velocity is increased to 5 m/s, the outlet humidity is limited to about 14.7 g_v/kg_{da}, and a clear separation between ω_w and ω_i persists along the channel.

The same trend becomes more pronounced in Figure 6.12-B ($T_{d,i} = 40\ °C$), where the thermodynamic driving force for evaporation is higher. At 1 m/s, the wet air exits the channel at approximately 32.3 g_v/kg_{da}, while at 5 m/s the outlet humidity decreases to 24.9 g_v/kg_{da}.

Under humid inlet conditions ($\omega_{d,i} = 18\ g_v/kg_{da}$), the humidity profiles exhibit a different behavior. At 3 m/s and 5 m/s, the increase in specific humidity is more pronounced in the upstream region of the channel compared to the 1 m/s case. However, this trend reverses along the channel length, leading to lower outlet humidity values at higher velocities. In Figure 6.12-C ($T_{d,i} = 30\ °C$), the outlet specific

humidity decreases only slightly from 24.5 g_v/kg_{da} at 1 m/s to 22.8 g_v/kg_{da} at 5 m/s. In Figure 6.12-D ($T_{d,i} = 40\ °C$), the outlet humidity decreases from about 35 g_v/kg_{da} at 1 m/s to 30.6 g_v/kg_{da} at 5 m/s.

At equal inlet temperature but different humidity levels (Figure 6.12-B-D), the increase in specific humidity along the channel is more limited under high-humidity conditions. Furthermore, the difference between the saturated humidity at the interface and the bulk humidity at the wet channel outlet is more pronounced in the high-humidity case across the investigated velocities.

Overall, lower inlet velocities allow the wet channel air to approach the saturated interface condition more closely, while higher velocities produce a leaner outlet mixture characterized by a smaller increase in specific humidity

Finally, Figure 6.13 presents the longitudinal profiles of the local evaporation rate along the channel for the three investigated inlet velocities, providing direct insight into how flow conditions redistribute the latent cooling source within the exchanger. In all inlet conditions, increasing the velocity systematically shifts the evaporation profiles upward. However, this increase is non-linear, with more pronounced variations occurring at lower velocities.

In Figure 6.13-A ($T_{d,i} = 25\ °C$, $\omega_{d,i} = 6\ g_v/kg_{da}$), the profiles for all velocities exhibit an initial decrease in the evaporation flux followed by a nearly constant trend along the rest of the duct.

In Figure 6.13-B ($T_{d,i} = 40\ °C$, $\omega_{d,i} = 6\ g_v/kg_{da}$), the higher inlet temperature results in overall higher evaporation fluxes compared to the previous case. After an initial decrease at the inlet, a progressive increase is observed toward the end of the channel. This rising trend is most pronounced for the low-velocity case (1 m/s), although its absolute values remain lower than those corresponding to higher velocities.

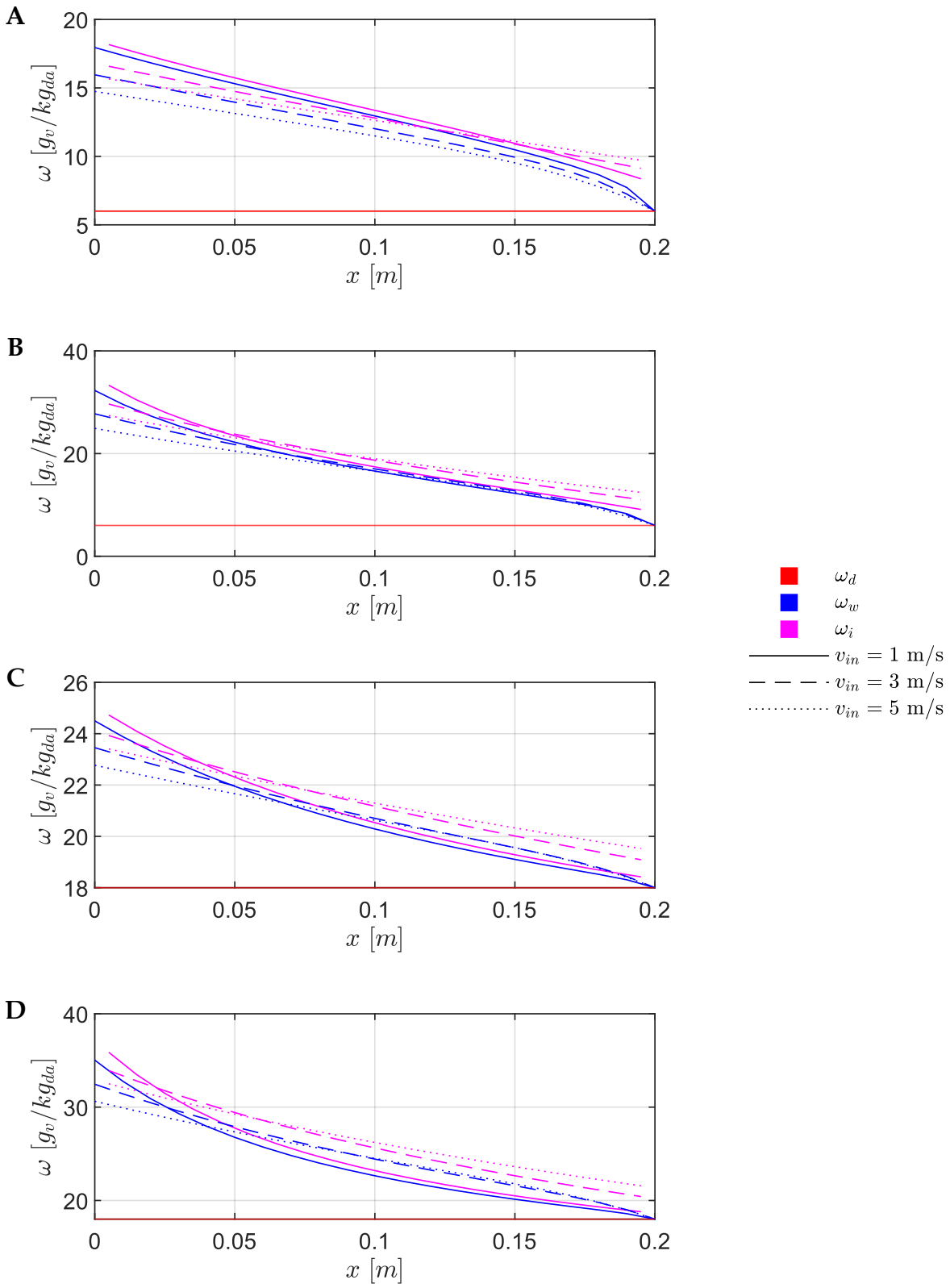

Figure 6.12. Specific humidity profiles of the dry channel, wet channel, and air-water interface at different inlet air velocities for $r_m = 0.3$ and different inlet conditions: $T_{d,i} = 25\ °C, \omega_{d,i} = 6\ g_v/kg_{da}$ (A); $T_{d,i} = 40\ °C, \omega_{d,i} = 6\ g_v/kg_{da}$ (B); $T_{d,i} = 30\ °C, \omega_{d,i} = 18\ g_v/kg_{da}$ (C); $T_{d,i} = 40\ °C, \omega_{d,i} = 18\ g_v/kg_{da}$ (D).

Under humid inlet conditions ($\omega_{d,i} = 18\ g_v/kg_{da}$), the profiles still exhibit an initial decrease followed by a subsequent increase. In Figure 6.13-C ($T_{d,i} = 30\ °C$), the low-velocity profile starts at a relatively low value at the wet channel inlet, decreases slightly, and then increases progressively, reaching a final value at $x = 0$ that is higher than the initial one. In contrast, for velocities of 3 and 5 m/s, the highest evaporation rates remain located at the wet-channel inlet.

A similar behavior is observed in Figure 6.13-D ($T_{d,i} = 40\ °C$), where the increase along the channel is even more pronounced. In this case, the low-velocity profile again reaches its maximum at the channel outlet. For the 3 m/s case, the progressive increase along the duct is sufficient to bring the evaporation rate at the outlet back to the same level observed at the inlet.

In the end, when all the coupled effects associated with increasing the inlet velocity are considered (the modification of the interface temperature profile and the higher wet channel air mass flow rate, which sustains a larger concentration gradient between the bulk flow and the interface) the resulting impact on the evaporation process is consistently an enhancement. Consequently, an increase in inlet velocity systematically leads to a higher total evaporated mass.

6.2.3. Effect of combined operating parameters

In this section, results obtained by simultaneously varying multiple operating parameters are compared to provide a comprehensive overview of the combined effects governing evaporative heat exchange in the M-cycle heat and mass exchanger. The geometric parameters of the exchanger correspond to those reported in Table 6.5, while the operating scenarios are defined in Table 6.4.

Figure 6.14 and Figure 6.15 illustrate the dry channel outlet temperature as a function of the recirculation ratio for different inlet air velocities. Across all four cases, increasing the recirculation ratio results in a progressive reduction of the dry-channel

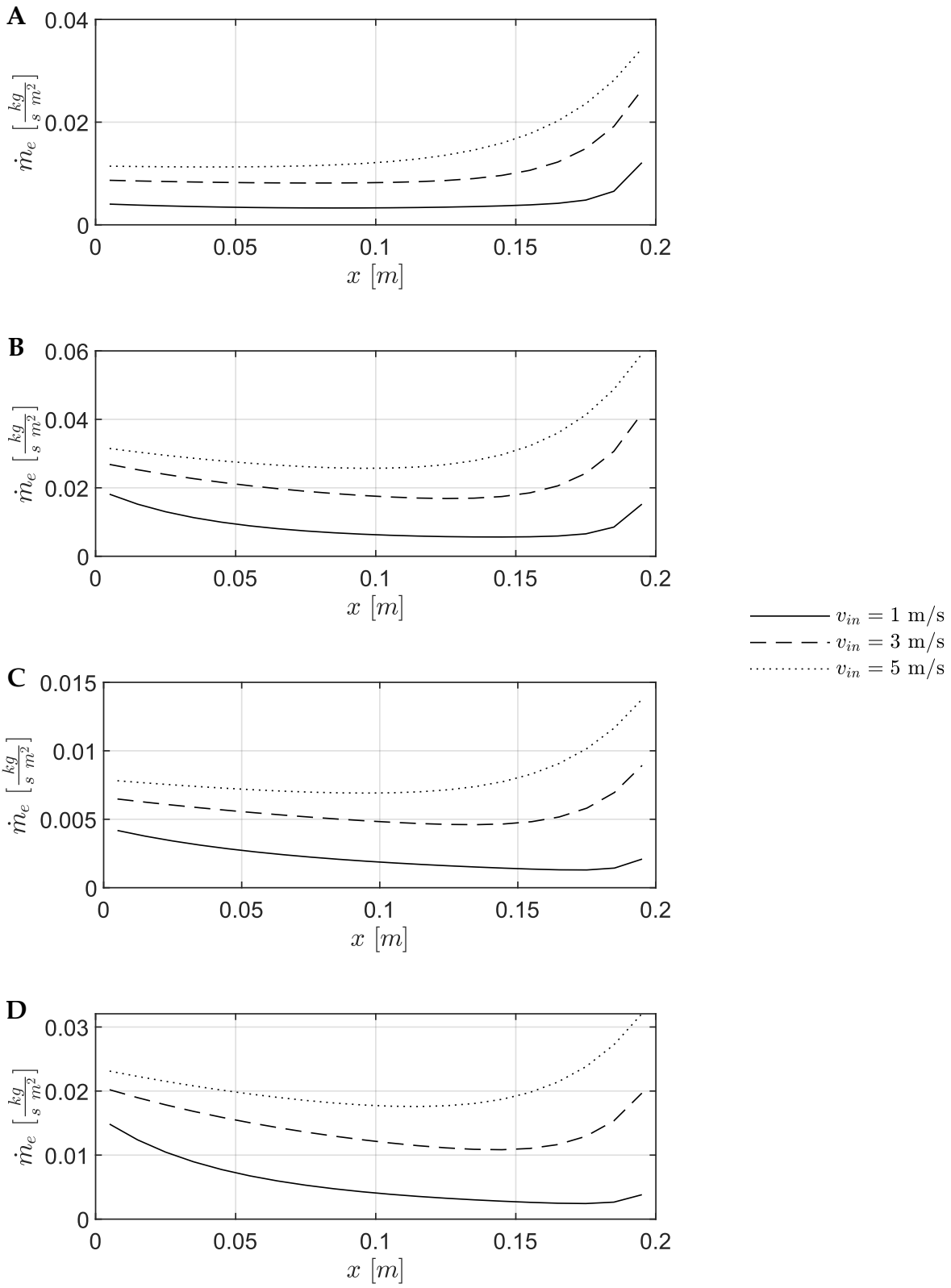

Figure 6.13. Local evaporation rate profiles along the wet channel length at different inlet air velocities for $r_m = 0.3$ *and different inlet conditions:* $T_{d,i} = 25\ °C, \omega_{d,i} = 6\ g_v/kg_{da}$ *(A);* $T_{d,i} = 40\ °C, \omega_{d,i} = 6\ g_v/kg_{da}$ *(B);* $T_{d,i} = 30\ °C, \omega_{d,i} = 18\ g_v/kg_{da}$ *(C);* $T_{d,i} = 40\ °C, \omega_{d,i} = 18\ g_v/kg_{da}$ *(D).*

outlet temperature. This trend reflects the fundamental behavior of the regenerative evaporative process: higher recirculation increases the mass flow rate in the wet channel, enhancing water evaporation and, consequently, the removal of sensible heat from the dry-channel air stream. This mechanism promotes a closer approach of the outlet air temperature toward the thermodynamic limits imposed by the inlet air conditions, namely the dew-point temperature. Across all operating conditions, the outlet temperature exhibits a larger sensitivity to recirculation when r_m is increased from low values, while the rate of decrease progressively diminishes as higher recirculation ratios is approached. For instance, in the low-temperature case in Figure 6.14-A at an inlet velocity of 1 m/s, the outlet temperature drops from 21.1 °C at $r_m =$ 0.1 to 9.2 °C at $r_m = 0.5$. However, a further increase to $r_m = 0.8$ yields a more moderate reduction, reaching a final temperature of 7.5 °C. The influence of inlet air velocity is also consistent among all scenarios. For a fixed recirculation ratio, higher velocities systematically lead to higher outlet temperatures, due to the reduced residence time of the air within the dry channel. At low recirculation ratios, the outlet temperature curves corresponding to different velocities tend to converge toward the inlet temperature, indicating limited regenerative action. Indeed, at $r_m = 0.1$, the temperature spread between the lowest (1 m/s) and highest (6.5 m/s) velocities is merely 0.46 °C (21.09 °C vs. 21.55 °C). As recirculation increases, the curves progressively diverge, with the strongest sensitivity observed at low velocities. At $r_m =$ 0.8, the divergence becomes substantial: the outlet temperature varies by nearly 10 °C across the investigated velocity range, rising from 7.5 °C at 1 m/s to 17.2 °C at 6.5 m/s. At high recirculation ratios, the curves exhibit a progressive reduction in slope, indicating diminishing incremental cooling benefits associated with further increases in recirculation. It is also observed that, in all investigated operating conditions, outlet temperatures below the inlet wet-bulb temperature are achieved only when sufficiently low inlet velocities are combined with sufficiently high recirculation ratios,

highlighting the capability of the M-cycle configuration to operate in the sub–wet-bulb regime. A distinctive behavior emerges under high specific humidity conditions (Figure 6.15). In these cases, at low inlet velocities, the outlet temperature rapidly approaches the dew-point temperature owing to the reduced difference between the inlet air temperature and the dew point. Consequently, the curves exhibit an early flattening and further increases in the recirculation ratio provide only marginal improvements. Moreover, under humid conditions, the effect of inlet velocity remains limited for moderate variations, as the outlet temperature curves are confined within a narrow temperature interval. This behavior is a direct consequence of the reduced evaporative potential of humid air, which constrains further cooling as the system approaches its thermodynamic limit.

Figure 6.16 and Figure 6.17 do not introduce new data but provide a complementary interpretation of the previously discussed results by reversing the independent variable. The figures present the dry channel outlet temperature as a function of the inlet air velocity for different recirculation ratios, allowing for a direct assessment of velocity-driven effects under fixed regenerative conditions. Across all operating scenarios, the outlet temperature exhibits a monotonic increase with inlet air velocity. The influence of the recirculation ratio is clearly reflected in the vertical displacement of the curves. Increasing the recirculation ratio leads to a systematic downward shift of the outlet temperature profiles, indicating enhanced cooling performance. At low recirculation ratios, the curves are relatively flat, suggesting a weak sensitivity of the outlet temperature to changes in velocity. As the recirculation ratio increases, the curves become steeper, reflecting a stronger dependence on residence time when regenerative effects are dominant. Consequently, large differences in outlet temperature are observed at low velocities, whereas at high velocities the impact of recirculation is reduced. Under high-humidity conditions (Figure 6.17), as the system approaches the thermodynamic lower bound imposed by the dew point temperature,

the outlet temperature curves exhibit a change in curvature, marking the transition toward a physically constrained operating region. While the present section discusses a limited number of representative operating cases, a more comprehensive set of three-dimensional performance maps is provided in Appendix A. These results extend the analysis across a wider range of inlet conditions, providing a more complete characterization of the HMX thermal behavior.

In the following section, the performance of the M-cycle heat and mass exchanger is analyzed in terms of effectiveness with respect to both the wet-bulb temperature ε_{wb} (equation 3.93), and the dew-point temperature ε_{dp} (equation 3.94). Since the reported figures describe system behavior at fixed inlet thermo-hygrometric conditions, the inlet air wet-bulb and dew-point temperatures remain constant within each figure.

Under these conditions, the two effectiveness definitions differ only in the normalization term appearing in the denominator, namely $(T_{d,i} - T_{wb,i})$ for ε_{wb} and $(T_{d,i} - T_{dp,i})$ for ε_{dp}. Given that the dry inlet temperature $T_{d,i}$ is fixed, the two effectiveness measures exhibit identical functional trends with respect to the operating parameters, differing only in magnitude. Consequently, wet-bulb and dew-point effectiveness are reported simultaneously using a dual-axis representation.

Figure 6.18 and Figure 6.19 present the effectiveness as a function of the recirculation ratio for different inlet air velocities. The trends of both wet-bulb and dew-point effectiveness inversely mirror the behavior previously observed for the dry channel outlet temperature. Conditions leading to lower outlet temperatures correspond to higher effectiveness values. In all cases, effectiveness increases monotonically with the recirculation ratio, conversely, for a fixed recirculation level, it systematically decreases as the inlet air velocity rises. At low inlet velocities and low recirculation ratios, the effectiveness curves exhibit a marked initial increase, indicating that even modest increments in recirculation produce substantial gains in cooling performance.

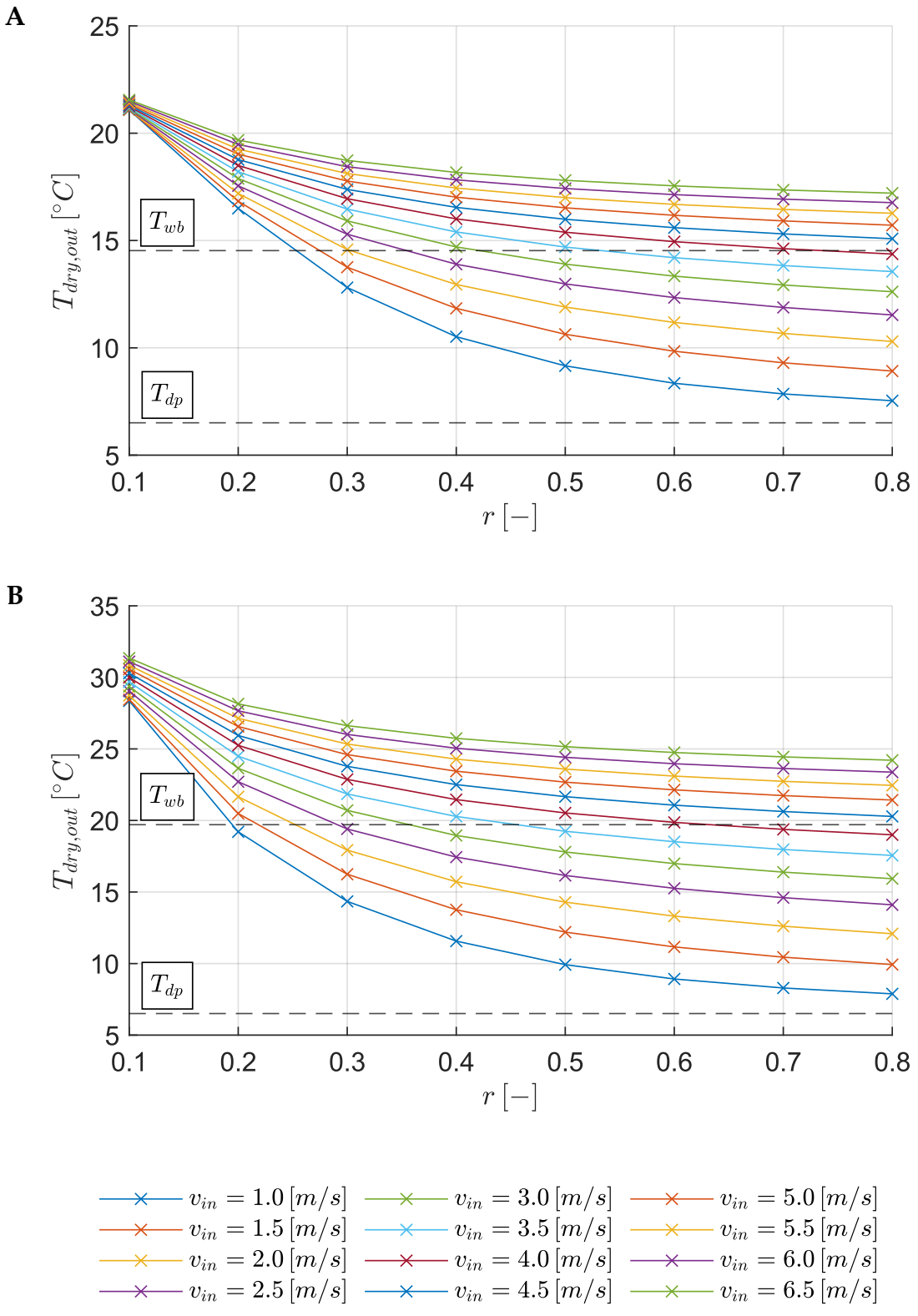

Figure 6.14. Dry-channel outlet temperature as a function of the recirculation ratio for different inlet air velocities. Operating conditions: inlet specific humidity of 6 g_v/kg_{da} and inlet air temperatures of 25°C (A) and 40°C (B).

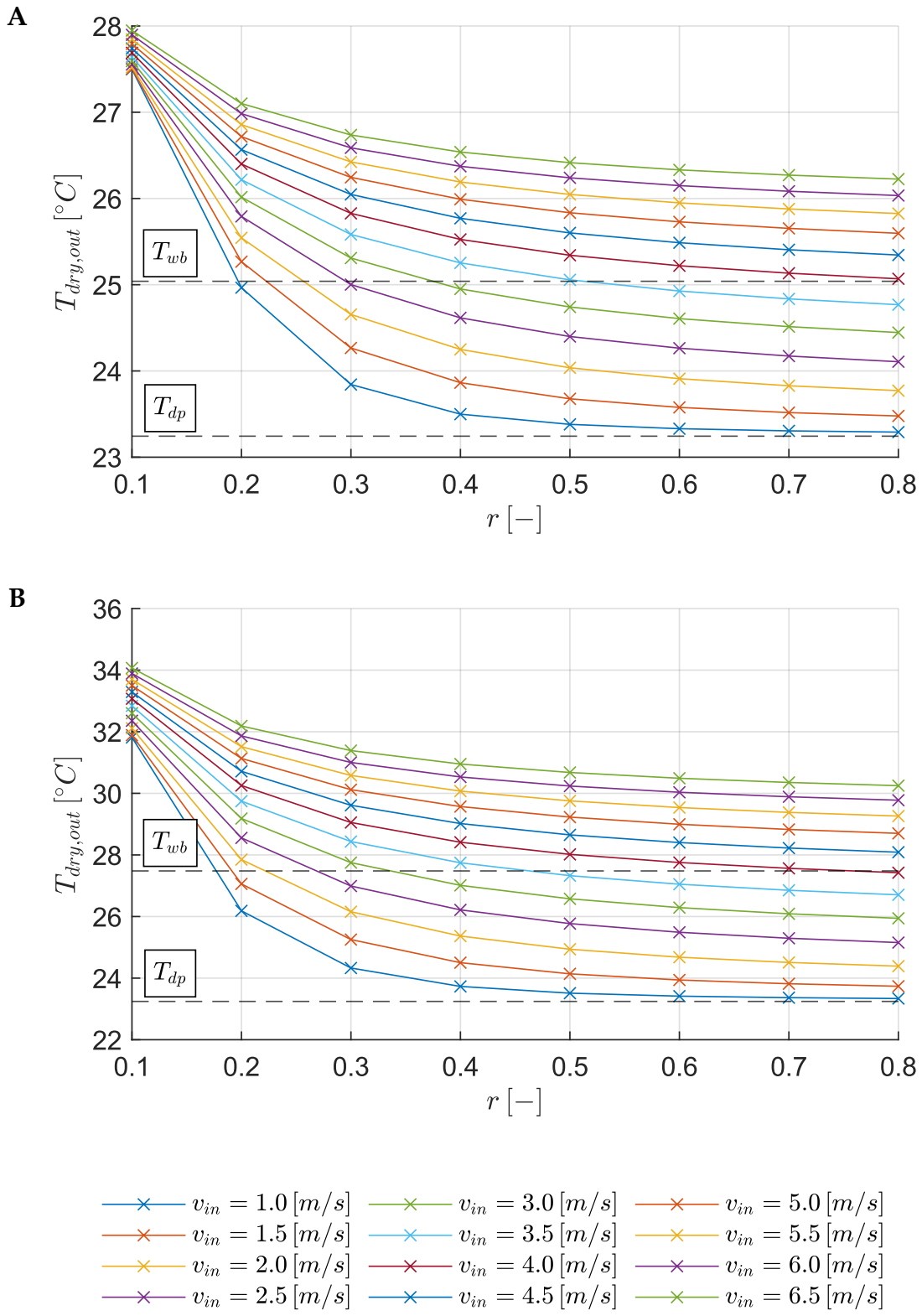

Figure 6.15. Dry-channel outlet temperature as a function of the recirculation ratio for different inlet air velocities. Operating conditions: inlet specific humidity of 18 g_v/kg_{da} *and inlet air temperatures of* 30°C *(A) and* 40°C *(B).*

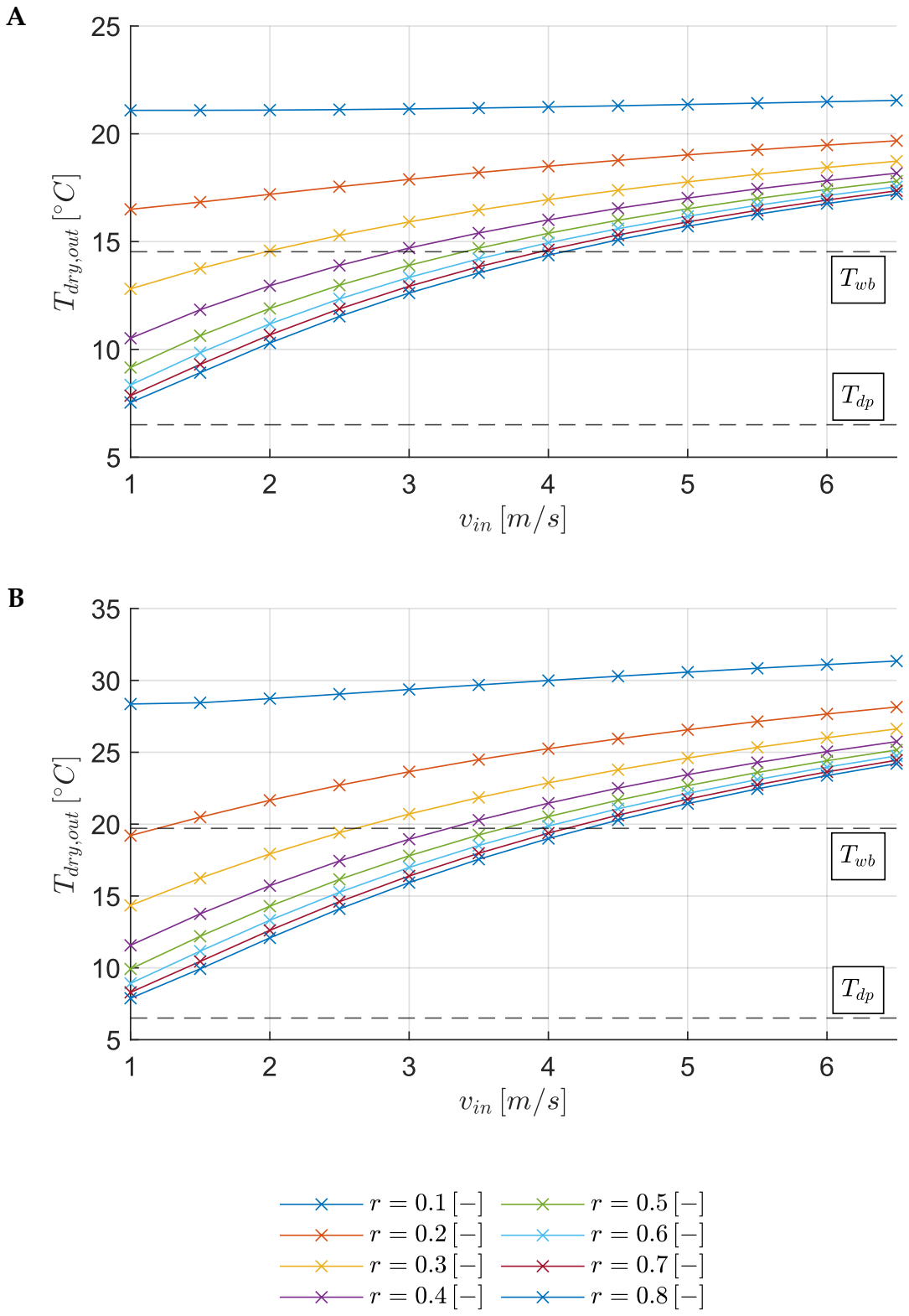

Figure 6.16. Dry-channel outlet temperature as a function of inlet air velocity for different recirculation ratios. Operating conditions: inlet specific humidity of 6 g_v/kg_{da} *and inlet air temperatures of* 25°C *(A) and* 40°C *(B).*

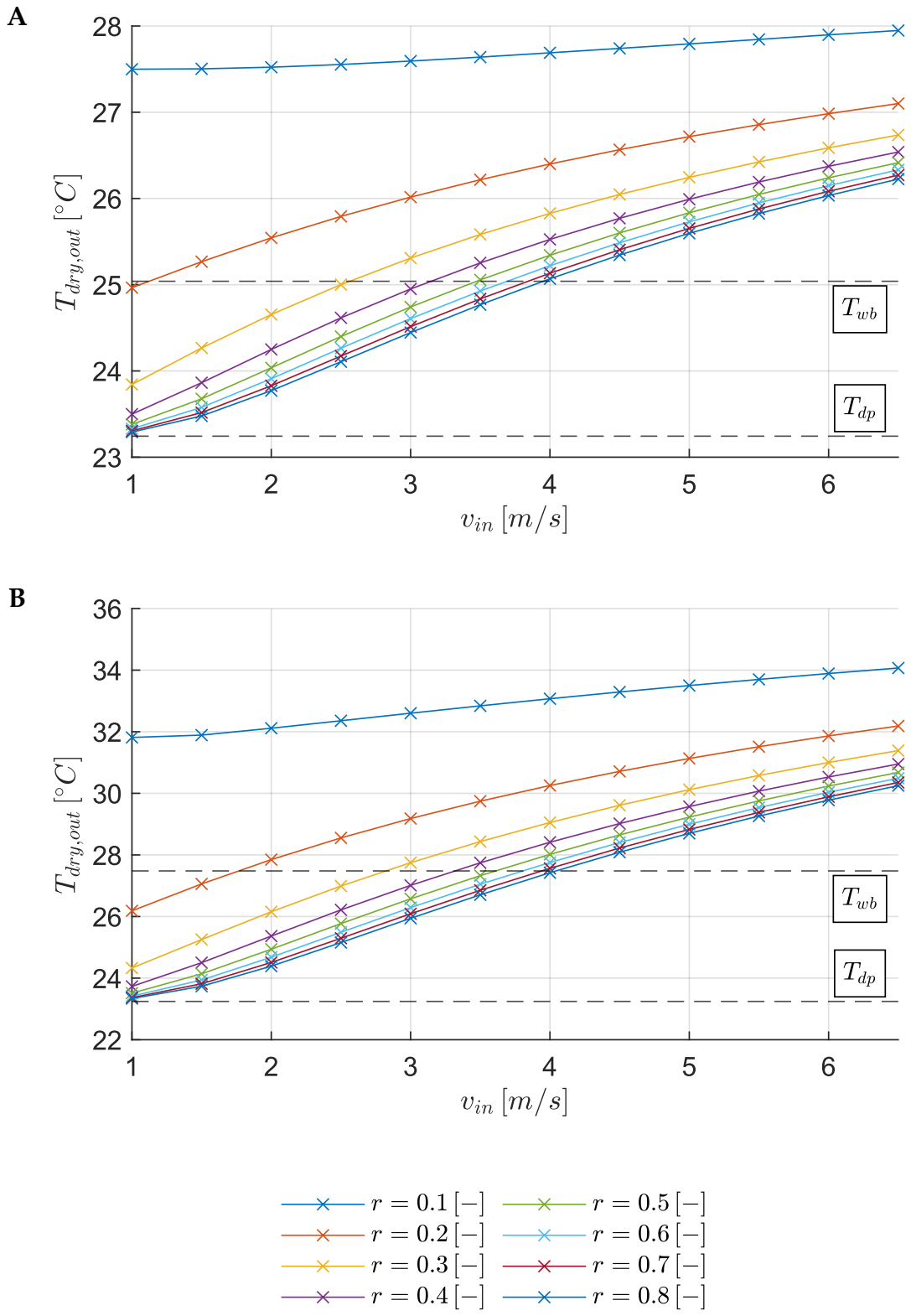

Figure 6.17. Dry-channel outlet temperature as a function of inlet air velocity for different recirculation ratios. Operating conditions: inlet specific humidity of 18 g_v/kg_{da} *and inlet air temperatures of* 30°C *(A) and* 40°C *(B).*

For example, in Figure 6.18-A at 1 m/s, shifting the recirculation ratio r_m from 0.1 to 0.2 causes ε_{wb} to increase from 37.4 % to 81.2 %, effectively doubling the performance with a minor operational adjustment. In this region, the regenerative mechanism operates with high marginal effectiveness, meaning small changes in operating conditions translate into large increases in effectiveness. As the recirculation ratio rises further, the curves progressively flatten, revealing diminishing returns. As inlet velocity increases, overall effectiveness levels are reduced across the entire recirculation range. The marginal gain in effectiveness per unit of recirculation decreases, and the curves exhibit reduced sensitivity to changes in the recirculation ratio. This indicates that high velocities penalize the regenerative process by limiting the time available for heat and mass transfer, even when large air fractions are recirculated. A notable feature common to all cases is the convergence of the effectiveness curves corresponding to different velocities at low recirculation ratios. In this region, effectiveness values converge toward a common trend regardless of velocity. Referring to Figure 6.18 at $r_m = 0.1$, the difference in ε_{wb} between the lowest velocity (1 m/s) and the highest (6.5 m/s) is remarkably small (37.4 % vs. 32.9 %), highlighting that when regenerative action is weak, the system performance is primarily constrained by the inlet air conditions rather than by flow residence time. As recirculation increases, the curves progressively diverge, with low-velocity cases benefiting more strongly from regeneration. At equal specific humidity, a comparison between cases at different inlet temperatures reveals that wet-bulb effectiveness exceeds 100 % at lower recirculation ratios for higher inlet temperatures. As shown in Figure 6.18-B ($T_{d,i} = 40\ °C$), ε_{wb} surpasses 100 % already at $r_m = 0.2$ for 1 m/s ($\varepsilon_{wb} =$ 102.5 %), whereas in Figure 6.18-A ($T_{d,i} = 25\ °C$), this threshold is crossed only at $r_m =$ 0.3. This occurs despite the larger temperature difference between the inlet air and the wet-bulb temperature, indicating that the higher evaporative driving potential associated with elevated inlet temperatures favors a faster relative approach to the

wet-bulb limit. Finally, under high specific humidity conditions, the curves indicate that the dew-point temperature is approached already at intermediate recirculation ratios. In this regime, ε_{dp} rapidly reaches a plateau, and further increases in recirculation yield negligible improvements, as the system operates near its physical limit. This asymptotic behavior is clearly observed in Figure 6.19-A: at $1\,m/s$, increasing r_m from 0.6 to 0.8 results in a minimal variation of ε_{dp} from 98.7 % to 99.3 %, demonstrating that once the dew-point constraint becomes dominant, additional regenerative enhancement is ineffective, regardless of inlet velocity.

Figure 6.20 and Figure 6.21 illustrate the effectiveness as a function of the inlet air velocity for different recirculation ratios. Across all operating conditions, effectiveness decreases monotonically as the inlet velocity increases. For a given velocity, higher recirculation ratios systematically lead to higher effectiveness values, confirming the dominant role of recirculation in enhancing regenerative evaporative cooling. Beyond this general behavior, the sensitivity of effectiveness to velocity varies markedly with the recirculation ratio. At low recirculation values, effectiveness exhibits a limited dependence on velocity: the corresponding curves are nearly flat, indicating that increasing the inlet velocity has a limited impact on performance. For instance, in Figure 6.20-A at $r_m = 0.1$, ε_{wb} decreases by less than 5 percentage points over the entire investigated velocity range (from 37.4 % to 32.9 %), with a correspondingly small variation in ε_{dp}. In contrast, at high recirculation ratios, effectiveness becomes highly sensitive to velocity variations. In this regime, ε_{wb} decreases markedly as velocity increases, transitioning from values well above the wet-bulb limit at low velocities to values well below 100% at the highest velocities considered. Specifically, at $r_m = 0.8$, ε_{wb} decreases from 166.8 % at 1 m/s to 74.4 % at 6.5 m/s. A similar, though bounded, trend is observed for ε_{dp}, which moves away from the dew-point limit as velocity increases. This pronounced decline highlights that the benefits of high recirculation are progressively reduced when residence time is reduced, resulting in a progressive

convergence of the curves at high velocities. Furthermore, specific behavior is observed under high-humidity conditions (Figure 6.21). Here, the curves associated with high recirculation ratios exhibit a distinct change in concavity within the low-velocity region. For example, in Figure 6.21-A at $r_m = 0.8$, the effectiveness shows only minor variations between $1\,m/s$ and $1.5\,m/s$, before beginning its descent. This inflection is associated with the asymptotic approach to the dew-point temperature constraint: as the system nears this thermodynamic limit, the rate of effectiveness improvement saturates, preventing further gains despite the favorable residence time. The intermediate curves are smoothly distributed between these two extremes, demonstrating that the influence of velocity on effectiveness becomes progressively stronger as the recirculation ratio increases. Overall, these results emphasize that optimal performance of the M-cycle exchanger arises from a careful balance between recirculation intensity and airflow velocity, rather than from the maximization of a single operating parameter.

The performance of the system is further characterized by analyzing the temperature drop achieved across the dry channel, defined in equation 3.92.

Figure 6.22 and Figure 6.23 display ΔT_d as a function of the recirculation ratio for various inlet velocities. Consistent with the outlet temperature results, an increase in the recirculation ratio invariably leads to a larger temperature drop. The magnitude of this improvement, however, depends strongly on the operating regime. At low recirculation ratios, the response exhibits a high sensitivity to recirculation, indicating high marginal gains. For instance, in the case shown in Figure 6.22-A at $1\,m/s$, increasing r_m from 0.1 to 0.5 quadruples the temperature difference, raising ΔT_d from $3.9\,°C$ to $15.8\,°C$. Conversely, as the recirculation ratio approaches unity, the curves exhibit diminishing returns. This progressive leveling-off becomes dominant under high-humidity conditions (Figure 6.23-A), where the system encounters the thermodynamic limit imposed by the dew point. In this specific scenario, at $1\,m/s$,

increasing recirculation from $r_m = 0.5$ to 0.8 yields a negligible gain, with ΔT_d stabilizing around $6.6 - 6.7\ °C$.

Figure 6.24 and Figure 6.25 illustrate the sensitivity of the temperature difference to the inlet air velocity. Across all cases, a monotonic decrease in ΔT_d is observed as velocity increases. At low recirculation ratios, the system operates in a regime where regenerative effects are weak; consequently, the thermal performance is relatively insensitive to velocity variations. In Figure 6.24-A with $r_m = 0.1$, ΔT_d remains nearly constant, decreasing only slightly from $3.9\ °C$ to $3.5\ °C$ across the entire velocity range. In contrast, at high recirculation ratios, the system typically becomes strongly dependent on residence time. For the low temperature case (Figure 6.24-A) at $r_m = 0.8$, the performance decreases substantially as velocity increases: ΔT_d falls from $17.5\ °C$ at $1\ m/s$ to $7.8\ °C$ at $6.5\ m/s$, corresponding to a reduction of over 55 %. However, a distinctive behavior emerges in high-humidity scenarios (Figure 6.25) within the low-velocity region. Even at high recirculation ($r_m = 0.8$), the curve exhibits a change in curvature as the inlet velocity increases. In this regime, increasing the velocity from $1\ m/s$ to $1.5\ m/s$ results in only a marginal reduction in ΔT_d (from $6.7\ °C$ to $6.5\ °C$) followed by a more pronounced decrease at higher velocities. This inflection is consistent with the onset of the thermodynamic constraint imposed by the dew-point temperature: once the air approaches this limit, further increases in residence time provide diminishing cooling benefits, and the system response becomes progressively governed by transport effects rather than evaporative potential.

The system performance can be evaluated in terms of SCC, defined in equation 3.96. This metric serves as a design parameter, as it quantifies the useful cooling energy per unit mass of air processed by the system.

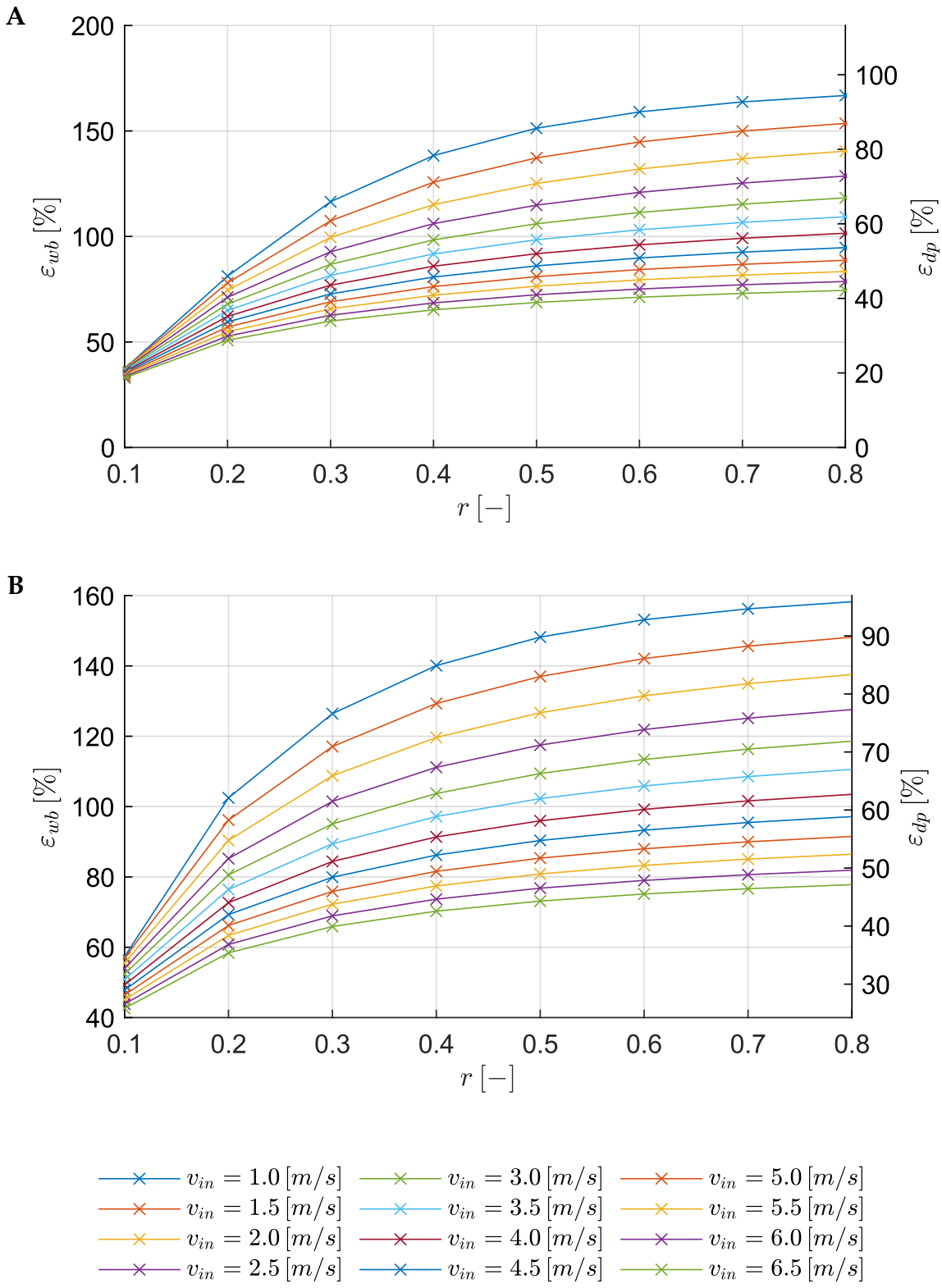

Figure 6.18. Wet-bulb and dew-point effectiveness as a function of the recirculation ratio for different inlet air velocities. Operating conditions: inlet specific humidity of 6 g_v/kg_{da} *and inlet air temperatures of* 25°C *(A) and* 40°C *(B).*

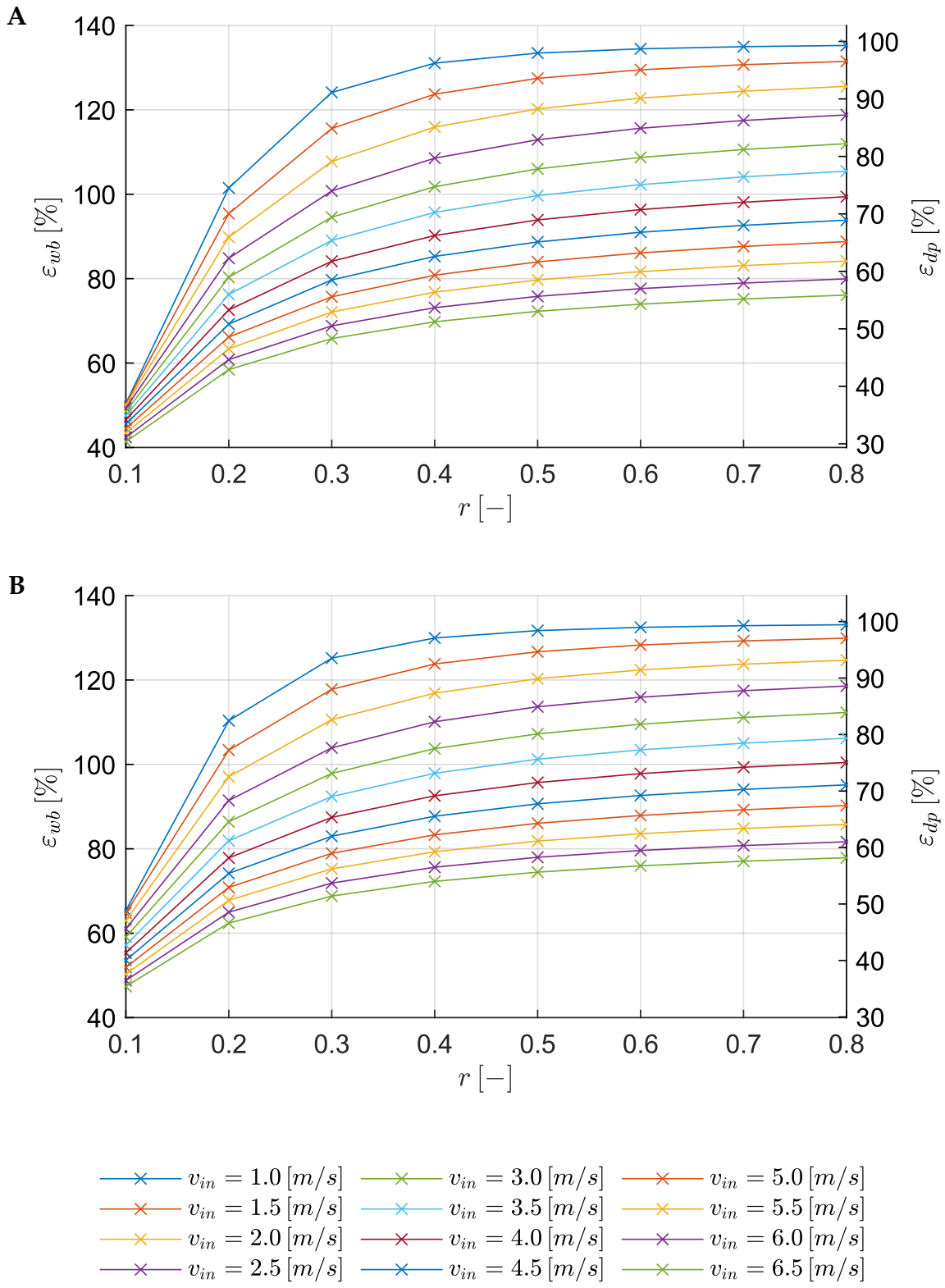

Figure 6.19. Wet-bulb and dew-point effectiveness as a function of the recirculation ratio for different inlet air velocities. Operating conditions: inlet specific humidity of 18 g_v/kg_{da} *and inlet air temperatures of* 30°C *(A) and* 40°C *(B).*

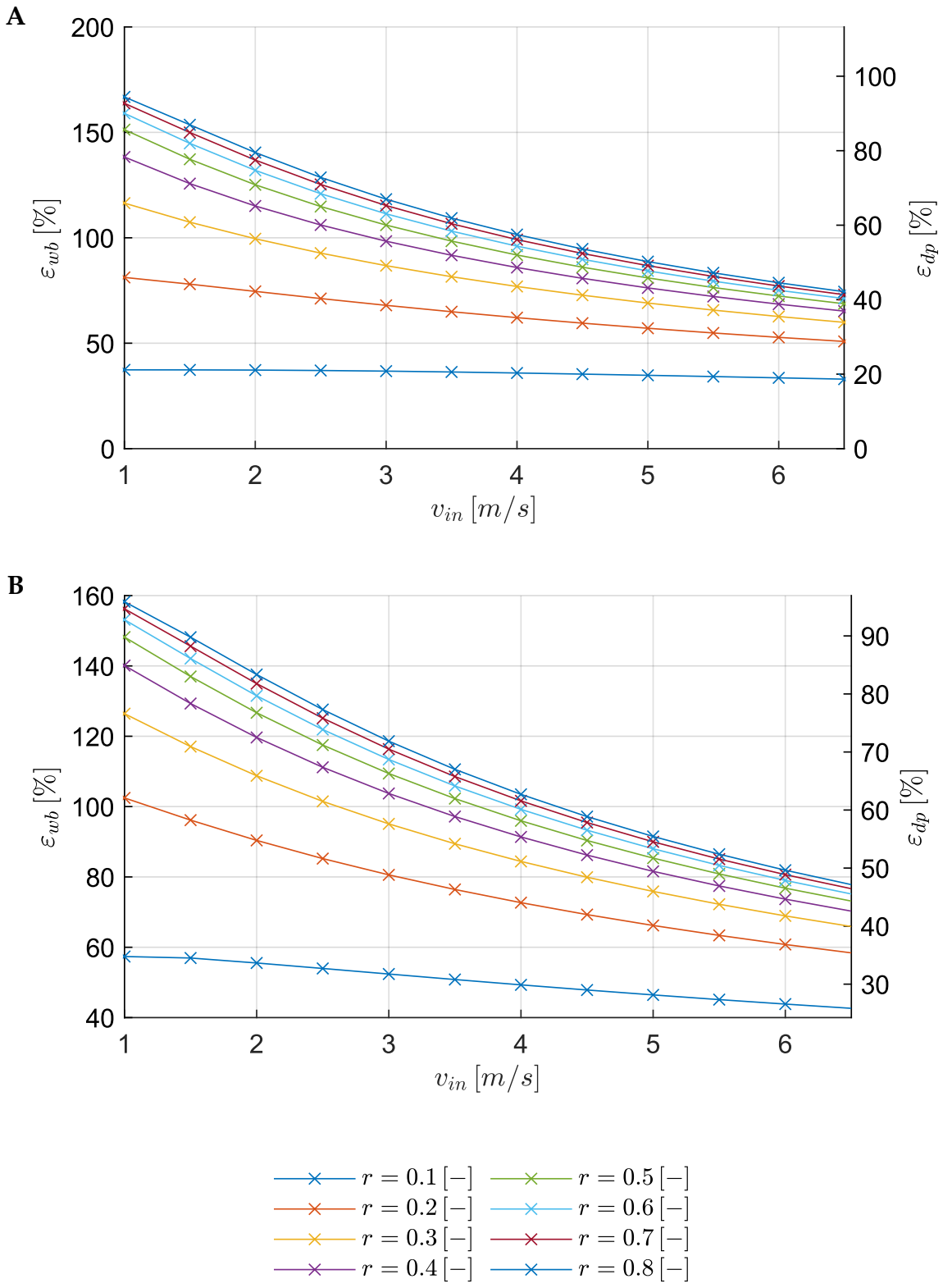

Figure 6.20. Wet-bulb and dew-point effectiveness as a function of inlet air velocity for different recirculation ratios. Operating conditions: inlet specific humidity of 6 g_v/kg_{da} *and inlet air temperatures of* 25°C *(A) and* 40°C *(B).*

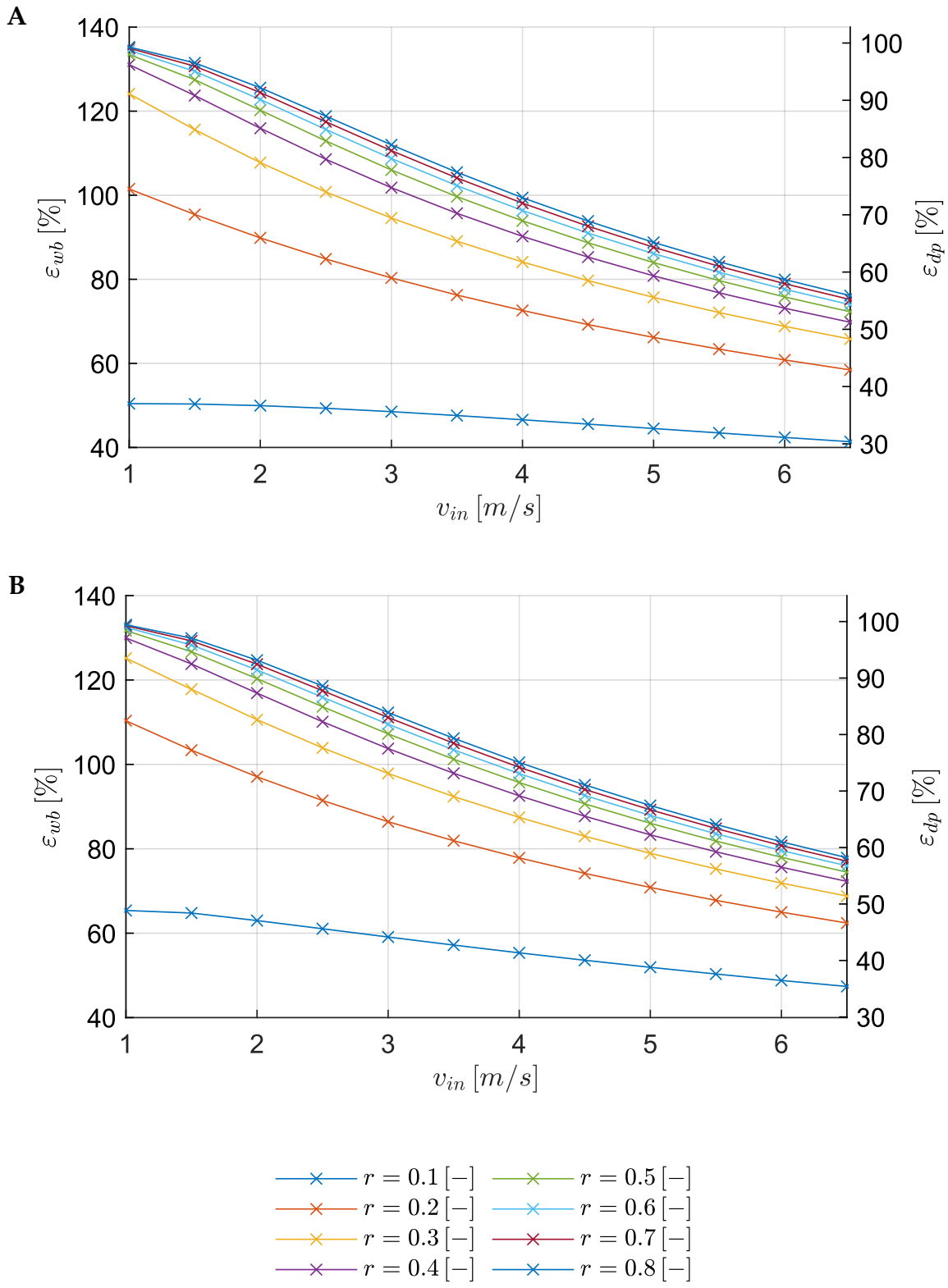

Figure 6.21. Wet-bulb and dew-point effectiveness as a function of inlet air velocity for different recirculation ratios. Operating conditions: inlet specific humidity of 18 g_v/kg_{da} *and inlet air temperatures of* 30°C *(A) and* 40°C *(B).*

Figure 6.26 and Figure 6.27 present the SCC as a function of the recirculation ratio. Unlike the outlet temperature and effectiveness, which exhibit monotonic trends, the SCC displays a distinct non-monotonic behavior, revealing a trade-off in M-cycle operation. The curves exhibit a clearly identifiable maximum, resulting from the balance between the increasing temperature drop (ΔT_d) and the decreasing product mass flow rate ($1 - r_m$). At low recirculation ratios, the increase in ΔT_d dominates the reduction in product mass flow, leading to a rise in SCC. The system reaches an optimal operating point where the balance between the temperature reduction and the recirculated mass flow is maximized. For the reference low-temperature case (Figure 6.26-A) at 1 m/s, this optimum is located at approximately $r_m = 0.4$, achieving a peak SCC of roughly 8850 J/kg_{da}. Beyond this optimum, further increases in recirculation produce diminishing gains in ΔT_d, while the product mass flow continues to decrease linearly. Consequently, the SCC declines progressively. At $r_m = 0.8$, the SCC drops back to approximately 3560 J/kg_{da}, a value comparable to that obtained at $r_m = 0.1$, despite the lower outlet temperature achieved at high recirculation.

A comparison with the high-temperature scenario (Figure 6.26-B) reveals significant differences. While the general trend remains consistent, the higher inlet temperature (40 °C) enhances the evaporative driving force, resulting in a larger temperature drop. Consequently, the peak SCC is more than doubled, reaching approximately 18285 J/kg_{da} at 1 m/s. Notably, the increased driving potential at higher temperatures allows the system to achieve significant cooling effects at lower recirculation ratios; this shifts the optimal operating point slightly toward lower values ($r_m \cong 0.3$) compared to the lower temperature case. The influence of humidity (Figure 6.27-A and Figure 6.27-B) imposes a stricter constraint. Under high-humidity conditions, the saturation of ΔT_d occurs early in the recirculation range due to the proximity of the dew-point limit. As a result, the penalty associated with reducing the product mass flow becomes significant at even lower recirculation values. Accordingly, the peak

shifts further to the left ($r_m \cong 0.3$ at 30 °C and $r_m \cong 0.2$ at 40 °C) and the maximum SCC is reduced compared to the maximum value at lower humidity. This indicates that in humid climates, excessive recirculation progressively degrades the energy density of the system. Furthermore, the optimal recirculation ratio is not constant but varies with the inlet air velocity. As observed in the figures, increasing the velocity tends to shift the peak performance toward lower recirculation ratios. For instance, in Figure 6.27-A, while the optimum at 1 m/s is at $r_m = 0.4$, at 6.5 m/s the maximum shifts to $r_m = 0.3$. This shift is associated with reduced residence time, which limits the marginal gain in ΔT_d obtained at high recirculation and makes it insufficient to compensate for the loss in product mass flow.

Figure 6.28 and Figure 6.29 illustrate the SCC as a function of the inlet air velocity. These results highlight the general degradation of SCC with increasing inlet velocity. In particular, the SCC decreases more markedly at low velocities and then tends to level off at higher velocities. An exception is observed under high-humidity conditions (Figure 6.29) at low velocities, where the curves corresponding to very low or very high recirculation ratios exhibit a change in concavity. It is also evident that the curves associated with intermediate recirculation ratios, which yield the highest SCC values, are the most sensitive to increases in inlet velocity. Furthermore, as the inlet velocity increases, the different curves intersect, clearly indicating that the optimal recirculation ratio is not constant but depends on the airflow rate. Another observation common to all cases is that the curve corresponding to the minimum recirculation ratio is the least affected by the reduction in SCC as the velocity increases. This behavior can be explained by the fact that, as discussed in chapter 6.2.1, such low recirculation ratios lead to a rapid attainment of plateau conditions in the temperature and humidity profiles of the working air stream. As a result, a significant portion of the exchanger becomes effectively underutilized for heat and mass transfer, thereby reducing the sensitivity of the system performance to the degradation effects associated with

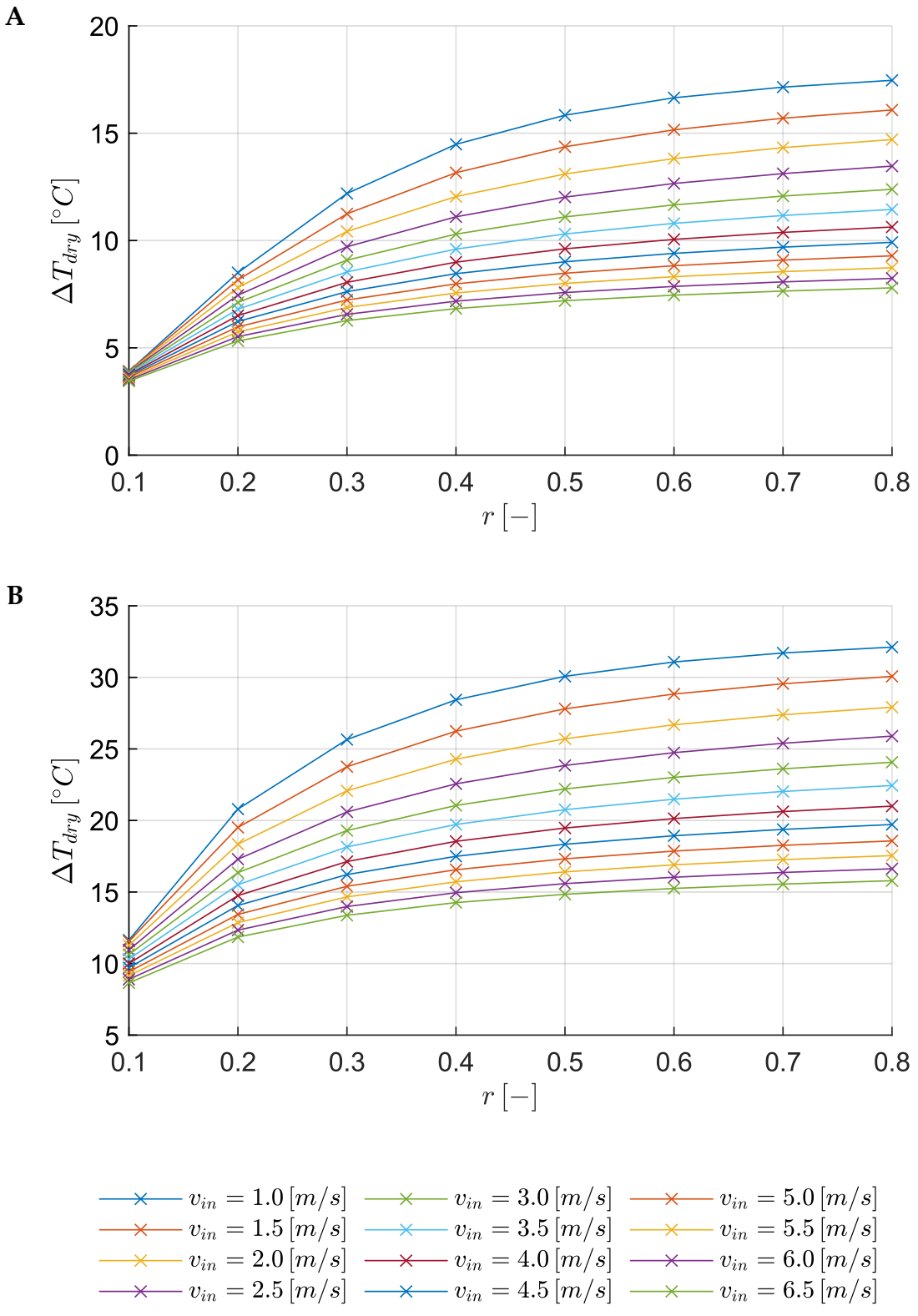

Figure 6.22. Dry-channel temperature difference as a function of the recirculation ratio for different inlet air velocities. Operating conditions: inlet specific humidity of 6 g_v/kg_{da} *and inlet air temperatures of* 25°C *(A) and* 40°C *(B).*

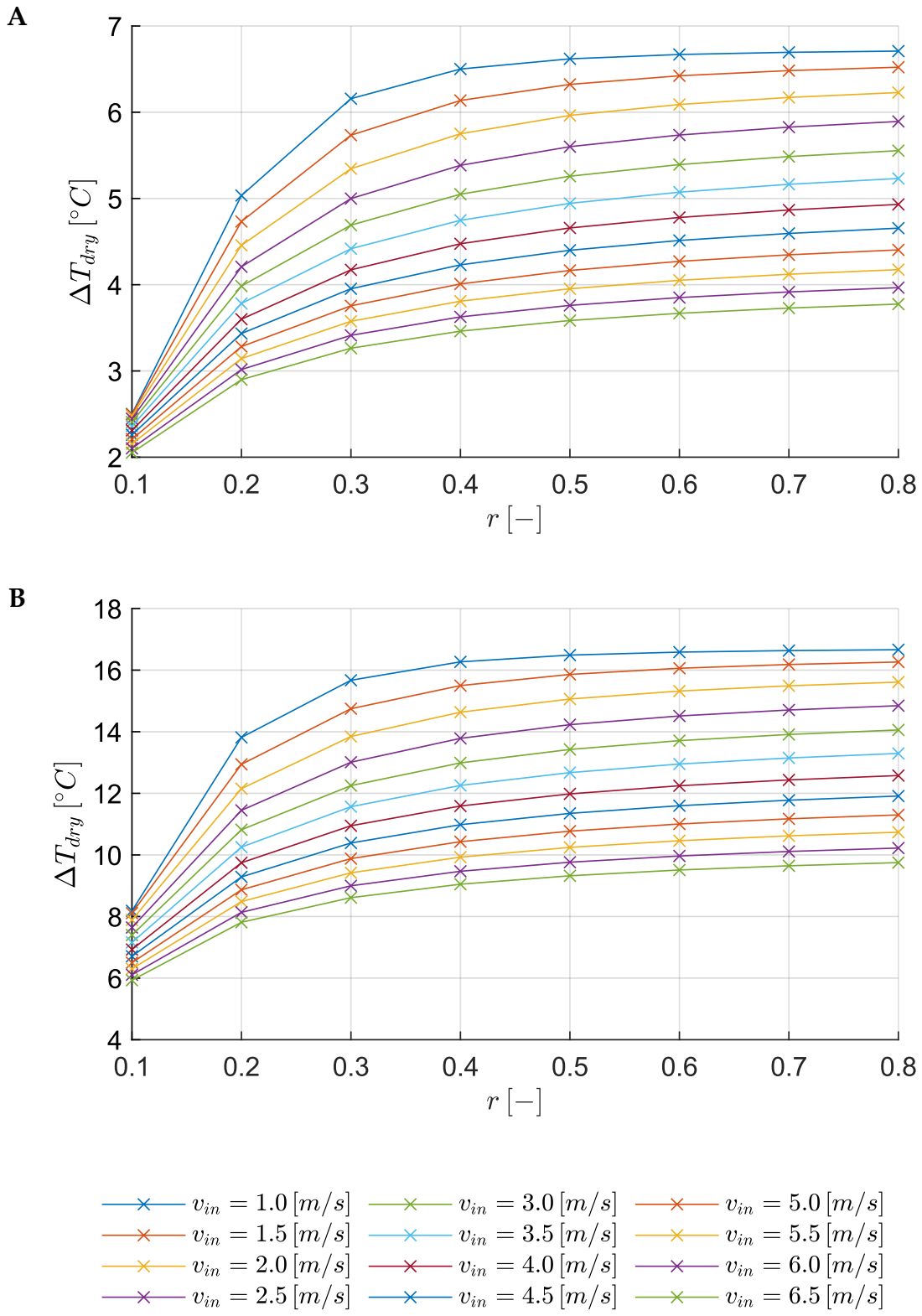

Figure 6.23. Dry-channel temperature difference as a function of the recirculation ratio for different inlet air velocities. Operating conditions: inlet specific humidity of 18 g_v/kg_{da} *and inlet air temperatures of* 30°C *(A) and* 40°C *(B).*

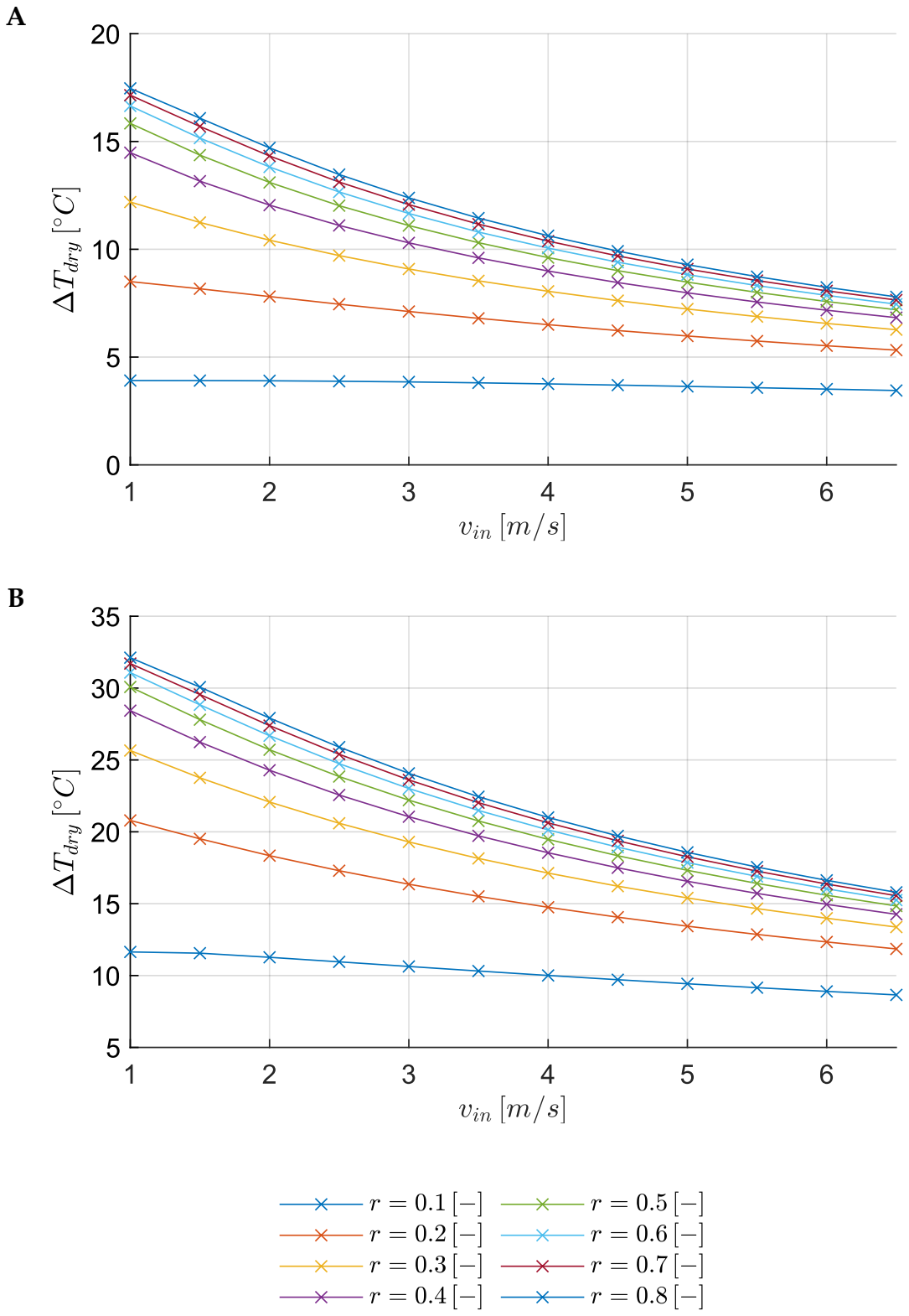

Figure 6.24. Dry-channel temperature difference as a function of inlet air velocity for different recirculation ratios. Operating conditions: inlet specific humidity of 6 g_v/kg_{da} *and inlet air temperatures of* 25°C *(A) and* 40°C *(B).*

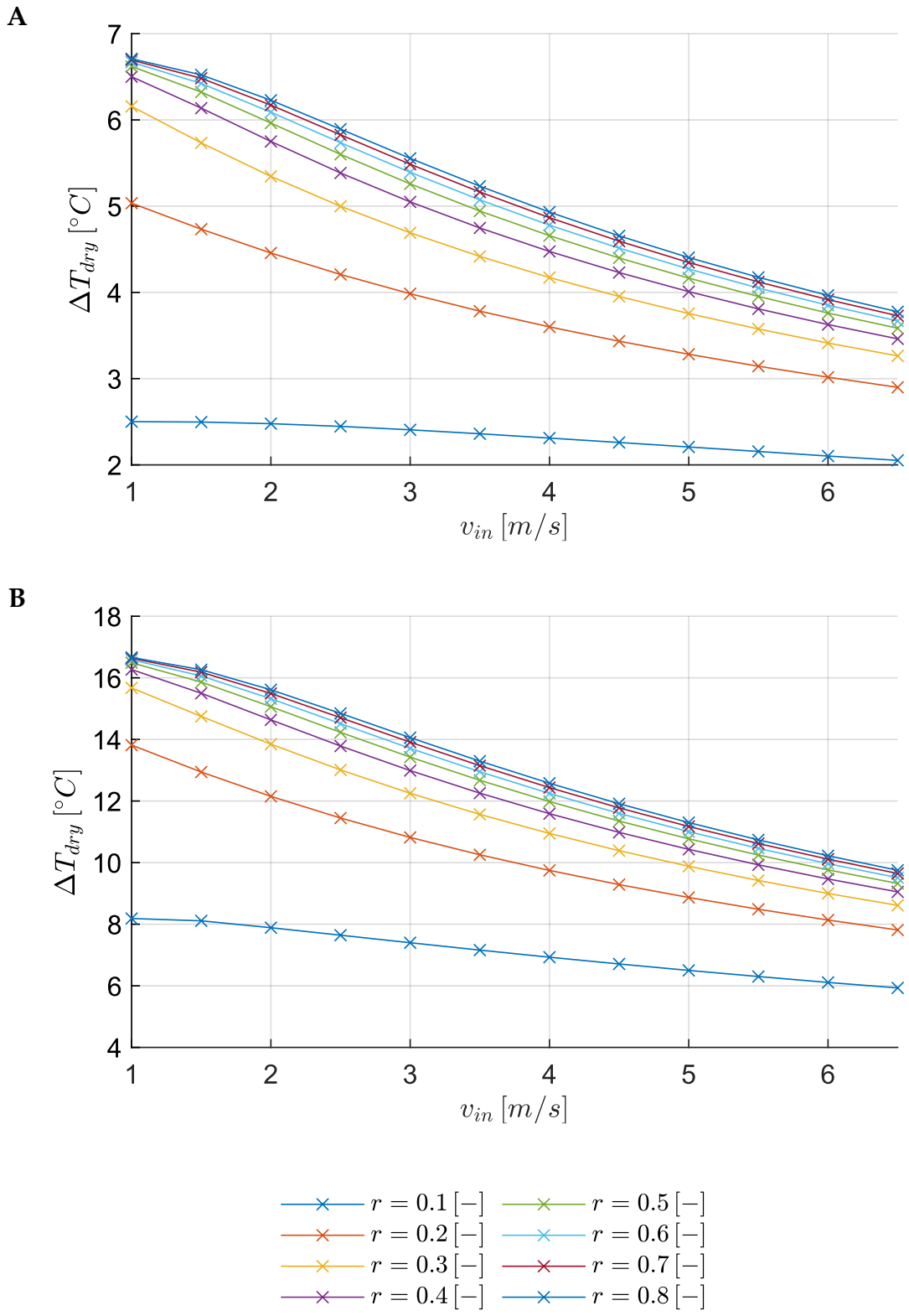

Figure 6.25. Dry-channel temperature difference as a function of inlet air velocity for different recirculation ratios. Operating conditions: inlet specific humidity of 18 g_v/kg_{da} *and inlet air temperatures of* 30°C *(A) and* 40°C *(B).*

increasing inlet air velocity. Overall, a moderate recirculation strategy ($r_m = 0.3 \div 0.4$), combined with low inlet air velocities, appears to provide the best compromise between achieving low outlet air temperatures and maximizing the useful CC delivered by the system.

Complementing the SCC analysis, the system performance is now assessed in terms of VCC, defined in equation 3.97. This metric is critical for evaluating system compactness, as it indicates the cooling power delivered per unit volume of the device.

Figure 6.30 and Figure 6.31 display the VCC as a function of the recirculation ratio. Also in this case, the curves exhibit a parabolic trend, reflecting the same underlying trade-off observed for the SCC. Consequently, an optimal recirculation ratio exists that maximizes the cooling density of the component. For the high-temperature case at 40 $°C$ and low humidity (Figure 6.30-B) at 1 m/s, the peak is observed at approximately $r_m \cong 0.3$, delivering about 40.6 kW/m^3. Under high-humidity conditions at the same inlet temperature (Figure 6.31-B) the maximum shifts toward lower recirculation values ($r_m \cong 0.2$), while the peak VCC decreases to approximately 25 kW/m^3. This represents a substantial reduction in cooling density compared to the drier case, highlighting the limiting effect of humidity on the evaporative process. However, a key difference distinguishes the VCC from the SCC described earlier. While in the case of SCC the curves progressively shift toward lower values with increasing inlet velocity, the opposite trend is observed for the VCC. This behavior arises because the volumetric cooling capacity directly depends on the processed airflow rate, which increases with velocity and plays a dominant role in determining the total heat removed by the air stream.

Figure 6.32 and Figure 6.33 further clarify this behavior by plotting the VCC as a function of inlet air velocity. As previously discussed, the trend observed here is opposite to that of the SCC. While the SCC decreases monotonically with increasing

velocity, the VCC increases monotonically. Although the temperature drop (ΔT_{dry}) decreases as the velocity rises, this reduction is outweighed by the linear increase in the processed air mass flow rate. However, the increase in VCC is not uniform and is more pronounced at low velocities, where ΔT_{dry} remains relatively high and only weakly affected by velocity. As the velocity increases further and the temperature drop progressively degrades, the growth of VCC becomes less steep.

A comparison between the two inlet conditions at 40 $°C$ highlights the strong impact of humidity. For the low-humidity case (Figure 6.32-B), increasing the inlet velocity from 1 m/s to 6.5 m/s at optimal recirculation ratio ($r_m \cong 0.3$) leads to an increase in VCC from approximately 40.6 kW/m^3 to about 67.7 kW/m^3. Under high-humidity conditions (Figure 6.33-B), the corresponding increase is from approximately 25 kW/m^3 to about 88.8 kW/m^3 (at $r_m \cong 0.3$), reflecting the dominant effect of mass flow rate despite the lower thermodynamic driving potential.

This reveals a critical design dichotomy: operating at low air velocities maximizes the temperature depression and the SCC, whereas operating at high velocities maximizes the compactness of the device (i.e., high VCC). Therefore, the optimal operating velocity must be selected based on the specific constraints of the application, depending on whether the priority is to maximize thermal effectiveness or minimize the physical footprint of the unit.

The analysis now considers the wet-channel outlet temperature ($T_{w,o}$). Although this airflow represents the exhaust stream of the M-cycle and is typically discharged into the environment, characterizing its thermal state is relevant for evaluating the potential recovery of this waste flow for secondary utilization (e.g., condenser cooling or auxiliary pre-cooling stages).

Figure 6.34 and Figure 6.35 display the wet-channel outlet temperature as a function of the recirculation ratio. A distinctive feature of the M-cycle configuration is that the

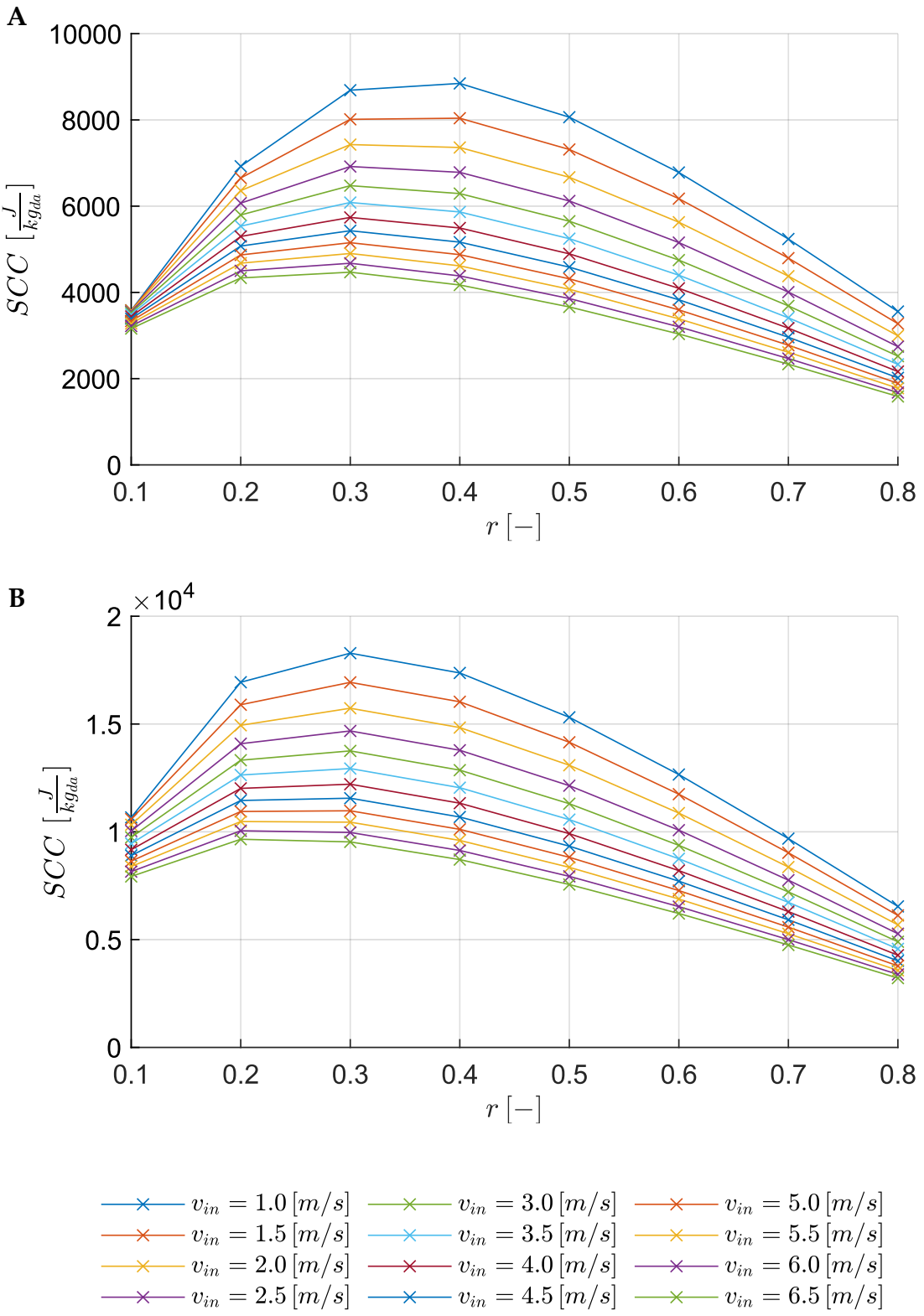

Figure 6.26. Specific Cooling Capacity as a function of the recirculation ratio for different inlet air velocities. Operating conditions: inlet specific humidity of 6 g_v/kg_{da} *and inlet air temperatures of* 25°C *(A) and* 40°C *(B).*

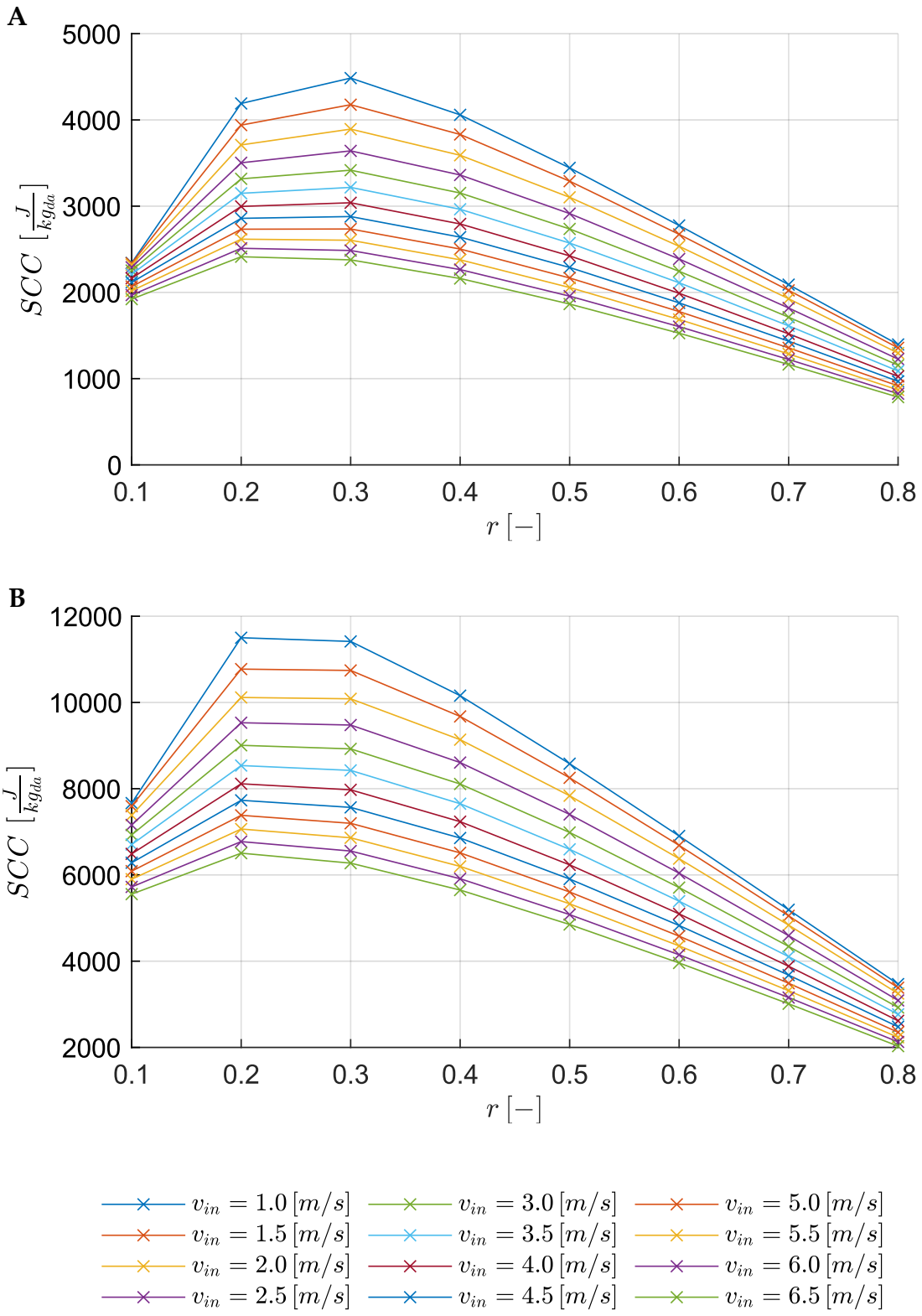

Figure 6.27. Specific Cooling Capacity as a function of the recirculation ratio for different inlet air velocities. Operating conditions: inlet specific humidity of 18 g_v/kg_{da} *and inlet air temperatures of* 30°C *(A) and* 40°C *(B).*

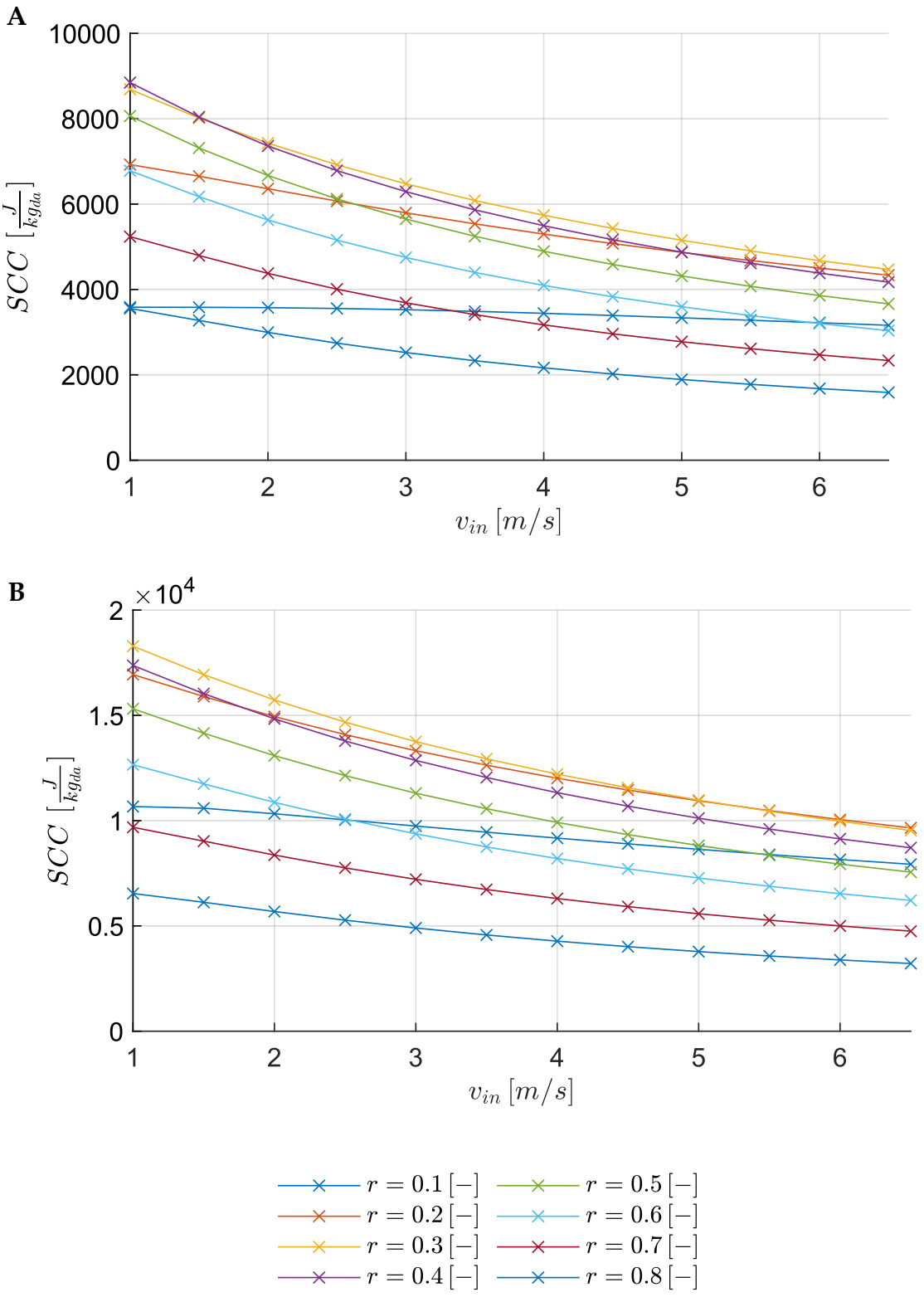

Figure 6.28. Specific Cooling Capacity as a function of inlet air velocity for different recirculation ratios. Operating conditions: inlet specific humidity of 6 g_v/kg_{da} and inlet air temperatures of 25°C (A) and 40°C (B).

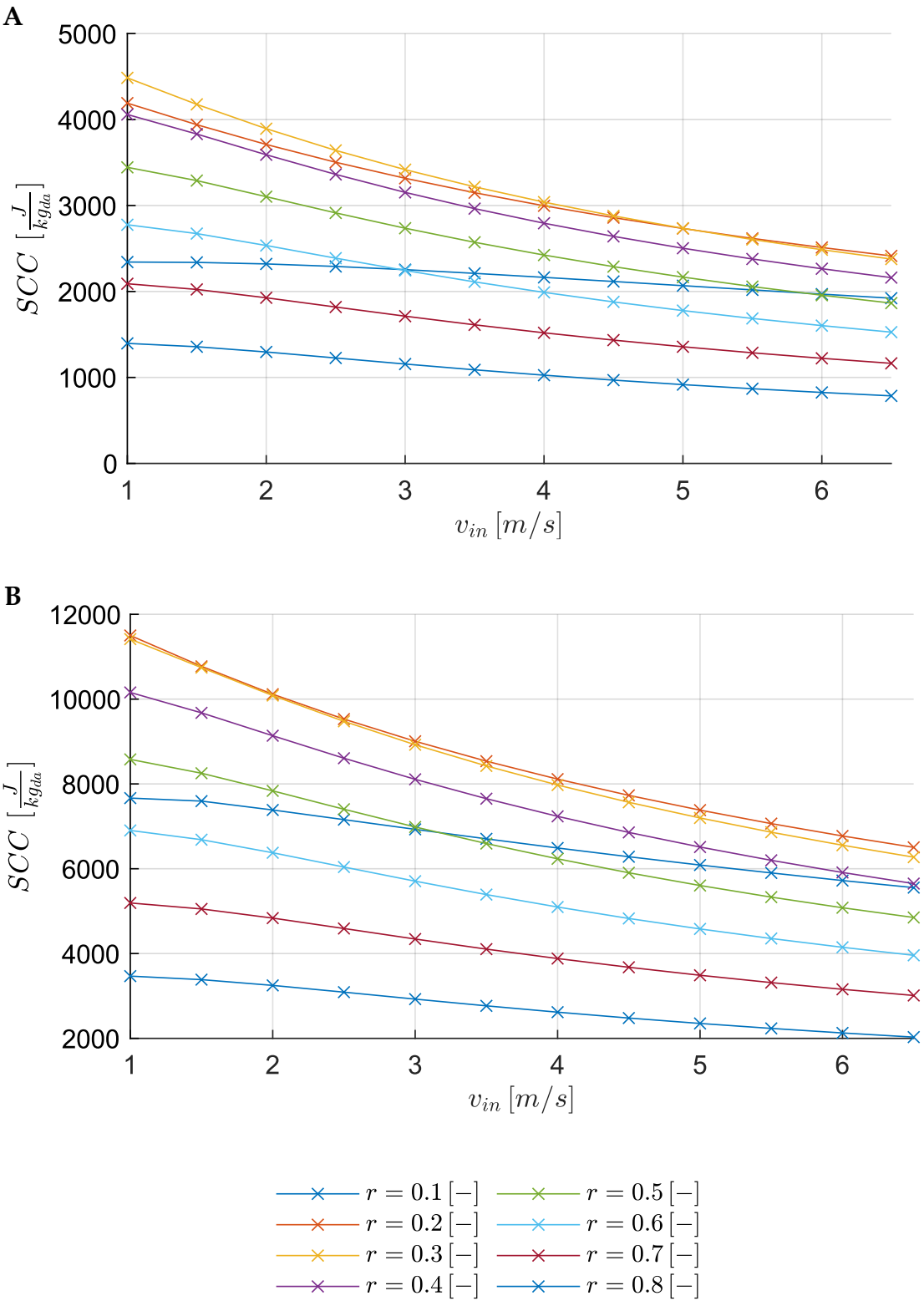

Figure 6.29. Specific Cooling Capacity as a function of inlet air velocity for different recirculation ratios. Operating conditions: inlet specific humidity of 18 g_v/kg_{da} *and inlet air temperatures of* 30°C *(A) and* 40°C *(B).*

inlet condition of the wet channel $T_{w,i}$ is determined by the outlet condition of the dry channel $T_{d,o}$. As a result, the thermal state of the exhaust stream is directly coupled to the cooling performance of the dry channel.

Across all investigated scenarios, the wet-channel outlet temperature $T_{w,o}$ exhibits a monotonic decrease as the recirculation ratio increases. Increasing r_m lowers the dry-channel outlet temperature, thereby feeding the wet channel with progressively colder air. For the reference low-temperature case in Figure 6.34-A at $1\,m/s$, the exhaust temperature drops from close to the outdoor temperature ($25\,°C$) at $r_m = 0.1$ to about $16\,°C$ at $r_m = 0.8$. This indicates that, when sufficiently high recirculation ratios are employed, the exhaust air temperature can be significantly lower than the ambient temperature, representing a valuable source of cooling potential that would otherwise be wasted.

In the high-temperature scenario (Figure 6.34-B), this effect is more evident due to the larger temperature range. At $1\,m/s$, $T_{w,o}$ decreases from values close to the inlet temperature to approximately $22\,°C$, corresponding to a reduction of nearly $18\,°C$. Furthermore, the interaction between recirculation and inlet velocity leads to a distinctive crossover of the temperature profiles. At low recirculation ratios (e.g., $r_m = 0.1$), the curves associated with higher velocities lie below those at lower velocities. Conversely, at high recirculation ratios (e.g., $r_m = 0.8$), this trend reverses, and the curves for higher velocities lie above those at lower velocities.

Under high-humidity conditions (Figure 6.35), the behavior remains qualitatively similar but is quantitatively compressed. Since the system cooling capability is constrained by the dew-point temperature, the dry channel outlet temperature cannot decrease as significantly. Consequently, the variation in exhaust temperature is reduced. At $40\,°C$ (Figure 6.35-B), increasing r_m from 0.1 to 0.8 at $1\,m/s$ reduces $T_{w,o}$ of approximately $11.5\,°C$, compared to the $18\,°C$ decrease observed under low-humidity conditions. This "flattening" of the curves at high humidity indicates that the exhaust

stream remains closer to ambient temperature, leading to a reduction in the cooling potential of the waste air as ambient humidity increases.

Figure 6.36 and Figure 6.37 illustrate the dependence of the wet channel outlet temperature on the inlet air velocity. The observed trends reveal a complex interaction between the wet-channel inlet condition and the heat and mass transfer processes, resulting in a transition in the shape of the curves as the recirculation ratio increases.

At low recirculation ratios (e.g., $r_m = 0.1$), the curves exhibit a downward concavity and a slight monotonic decrease in temperature with increasing velocity. At intermediate recirculation ratios (e.g., $r_m = 0.2 - 0.5$), the profiles undergo a change in curvature, becoming steeper and exhibiting an upward concavity. In this range, the reduction in outlet temperature with increasing velocity is more pronounced. Finally, at high recirculation ratios (e.g., $r_m > 0.5$), the behavior becomes non-monotonic. The temperature initially decreases to a shallow local minimum and then shows a slight increase as the velocity increases further. This weak non-monotonic behavior results in a final value at $6.5\,m/s$ that slightly exceeds the value observed at $1\,m/s$ (e.g. $16.08\,°C$ vs. $15.95\,°C$ for Figure 6.36-A).

Finally, the resource intensity of the system is evaluated through the Volumetric Water Consumption (VWC), defined in equation 3.100. This metric characterizes the water demand relative to the installed hardware size.

Figure 6.38 and Figure 6.39 present the VWC as a function of the recirculation ratio. Across all operating conditions, water consumption exhibits a monotonic increase with increasing recirculation ratio. This trend is expected since higher recirculation implies a larger mass flow rate diverted into the wet channel, thereby supporting higher evaporation rates.

Analyzing the case with low temperature and low humidity (Figure 6.38-A), it is observed that at $1\,m/s$, increasing the recirculation ratio r_m from 0.1 to 0.8 leads to an

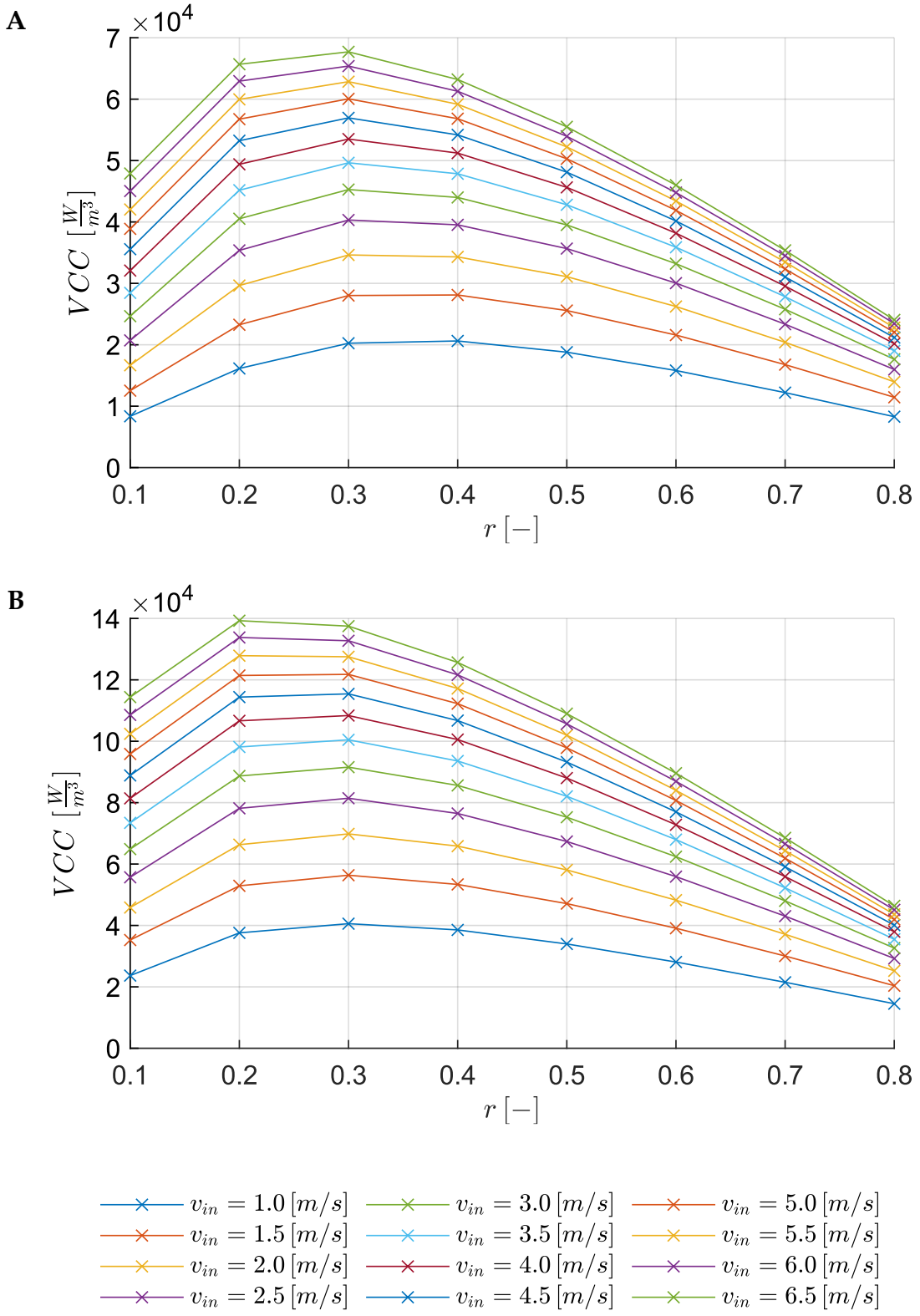

Figure 6.30. Volumetric Cooling Capacity as a function of the recirculation ratio for different inlet air velocities. Operating conditions: inlet specific humidity of 6 g_v/kg_{da} *and inlet air temperatures of* 25°C *(A) and* 40°C *(B).*

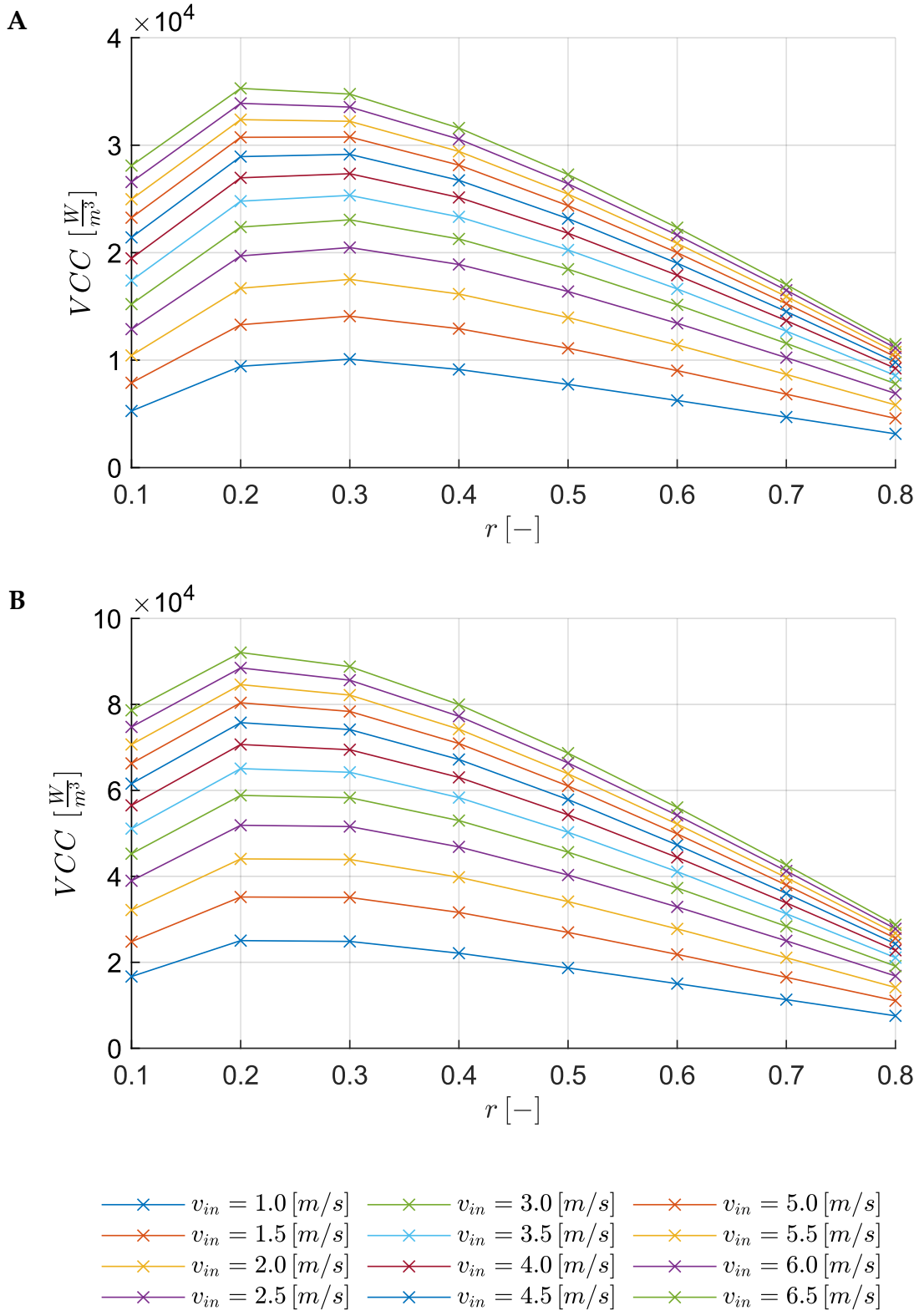

Figure 6.31. Volumetric Cooling Capacity as a function of the recirculation ratio for different inlet air velocities. Operating conditions: inlet specific humidity of 18 g_v/kg_{da} *and inlet air temperatures of* 30°C *(A) and* 40°C *(B).*

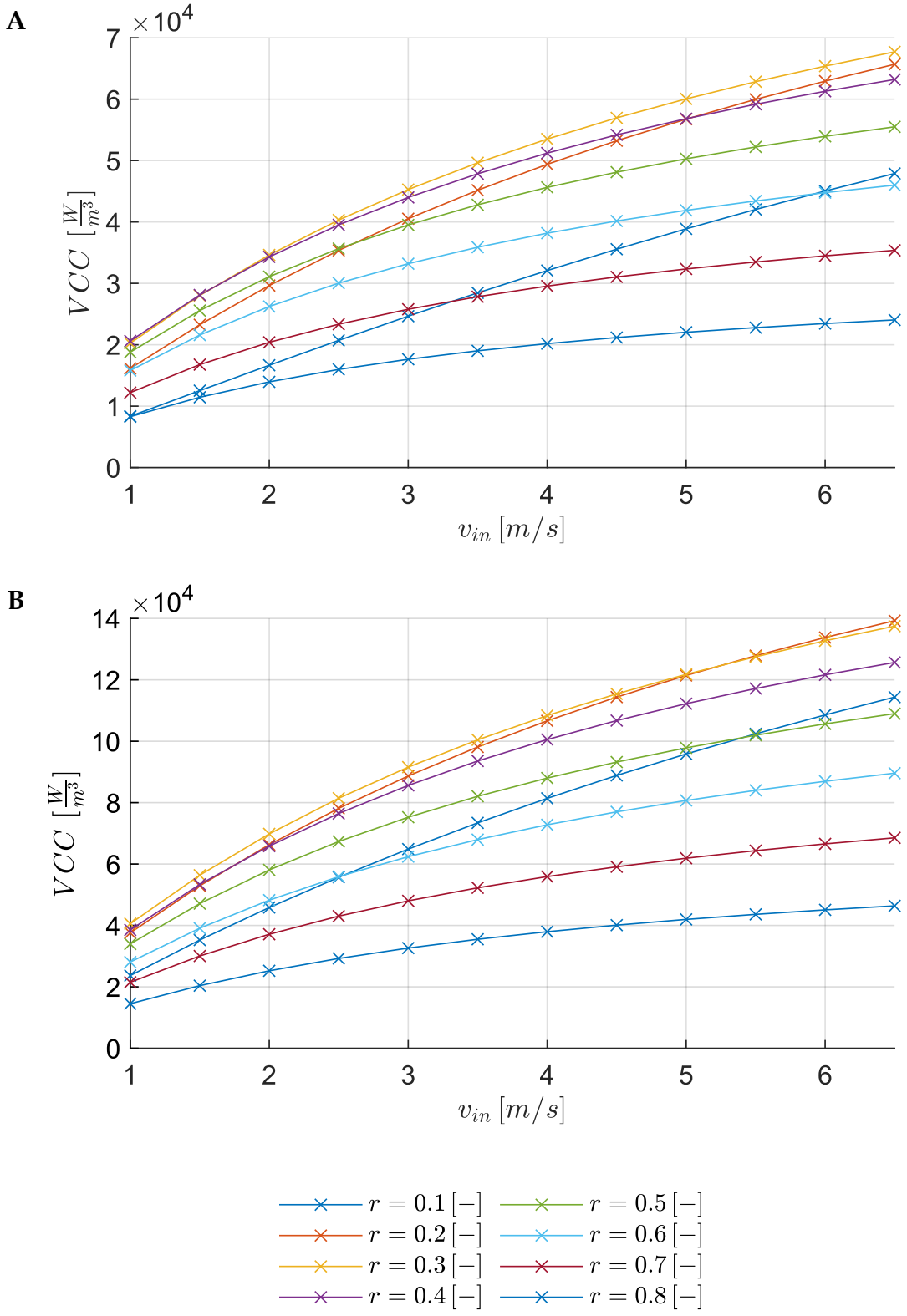

Figure 6.32. Volumetric Cooling Capacity as a function of inlet air velocity for different recirculation ratios. Operating conditions: inlet specific humidity of 6 g_v/kg_{da} *and inlet air temperatures of* 25°C *(A) and* 40°C *(B).*

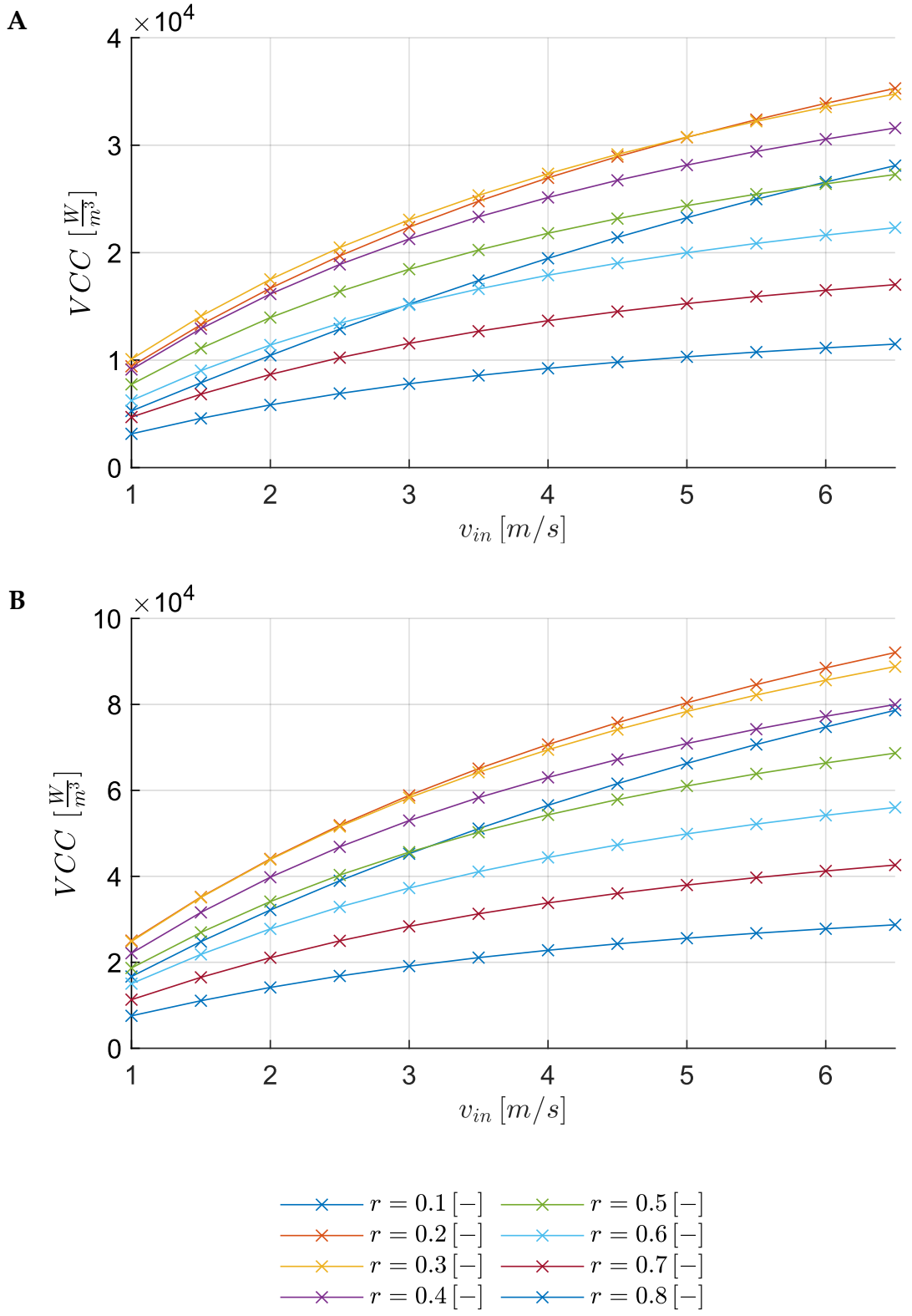

Figure 6.33. Volumetric Cooling Capacity as a function of inlet air velocity for different recirculation ratios. Operating conditions: inlet specific humidity of 18 g_v/kg_{da} *and inlet air temperatures of* 30°C *(A) and* 40°C *(B).*

increase in water consumption from 11.80 $kg/(h\,m^3)$ to 36.21 $kg/(h\,m^3)$. This effect is significantly amplified at higher velocities. At 6.5 m/s, the water consumption at the maximum tested recirculation condition ($r_m = 0.8$) reaches 190.73 $kg/(h\,m^3)$. In the high inlet temperature case (Figure 6.38-B), the water consumption values are significantly higher. Under these conditions, at 1 m/s, the consumption for $r_m = 0.8$ rises to 67.49 $kg/(h\,m^3)$, while at a velocity of 6.5 m/s, an absolute peak of approximately 364.38 $kg/(h\,m^3)$ is reached. In Figure 6.39-A (moderate temperature, high humidity), the water consumption at 1 m/s reaches a maximum value of 16.63 $kg/(h\,m^3)$, while at 6.5 m/s, the maximum value settles at 92.09 $kg/(h\,m^3)$. Finally, in Figure 6.39-B (high temperature and high humidity), despite the higher inlet air temperature favoring evaporation, the high humidity limits the consumption at 1 m/s to around 40.75 $kg/(h\,m^3)$, reaching a maximum of 228.48 $kg/(h\,m^3)$ at 6.5 m/s.

Figure 6.40 and Figure 6.41 illustrate the dependence of VWC on inlet velocity. The mpact of velocity is dominant and results in an increase in water consumption across the board. Overall, these trends appear more linear than those observed for the recirculation ratio dependence, exhibiting lower curvature. Although the specific evaporation decreases at high velocities due to the reduced residence time, the increase in the processed mass flow rate dominates this effect. Referring to Figure 6.40-A at maximum recirculation ($r_m = 0.8$), increasing the velocity from 1 m/s to 6.5 m/s causes the water consumption to increase from 36.21 $kg/(h\,m^3)$ to 190.73 $kg/(h\,m^3)$, representing a more than five-fold increase. Similar magnitudes of increase are observed across all other inlet air conditions. At the maximum velocity of 6.5 m/s, the VWC consistently increases by a factor between 5.4 and 5.6 compared to the values at 1 m/s. Notably, this proportionality remains consistent even at low recirculation ratios. For $r_m = 0.1$, the increase in water consumption over the same velocity range remains between 5 and 6 times across all examined climatic configurations. This

introduces an additional operational trade-off, where gains in compactness are accompanied by increased water intensity.

This chapter presented the numerical results of the M-cycle heat and mass exchanger under varying operating conditions. The analysis quantified the interplay between temperature reduction, cooling capacity metrics, exchanger compactness, and water consumption, thereby establishing a consistent basis for subsequent performance mapping and design-oriented analysis.

6.3. Analysis of the proposed model

This section presents a comparative analysis between the proposed computational model and the original formulation developed by Hasan [92] described in section 3.9. This comparison aims to evaluate the impact of the new physical assumptions and spatial refinement on the numerical results, rather than providing direct validation against experimental data, which is addressed in Chapter 8. A significant distinction between the two implementations is the spatial discretization: the Hasan model operates with a 1 cm nodal step, whereas the current model utilizes a 1 mm step. This refinement enables a more detailed observation of heat and mass transfer dynamics, particularly at the channel inlets. It should also be emphasized that, for simplicity and to enable an initial comparison with the previous model, the results presented here were obtained by assuming a constant volumetric flow rate in the wet channel, thus neglecting the slight increase due to the addition of evaporated water vapor.

The simulation considers the test case from Riangvilaikul and Kumar [108], characterized by an inlet dry-bulb temperature of 45 $°C$ and a specific humidity of 6.9 g_v/kg_{da}. Figure 6.42 illustrates the axial temperature distribution for the dry channel (T_d), the wet channel (T_w), and the liquid film interface (T_i). In the dry channel, the proposed model captures a higher temperature gradient at the immediate inlet compared to Hasan's results. Although this difference is subtle, it reflects a distinct

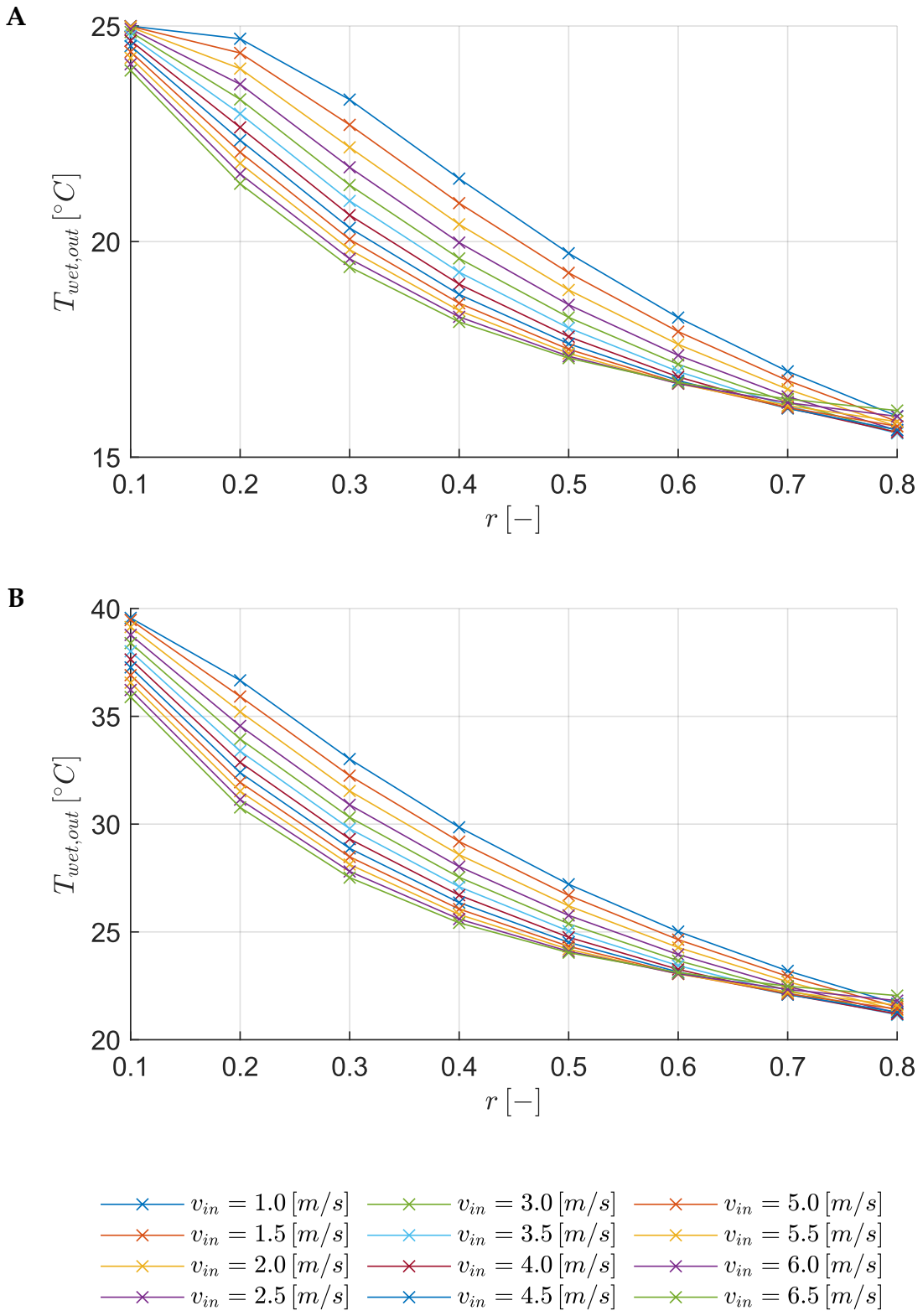

Figure 6.34. Wet-channel outlet temperature as a function of the recirculation ratio for different inlet air velocities. Operating conditions: inlet specific humidity of 6 g_v/kg_{da} *and inlet air temperatures of* 25°C *(A) and* 40°C *(B).*

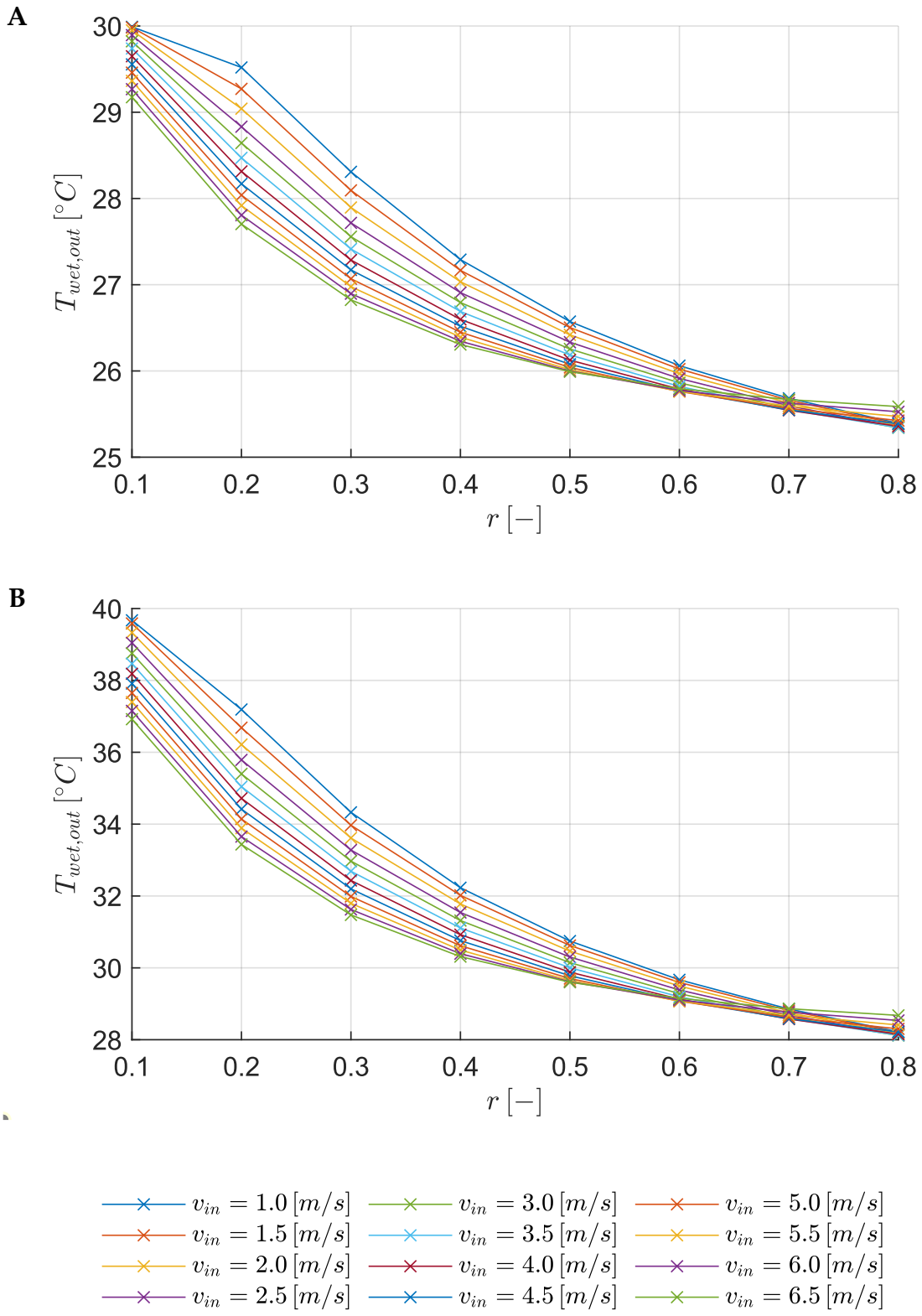

Figure 6.35. Wet-channel outlet temperature as a function of the recirculation ratio for different inlet air velocities. Operating conditions: inlet specific humidity of 18 g_v/kg_{da} *and inlet air temperatures of* 30°C *(A) and* 40°C *(B).*

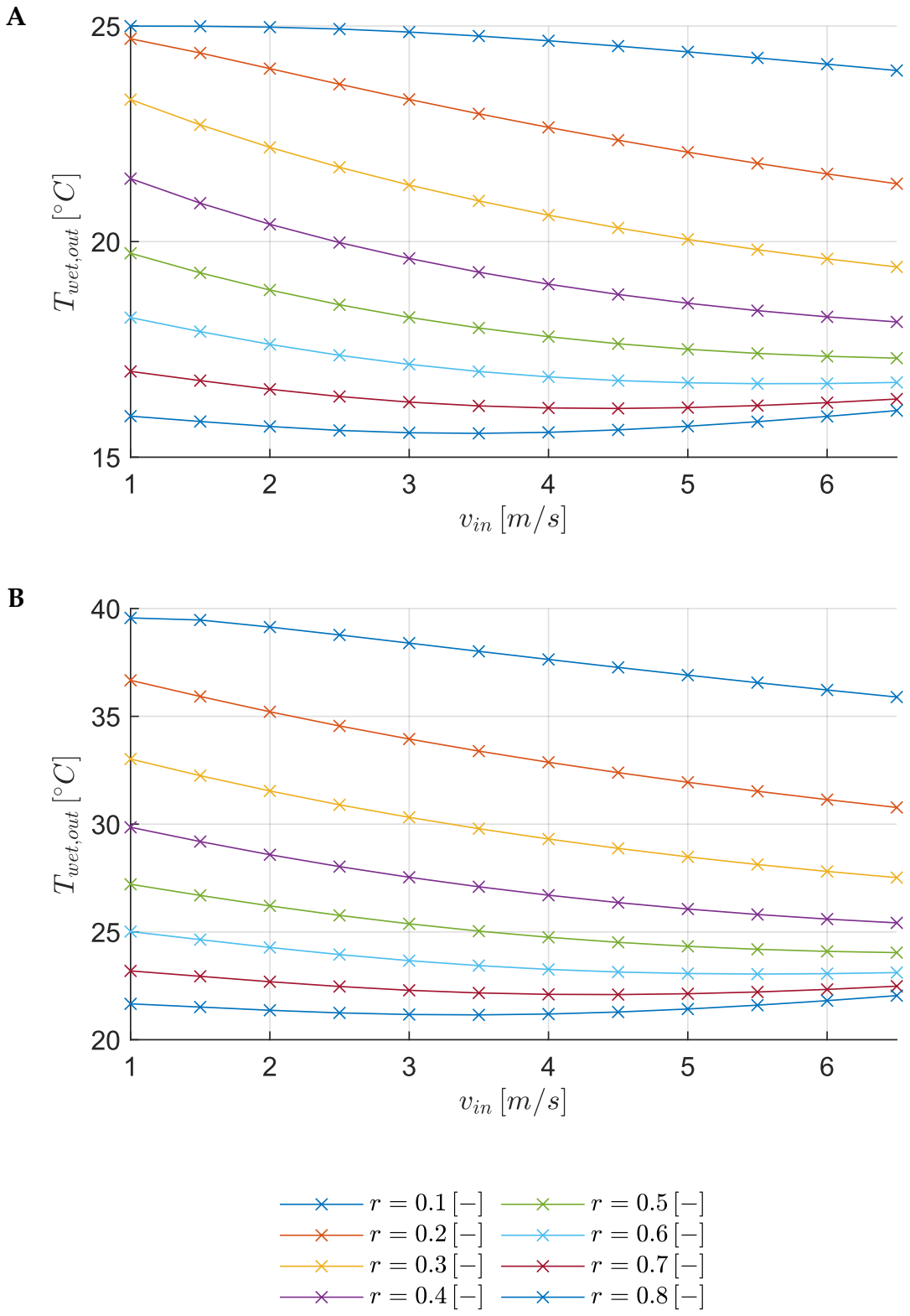

Figure 6.36. Wet-channel outlet temperature as a function of inlet air velocity for different recirculation ratios. Operating conditions: inlet specific humidity of 6 g_v/kg_{da} and inlet air temperatures of 25°C (A) and 40°C (B).

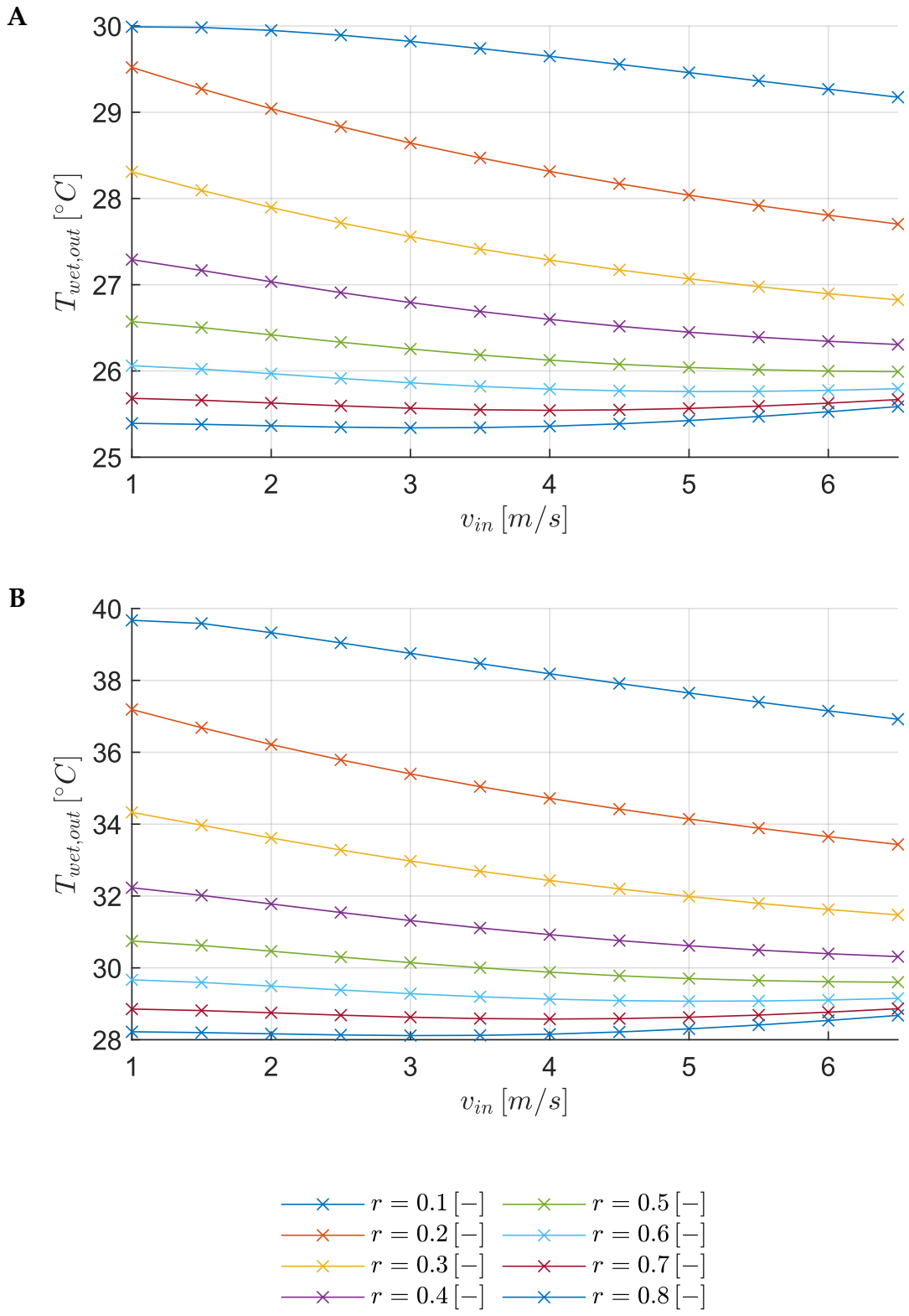

Figure 6.37. Wet-channel outlet temperature as a function of inlet air velocity for different recirculation ratios. Operating conditions: inlet specific humidity of 18 g_v/kg_{da} *and inlet air temperatures of* 30°C *(A) and* 40°C *(B).*

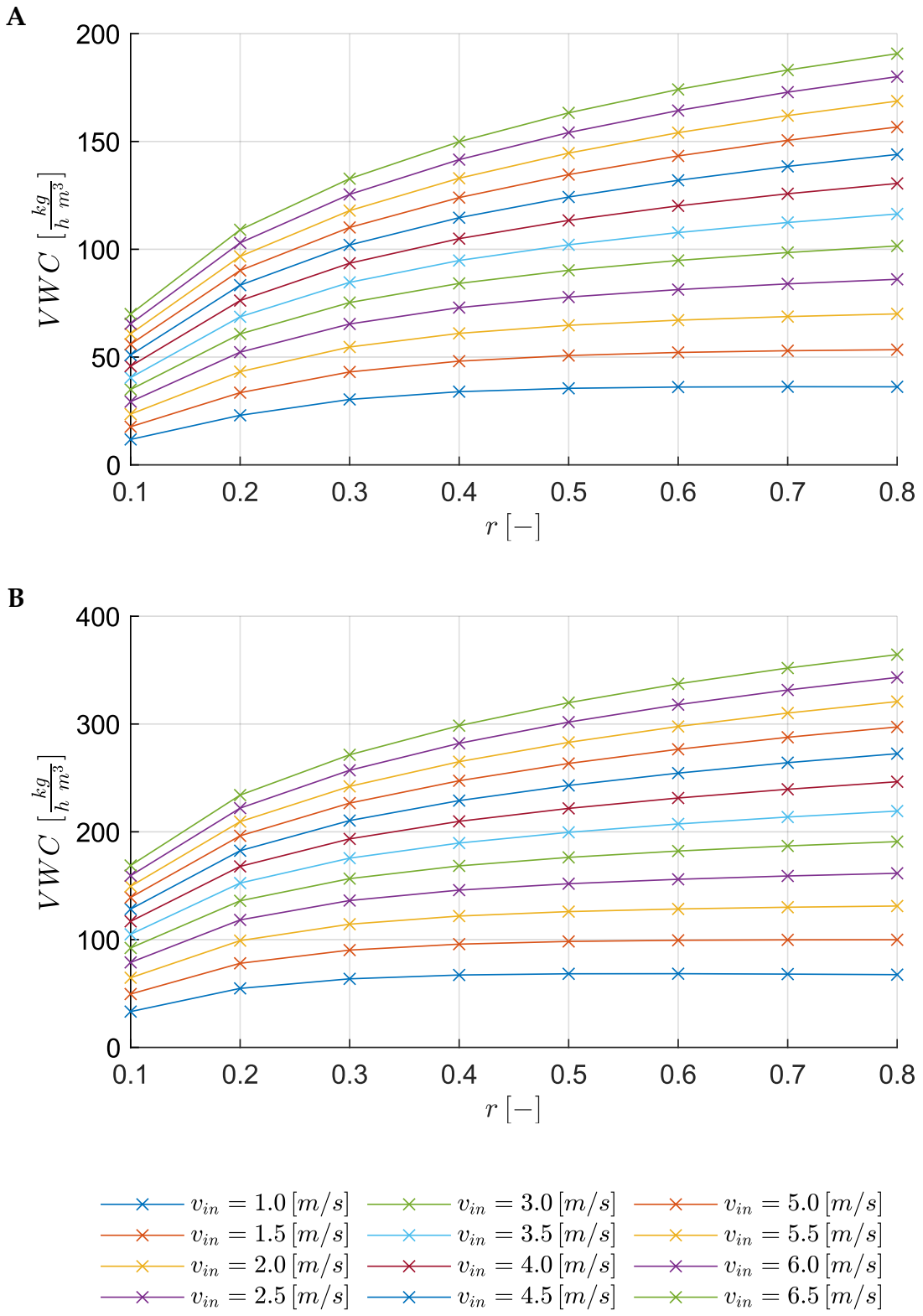

Figure 6.38. Hourly volumetric water consumption as a function of the recirculation ratio for different inlet air velocities. Operating conditions: inlet specific humidity of 6 g_v/kg_{da} *and inlet air temperatures of* 25°C *(A) and* 40°C *(B).*

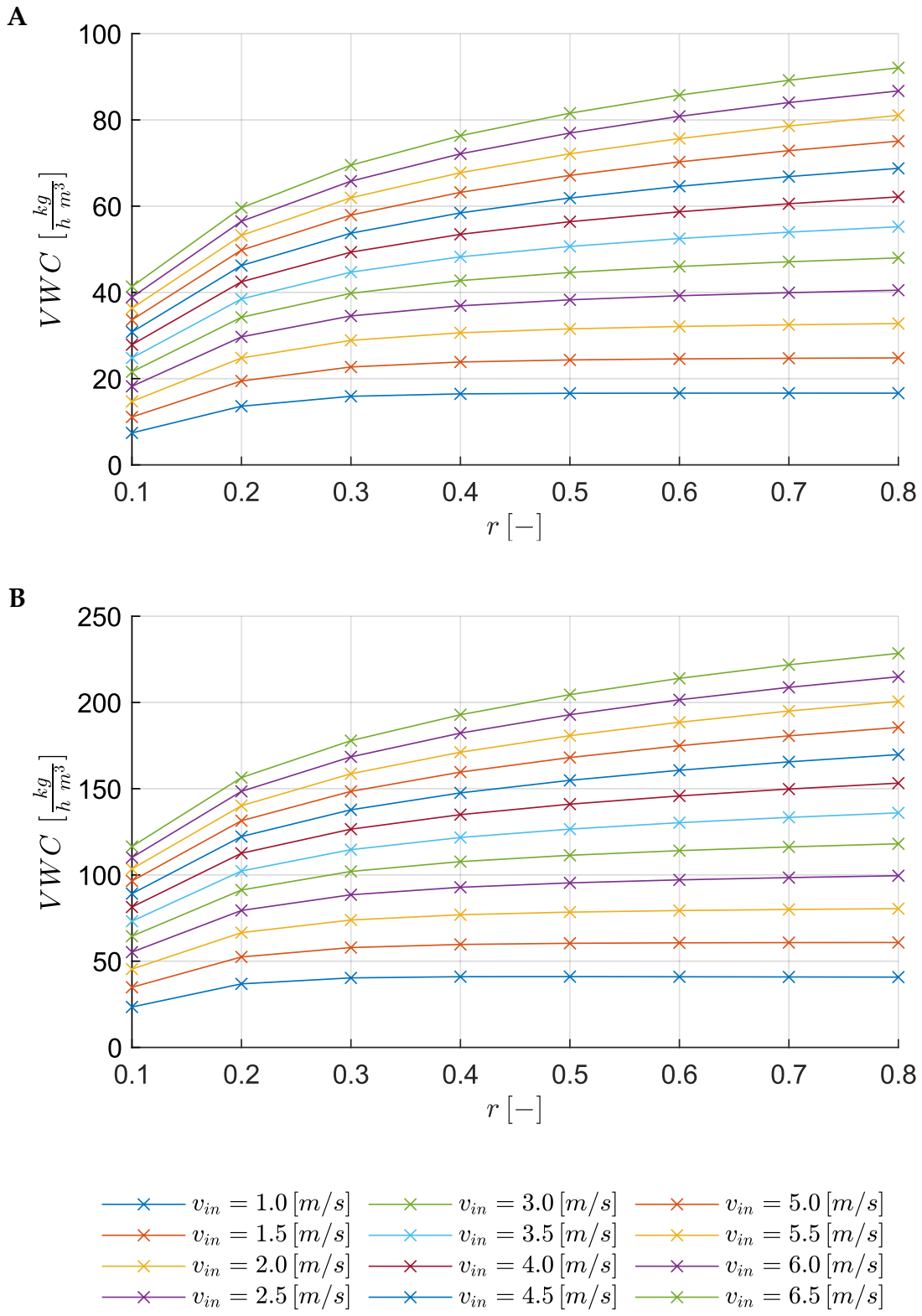

Figure 6.39. Hourly volumetric water consumption as a function of the recirculation ratio for different inlet air velocities. Operating conditions: inlet specific humidity of 18 g_v/kg_{da} *and inlet air temperatures of* 30°C *(A) and* 40°C *(B).*

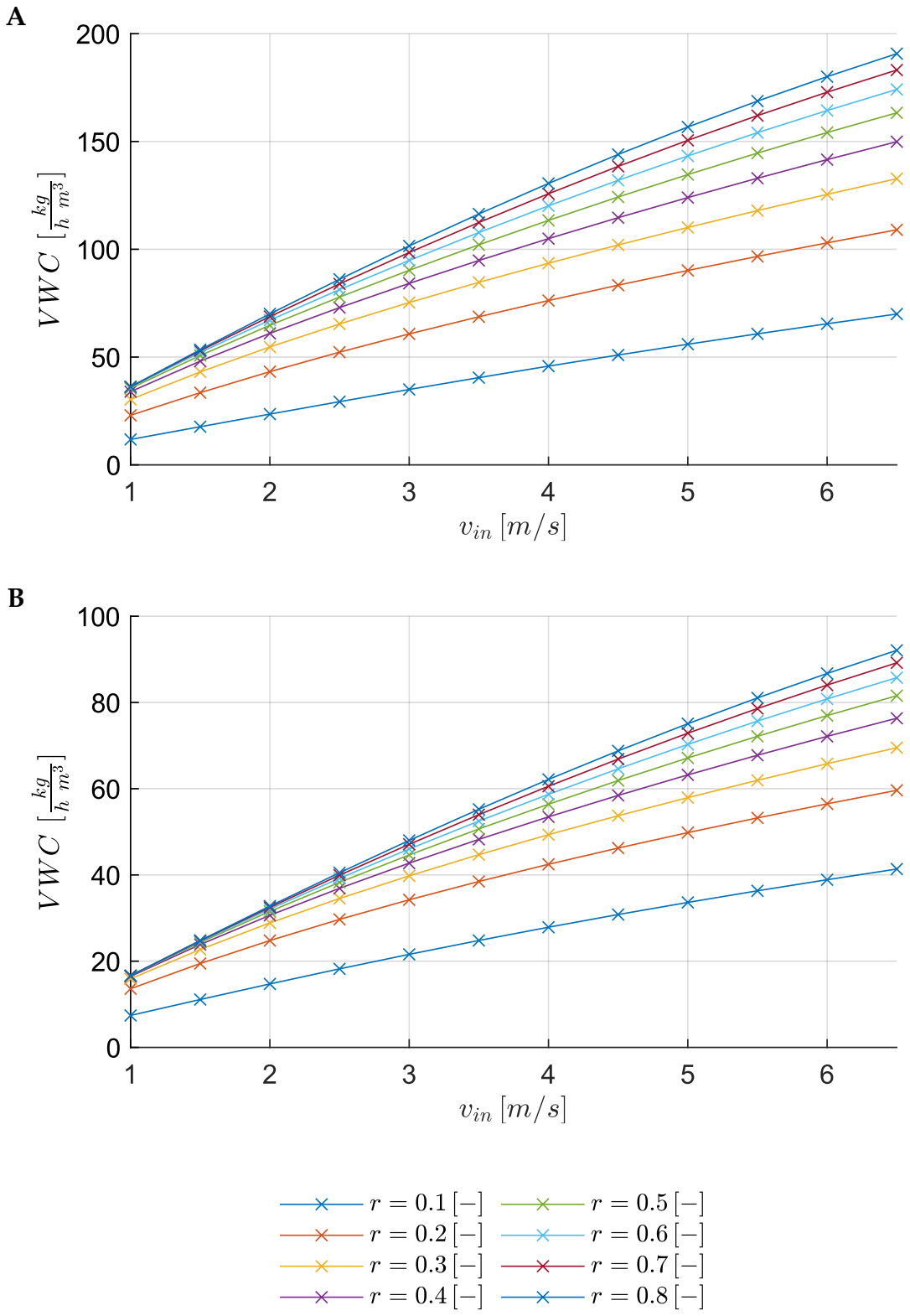

Figure 6.40. Hourly volumetric water consumption as a function of inlet air velocity for different recirculation ratios. Operating conditions: inlet specific humidity of $6\ g_v/kg_{da}$ *and inlet air temperatures of* $25°C$ *(A) and* $40°C$ *(B).*

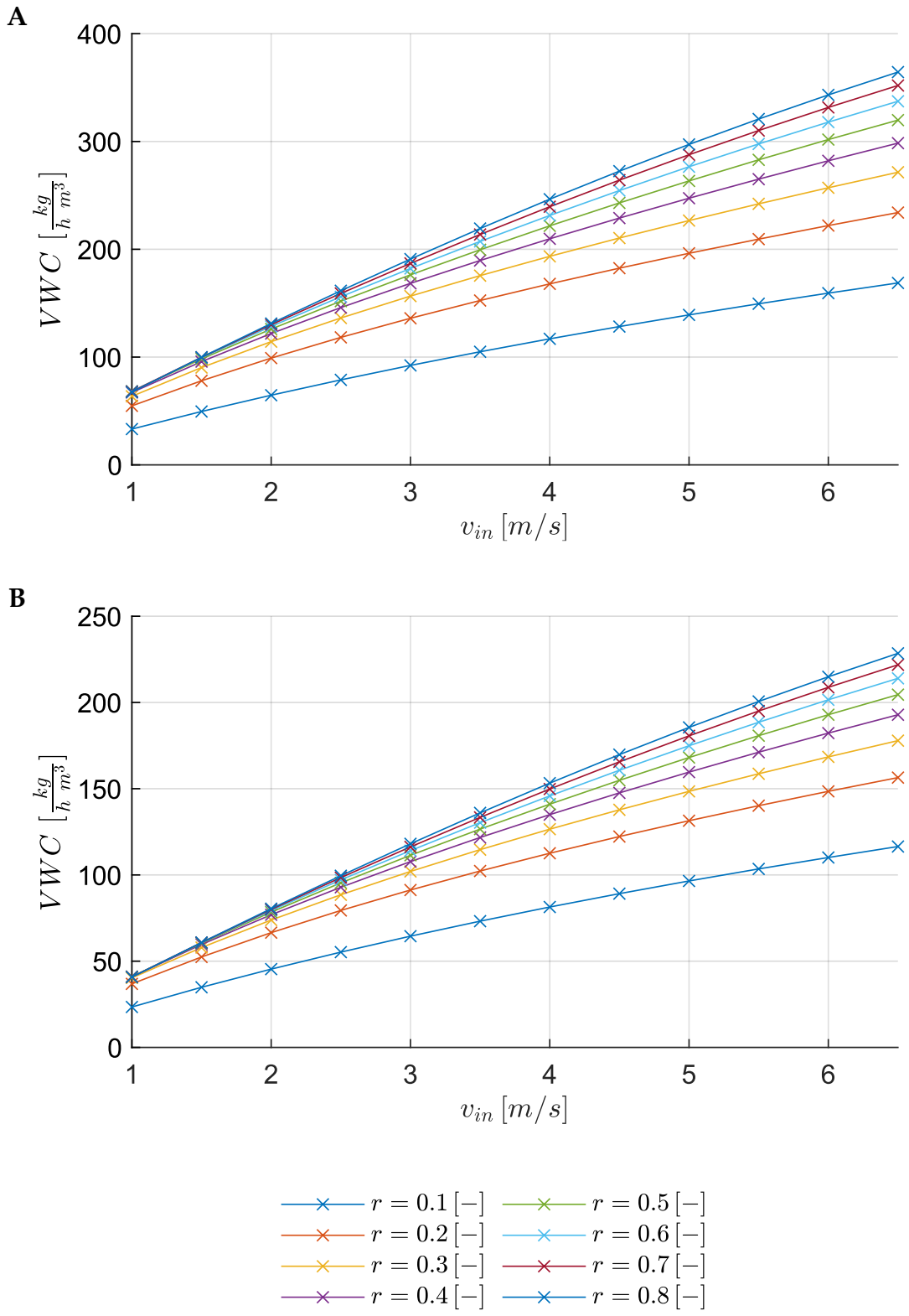

Figure 6.41. Hourly volumetric water consumption as a function of inlet air velocity for different recirculation ratios. Operating conditions: inlet specific humidity of 18 g_v/kg_{da} *and inlet air temperatures of* 30°C *(A) and* 40°C *(B).*

thermal behavior. As the flow progresses, the temperature gradient predicted by the current model becomes lower than that of the Hasan model, ultimately leading to a slightly higher outlet temperature. In the wet channel, the temperature profiles are nearly identical at the inlet. However, the proposed model predicts an earlier temperature increase during the transition from evaporative cooling to reheating. Near the wet channel outlet, a minor influence of the dry channel inlet gradient is observed. The most pronounced differences appear in the liquid film interface temperature. The present model calculates a generally higher interface temperature throughout the exchanger length. A notable reversal occurs at the exchanger extremity, where the entrance effect at the wet channel inlet causes the interface temperature in the proposed model to drop below the value calculated by Hasan.

Figure 6.43 presents the specific humidity profiles for the wet channel and the saturated interface. At the wet channel inlet, the specific humidity calculated by the

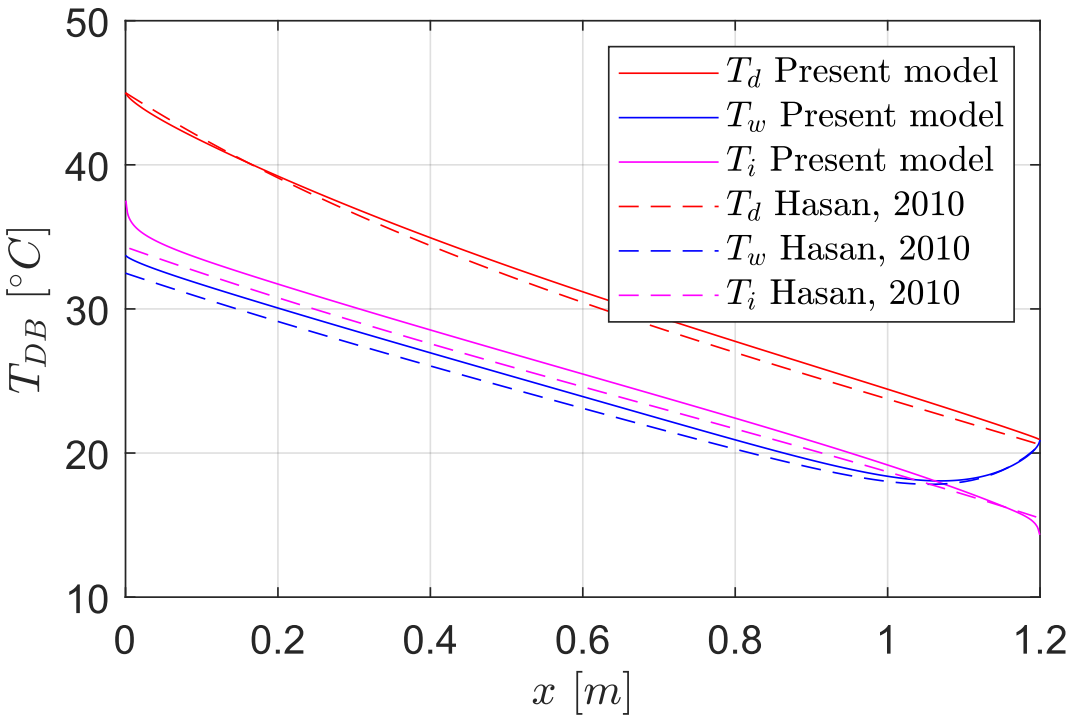

Figure 6.42. Comparison of temperature profiles obtained with Hasan's model and the present model for the Riangvilaikul and Kumar test case with inlet conditions of $T_{d,i} = 45\ °C$ and $\omega_{d,i} = 6.9\ g_v/kg_{da}$.

proposed model increases more rapidly than in Hasan's profile. This initial difference is subsequently recovered by the Hasan model, such that at the wet channel exit, the humidity values from both models are near identical, reaching approximately 32 g_v/kg_{da}. The saturation humidity at the interface directly reflects the trends observed for the interface temperature. Consequently, the proposed model predicts a higher saturation humidity along most of the channel length.

To further evaluate the robustness of the proposed model, two additional test cases were conducted by modifying the exchanger geometry and operating parameters relative to the baseline configurations discussed in previous chapters. The geometric parameters, summarized in Table 6.5, were adjusted to a channel height of 2 mm and a total exchanger length of 0.2 m. The inlet air velocity was maintained at 1 m/s, while the working-to-inlet air ratio was varied between 0.4 (Figure 6.44) and 0.7 (Figure 6.45).

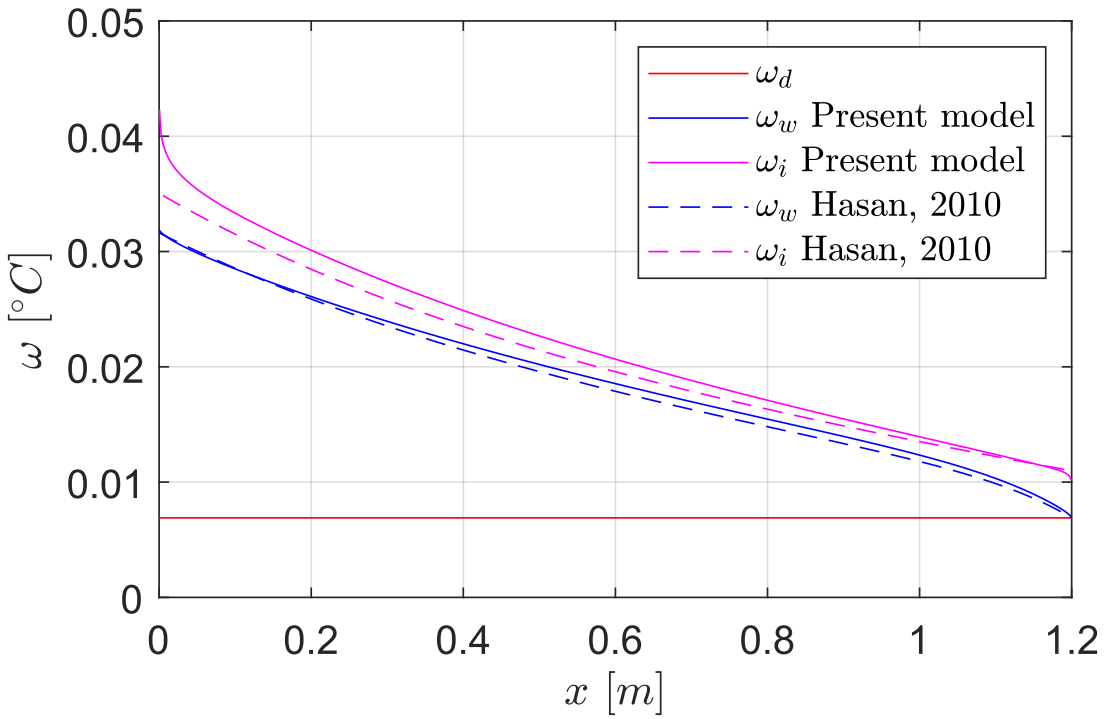

Figure 6.43. Comparison of humidity profiles obtained with Hasan's model and the present model for the Riangvilaikul and Kumar test case with inlet conditions of $T_{d,i} = 45\ °C$ and $\omega_{d,i} = 6.9\ g_v/kg_{da}$.

The results indicate that the thermodynamic trends previously discussed are reproduced in both scenarios. However, the magnitude of the discrepancies between the proposed model and the Hasan formulation appears to be influenced by the recirculation ratio. The comparative analysis reveals that increasing the working air fraction leads to a significant reduction in the deviation between the two models. For the case with $r_m = 0.4$, the percentage errors for the outlet temperatures of the dry and wet channels are 2.7% and 4.7%, respectively. When the ratio is increased to $r_m = 0.7$, these errors decrease substantially to 0.2% for the dry channel and 3.0% for the wet channel. Regarding the mass transfer performance, the outlet specific humidity of the wet channel remains virtually identical in both models across all tested conditions.

A detailed analysis of the proposed model enables a localized examination of heat flux trends and transport parameters along the exchanger. Figure 6.46 (referring to the operating case previously described and shown in Figure 6.44) illustrates the local transport fluxes and the corresponding dimensionless parameters. These results clearly highlight the presence of steep gradients at the inlet and recirculation zones, effects that cannot be captured by traditional approaches based on constant transfer coefficients. Regarding the dry channel (Figure 6.46-A), an extremely pronounced heat transfer gradient is observed at the duct inlet. The sensible heat flux $\dot{Q}_d$ released by the air starts at a peak value of $-640\ W/m^2$, reflecting both the large temperature difference and the initial development of the thermal boundary layer. Moving along the axial coordinate, the heat flux gradient gradually decreases until it reaches a minimum value of approximately $-104\ W/m^2$. Near the recirculation region, the profile undergoes a secondary variation characterized by an increase in the heat transferred toward the wet channel, reaching a value of $-138\ W/m^2$ at the duct extremity. These thermal dynamics are directly reflected in the local Nusselt number (Nu_d) of the dry channel. At the duct entrance, the Nusselt number exceeds 15, emphasizing the intensity of the exchange in the inlet region. Within the first 1.5 cm of

length, the parameter stabilizes rapidly around a value of 8, followed by a slight, steady increase to 8.3 in the central section. Consistent with the heat flux observations, an additional increase in the Nusselt number (up to 8.6) occurs in the recirculation region. The study of the wet channel reveals a more complex distribution of thermal loads, influenced by both evaporation and the counter-current interaction with the primary flow. Examining the sensible exchange parameters (Figure 6.46-B), the sensible heat flux profile ($\dot{Q}_w$) at the wet channel inlet exhibits marked negative values, reaching approximately $-161\ W/m^2$. In this section, the air diverted from the dry channel meets the colder liquid film, thereby releasing sensible heat. As the air flows toward the wet channel outlet, the magnitude of this exchange decreases until it encounters a thermal inversion point. Beyond this point, the flux becomes positive, indicating that the air starts absorbing sensible heat from the interface. This value grows progressively, reaching a peak of approximately 138 W/m^2 at the outlet section. The wet channel Nusselt number (Nu_w) reflects these transitions. In the wet flow inlet zone, Nu_w assumes initially high values before stabilizing around 8.2 in the central region, where the thermal profile approaches a fully developed laminar condition. However, a singularity in the Nu_w trend is observed at the sensible heat flux inversion zone, where the value drops sharply and changes sign. This singularity arises from the definition of the convective heat transfer coefficient. At the point where the temperature difference between the wet air and the interface becomes zero, the Nusselt number approaches an asymptote. It then stabilizes at positive values beyond the inversion zone. The final stage of the local analysis concerns the mass transfer within the wet channel, described by the evaporated mass flux profile ($\dot{m}_e$) and the corresponding Sherwood number (Sh), which defines its non-dimensionalization (Figure 6.46-C). Consistent with the system physics, mass transfer is strictly coupled to the thermal and concentration gradients discussed earlier. At the wet channel inlet, the evaporated mass flux exhibits high values, approximately $0.12 \cdot 10^{-3}\ kg/(s\ m^2)$.

A

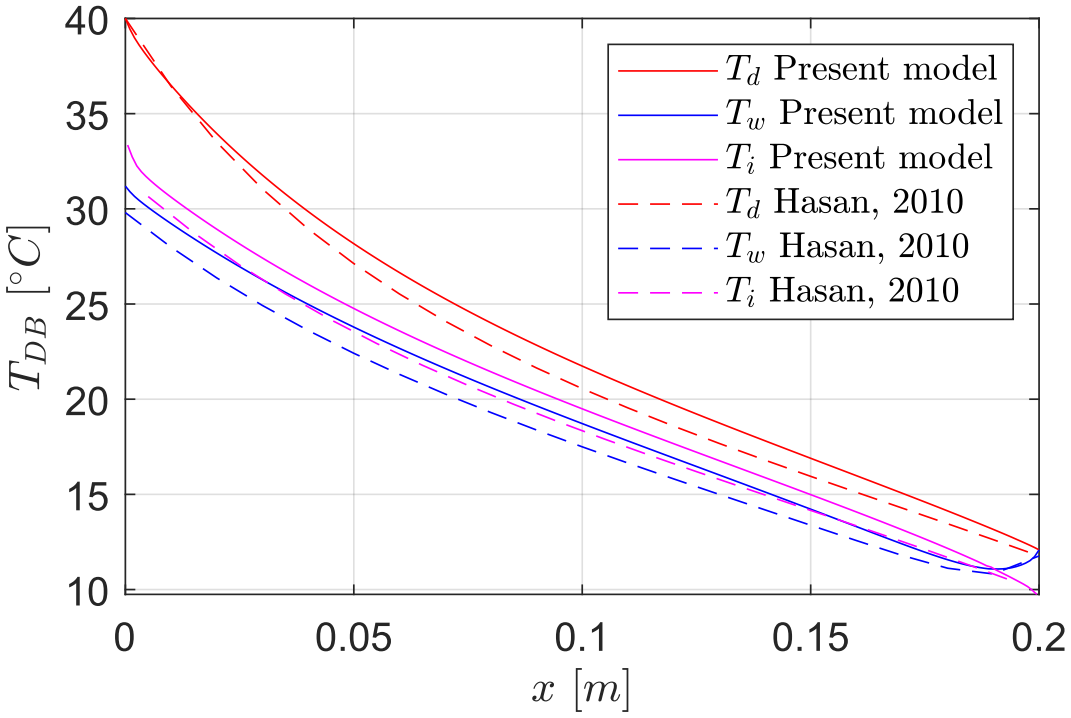

B

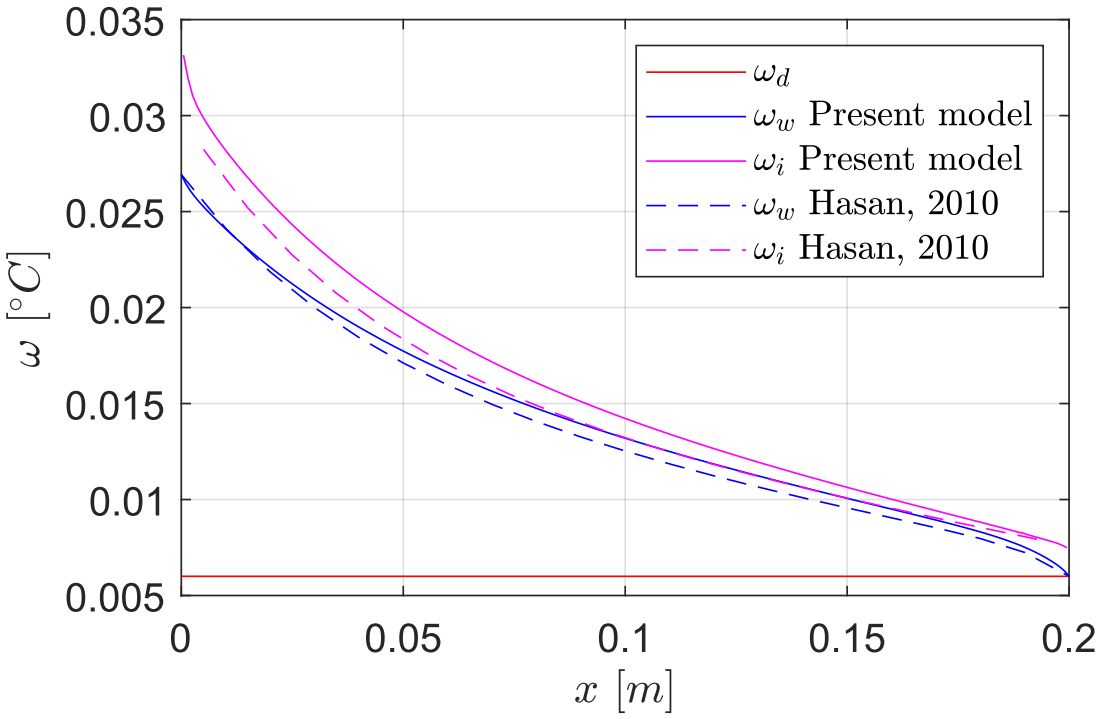

Figure 6.44. Comparison of temperature profiles (A) and humidity profiles (B) obtained with Hasan's model and the present model for an HMX with $L = 0.2\ m$, $s_d = s_w = 2\ mm$, $r_m = 0.4$ and inlet conditions of $T_{d,i} = 40\ °C$ and $\omega_{d,i} = 6\ g_v/kg_{da}$.

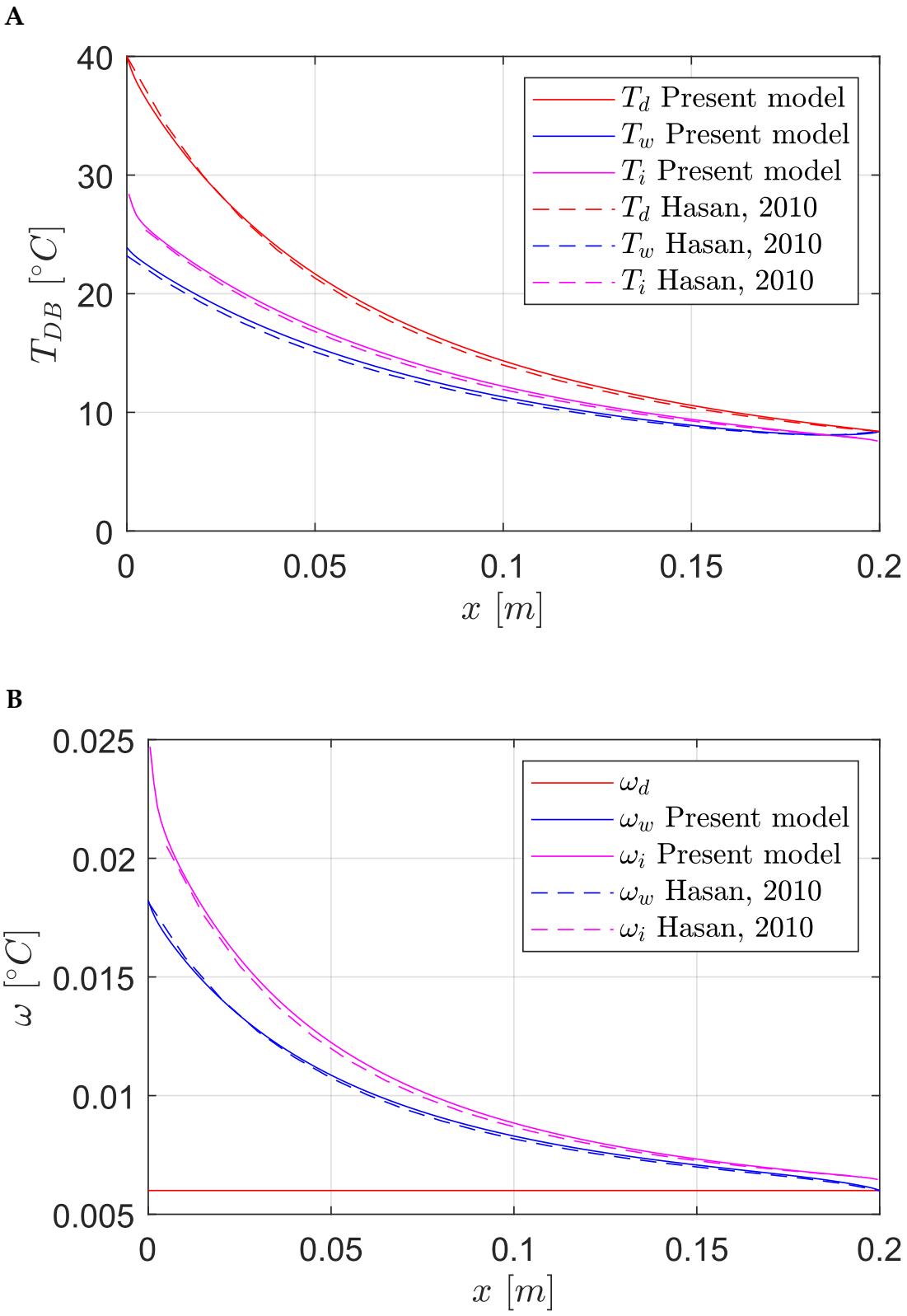

Figure 6.45. Comparison of temperature profiles (A) and humidity profiles (B) obtained with Hasan's model and the present model for an HMX with $L = 0.2\ m$, $s_d = s_w = 2\ mm$, $r_m = 0.7$ and inlet conditions of $T_{d,i} = 40\ °C$ and $\omega_{d,i} = 6\ g_v/kg_{da}$.

This peak is justified by the fact that the air, newly diverted from the dry channel, possesses the minimum specific humidity of the entire cycle, thereby maximizing the evaporative potential of the liquid film. Toward the wet channel outlet, the evaporated flux tends to decrease progressively as the air moisture content increases, reaching a minimum of approximately $0.025 \cdot 10^{-3}\ kg/(s\ m^2)$ in the central zone. However, near the outlet, the flux rises again to approximately $0.2 \cdot 10^{-3}\ kg/(s\ m^2)$. This final increase is due to the high interface temperature in this region, which significantly raises the surface saturation vapor pressure and, consequently, the mass transfer potential. The Sherwood number follows a trend reflecting the laminar nature of the flow while highlighting the system singularities. At the wet channel inlet, Sh assumes initially high values near 11 before stabilizing around 8.2 in the central region, indicating a fully developed mass transport regime in a parallel-plate duct. At the wet channel exit, the parameter rises again to values exceeding 10. This final variation is attributable to the strong local concentration gradients induced by the thermal entrance effects of the adjacent dry channel.

In conclusion, several observations can be made regarding the numerical implementation and physical assumptions of the proposed model. It should be noted that the local values of the dimensionless profiles, particularly at the channel entrances, are inherently dependent on the computational grid resolution. In these regions, the Nusselt and Sherwood numbers reach values that become progressively higher as the calculation points approach the entry coordinate. Consequently, capturing these steep gradients requires a highly refined mesh, increasing the computational cost depending on the desired level of precision in the entrance region.

The implementation of the proposed model is considerably more complex than conventional methods. The calculation of dimensionless parameters requires a continuous extrapolation of the flux profiles from the previous iteration, followed by the re-evaluation of these parameters and the re-execution of the cycle until

convergence is achieved. Despite this added complexity, the results demonstrate that the outlet performance parameters do not deviate significantly from those obtained through conventional calculations.

However, it can be argued that while constant dimensionless parameters for constant wall heat flux boundary conditions predict HMX performance with an adequate level of precision, they do not represent a fully rigorous physical description. The approach proposed here may not be strictly necessary from a practical engineering standpoint, yet it represents an attempt to move beyond conventional assumptions to gain a deeper understanding of the underlying physical phenomena.

It is important to remember that the present calculation still relies on several strong assumptions. For instance, the Nusselt number theory utilized in this development continues to assume constant properties for the airflow. In an evaporative HMX, where a vapor boundary layer is formed, calculating the sensible heat transfer using a constant and uniform specific heat (referenced to the inlet airflow) remains a potentially significant hypothesis.

In light of these findings, it can be concluded that while the proposed model provides a superior descriptive capability of local gradients, Hasan's formulation remains a highly efficient and sufficiently accurate tool for predicting overall device performance. This new computational approach is intended to be a first step toward a more rigorous characterization of the evaporative phenomena within heat exchangers.

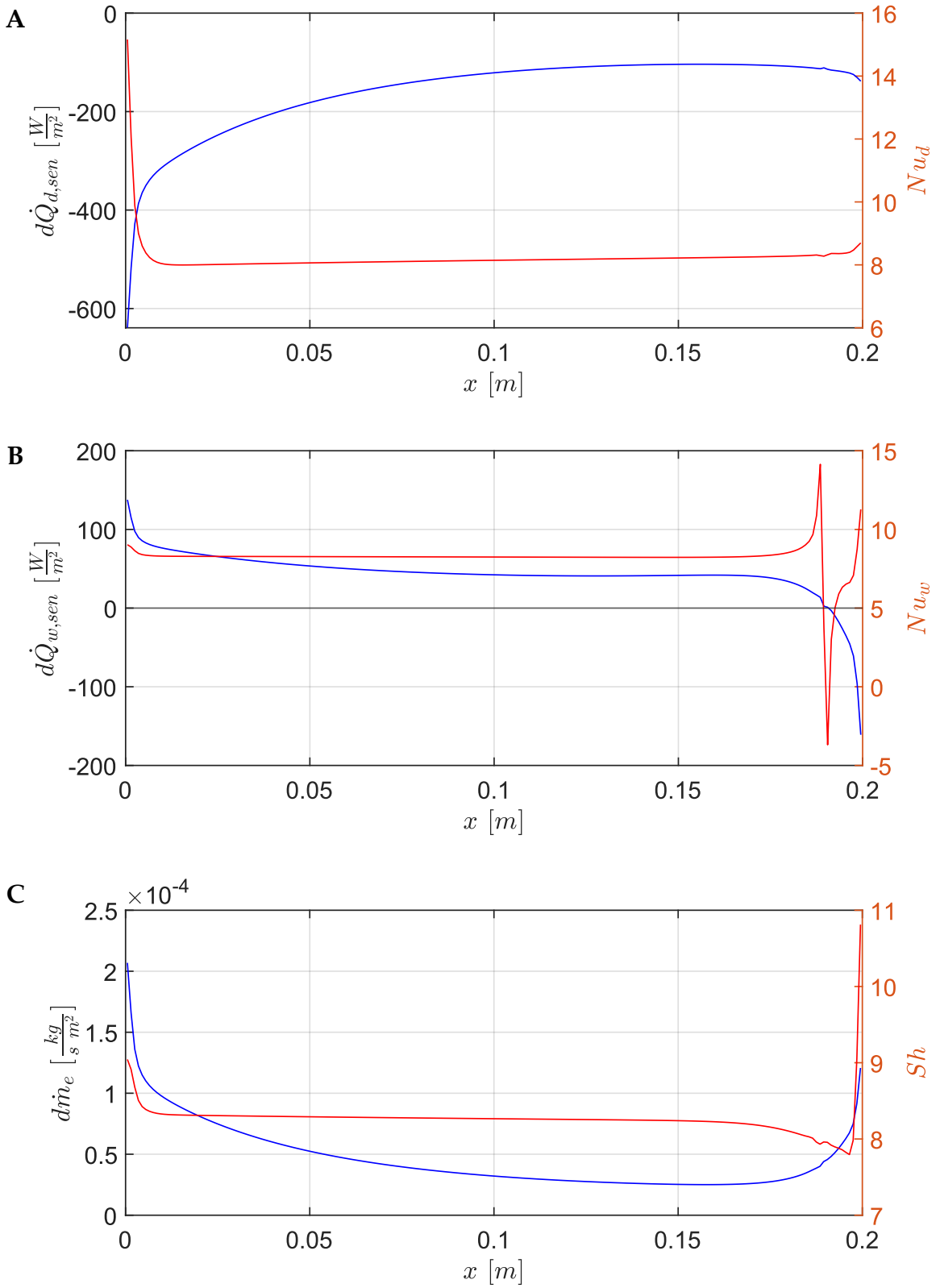

Figure 6.46. Present model profiles for (A) dry channel sensible heat flux and Nusselt number, (B) wet channel sensible heat flux and Nusselt number, and (C) evaporated mass flux and Sherwood number for an HMX with $L = 0.2\ m$, $s_d = s_w = 2\ mm$, $r_m = 0.4$ *and inlet conditions of* $T_{d,i} = 40\ °C$ *and* $\omega_{d,i} = 6\ g_v/kg_{da}$.

7. Development of the ANN

To extend the applicability of the numerical results obtained from the detailed physical model of the M-cycle heat and mass exchanger and to enable rapid performance evaluation over a continuous operating domain, an Artificial Neural Network (ANN)–based surrogate model was developed. While the numerical model presented in the previous chapter is grounded in first-principles heat and mass transfer equations, its computational cost remains non-negligible, especially when embedded within dynamic simulations, optimization procedures, or annual performance assessments.

The ANN approach provides an efficient data-driven alternative, capable of approximating the nonlinear input–output relationships of the exchanger with minimal computational cost. Rather than replacing the physical model, the neural network acts as a high-fidelity interpolator, reproducing its behavior within the boundaries of the training domain.

7.1. Dataset construction and network architecture

The training dataset was generated by collecting the results of the parametric simulations discussed in the previous chapters. Each simulation corresponds to a distinct operating point of the exchanger and is characterized by four independent input variables describing the inlet air conditions and flow configuration. These variables are the dry-channel inlet temperature ($T_{d,i}$), the dry-channel inlet specific humidity ($\omega_{d,i}$), the dry-channel inlet dry-air mass flow rate ($\dot{m}_{d,i,da}$), and the ratio between the working-air and inlet dry-air mass flow rates (r_m).

For each operating point, the numerical model provides several performance indicators. In the present implementation, each target variable is approximated by an independent neural network, trained using the same input dataset and identical network topology. The exported network corresponds to a single-output

configuration, which is representative of the approach adopted for all predicted quantities, such as dry-channel outlet temperature, wet-channel outlet temperature, or evaporated water mass flow rate.

A feed-forward neural network architecture with backpropagation learning was selected. The network was implemented using the MATLAB Deep Learning Toolbox through the fitnet function, which is specifically designed for nonlinear regression problems. The adopted topology consists of an input layer with four neurons, corresponding to the physical input variables, followed by two hidden layers with fifteen neurons each, and a single linear output neuron. The use of two hidden layers enables the representation of the nonlinear coupling between heat and mass transfer phenomena, while the selected number of neurons reflects a compromise between approximation accuracy and robustness against overfitting.

The hidden layers employ the hyperbolic tangent sigmoid activation function, which is well suited for smooth thermodynamic mappings due to its continuous and bounded nature. The output layer adopts a linear activation function, ensuring that the predicted variable is not artificially constrained and can span the full physical range observed in the training data.

7.2. Training algorithm and data pre-processing

Network training was carried out using the Levenberg–Marquardt backpropagation algorithm, which is the default optimization method for *fitnet*. This algorithm combines the rapid convergence properties of second-order methods with the numerical stability of gradient descent and is widely recognized as one of the most efficient training algorithms for medium-sized feed-forward networks applied to function approximation problems [110].

Prior to training, both input and output variables were subjected to min–max normalization using the *mapminmax* procedure. This preprocessing step linearly maps

each variable to the interval [−1,1], based on the minimum and maximum values observed in the training dataset. Normalization plays a crucial role in ANN training by preventing variables with large numerical magnitudes from dominating the error function and by ensuring that the inputs remain within the most sensitive region of the hyperbolic tangent activation function, thereby improving convergence speed and numerical stability.

7.3. Training process and standalone implementation

The network training and deployment process was automated through a custom MATLAB function. Simulation results are first imported from a structured data file and arranged into input and target matrices. The network is then initialized and trained by minimizing the mean squared error between the ANN predictions and the corresponding numerical-model outputs.

Once training is complete, the network is exported as a standalone MATLAB function using the *genFunction* utility with the *MatrixOnly* option enabled. This step converts the trained neural network into an explicit algebraic formulation composed exclusively of matrix operations and elementary functions. As a result, the exported predictor is entirely independent of the MATLAB Deep Learning Toolbox and can be seamlessly integrated into external simulation environments, optimization routines, or system-level performance models.

7.4. Mathematical formulation of the ANN predictor

The exported neural network implements a deterministic nonlinear mapping between the normalized input vector and the predicted output. For a given operating condition, the input vector $\underline{X}$ is composed of four elements representing the dry-channel inlet temperature, the inlet specific humidity, the inlet dry-air mass flow rate, and the working-to-inlet mass flow rate ratio. These variables are characterized by different

physical units and numerical ranges. In order to ensure numerical stability and effective use of the nonlinear activation functions, the raw inputs are first subjected to a linear normalization procedure.

The normalization is performed according to

$$\underline{X}_{norm} = \left(\underline{X} - \underline{X}_{offset}\right) * \underline{g}_{in} + y_{min,in} \qquad 7.1$$

Where $\underline{X}_{offset}$ is a vector containing, for each input variable, the minimum value observed in the training dataset, and $\underline{g}_{in}$ is a gain vector derived from the corresponding input ranges, defined as the ratio between the normalized interval width and the physical data range. The operator $*$ denotes element-wise multiplication. The constant $y_{min,in}$, which represents the lower bound of the normalized input space, is equal to -1 in the present implementation, shifts the normalized variables so that all inputs lie within the interval $[-1,1]$. This transformation corresponds exactly to the *mapminmax* preprocessing function used during training and implemented in the exported code.

Once normalized, the input vector is propagated through the first hidden layer of the network. Each neuron in this layer computes a weighted linear combination of all normalized inputs, adds a bias term, and applies a nonlinear activation function. The resulting activation vector $\underline{a}^{(1)}$ is given by

$$\underline{a}^{(1)} = \tanh\left(\underline{W}^{(1)}\,\underline{X}_{norm} + \underline{b}^{(1)}\right) \qquad 7.2$$

where $\underline{W}^{(1)}$ is the weight matrix connecting the input layer to the first hidden layer and constitutes a set of parameters optimized during the training process, and $b^{(1)}$ is the corresponding bias vector, also determined through training.

The output of the first hidden layer is then used as input to the second hidden layer, where the same computational structure is repeated. The activation vector of the second hidden layer is therefore computed as

$$\underline{a}^{(2)} = \tanh\left(\underline{W}^{(2)}\,\underline{a}^{(1)} + \underline{b}^{(2)}\right) \qquad 7.3$$

with $\underline{W}^{(2)}$ and $\underline{b}^{(2)}$ denoting the trained weights and biases connecting the two hidden layers. The use of two successive nonlinear transformations enables the network to capture the strong nonlinear coupling between heat and mass transfer processes that characterize the M-cycle exchanger.

The final layer of the network performs a purely linear transformation of the second hidden-layer activations. This choice reflects the regression nature of the problem and avoids artificially constraining the output range. The network output in normalized form is computed as

$$\underline{a}^{(3)} = \underline{W}^{(3)}\,\underline{a}^{(2)} + \underline{b}^{(3)} \qquad 7.4$$

where $\underline{W}^{(3)}$ is the trained row vector of output weights and $\underline{b}^{(3)}$ is the trained output bias.

Finally, the normalized network output is converted back into a physical quantity Y_{pred} through the inverse of the normalization applied during training. This denormalization step is expressed as

$$Y_{pred} = \frac{\left(\underline{a}^{(3)} - y_{min,out}\right)}{g_{out}} + x_{offset,out} \qquad 7.5$$

where g_{out} is the output gain computed from the range of the target variable in the training dataset, $x_{offset,out}$ corresponds to the minimum value of the output variable within the training domain, and $y_{min,out}$ denotes the lower bound of the normalized output space, equal to -1 in the present implementation. These parameters are fixed

prior to training and are not subject to optimization and are stored within the exported network function and ensure that the predicted value is expressed in the same physical units and numerical range as the original simulation data.

Through this sequence of normalization, nonlinear transformations, and denormalization, the ANN implements a continuous and differentiable approximation of the underlying numerical model. Within the bounds of the training dataset, the resulting predictor reproduces the behavior of the detailed physical model with negligible loss of accuracy, while reducing the computational cost to a set of simple matrix operations.

7.5. Generalization capability and overfitting prevention

A critical aspect in the development of data-driven surrogate models is the prevention of overfitting, which would compromise predictive accuracy under unseen operating conditions. In the present work, this issue is addressed through the standard data-division and early-stopping mechanisms embedded in the *fitnet* training procedure.

The available dataset is randomly divided into training, validation, and test subsets, accounting respectively for 70%, 15%, and 15% of the total samples. The training subset is used to update the network weights, while the validation subset is employed to monitor the generalization error during training. When the validation error ceases to decrease and begins to increase, training is automatically terminated, preventing the network from memorizing the training data. The test subset is used exclusively for post-training performance assessment, providing an unbiased estimate of the model's predictive capability.

Thanks to this strategy, the resulting ANN-based performance map is not a simple interpolation of discrete simulation points but a robust continuous surrogate model, capable of accurately predicting the performance of the M-cycle heat and mass

exchanger throughout the entire operating domain explored by the numerical simulations, with low residual error and reduced computational cost.

7.6. ANN performance evaluation

The performance of the developed Artificial Neural Network (ANN) was assessed by comparing its predictions against the reference numerical model outputs, with the objective of evaluating both numerical accuracy and physical consistency.

The training dynamics of the ANN for the $T_{d,o}$ is illustrated in Figure 7.1-A, which reports the evolution of the MSE for the training, validation, and test datasets as a function of the number of epochs. A monotonic decrease of the error is observed throughout the training process, indicating stable convergence behavior. No divergence between training and validation curves is observed, suggesting that overfitting is negligible. The training process reaches the maximum number of epochs (1000), indicating that the stopping condition is determined by the predefined training limit. However, the rate of error reduction in the final epochs is minimal, suggesting that the model is already close to convergence.

The distribution of prediction errors on the test dataset is shown in Figure 7.1-B. The histogram is centered around zero, indicating that the ANN predictions are essentially unbiased. The relatively narrow spread of the distribution confirms the high accuracy of the model, while the limited presence of extreme values indicates that large prediction errors are rare.

The quantitative evaluation of the ANN performance in terms of absolute temperature prediction is summarized in Table 7.1. Standard statistical indicators, including MAE, $RMSE$, $CV(RMSE)$, $NMBE$, and R^2 (equations 5.2, 5.3, 5.5, 5.6 and 5.7), are employed. The results show extremely low error values, with $RMSE$ on the order of $10^{-2}\ °C$ and $CV(RMSE)$ below 0.04%, indicating a near-perfect agreement between the ANN predictions and the reference model. The coefficient of determination ($R^2 \cong 1$) further

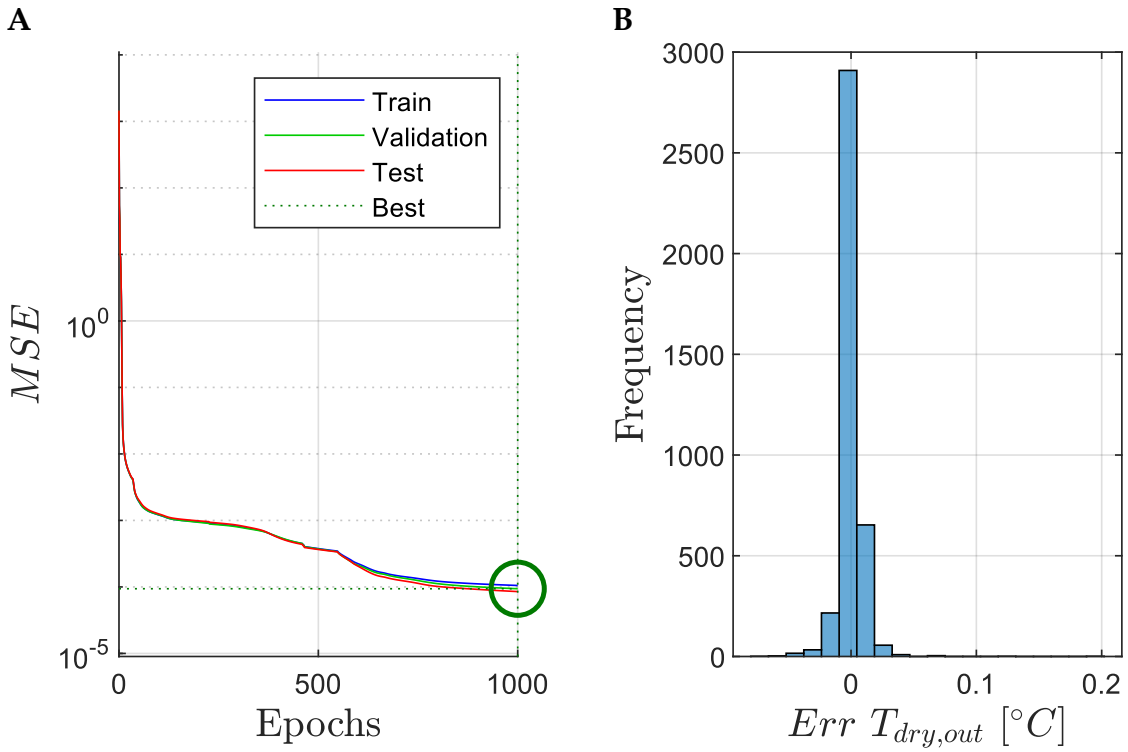

Figure 7.1. ANN performance evaluation: evolution of the Mean Squared Error (MSE) during the training process for training, validation, and test datasets (A); distribution of prediction errors on the test dataset (B).

confirms the excellent fitting capability of the network, while the near-zero *NMBE* highlights the absence of systematic bias.

The extremely high level of accuracy achieved by the ANN can be primarily attributed to the nature of the training dataset. The reference data were generated through a deterministic numerical model, resulting in smooth, noise-free, and highly consistent input–output relationships. Under these conditions, the ANN effectively operates as a surrogate interpolator, learning a well-defined functional mapping rather than approximating noisy experimental observations. Furthermore, the relatively uniform coverage of the input domain and the absence of discontinuities or stochastic variability significantly facilitate the training process, enabling the network to achieve near-perfect fitting performance while maintaining excellent generalization capability across validation and test datasets.

Table 7.1. Statistical performance metrics for ANN prediction of dry channel outlet temperature.

Phase	$\boldsymbol{MAE}$ $[°C]$	$\boldsymbol{RMSE}$ $[°C]$	$\boldsymbol{R^2}$ $[-]$	$\boldsymbol{CV(RMSE)}$ $[\%]$	$\boldsymbol{NMBE}$ $[\%]$
Train	0.00548	0.01026	0.999998	0.03792	$4.478e-5$
Validation	0.00528	0.00969	0.999998	0.03600	$-1.323e-4$
Test	0.00547	0.00923	0.999998	0.03422	$8.811e-4$

To complement the analysis, a relative error evaluation was performed on the ΔT_d. The $MAPE$ (equation 5.4) was adopted as the primary indicator, excluding cases where ΔT_d approaches zero to ensure numerical stability. The results, reported in Table 7.2, show $MAPE$ values of approximately 0.16% across all datasets, confirming the high predictive reliability of the ANN in capturing the thermodynamic behavior of the system.

Table 7.2. Mean Absolute Percentage Error ($MAPE$) of the dry channel temperature difference.

Phase	$\boldsymbol{MAPE}$ $[\%]$
Train	0.16252
Validation	0.16593
Test	0.16587

This dual-level evaluation framework allows distinguishing between the numerical accuracy of the surrogate model (temperature prediction) and the physical reliability of the system representation (temperature difference prediction), providing a comprehensive assessment of the ANN performance.

7.7. ANN-based performance maps

This section presents the results obtained via the ANN-based surrogate model in the form of two-dimensional performance maps as functions of the inlet air temperature

($T_{d,i}$) and inlet specific humidity ($\omega_{d,i}$). To ensure a comprehensive characterization of the system behavior, the analysis is conducted over a structured matrix of operating conditions. The following performance maps are generated for three inlet dry-air mass flow rates ($\dot{m}_{da,d} = 0.1, 0.3$ and $0.5\ kg/s$) and four recirculation ratios ($r_m = 0.1, 0.3, 0.5$ and 0.7). In the figures below, rows correspond to increasing mass flow rates, while columns represent increasing recirculation ratios, enabling a direct comparison of their combined effects on system performance.

Figure 7.2 and Figure 7.3 illustrate the outlet temperature of the primary air stream ($T_{d,o}$). Across all configurations, $T_{d,o}$ increases monotonically with both $T_{d,i}$ and $\omega_{d,i}$. Higher $T_{d,i}$ values raise the inlet enthalpy, while higher $\omega_{d,i}$ values reduce the evaporative potential, thereby limiting the achievable temperature depression. Under dry inlet conditions, the cooling process is highly effective, resulting in outlet temperatures significantly lower than the inlet temperature. Conversely, at high humidity levels, $T_{d,o}$ approaches $T_{d,i}$, particularly at low recirculation ratios. The morphology of the iso-$T_{d,o}$ lines highlights a transition in system behavior governed by the recirculation ratio. At low r_m, the isolines are nearly vertical in the $T_{d,i} - \omega_{d,i}$ plane, indicating a dominant dependence on the inlet temperature. As r_m increases, the isolines progressively rotate and become more horizontal, revealing an increasing sensitivity to $\omega_{d,i}$. For $r_m \geq 0.5$, system performance becomes primarily constrained by the dew-point temperature rather than the dry-bulb temperature.

The marginal benefit of increasing the recirculation ratio progressively diminishes, as configurations with $r_m = 0.5$ and $r_m = 0.7$ exhibit only limited differences, indicating a saturation of thermal performance.

An increase in the $\dot{m}_{da,d}$ leads to higher $T_{d,o}$ under comparable inlet conditions. In addition, the $T_{d,o}$ becomes progressively more sensitive to $T_{d,i}$.

Figure 7.4 and Figure 7.5 present the SCC. The dependence of SCC on inlet temperature and humidity reflects the same trends observed for $T_{d,o}$.

For a fixed r_m, increasing the inlet dry-air mass flow rate leads to a reduction in SCC, particularly at high $T_{d,i}$. This effect is more pronounced at low flow rates and becomes progressively less significant as the mass flow rate increases.

The influence of r_m exhibits a non-monotonic behavior. For a given inlet condition, increasing r_m initially enhances the SCC due to improved regenerative effectiveness. However, further increases reduce the SCC, as a larger fraction of air is recirculated rather than contributing to useful cooling. Moreover, the morphology of the isolines shows divergent trend decreasing $T_{d,i}$ and $\omega_{d,i}$. As the recirculation ratio increases, the curves progressively tend to exhibit a more uniform curvature across the domain, indicating a more homogeneous response of the system to the inlet thermo-hygrometric conditions. Overall, the highest SCC values are obtained under hot and dry conditions, combined with moderate r_m and low $\dot{m}_{da,d}$.

Figure 7.6 and Figure 7.7 show the VCC. The dependence of VCC on inlet temperature and humidity follows the same trends observed for the other performance indicators.

Unlike SCC, the VCC is strongly influenced by the dry-air mass flow rate. Although higher flow rates reduce the achievable temperature drop, the increased airflow processed within a fixed volume leads to a significant increase in VCC. However, this increase is nonlinear, with diminishing returns at higher flow rates.

The effect of the recirculation ratio follows a trend similar to that observed for SCC. An initial increase in r_m improves the VCC, while further increases lead to a reduction due to the decreasing fraction of air effectively contributing to useful cooling.

The morphology of the isolines follows the same behavior observed for SCC. At low recirculation ratios, the isolines are more divergent, especially under low $T_{d,i}$ and low

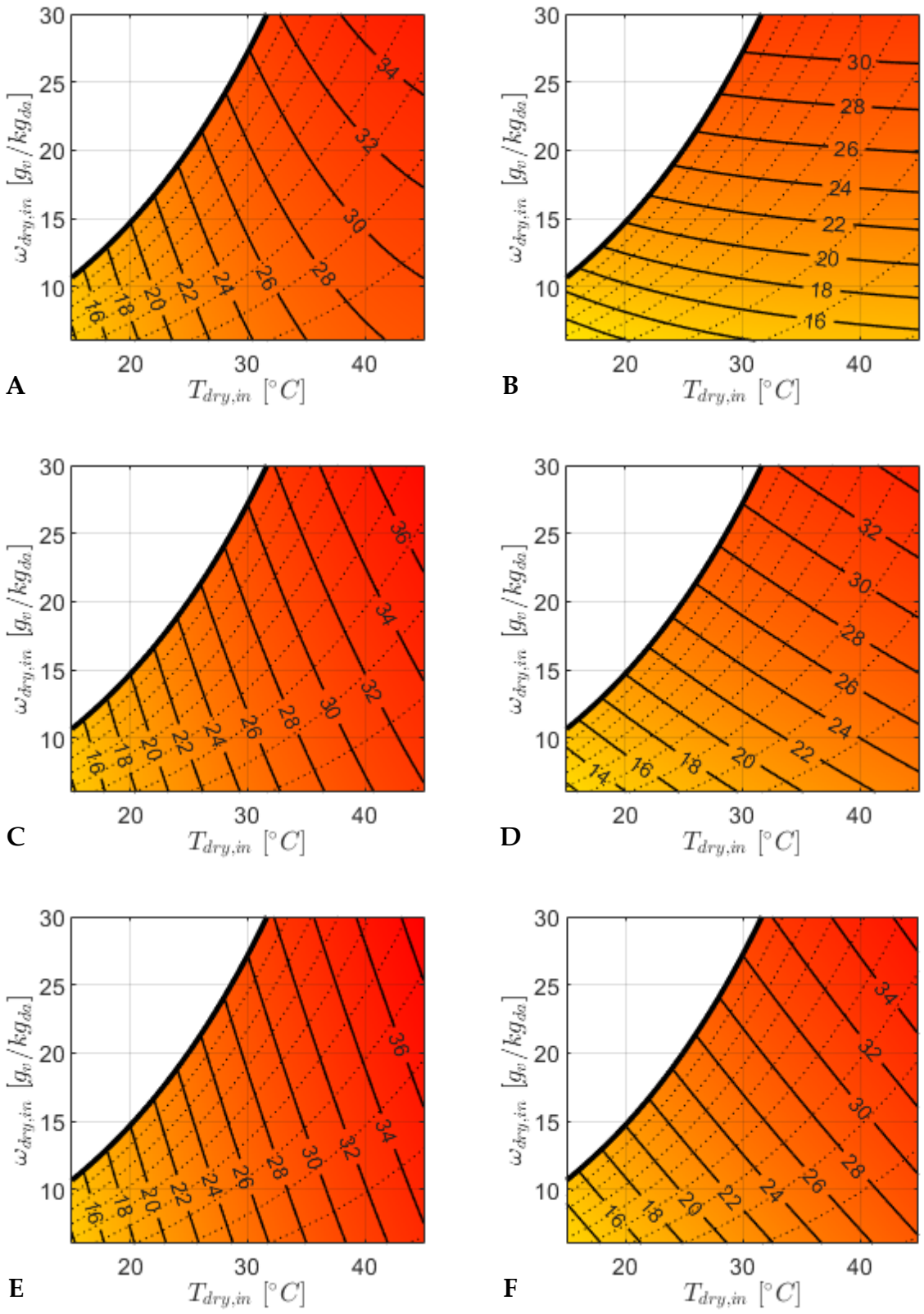

Figure 7.2. Dry-channel outlet temperature $[°C]$ *as a function of inlet temperature* ($T_{d,i}$) *and specific humidity* ($\omega_{d,i}$). *Dry channel dry air mass flow rates* $\dot{m}_{da,d} = 0.1$ *(A, B),* 0.3 *(C, D),* 0.5 *(E, F)* kg/s. *Recirculation ratios* $r_m = 0.1$ *(A, C, E) and* $r_m = 0.3$ *(B, D, F).*

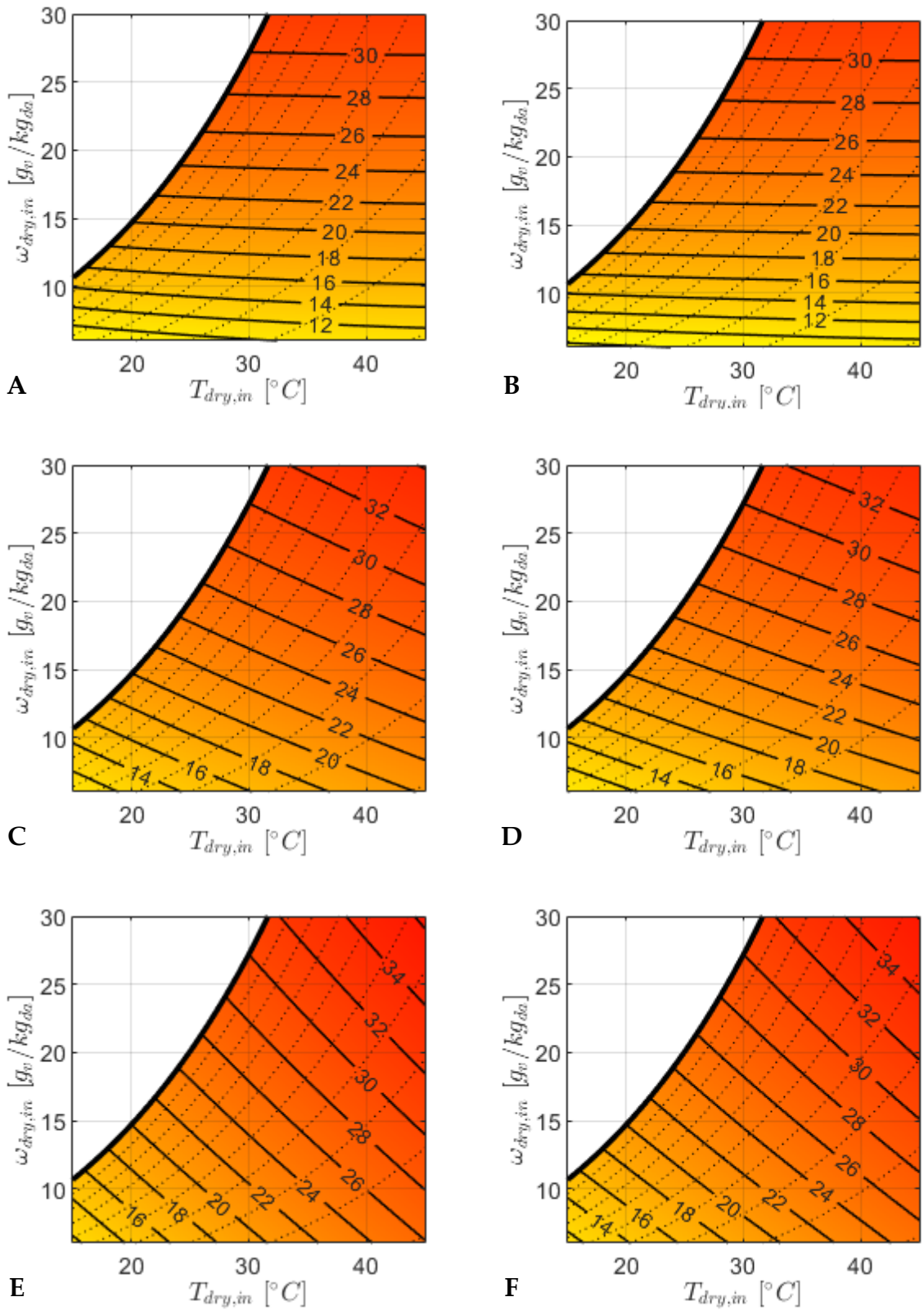

Figure 7.3. Dry-channel outlet temperature $[°C]$ *as a function of inlet temperature* ($T_{a,i}$) *and specific humidity* ($\omega_{a,i}$). *Dry channel dry air mass flow rates* $\dot{m}_{da,d} = 0.1$ *(A, B),* 0.3 *(C, D),* 0.5 *(E, F)* kg/s. *Recirculation ratios* $r_m = 0.5$ *(A, C, E) and* $r_m = 0.7$ *(B, D, F).*

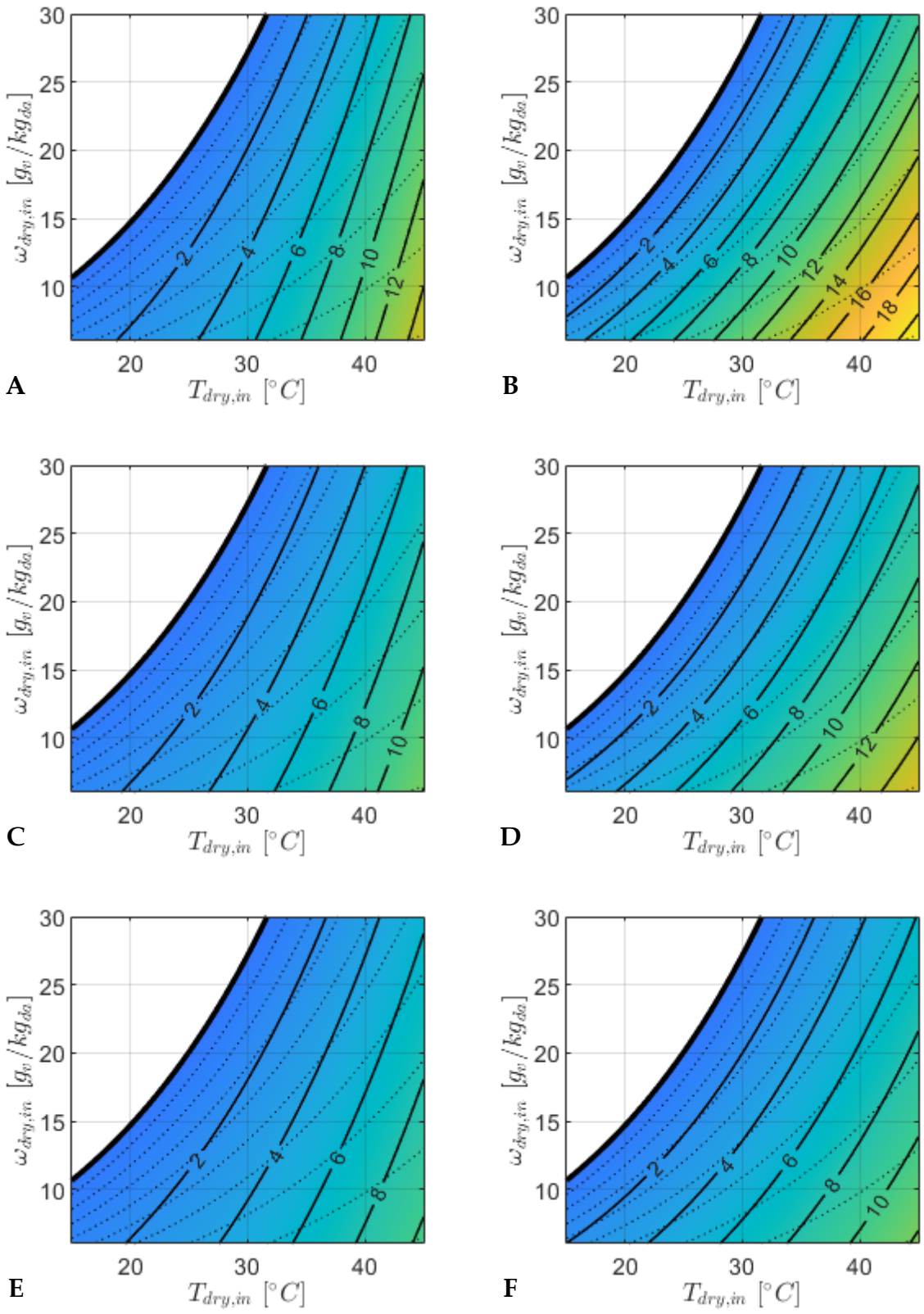

Figure 7.4. Specific Cooling Capacity $[kJ/kg_{da}]$ *as a function of inlet temperature* ($T_{d,i}$) *and specific humidity* ($\omega_{d,i}$). *Dry channel dry air mass flow rates* $\dot{m}_{da,d} = 0.1$ *(A, B),* 0.3 *(C, D),* 0.5 *(E, F)* kg/s. *Recirculation ratios* $r_m = 0.1$ *(A, C, E) and* $r_m = 0.3$ *(B, D, F).*

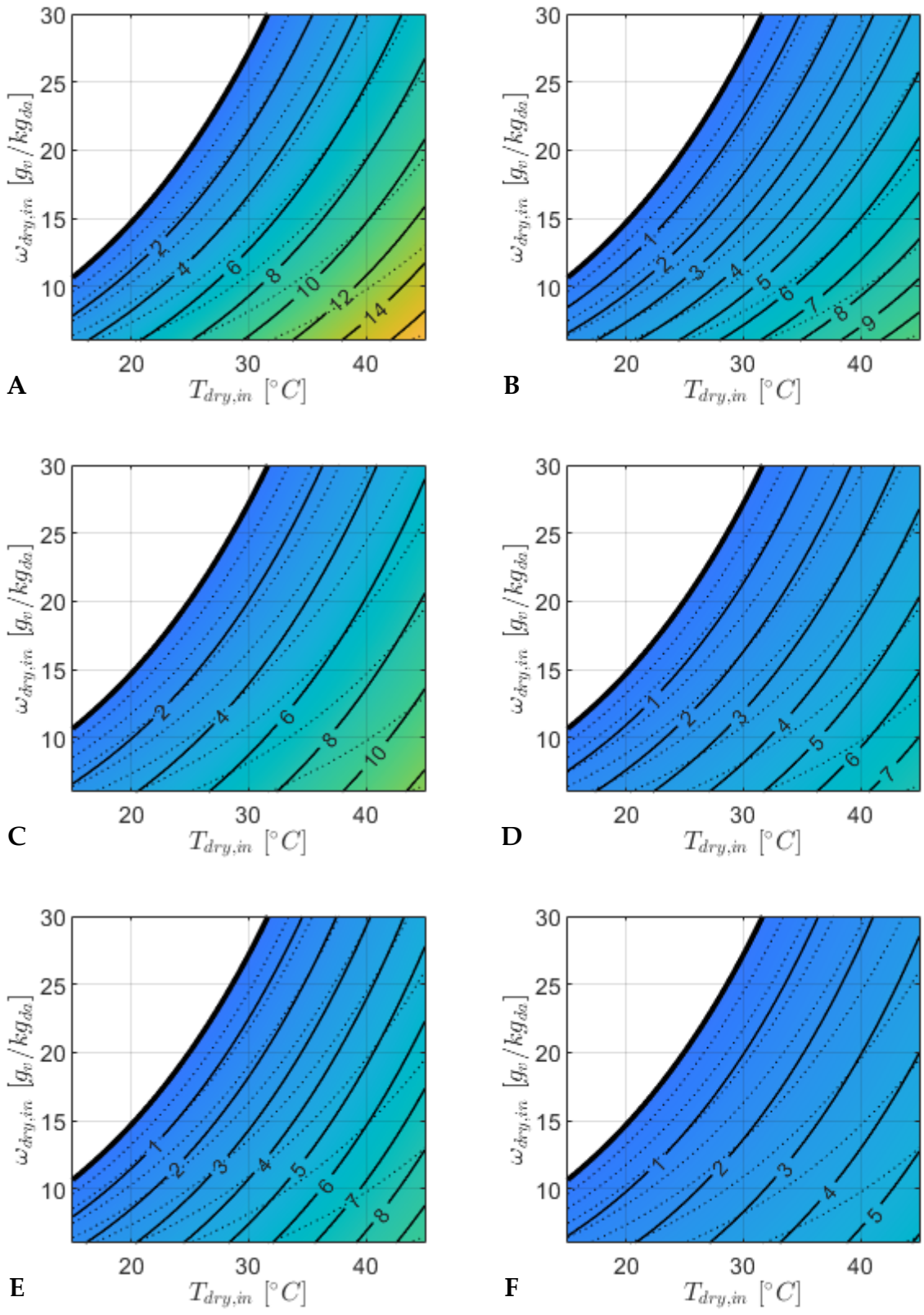

Figure 7.5. Specific Cooling Capacity $[kJ/kg_{da}]$ *as a function of inlet temperature* ($T_{a,i}$) *and specific humidity* ($\omega_{a,i}$). *Dry channel dry air mass flow rates* $\dot{m}_{da,d} = 0.1$ *(A, B),* 0.3 *(C, D),* 0.5 *(E, F)* kg/s. *Recirculation ratios* $r_m = 0.5$ *(A, C, E) and* $r_m = 0.7$ *(B, D, F).*

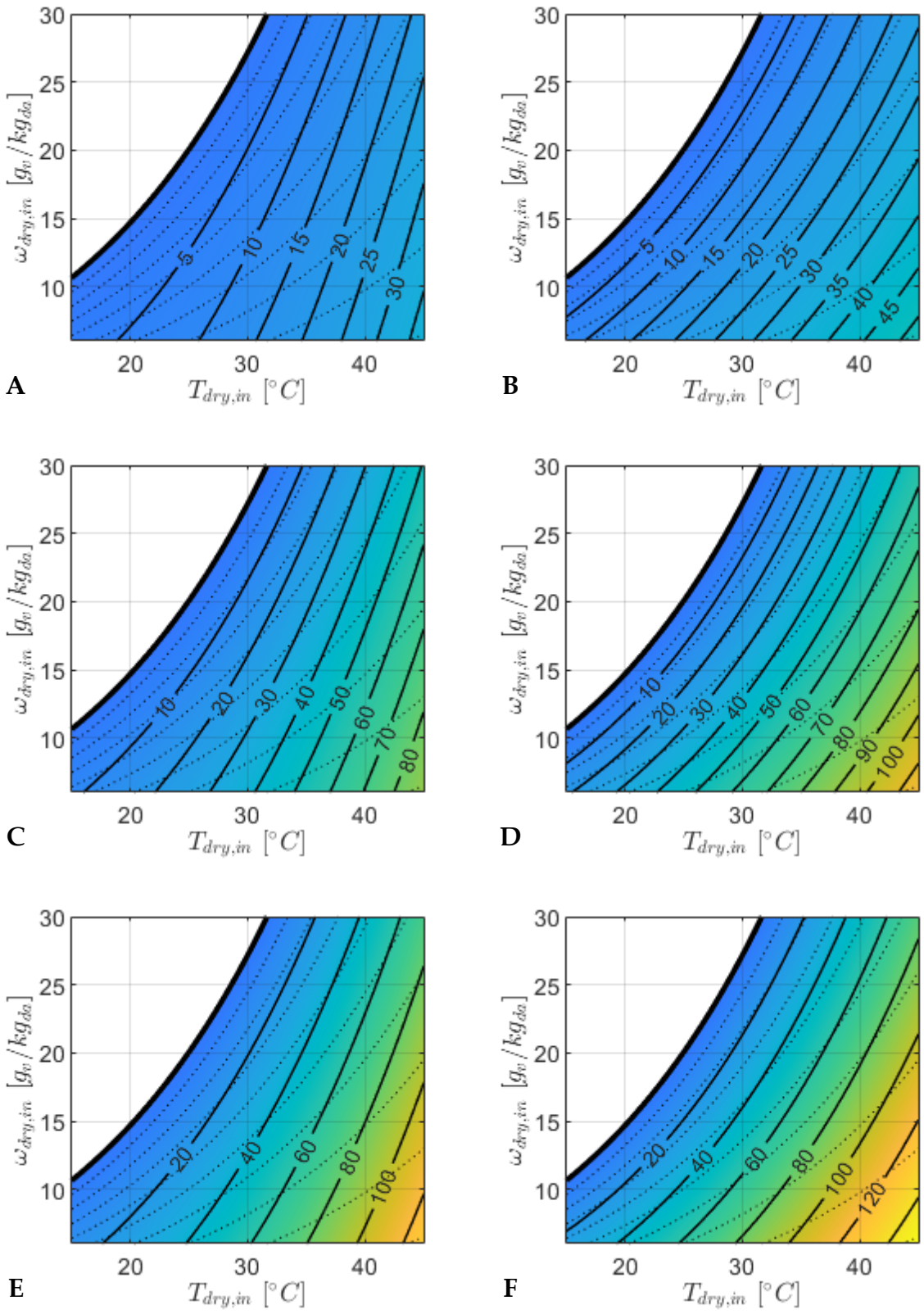

Figure 7.6. Volumetric Cooling Capacity $[kW/m^3]$ *as a function of inlet temperature* ($T_{d,i}$) *and specific humidity* ($\omega_{d,i}$). *Dry channel dry air mass flow rates* $\dot{m}_{da,d} = 0.1$ *(A, B),* 0.3 *(C, D),* 0.5 *(E, F)* kg/s. *Recirculation ratios* $r_m = 0.1$ *(A, C, E) and* $r_m = 0.3$ *(B, D, F).*

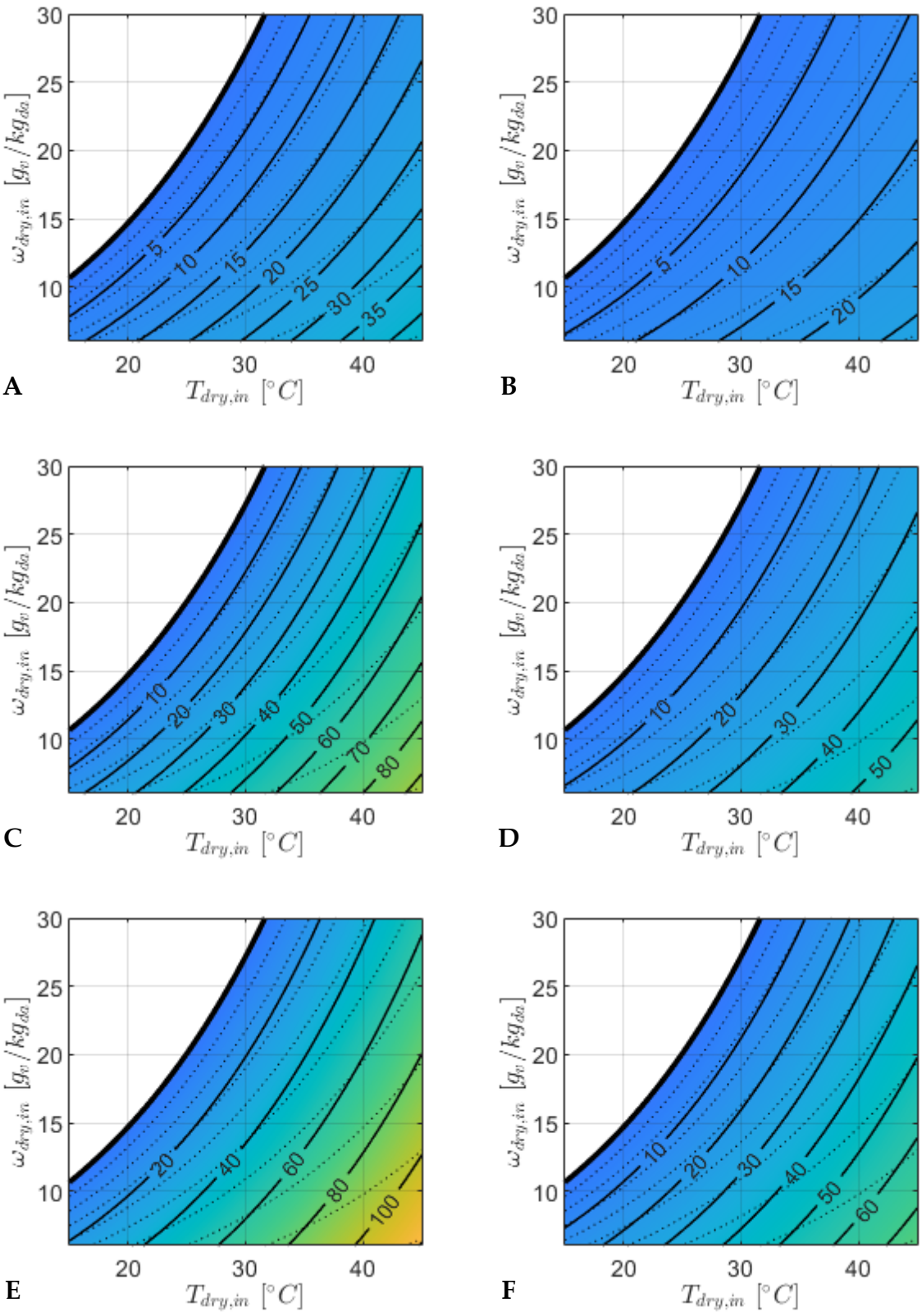

Figure 7.7. Volumetric Cooling Capacity $[kW/m^3]$ *as a function of inlet temperature* ($T_{a,i}$) *and specific humidity* ($\omega_{a,i}$). *Dry channel dry air mass flow rates* $\dot{m}_{da,d} = 0.1$ *(A, B),* 0.3 *(C, D),* 0.5 *(E, F)* kg/s. *Recirculation ratios* $r_m = 0.5$ *(A, C, E) and* $r_m = 0.7$ *(B, D, F).*

$\omega_{d,i}$. As the recirculation ratio increases, the curves tend to assume a more uniform curvature.

Overall, the results highlight a fundamental trade-off between different performance objectives. Maximum temperature reduction is achieved at high r_m and low $\dot{m}_{da,d}$, while the SCC is maximized at moderate r_m and low $\dot{m}_{da,d}$. In contrast, the VCC is favored by higher $\dot{m}_{da,d}$ combined with moderate r_m.

8. Experimental assessment of the M-Cycle HMX

This chapter presents the technical architecture and the methodological framework adopted for the preliminary experimental validation of the M-cycle evaporative HMX. The primary objective is the design and implementation of an experimental apparatus aimed at characterizing the thermo-fluid dynamic performance of the exchanger under laminar flow regimes, while ensuring full control of the boundary conditions. The test bench was designed to generate and regulate the two distinct airflows required for the regenerative evaporative cycle, while enabling systematic acquisition of thermo-hygrometric variables, including temperature, humidity, and channel mass flow rates.

8.1. Heat and mass exchanger (HMX)

The core of the experimental investigation is a commercial HMX manufactured by Seeley International, a global leader in evaporative cooling technologies. The unit belongs to the Climate Wizard product range, specifically the CW-3 model, an advanced compact device based on M-cycle evaporative cooling principles.

The unit features a modular and integrated architecture designed to maximize heat transfer while minimizing the overall system footprint. The internal configuration consists of eight independent modules arranged radially along the perimeter of the main structure. These modules are positioned around the primary supply fan and the secondary extraction fan. They process the airflows in parallel, minimizing the need for external ducting, as all flow passages are integrated within the structural frame.

Each element (Figure 8.1) features a parallel-plate geometry with alternating dry and wet channels separated by a polymeric sheet. The wet side is treated with a highly absorbent hydrophilic coating. In addition, the sheets undergo a specialized embossing process that creates localized protrusions, which maintain a constant gap

A

B

Figure 8.1. M-cycle unit from Seeley CW3: front view (A) and back view (B).

between adjacent surfaces, ensuring unobstructed airflow while promoting localized turbulence and enhancing heat and mass transfer.

The front section of the HMX is composed of thirteen intake ports supplying the dry channels, alternating with fourteen working air manifolds that collect the saturated air exiting the wet channels. Each intake port has a height of 25 mm, while the separation between adjacent ports is defined by 20 mm wide manifolds that convey the exhaust air laterally toward the extraction fan. Downstream of the inlet section, the discrete channel separation imposed by the inlet geometry is no longer present, and the channels extend continuously over the entire height of the HMX.

In the rear section, the outlets of the dry channels and the inlets of the wet channels are located. This configuration enables partial recirculation of air from the dry channels into the wet channels, driven by the pressure differential generated by the extraction fan.

The exchanger unit comprises eighty-seven dry channels and eighty-eight wet channels. The dry channels have a height of 1.0 mm, while the wet channels have a height of 1.5 mm. The channel length is 10 cm. The separating polymeric sheets, including the hydrophilic coating, have a thickness of approximately 0.3 mm. The geometric characteristics of the heat exchanger are reported in Table 8.1.

The wetting system consists of a conduit supplied by a pump that draws water from the bottom of the device and feeds a distributor located at the top, ensuring uniform wetting of the channels.

The original commercial unit also includes Kraft paper pads for direct evaporative cooling at the outlet, supplied by a secondary water distribution system. These components were removed to isolate the performance of the regenerative M-cycle, thereby excluding any contribution from direct evaporative cooling.

8.2. Test bench description

To characterize the thermo-fluid dynamic performance of the heat exchanger, a dedicated experimental facility was developed. The test bench was designed to control and measure the fundamental quantities (temperature, relative humidity, and mass flow rate) at both the inlet and outlet, enabling the simulation of multiple operating conditions in a controlled environment. A schematic of the setup is shown in Figure 8.2. Regarding the air circuit, airflow is provided by a centrifugal fan operating in draw-through configuration. The air pre-treatment section is located upstream of the test section and includes independently controlled electric heaters for temperature regulation, as well as evaporative pads for adiabatic humidification. A digital thermohygrometer (Table 8.3) is used to determine the inlet air humidity under different operating conditions. When the humidification system is inactive, the instrument measures ambient humidity, which is assumed to coincide with the inlet condition. Conversely, when the evaporative pads are kept wet, the

Table 8.1. Geometric parameters of the Seeley CW3 HMX.

HMX geometric parameters			
Length	L	0.1	m
Dry channel height	s_d	1.0	mm
Wet channel height	s_w	1.5	mm
Wall thickness	s_{wall}	0.3	mm
Number of dry channels	N_d	87	
Number of wet channels	N_w	88	

thermohygrometer is positioned inside the inlet duct downstream of the humidification section, allowing direct measurement of the modified thermo-hygrometric properties of the airflow supplied to the heat exchanger.

The conditioned air flows through a straight duct equipped with a vane anemometer (Table 8.4) to measure the inlet volumetric flow rate. The connection to the HMX is made through a diverging cone, designed to improve velocity uniformity at the channel inlets, while a converging cone is installed at the outlet section. Due to the large size of the HMX, the inlet and outlet sections were partially sealed to reduce the effective flow area. Only a 21 cm high portion of the exchanger was left open, while the remaining section was sealed. This modification enables operation with laboratory-scale equipment while maintaining sufficiently high air velocities within the channels. Thermal measurements of the product air are performed using Type T thermocouples (Table 8.2) arranged in arrays at both the inlet and outlet of the dry channels. Multiple thermocouples are distributed across each section to monitor temperature non-uniformities. However, for performance evaluation, only the thermocouples located at the geometric center of each section are considered. These measurements are assumed to be representative of the core flow, minimizing the influence of edge effects and lateral gradients. The remaining thermocouples are used for diagnostic purposes, allowing identification of anomalous behavior or flow maldistribution. This approach

TI,a: Ambient thermohygrometer	*TI,i: Inlet thermohygrometer*
AN,i: Inlet anemometer	*AN,o: Outlet anemometer*
TC,i: Inlet thermocouples	*TC,o: Outlet thermocouples*

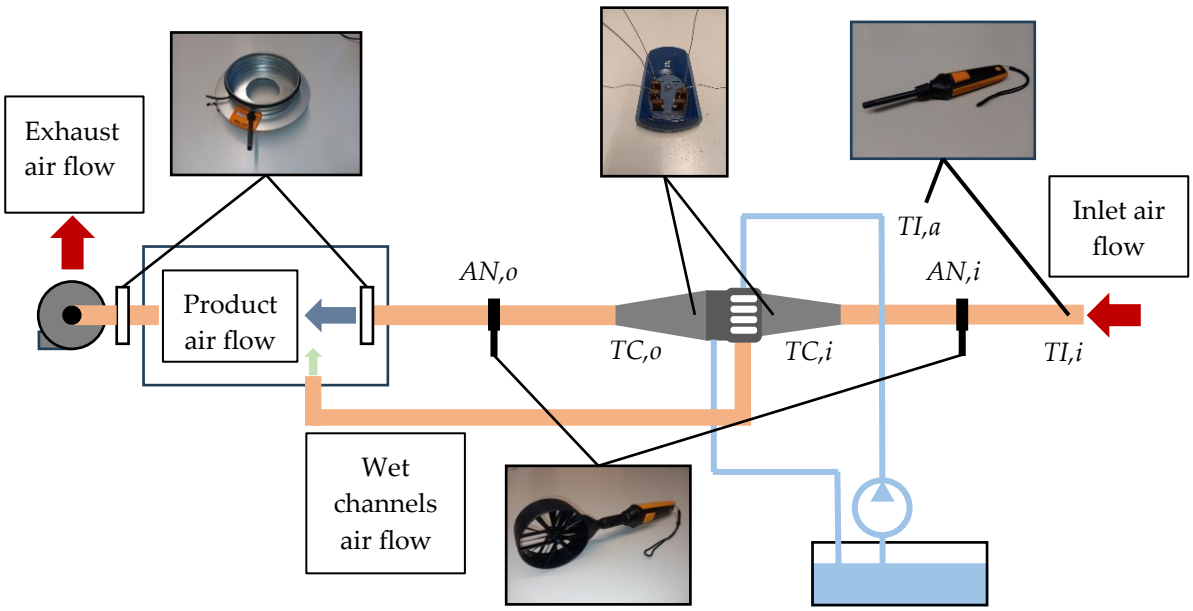

Figure 8.2. Schematic representation of the experimental test bench.

ensures consistency with the numerical model, which neglects edge effects and spatial non-uniformities, thus enabling meaningful comparison between experimental and numerical results. The internal geometry of the exchanger, characterized by interconnected channels in the downstream section, naturally promotes partial recirculation of air from the dry channels into the wet channels, driven by the internal pressure gradients. The fraction of air that is not recirculated exits the dry channels and enters the product air duct through the converging outlet cone. This duct is equipped with a second vane anemometer (Table 8.4), allowing determination of the product air flow rate and, by difference from the inlet flow rate, estimation of the recirculated fraction. The recirculated air enters the wet channels, where it undergoes evaporative cooling before being discharged through a dedicated exhaust duct. Both product and exhaust streams are conveyed into a common outlet plenum.

Flow distribution between the two streams is controlled by an iris diaphragm valve installed upstream of the plenum, which regulates the split between product and exhaust air. A second iris valve, located downstream and connected to the fan, provides additional control over the total flow rate and system pressure. The fan operates under suction, generating the pressure difference that drives airflow through both dry and wet channels.

Prior to their use in the test bench, the vane anemometers were calibrated against a hot-wire probe (Table 8.5) to determine their effective diameter and improve flow rate estimation accuracy. This calibration enabled the definition of a correlation for estimating the volumetric flow rate from the measured average air velocity (Figure 8.3).

Finally, the hydraulic circuit consists of a closed-loop water system, in which a diaphragm pump supplies water from a storage tank to the upper distributor. Unevaporated water is collected at the bottom of the exchanger and recirculated, minimizing overall water consumption.

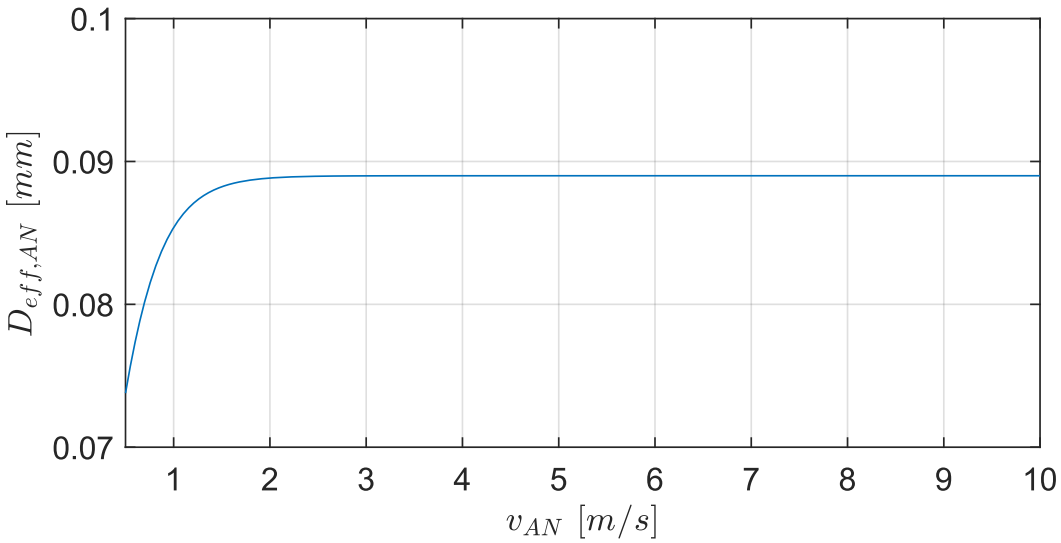

Figure 8.3. Calibration curve of the vane anemometer showing the effective diameter as a function of the measured average air velocity.

Table 8.2. Technical specifications of the Type T thermocouples.

Temperature	
Measuring range	$from\ -75\ to\ +250\ °C$
Accuracy	$\pm 1\ °C$

Table 8.3. Technical specifications of the digital thermohygrometer (Testo).

Temperature	
Measuring range	$from\ -20\ to\ +70\ °C$
Accuracy	$\pm 0.5\ °C$
Resolution	$0.1\ °C$

Relative humidity	
Measuring range	*from* 0 *to* 100 %
Accuracy	$\pm 1\ \%/year$ ± 2 % (*from 5 to* 90 %) $\pm 0.03\ \%/K$
Resolution	0.1 %

Table 8.4. Technical specifications of the vane anemometer (Testo).

Volumetric flow rate	
Measuring range	*from* 0.3 *to* 35 m/s
Accuracy	$\pm(0.2\ m/s + 1.5\ \%\ m.v.)$ *from* 20.01 *to 35 m/s* $\pm(0.1\ m/s + 1.5\ \%\ m.v.)$ *from* 0.3 *to 20 m/s*
Resolution	$0.01\ m/s$
Temperature	
Measuring range	$from\ -20\ to\ +70\ °C$
Accuracy	$\pm 0.5\ °C$
Resolution	$0.1\ °C$

Table 8.5. Technical specifications of the hot bulb probe (Testo).

Volumetric flow rate	
Measuring range	$from\ 0.3\ to\ 10\ m/s$
Accuracy	$\pm(0.03\ m/s + 5\ \%\ m.v.)$
Resolution	$0.01\ m/s$
Temperature	
Measuring range	$from\ -20\ to\ +70\ °C$
Accuracy	$\pm 0.5\ °C$
Resolution	$0.1\ °C$

8.3. Experimental results

Each experimental test was conducted by setting the iris valves, the inlet heater, and, when required, the evaporative pads. Subsequently, the HMX water distribution system was activated to ensure complete wetting of the hydrophilic surfaces.

After imposing the boundary conditions, sufficient time was allowed for all measured variables to reach steady-state conditions. Figure 8.4 illustrates the temperature profiles recorded during the transient phase between two tests performed under different operating conditions. The ambient temperature remains nearly constant, as measurements were carried out in a climatized laboratory environment. In contrast, the inlet air temperature varies due to regulation of the pre-heating system, while the outlet temperature is influenced both by inlet conditions and by the injection of water at ambient temperature. As shown in the figure, water was supplied multiple times prior to each test to ensure complete re-wetting of the hydrophilic surfaces. This procedure was necessary because previous tests, conducted at high inlet temperatures, resulted in significant evaporation and partial drying of the wetted surfaces. Following the final water injection, the outlet temperature gradually stabilizes, indicating that steady-state conditions have been achieved. At this stage, the measured values are considered representative and are used for the experimental analysis.

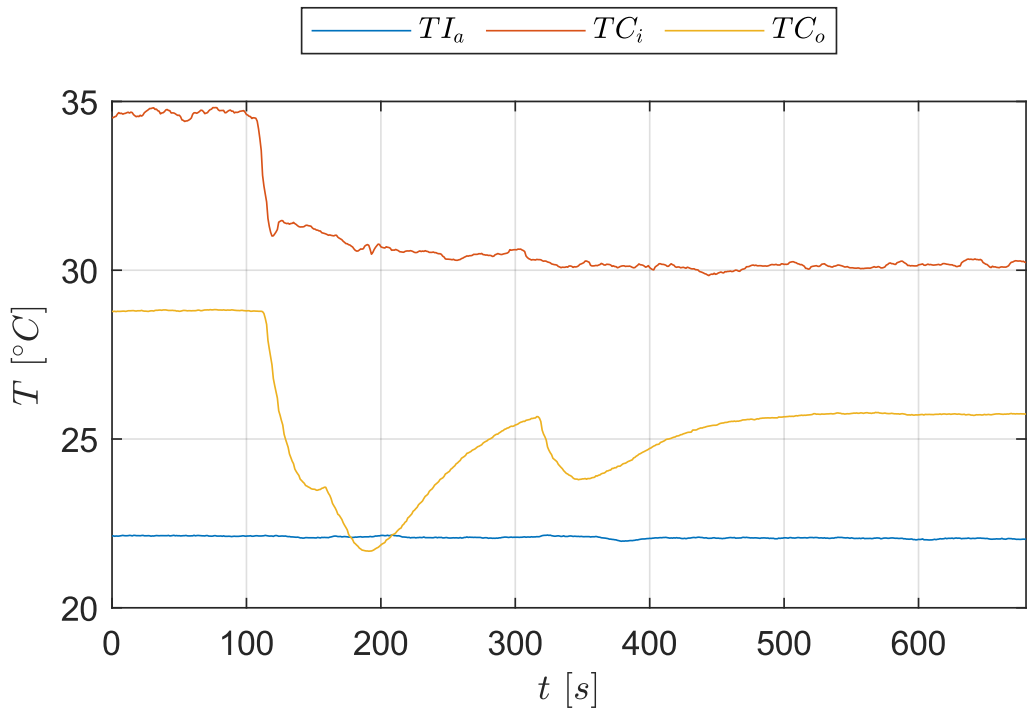

Figure 8.4. Example of temperature profiles recorded during the transient phase between two tests conducted under different boundary conditions.

Table 8.6 and Table 8.7 report the experimental data collected under steady-state conditions. The tests are divided into two categories:

- tests conducted under ambient humidity conditions, in which the evaporative pads were not used (Table 8.6);
- tests performed at increased humidity levels, achieved by activating the evaporative pads (Table 8.7).

In the first case, the inlet humidity was assumed equal to the ambient laboratory humidity. In the second case, the thermohygrometer was positioned within the inlet duct to directly measure the air properties downstream of the pre-treatment section.

The reported variables include: test ID, inlet air temperature ($T_{TI,a}$) and relative humidity ($\varphi_{TI,a}$), inlet duct temperature ($T_{AN,i}$) and velocity ($v_{AN,i}$), temperatures at the inlet ($T_{TC,i}$) and outlet ($T_{TC,o}$) of the HMX (based on the central thermocouples), and outlet duct temperature ($T_{AN,o}$) and velocity ($v_{AN,o}$).

Table 8.8 e Table 8.9 present the derived quantities, including $\omega_{d,i}$, $\dot{m}_{da,d}$, r_m and Reynolds number of the dry channel (Re_d). The test IDs correspond to those reported in Table 8.6 and Table 8.7, maintaining the same classification based on humidity conditions.

Figure 8.5 and Figure 8.6 compare the experimental measurements with the predictions of the Hasan numerical model for ambient and increased humidity conditions, respectively. Figure 8.5 reports the percentage error in ΔT_d and the absolute error in $T_{d,o}$ for tests at ambient humidity, while Figure 8.6 presents the corresponding results for increased humidity conditions. All plots are three-dimensional, with the input parameters $T_{TC,i}$, $\dot{m}_{da,d}$ and r_m represented along the axes. Each point corresponds to a specific set of boundary conditions, while the error is represented through a color scale. For tests conducted under ambient humidity conditions, the percentage error in the temperature drop is generally below 15%. Higher errors, occasionally reaching or exceeding 20%, are observed primarily at low values of r_m where the temperature drop is inherently small and thus more sensitive to measurement uncertainties. These cases are often also associated with low inlet temperatures, further reducing the expected temperature difference. The analysis of the absolute error in $T_{d,o}$ supports this interpretation. Under low r_m and low $T_{d,i}$, the error is typically around 0.5 $°C$. In some cases, it increases to approximately 1 $°C$, while the highest values, exceeding 2 $°C$, are observed at high $T_{d,i}$. These discrepancies can be attributed to limitations in the water supply system. As previously described, water was introduced only during the initial phase of each test, since the system was not capable of delivering a sufficiently small and continuous flow rate. Instead, it supplied excessive amounts of water when activated. As shown in Figure 8.4, this resulted in a temporary disturbance of the outlet temperature, requiring a stabilization period before measurements could be taken. Under high inlet temperature conditions, this limitation likely led to excessive drying of the wetted surfaces during operation,

thereby reducing the exchanger performance and increasing the deviation from numerical predictions. However, in these cases the expected temperature drop is relatively large, which explains why the percentage error remains moderate, typically around $15-20\%$. For tests conducted at increased humidity, the deviations are generally smaller. This behavior can be attributed to both the reduced expected temperature drop and the lower degree of surface drying, due to the higher inlet humidity. In contrast to the previous case, the largest deviations are not associated with specific ranges of $T_{d,i}$ or r_m, but are more randomly distributed. This is likely due to the difficulty of maintaining a stable and uniform artificially humidified airflow over time, which may have prevented the system from fully reaching steady-state conditions in some tests. Nevertheless, the results can be considered satisfactory, with percentage errors consistently below 20% and absolute errors generally below $1\ °C$.

A more detailed analysis of the error distribution reveals a systematic bias in the model predictions. As shown in Figure 8.7, under ambient humidity conditions the model tends to underestimate the outlet air temperature compared to experimental measurements. Overestimation occurs only in cases characterized by negligible errors. This trend is in contrast with the findings of Riangvilaikul and Kumar, where a systematic overprediction of the outlet temperature was observed. For tests conducted under increased humidity conditions, the model behavior changes. In this case, overestimation is primarily observed at high inlet temperatures. This behavior may also be influenced by the increased difficulty in maintaining stable and well-controlled inlet conditions at elevated temperatures.

Overall, the experimental results show good agreement with the numerical model predictions. The observed trends with respect to inlet and operating conditions are consistent with those discussed in the previous chapters, confirming the reliability of the modeling approach.

Table 8.6. Experimental measurements obtained under ambient humidity conditions.

ID	$T_{TI,a}$ °C	$\varphi_{TI,a}$ %	$T_{AN,i}$ °C	$v_{AN,i}$ m/s	$T_{TC,i}$ °C	$T_{TC,o}$ °C	$T_{AN,o}$ °C	$v_{AN,o}$ m/s
L1	21.3	35.9	21.8	3.64	21.2	9.9	16.2	2.27
L2	21.6	32.1	21.6	5.48	21.6	19.4	19.0	4.96
L3	21.5	31.9	21.6	6.81	21.6	19.3	19.3	6.15
L4	21.6	32.1	21.8	4.36	21.7	14.7	17.8	3.38
L5	21.5	31.9	21.7	6.25	21.7	19.3	19.4	5.64
L6	22.7	31.6	21.7	4.83	21.9	19.6	19.5	4.45
L7	22.5	32.2	22.1	3.23	22.0	19.4	19.9	2.94
L8	22.5	32.2	22.2	4.13	22.1	19.6	19.9	3.80
L9	22.2	33.9	22.3	3.48	22.2	9.8	16.4	2.13
L10	22.3	33.5	22.6	2.93	22.4	15.2	18.8	2.30
L11	21.5	31.9	23.5	6.95	23.4	20.8	19.8	6.31
L12	21.5	31.9	23.7	5.16	23.5	16.1	18.5	4.03
L13	21.6	32.1	23.9	6.20	23.7	21.0	20.4	5.65
L14	21.6	32.1	23.9	5.53	23.9	21.0	19.9	4.93
L15	21.3	32.8	23.8	4.95	23.9	16.3	18.2	3.89
L16	21.6	32.8	24.5	4.40	24.6	16.0	18.6	3.39
L17	21.4	36.5	25.7	7.18	25.9	21.6	20.6	6.18
L18	21.6	32.1	26.2	6.32	25.9	22.7	21.5	5.65
L19	21.6	32.1	27.8	5.54	26.6	23.2	21.1	4.97
L20	22.7	31.6	26.5	4.56	26.6	23.4	21.3	4.16
L21	22.2	33.9	27.3	3.52	27.0	10.5	16.7	2.13
L22	21.5	31.9	28.0	5.18	27.3	17.7	19.8	4.06
L23	22.5	32.2	27.3	4.10	27.4	23.9	22.2	3.77
L24	21.6	32.1	27.9	5.51	27.8	24.0	21.7	4.96
L25	21.5	31.9	27.7	6.91	27.8	24.2	21.6	6.33
L26	21.6	32.7	28.1	4.40	28.0	17.2	19.1	3.38
L27	22.5	32.2	28.3	3.24	28.7	24.6	22.1	2.95
L28	21.6	32.7	30.0	4.43	28.9	18.0	19.5	3.39
L29	21.2	34.5	30.7	3.70	29.1	11.2	17.1	2.27
L30	22.2	33.9	30.3	3.57	29.1	11.1	16.9	2.13
L31	22.3	33.5	29.1	2.96	29.7	17.3	20.0	2.30
L32	21.3	32.8	31.8	5.09	30.0	18.6	19.6	3.90
L33	21.6	32.1	29.8	6.23	30.1	25.7	23.0	5.65
L34	21.6	32.1	31.9	5.57	31.4	26.8	23.3	4.98
L35	*21.5*	*31.9*	*31.9*	*7.05*	*31.9*	*27.3*	*23.4*	*6.35*

ID	$T_{TI,a}$ °C	$\varphi_{TI,a}$ %	$T_{AN,i}$ °C	$v_{AN,i}$ m/s	$T_{TC,i}$ °C	$T_{TC,o}$ °C	$T_{AN,o}$ °C	$v_{AN,o}$ m/s
L36	21.6	32.7	32.9	4.50	32.0	18.7	19.7	3.40
L37	22.7	31.6	34.1	4.65	32.5	27.8	23.8	4.20
L38	21.5	31.9	34.4	6.06	33.8	24.4	22.9	5.06
L39	21.3	36.0	32.3	8.51	34.0	30.1	24.9	7.85
L40	21.6	32.1	34.6	6.35	34.5	28.8	24.6	5.64
L41	22.7	31.6	36.2	4.07	34.7	28.8	24.2	3.61
L42	21.5	31.9	35.2	7.10	34.9	29.3	24.6	6.35
L43	22.4	32.7	36.9	3.31	35.0	28.7	24.4	2.95
L44	21.5	31.9	35.9	5.30	35.4	20.3	21.6	4.06
L45	21.3	32.8	36.8	5.08	35.4	20.6	20.9	3.90
L46	21.6	32.1	37.8	6.30	37.5	30.7	25.6	5.56
L47	21.6	32.1	39.5	5.63	38.8	31.4	25.7	4.96
L48	21.2	34.5	41.0	3.76	40.6	12.7	17.7	2.27

Table 8.7. Experimental measurements obtained under increased humidity conditions.

ID	$T_{TI,i}$ °C	$\varphi_{TI,i}$ %	$T_{AN,i}$ °C	$v_{AN,i}$ m/s	$T_{TC,i}$ °C	$T_{TC,o}$ °C	$T_{AN,o}$ °C	$v_{AN,o}$ m/s
H1	18.5	55.0	16.8	3.94	17.4	12.5	17.4	2.64
H2	18.0	57.4	17.4	4.97	17.6	14.3	18.0	3.92
H3	18.2	57.0	17.4	3.65	17.7	12.2	18.4	2.32
H4	17.9	59.3	17.8	6.57	17.7	16.4	18.7	5.91
H5	19.8	67.5	20.3	6.61	20.4	19.0	19.6	5.92
H6	23.8	55.0	22.5	3.43	22.2	15.1	18.8	2.12
H7	26.8	50.0	25.6	6.59	26.2	23.5	22.5	5.83
H8	28.2	57.0	29.1	4.02	27.5	20.3	21.5	2.66
H9	31.9	52.0	29.1	3.73	28.1	20.3	21.8	2.33
H10	31.7	52.0	29.5	3.45	28.3	20.4	21.6	2.14
H11	33.8	45.2	32.0	4.11	30.4	20.6	22.0	2.72
H12	36.8	48.0	37.7	4.13	33.1	23.5	23.6	2.73

Table 8.8. Derived parameters for tests conducted under ambient humidity conditions.

ID	$\omega_{d,i}$	$\dot{m}_{da,d}$	r_m	Re_d
	kg_v/kg_{da}	kg/s	$-$	$-$
L1	0.0056	0.0269	0.365	163
L2	0.0051	0.0405	0.087	246
L3	0.0051	0.0503	0.090	306
L4	0.0051	0.0322	0.214	196
L5	0.0051	0.0462	0.091	281
L6	0.0054	0.0357	0.072	217
L7	0.0054	0.0238	0.083	145
L8	0.0054	0.0304	0.073	185
L9	0.0056	0.0256	0.377	156
L10	0.0056	0.0216	0.206	131
L11	0.0051	0.051	0.081	310
L12	0.0051	0.0379	0.205	230
L13	0.0051	0.0455	0.078	276
L14	0.0051	0.0405	0.096	246
L15	0.0051	0.0363	0.199	221
L16	0.0052	0.0322	0.214	196
L17	0.0058	0.0523	0.124	99
L18	0.0051	0.046	0.092	279
L19	0.0051	0.0401	0.082	244
L20	0.0054	0.0331	0.072	201
L21	0.0056	0.0255	0.374	155
L22	0.0051	0.0375	0.194	228
L23	0.0054	0.0297	0.065	181
L24	0.0051	0.0399	0.081	242
L25	0.0051	0.05	0.065	304
L26	0.0052	0.0318	0.208	193
L27	0.0054	0.0234	0.070	142
L28	0.0052	0.0318	0.207	193
L29	0.0054	0.0265	0.359	161
L30	0.0056	0.0256	0.377	156
L31	0.0056	0.0213	0.200	130
L32	0.0051	0.0363	0.202	221
L33	0.0051	0.0448	0.072	272
L34	0.0051	0.0398	0.080	242
L35	0.0051	0.0503	0.073	306

ID	$\omega_{d,i}$	$\dot{m}_{da,d}$	r_m	Re_d
	kg_v/kg_{da}	kg/s	$-$	$-$
L36	0.0052	0.032	0.210	195
L37	0.0054	0.0329	0.065	200
L38	0.0051	0.0429	0.133	261
L39	0.0056	0.0606	0.055	115
L40	0.0051	0.0449	0.082	273
L41	0.0054	0.0286	0.077	174
L42	0.0051	0.0501	0.074	305
L43	0.0055	0.0232	0.071	141
L44	0.0051	0.0373	0.197	227
L45	0.0051	0.0357	0.191	217
L46	0.0051	0.0441	0.081	268
L47	0.0051	0.0392	0.078	238
L48	0.0054	0.0261	0.349	158

Table 8.9. Derived parameters for tests conducted under increased humidity conditions.

ID	$\omega_{d,i}$	$\dot{m}_{da,d}$	r_m	Re_d
	kg_v/kg_{da}	kg/s	$-$	$-$
H1	0.0073	0.0295	0.332	180
H2	0.0074	0.0371	0.213	226
H3	0.0074	0.0273	0.367	166
H4	0.0076	0.049	0.103	298
H5	0.0097	0.0487	0.102	297
H6	0.0101	0.0251	0.376	153
H7	0.011	0.0476	0.106	291
H8	0.0137	0.0286	0.322	175
H9	0.0155	0.0264	0.361	162
H10	0.0153	0.0244	0.365	150
H11	0.0149	0.0289	0.316	177
H12	0.0188	0.0283	0.308	174

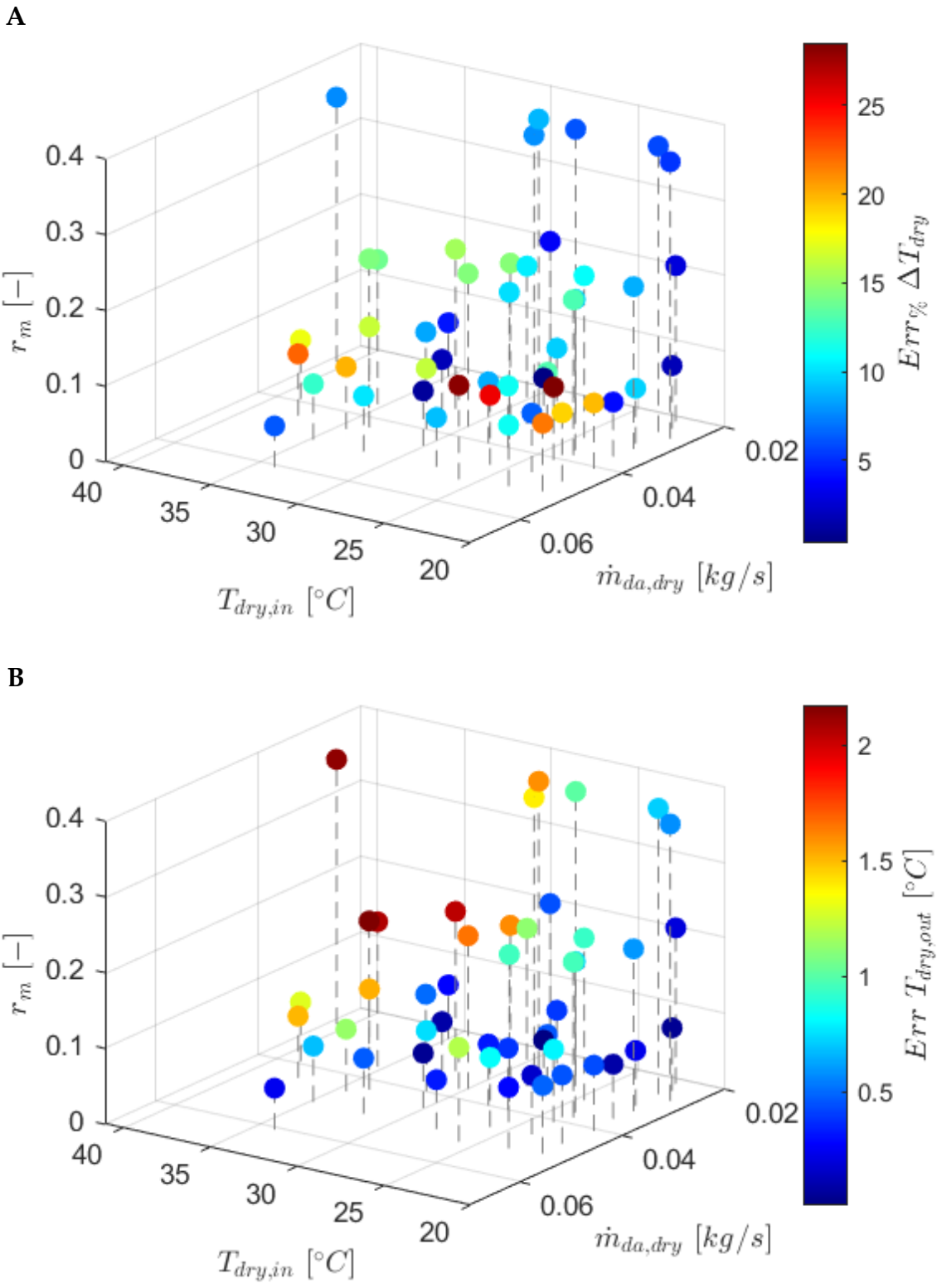

Figure 8.5. Relative error in dry channel temperature drop (A) and absolute error in dry channel outlet temperature (B) for tests conducted under ambient humidity conditions.

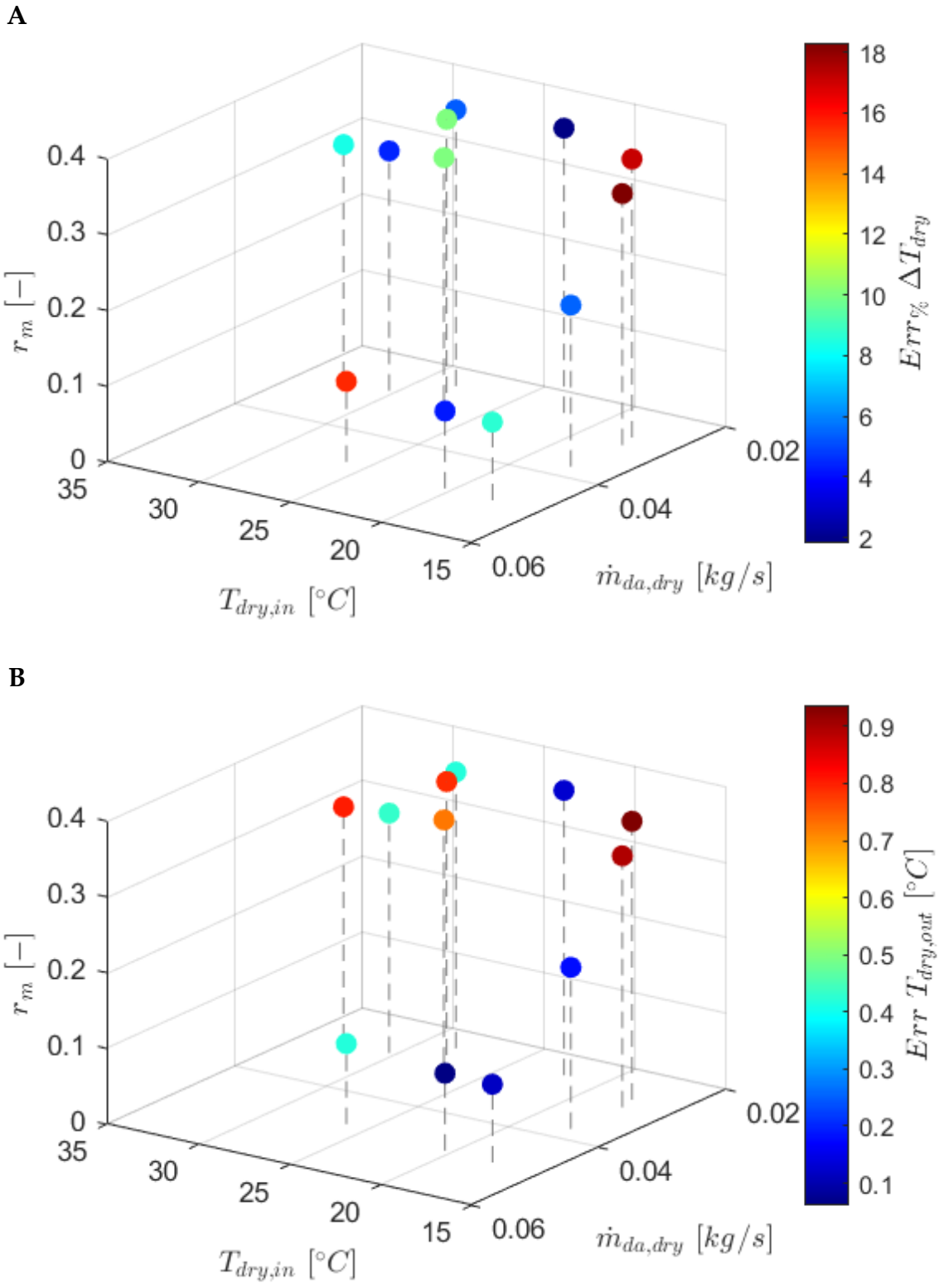

Figure 8.6. Relative error in dry channel temperature drop (A) and absolute error in dry channel outlet temperature (B) for tests conducted under increased humidity conditions.

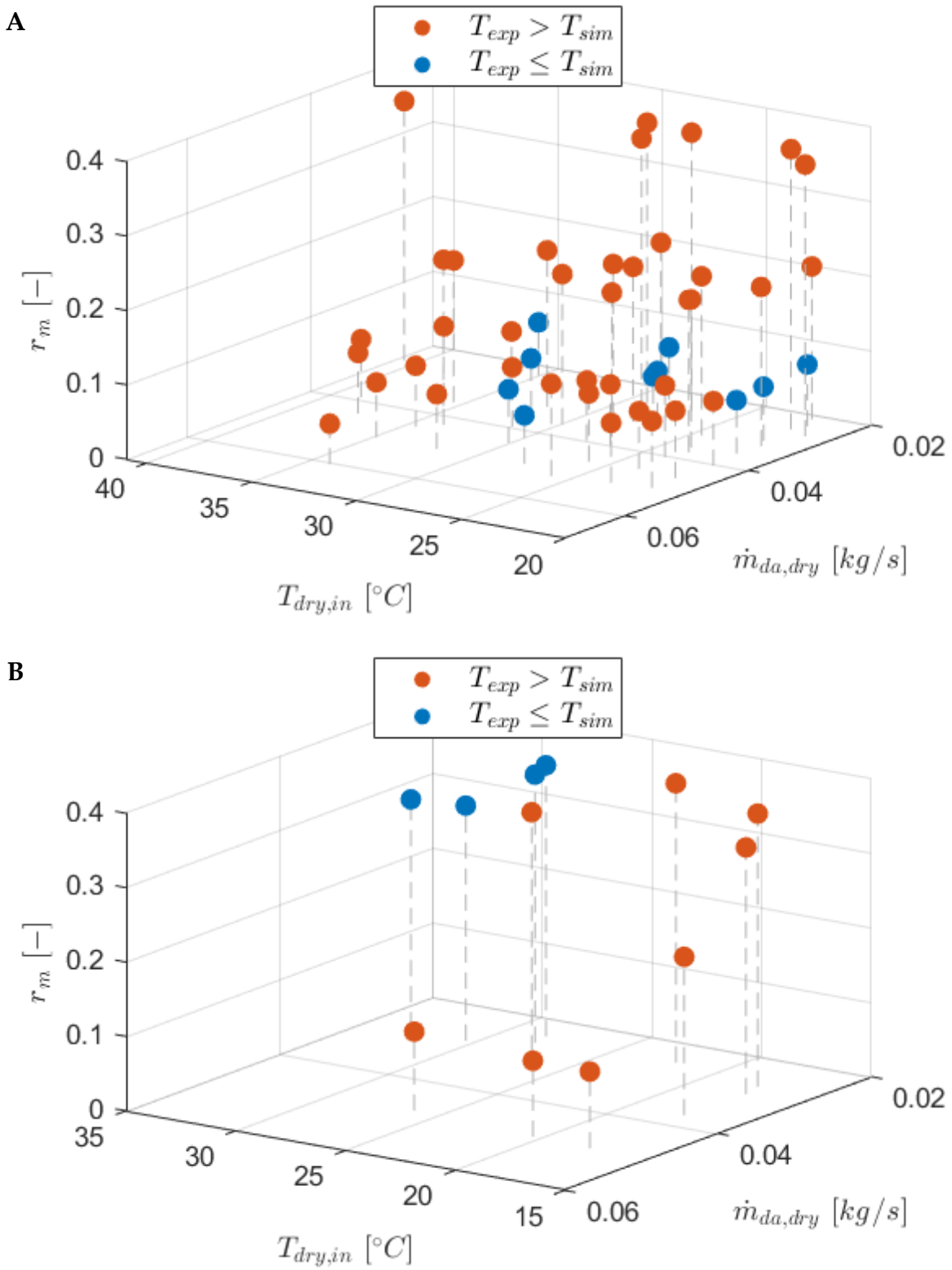

Figure 8.7. Distribution of model overestimation and underestimation with respect to experimental results under ambient humidity conditions (A) and increased humidity conditions (B).

9. Application of the M-cycle to building cooling scenarios

As introduced at the beginning of this work, building conditioning accounts for a significant share of global energy consumption, following a steadily increasing trend that, under current conditions, does not appear likely to decline. This growth is primarily attributable to the expansion of built surfaces and the consequent rise in energy demand. HVAC systems, once considered a luxury solution only a few decades ago, are now widely adopted [111]; therefore, it has become essential to focus research and development efforts on new technologies and alternative solutions capable of ensuring more efficient energy use.

Occupant well-being represents a primary objective in building design; however, it depends on multiple factors such as thermal, acoustic, and visual conditions, that are often partially conflicting with one another [112]. The factors defining Indoor Environmental Quality (IEQ) include indoor air quality and ventilation, thermal comfort, lighting, noise and acoustics, as well as spatial layout and view quality [113]. In recent years, driven also by growing political and regulatory interest, research on thermal comfort and indoor environmental well-being has intensified significantly. These studies have demonstrated that ensuring good indoor air quality affects not only occupant comfort and long-term health but also plays a decisive role in productivity in office buildings and learning performance in educational facilities [114].

Environments characterized by high occupant density are particularly critical, as IEQ factors tend to manifest more acutely. In such contexts, indoor air quality can deteriorate rapidly in the absence of adequate ventilation and air treatment strategies, which must simultaneously ensure the maintenance of thermally comfortable

conditions. This must be achieved while minimizing associated energy and economic costs.

Schools and offices are among the most densely occupied environments, where individuals spend a substantial portion of their daily time. Office workers and teachers are among the groups most frequently reporting acute symptoms such as eye, nasal, and skin irritation, headaches, fatigue, and respiratory difficulties [115]. Common building-related complaints include allergies, sore throat, irritated nose or sinuses, combined mucous membrane symptoms, chest tightness, and wheezing [116], [117]. These nonspecific respiratory symptoms, irritations, and general fatigue associated with the indoor environment are commonly referred to as sick building syndrome (SBS). The primary causes of SBS are attributed to elevated levels of CO_2, volatile organic compounds (VOCs), formaldehyde, particulate matter, and bioaerosol contaminants in indoor environments [118].

Statistically significant dose–response relationships have also been identified between CO_2 and particulate matter (PM) concentrations and the onset of symptoms attributable to SBS or allergic manifestations [116], [117]. However, the specific role of CO_2 remains a subject of debate within the scientific literature. Several studies suggest that CO_2 does not have a direct causal relationship with SBS symptoms but rather serves as a proxy indicator for the presence of other indoor air pollutants responsible for the observed effects [116]. This interpretation is supported by experimental studies in which CO_2 levels were manipulated using different approaches, such as direct CO_2 injection or reduced ventilation rates. Comparative results show that these two methods produce different effects, highlighting that reduced ventilation simultaneously increases concentrations of other indoor air contaminants [119]. More recent analyses have nevertheless proposed the possibility of a direct causal relationship between exposure to elevated CO_2 levels and impaired cognitive function. In particular, two main mechanisms have been hypothesized: on the one hand,

physiological and psychological responses associated with CO_2 accumulation in the body; on the other, potential changes in cerebral blood flow or reduced oxygen availability at the cerebral level [120]. These hypotheses are further supported by studies on brain activity, which indicate that increased CO_2 exposure induces changes in neuronal activity associated with alertness and cognitive processing, particularly during prolonged exposures (>10 minutes) or while performing mental tasks [121].

Beyond health implications, poor indoor air quality has been widely associated with reduced cognitive performance, attention, and occupant productivity, which are critical factors in schools and offices. It has been demonstrated that, during complex task execution, CO_2 concentrations between 1000 and 1500 ppm are already sufficient to cause a marked decline in cognitive performance. This deterioration tends to intensify proportionally with increased exposure duration, with particularly evident negative effects beyond 120 minutes [119]. Despite this evidence, numerous studies conducted in school environments have shown that average and median values of maximum CO_2 concentrations exceed 1000 ppm in all analyzed cases, often exceeding 2000 ppm. Maximum recorded concentrations generally range between approximately 3000 and 6000 ppm. Similarly, most mean and median time-averaged concentrations exceed 1000 ppm, with peak values ranging from 1400 to 5200 ppm [122]. Literature reviews consistently conclude that ventilation rates significantly affect students' performance [123]. In particular, it has been observed that the maximum indoor CO_2 concentration at which no health risk has been identified appears to be around 900 ppm [124]. Although subject to considerable uncertainty, minimum ventilation thresholds have also been identified, below which worse outcomes related to health and perceived air quality are observed [125]. Based on these findings, regulatory reference limits have been established; however, it has been shown that air exchange rates in schools, offices, hospitals, and residential buildings are below the minimum values required by reference standards in the vast majority of cases [126].

In parallel, numerous studies have shown that indoor thermal conditions are also closely correlated with human performance and productivity. In particular, temperature variations of only a few degrees Celsius can influence performance in activities such as typing, factory work, signal recognition, response time, learning performance, reading speed and reading comprehension, multiplication speed, and word memory [115]. It has also been observed that as children's perception of indoor air quality worsens, the range of acceptable temperatures shifts toward lower values; in other words, the fresher the air is perceived, the higher the tolerable operative temperature [127]. Finally, a clear relationship between performance and ventilation rate has been identified: increased ventilation reduces CO_2 levels and enhances perceived air freshness, while lowering classroom temperature is associated with improved performance in terms of speed [128]. Thermal discomfort, whether due to cold or heat, can distract attention and reduce motivation, negatively affecting cognitive abilities. These conditions may also have direct health impacts, including headaches and difficulty concentrating, as discussed within the concept of psychological and physiological adaptability zones [129]. In light of this experimental and observational evidence, relationships have been developed linking student performance to temperature, relative humidity, and CO_2 concentration [130], as well as to synthetic comfort indices such as Predicted Mean Vote (PMV) [131].

From the analyzed literature review, a clear need emerges to focus on air treatment systems. At present, the dominant technology for building conditioning relies on traditional vapor-compression HVAC systems. These systems control temperature and humidity simultaneously by cooling air below the dew point through cooling coils, deliberately generating condensation to achieve dehumidification. Although thermally effective, such configurations present intrinsic hygienic issues. Condensate water accumulates in drainage pans and, if not properly removed, creates humid, stagnant environments conducive to microbial growth.

Epidemiological studies have shown that the maintenance and physical characteristics of these systems are directly correlated with occupant health. Symptoms such as wheezing, coughing, and shortness of breath have been found to be strongly associated with specific environmental risks related to HVAC systems, including "residue in drain pans", "debris in air intakes", and "standing water near the intake". Asthmatic individuals are more sensitive to such exposures [132]. The severity of inadequate system management is underscored by data on Legionnaires' disease, with an estimated 2,700–6,000 cases annually, often with severe clinical outcomes. Even in the absence of acute illnesses, the economic impact is substantial: an estimated 35–60 million workers report weekly nonspecific building-related symptoms (irritations, headaches, fatigue), generating total costs estimated between 7 and 75 billion USD per year in the United States alone due to healthcare expenses and productivity losses [133].

In response to these hygienic and economic challenges, there is an urgent need to explore alternative technologies capable of ensuring thermal comfort while minimizing both health risks and energy consumption. In this context, evaporative cooling systems represent a promising solution, particularly for high-occupancy environments such as schools and offices. Unlike traditional vapor-compression systems, which often rely on air recirculation to optimize costs, evaporative systems inherently operate in a once-through mode, continuously supplying large volumes of outdoor air. Moreover, in the context of preventing airborne transmissible diseases such as COVID-19, air flow management has assumed a central role. International guidelines, when analyzed comparatively, converge on the need to avoid air recirculation, recommending operation in once-through mode (100% outdoor air) and extending ventilation system operating hours to ensure effective contaminant dilution both before and after space occupancy [134]. However, it is not sufficient to consider air renewal rates alone; airflow distribution dynamics are also critical. Mixing

ventilation systems, typical of conventional air conditioning, can generate turbulence that disperses infected droplets throughout the space, extending infection risk beyond standard safety distances. In contrast, displacement ventilation strategies, often associated with evaporative or natural systems, tend to direct contaminated air toward exhaust paths in a more laminar and targeted manner, reducing aerosol concentrations in the occupants' breathing zone and minimizing cross-infection risk [135].

From a thermal comfort perspective, the application of evaporative systems requires an adaptive approach. Although these systems may result in slightly higher indoor air temperatures compared to mechanical chillers, comfort is maintained through increased air velocity. Field studies indicate that air movement can compensate for higher operative temperatures, extending the thermal comfort zone in accordance with adaptive models, particularly in warm climates where occupants tolerate higher air velocities than those prescribed by conventional standards [114]. Finally, energy efficiency remains a fundamental pillar of this technology. The introduction of large volumes of outdoor air, essential for indoor air quality, would entail prohibitive costs with traditional chillers. Evaporative systems, by contrast, exploit the latent heat of evaporation to condition air with dramatically lower electrical consumption, estimated to be up to 85% lower than that of conventional split air-conditioning units [136], thereby making the maintenance of a healthy and productive indoor environment sustainable.

9.1. Environmental data

The accurate definition of meteorological boundary conditions is a prerequisite for reliable dynamic energy simulations, as the thermal performance of the building envelope and HVAC systems is governed by their instantaneous interaction with the outdoor environment. To this end, Typical Meteorological Year (TMYx) files, derived from long-term historical records and provided by the OneBuilding database, were

adopted. This methodology synthesizes local climate variability by concatenating statistically representative months, ensuring robust and reproducible simulation inputs.

For the temperate–humid European context, the climate of Bologna (Italy) was selected, using data from the Guglielmo Marconi Airport weather station. Specifically, the month of June (sourced from the year 2018) was selected to represent operating conditions for school buildings. The hourly evolution of dry-bulb temperature, relative humidity, global horizontal irradiance (GHI), and direct normal irradiance (DNI) for this period is illustrated in Figure 9.1. The climatic data for Bologna highlight a typical temperate–humid continental behavior. June (Figure 9.1) is characterized by progressively increasing outdoor air temperatures over the month. Daytime peaks reach approximately $34\ °C$ during the warmest days, although typical daily maxima are more frequently in the range of $28 - 32\ °C$. Relative humidity exhibits a clear inverse correlation with temperature, consistent with diurnal heating cycles, decreasing during the warmest hours. During this month, relative humidity drops to minimum values close to $30 - 32\ \%$ during the driest conditions but rises rapidly during nighttime hours, often exceeding $70 - 80\ \%$. Solar radiation represents an additional significant component of the summer thermal load in Bologna. In addition, GHI frequently reaches peak values between 850 and 900 W/m^2 during midday hours, confirming the relevance of solar gains even in a temperate–humid context. The radiation profiles highlight high atmospheric transmissivity, with recurrent DNI values exceeding $800\ W/m^2$and peak values approaching $820 - 900\ W/m^2$ under clear-sky conditions. These strong direct solar gains contribute to indoor overheating, particularly in buildings with extensive glazed surfaces. This reinforces the need for an integrated approach combining solar control, ventilation, and cooling strategies.

To assess the performance of evaporative cooling under different boundary conditions, the analysis was extended to an arid desert climate represented by Riyadh (Saudi

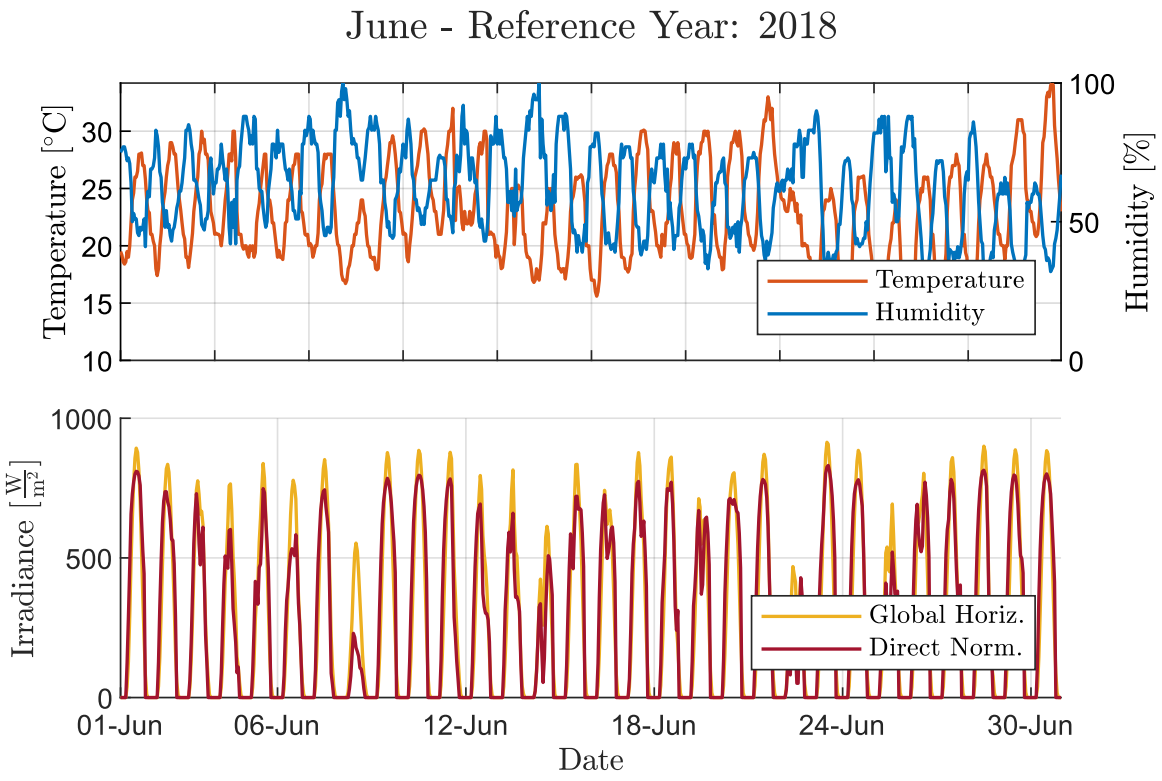

Figure 9.1. Hourly profiles of dry bulb temperature, relative humidity, and solar irradiance (Global and Direct) for the city of Bologna. Data refers to the months of June.

Arabia) again in the month of June. The hourly trends of temperature, humidity, GHI, and DNI for Riyadh are shown in Figure 9.2. The climatic data depict a highly severe thermal regime, with mean daytime temperatures generally ranging between 38 and 42 $°C$ and peak values reaching approximately 44 $°C$ during the hottest hours. Nighttime temperatures remain consistently high, typically above 30 $°C$, indicating limited nocturnal cooling potential. However, the defining characteristic of this climate is the low moisture content. Relative humidity remains consistently low throughout the day, with typical daytime values between 3 % and 10 %, while nighttime and early morning values can increase to $20 - 30$ %, with occasional peaks exceeding 40 %. In addition, solar radiation levels are extremely high, with GHI frequently exceeding 1000 W/m^2 and DNI values approaching $900 - 950\ W/m^2$ during peak hours, indicating predominantly clear-sky conditions and high atmospheric transmissivity.

This combination of high dry-bulb temperatures and low specific humidity results in low dew-point temperatures for most of the daytime period, creating highly favorable thermodynamic conditions for evaporative cooling technologies.

The comparison between the temperate–humid climate of Bologna and the arid desert climate of Riyadh suggests the critical role of ambient thermo-hygrometric conditions on the thermodynamic feasibility of evaporative cooling. While in the city of Bologna the applicability of the M-cycle is limited by relatively high humidity levels, especially during nighttime and morning hours, the extremely dry climate of Riyadh is clearly favorable, at least in terms of achieving significant reductions in electrical energy consumption through the use of evaporative systems.

9.2. Numerical modeling of a representative educational case study

The numerical analysis focuses on a representative educational environment modeled using the EnergyPlus simulation engine. The case study consists of a single-story school building. The simulation domain is restricted to a single thermal zone representing a standard classroom. This modeling framework provides a basis for evaluating alternative cooling technologies under realistic operating conditions.

The modeled classroom has a rectangular floor plan ($8.25\ m \times 6.00\ m$), resulting in a gross floor area of $49.5\ m^2$ and a net ceiling height of $3.50\ m$. To simulate a typical classroom located within a larger building complex, the three internal walls are modeled with adiabatic boundary conditions; this assumption implies that adjacent spaces (e.g., corridors or other classrooms) are conditioned to the same temperature, thus eliminating heat transfer across these surfaces. Consequently, the thermal balance of the zone is driven by dynamic interactions through the external envelope components, ground coupling, and internal heat gains.

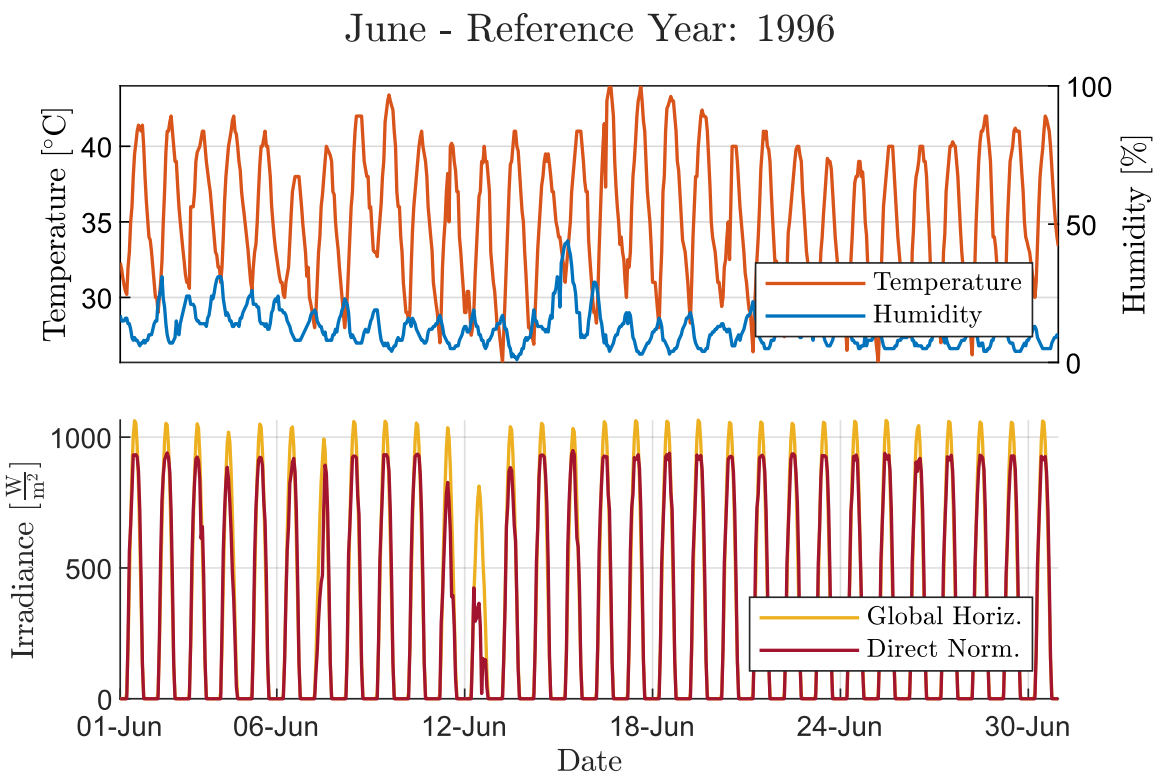

Figure 9.2. Hourly profiles of dry bulb temperature, relative humidity, and solar irradiance (Global and Direct) for the city of Riyadh. Data refers to the months of June.

The building envelope characteristics are defined to represent a heavy masonry structure, typical of the existing school building stock in the Mediterranean area. A significant portion of these educational facilities was constructed before the implementation of stringent energy efficiency regulations. As a result, these buildings exhibit high thermal mass but poor insulation levels. Consequently, these buildings often suffer from inadequate indoor comfort and high operational costs. To address these critical issues, this study not only evaluates the baseline performance but also investigates a cost-effective energy retrofit scenario. The retrofit strategy focuses on internal insulation solutions, selected to minimize installation complexity and costs, a primary constraint for public school renovations. Accordingly, rock wool was selected as the insulation material due to its widespread availability and favorable balance between thermal performance and cost.

The thermophysical properties of the existing materials and the stratigraphy of the baseline components are derived from the Italian standard UNI/TR 11552:2014 [137]. For the retrofit scenario, material properties were selected in accordance with UNI 10351:2021 [138] for rock wool and UNI EN ISO 10456:2008 [139] for gypsum plasterboards.

The vertical opaque envelope consists of solid brick masonry layers with varying thickness. The external walls are composed of a two-wythe solid brick layer (25 cm), whereas the internal partition walls are modeled as single-wythe masonry (12 cm). The surface finishes are defined according to their exposure. Consequently, the external walls feature an asymmetric stratigraphy with a high-density lime-cement plaster on the exterior façade and a standard lime-gypsum plaster on the room side. In contrast, the internal partitions are finished symmetrically with lime-gypsum plaster on both faces. All plaster layers are modeled with a thickness of 2 cm. In the retrofit configuration, the external walls are upgraded by installing an internal insulation layer consisting of 6 cm of rock wool, finished with a 1.25 cm light gypsum plasterboard. This solution is designed to increase the thermal resistance of the envelope while preserving a low-impact and cost-effective retrofit strategy, suitable for application in existing school buildings.

The ground floor is modeled as a slab-on-grade. Heat transfer between the floor slab and the ground is computed using the Kiva auxiliary module, which performs a two-dimensional finite-difference calculation to resolve heat flux through the foundation and surrounding soil. The floor stratigraphy is defined from the soil interface upwards by a 20 cm gravel drainage layer, followed by a 10 cm layer of concrete serving as the sub-base. The finishing sequence consists of a 3 cm cement mortar screed and ceramic tiles. The foundation geometry includes an external perimeter foundation wall, extending 0.5 m below the slab and rising 0.2 m above the ground level. The foundation wall is applied only along the external building perimeter, while the

remaining floor boundaries correspond to adiabatic internal interfaces. The soil thermal properties adopted for the simulation are listed in Table 9.1.

The roof structure consists of a mixed hollow-brick and reinforced concrete slab. The UNI/TR 11552:2014 standard provides the thermal resistance of the structural slab (R_{strslb}) for the composite block (hollow bricks with concrete joists, reinforced concrete topping and cement mortar) but does not detail the conductivity of the individual sub-layers required for dynamic modeling. To address this limitation, a single equivalent homogeneous material layer was defined for use in EnergyPlus.

Table 9.1. Thermo-physical properties of the soil used in the Kiva foundation model.

Parameter	***Value***	***Unit***
Thermal conductivity	1.5	$W/(m\,K)$
Density	1800	kg/m^3
Specific heat capacity	1600	$J/(kg\,K)$
Surface roughness	0.03	
Solar absorptivity	0.7	
Thermal absorptivity	0.9	

The properties of this equivalent layer were calculated to match the total thermal resistance provided by the standard ($R_{strslb} = 0.33\ (m^2\,K)/W$) and the weighted average of the density and heat capacity of the components. First, the total thickness of the structural slab t_{strslb} is calculated by summing the thickness of the constituent layers

$$t_{strslb} = t_1 + t_2 + t_3 \qquad 9.1$$

where indices 1, 2, and 3 represent the hollow bricks with concrete joists, the reinforced concrete topping, and the cement mortar, respectively. Subsequently, using the total thermal resistance provided by the standard, the equivalent thermal conductivity k_{eq} is determined

$$k_{eq} = \frac{t_{strslb}}{R_{strslb}} \quad 9.2$$

The equivalent density ρ_{eq} is calculated by summing the mass per unit area of each layer of the structural slab and dividing by the total thickness

$$\rho_{eq} = \frac{\sum_{i=1}^{N_{strslb}} \rho_i \, t_i}{t_{strslb}} \quad 9.3$$

Regarding the specific heat capacity (c_{eq}), since the values for all three cementitious and ceramic components are approximately equal ($c = 1000\, J/(kg\, K)$), the weighted average is assumed to be $1000\, J/(kg\, K)$.

The input values derived from the standard and the calculated equivalent properties are listed in Table 9.2.

The roof assembly is completed externally by a protective screed and a bituminous waterproofing membrane. Internally, a false ceiling consisting of an air gap and acoustic tiles are applied. The thermal resistance of the air gap is derived from UNI EN ISO 6946:2018 [140]. Assuming a cavity height of 0.3 m to facilitate inspection, the thermal resistance for downward heat flow (summer condition) is set to 0.23 $(m^2\, K)/W$. For the insulated retrofit scenario, the roof stratigraphy is enhanced by installing a layer of rock wool within the plenum, positioned directly above the acoustic tiles.

The detailed stratigraphy of the opaque envelope is summarized from Table 9.3 to Table 9.6.

The external façade is heavily glazed to maximize natural daylight utilization, which is a critical requirement for educational spaces. Accordingly, no external shading devices or overhangs are applied in the reference model. The fenestration system consists of three large windows, each measuring 2.0 m in width and 2.2 m in height, resulting in a total glazed area of 13.2 m^2 and a window-to-wall ratio (WWR) of

Table 9.2. Equivalent structural slab layer properties.

Layer	$\boldsymbol{t}$ m	$\boldsymbol{k}$ $\frac{W}{m\,K}$	$\boldsymbol{\rho}$ $\frac{kg}{m^3}$	$\boldsymbol{c}$ $\frac{J}{kg\,K}$	$\boldsymbol{R}$ $\frac{m^2\,K}{W}$
Hollow bricks with concrete joists	0.16		900	1000	0.33
Reinforced concrete topping	0.04		2400	1000	
Cement mortar	0.02		2000	1000	
Equivalent slab	0.22	0.67	1273	1000	

Table 9.3. Stratigraphy and thermal properties of the external walls.

Layer		$\boldsymbol{t}$ m	$\boldsymbol{k}$ $\frac{W}{m\,K}$	$\boldsymbol{\rho}$ $\frac{kg}{m^3}$	$\boldsymbol{c}$ $\frac{J}{kg\,K}$
External Plaster		0.02	0.9	1800	1000
Solid Brick		0.25	0.72	1800	1000
Internal Plaster		0.02	0.7	1400	1000
Rock wool	*i.c.*	0.06	0.033	50	1000
Gypsum plasterboard	*i.c.*	0.0125	0.25	900	1000

i.c.: Insulated case.

Table 9.4. Stratigraphy and thermal properties of the internal walls.

Layer	$\boldsymbol{t}$ m	$\boldsymbol{k}$ $\frac{W}{m\,K}$	$\boldsymbol{\rho}$ $\frac{kg}{m^3}$	$\boldsymbol{c}$ $\frac{J}{kg\,K}$
Internal Plaster	0.02	0.7	1400	1000
Solid Brick	0.12	0.72	1800	1000
Internal Plaster	0.02	0.7	1400	1000

Table 9.5. Stratigraphy and thermal properties of the roof.

Layer		$\boldsymbol{t}$ m	$\boldsymbol{k}$ $\frac{W}{m\,K}$	$\boldsymbol{\rho}$ $\frac{kg}{m^3}$	$\boldsymbol{c}$ $\frac{J}{kg\,K}$
Bituminous membrane		0.01	0.17	1200	1000
Ordinary cement screed		0.02	1.06	2000	1000
Equivalent structural slab		0.22	0.67	1273	1000
Air gap	$R_{th} = 0.23$	0.3	–	–	–
Rock wool	*i.c.*	0.06	0.033	50	1000
Acoustic tiles		0.0125	0.25	900	1000

i.c.: Insulated case.

Table 9.6. Stratigraphy and thermal properties of the floor.

Layer	$\boldsymbol{t}$ m	$\boldsymbol{k}$ $\frac{W}{m\,K}$	$\boldsymbol{\rho}$ $\frac{kg}{m^3}$	$\boldsymbol{c}$ $\frac{J}{kg\,K}$
Gravel	0.2	1.2	1700	1000
Ordinary concrete	0.1	1.16	2000	1000
Cement mortar	0.03	1.4	2000	670
Ceramic Tiles	0.015	1.47	1700	710

Table 9.7. Characteristics of transparent components.

Layer	$\boldsymbol{t}$ m	$\boldsymbol{\tau_{sol}}$ –	$\boldsymbol{\rho_{sol,front}}$ –	$\boldsymbol{\rho_{sol,back}}$ –	$\boldsymbol{k}$ $\frac{W}{m\,K}$
Glass	0.006	0.765	0.073	0.073	1
Air gap	0.01	–	–	–	–*
Glass	0.006	0.765	0.073	0.073	1

**The thermal behavior of the air gap is calculated dynamically by EnergyPlus based on gas properties (Air) and cavity geometry.*

approximately 46% for the external façade. The glazing system is a double-pane clear glass unit with an air gap. The optical and thermal characteristics of the window system are reported in Table 9.7. To assess the impact of solar gains and the robustness of the cooling strategy under varying exposure conditions, the building orientation is treated as a parametric variable. Simulations are performed by rotating the building to expose the glazed façade from East to West, considering East (90°), South (180°), South-West (225°), and West (270°) orientations.

Internal heat gains are defined based on typical occupancy densities and lighting loads. Following the recommendations of UNI CEN/TR 16798-2:2020 [141], the classroom occupancy density is set to 0.5 $people/m^2$, corresponding to a class of 24 people. According to UNI EN 16798-1:2019 [142], the minimum hygienic air-change flow rate ($\dot{V}_{hygienic}$) was calculated using the standard design ventilation equation

$$\dot{V}_{hygienic} = n\,\dot{V}_p + A_R\,\dot{V}_B \qquad 9.4$$

where n is the number of occupants, $\dot{V}_p$ is the ventilation rate for occupancy per person, A_R is the floor area, and $\dot{V}_B$ is the ventilation rate for building emissions. The calculation considers a medium expectation level (Category II) for air quality, which is considered the norm for healthy environments in the absence of vulnerable occupants. Furthermore, the design values for non-adapted persons were adopted as required for non-residential buildings, combined with a Low-Polluting Building classification for the material emissions.

The metabolic load of the occupants is set to 120 $W/person$ in accordance with UNI EN ISO 8996:2021 [143] for sedentary activity. The latent heat gain is subsequently calculated via the Fanger model also used in the standard regulation [144], while a constant fraction of 0.3 is assumed for the radiant component of the sensible heat. The remaining portion represents the convective heat exchange with the room air. The occupancy schedule follows a standard school profile with presence between 08:00 and

13:00 for morning hours and between 14:00 and 16:00 for afternoon sessions. The mechanical ventilation system is active during lesson hours consistent with the occupancy schedule. Additionally, a 10-minute pre-ventilation period is implemented before the occupants' arrival in both the morning and afternoon. This strategy aims to dilute indoor CO_2 levels and condition the room temperature prior to the start of lessons. The pre-ventilation airflow rate is set to the minimum design flow rate calculated for the occupied hours. An additional one-hour post-ventilation period is implemented after the afternoon schedule. During this phase, the system operates at the minimum design airflow rate with $r_m = 0$ (i.e., mechanical ventilation without cooling) to dilute pollutants accumulated during the day. Internal loads associated with lighting are modeled with a power density of $7.64\,W/m^2$. A summary of the internal gains and the parameters utilized for the calculation of the minimum ventilation rate is provided in Table 9.8.

9.3. Analysis of indoor cooling performance

In this study, the M-cycle HMX is analyzed as a standalone space cooling system. Under this configuration, the most appropriate performance indicator for evaluating the heat removed from the conditioned space is the $VICC$, introduced in equation 3.98.

The relevance of this distinction with respect to the VCC defined in equation 3.97 becomes evident under high inlet air temperature conditions. In such cases, the temperature drop across the HMX may be significant. This leads to high values of conventional cooling capacity metrics. However, if the supply air temperature remains higher than the indoor temperature, the ventilation process contributes to heating the space rather than cooling it, despite the apparently high performance of the device. Consequently, performance indicators based exclusively on the inlet–outlet temperature difference of the HMX may be misleading when evaluating the actual space cooling demand.

Table 9.8. Occupancy and ventilation design parameters.

Parameter	***Value***	***Unit***
A_R	49.5	m^2
n_{occ}	0.5	$person/m^2$
$\dot{Q}_{occ}$	120	$W/person$
q_p	7	$l/(s\ person)$
q_B	0.7	$l/(s\ m^2)$

The space cooling power is evaluated through a sensible energy balance, assuming constant specific heat capacity. In a rigorous room energy balance, the enthalpy difference should be evaluated using the indoor air humidity ratio. This parameter depends on internal moisture generation and cannot be uniquely determined for each operating condition. For this reason, in the present analysis the specific humidity of the air exiting the HMX is used instead. Since this value is systematically lower than the indoor humidity ratio in occupied spaces, the resulting $VICC$ estimation is conservative and therefore suitable for comparative performance assessment. The indoor air temperature is fixed at 26 $°C$, in accordance with typical comfort criteria during the cooling season. The $VICC$ is thus formulated by considering the sensible heat exchange between the supplied air and the indoor environment. The formulation accounts for the fraction of dry air effectively contributing to space cooling.

Figure 9.3, Figure 9.4, Figure 9.5 and Figure 9.6 report the $VICC$ obtained using the HMX geometric specifications listed in Table 6.5, as a function of inlet velocity and recirculation ratio, under the four representative inlet conditions previously introduced and summarized in Table 6.4. For the inlet condition at 25 $°C$ and 6 g/kg (Figure 9.3-A and Figure 9.5-A), the shape of the $VICC$ curves is similar to that of the VCC. This occurs because the inlet air temperature is already lower than the considered room temperature, so that the temperature differences used to compute both metrics follow similar trends. Figure 9.3 and Figure 9.4 show the variation of $VICC$ with

recirculation ratio for different inlet velocities. For all inlet conditions in which the inlet air temperature exceeds the room temperature, the curves lose the characteristic bell-shaped trend observed for the VCC. At 40 °C and 6 g_v/kg_{da} (Figure 9.3-B), strongly negative $VICC$ values are observed at low recirculation ratios, because the outlet air temperature remains significantly higher than the room temperature. This is followed by a pronounced increase in $VICC$ with increasing recirculation ratio for all inlet velocities. Beyond a certain recirculation level, all curves reach positive $VICC$ values and attain a maximum. A subsequent decrease is then observed, which becomes increasingly pronounced as the inlet velocity decreases. Unlike the VCC curves, those corresponding to lower inlet velocities intersect those at higher velocities. As a result, the maximum $VICC$ under this inlet condition is not achieved at the highest inlet velocity. At 30 °C and 18 g_v/kg_{da} (Figure 9.4-A), similar qualitative trends are observed. However, the initial increase in $VICC$ with r_m is less pronounced. Moreover, the curves corresponding to higher inlet velocities may fail to reach positive $VICC$ values or to attain a maximum within the high-recirculation region. This behavior further highlights the performance degradation of the system under high inlet humidity conditions.

Finally, under combined high-temperature and high-humidity inlet conditions (At 40 °C and 18 g_v/kg_{da}, Figure 9.4-B), positive $VICC$ values are attained only in a very limited number of operating conditions. In this case, the $VICC$ curves exhibit a predominantly monotonic increase with recirculation ratio, even at low inlet velocities.

Figure 9.5 and Figure 9.6 present the $VICC$ as a function of inlet dry channel velocity for different values of the recirculation ratio. For inlet conditions characterized by temperatures higher than the room temperature, the $VICC$ curves no longer exhibit the uniformly increasing monotonic behavior observed for the VCC. Under the inlet conditions at 40 °C and 6 g_v/kg_{da} (Figure 9.5-B) and at 30 °C and 18 g_v/kg_{da} (Figure 9.6-A), bell-shaped trends are observed for selected recirculation ratios, with the

presence of a distinct maximum as the inlet velocity increases. In these cases, $VICC$ values remain negative only at very low recirculation ratios. As the recirculation ratio increases, the curves transition to positive values and exhibit a maximum, followed by a progressive decrease at higher inlet velocities. These non-monotonic behaviors become less pronounced as the inlet humidity increases, indicating a reduced sensitivity of the space cooling performance to airflow rate under more humid conditions. In the combined high-temperature and high-humidity inlet condition ($40\,°C$ and $18\ g_v/kg_{da}$, Figure 9.6-B), the $VICC$ trends differ markedly. For low recirculation ratios, the curves are strongly monotonically decreasing, with increasingly negative $VICC$ values as the inlet velocity rises. As the recirculation ratio increases, the curves progressively flatten or become weakly non-monotonic, showing slightly positive $VICC$ values at low inlet velocities, followed by a gradual decline as the velocity increases.

Figure 9.7 and Figure 9.8 show the $VICC$ as a function of inlet dry-bulb temperature and specific humidity for different dry-air mass flow rates and recirculation ratios. For all operating conditions, the shape of the iso-$VICC$ curves resembles that of the iso-$T_{d,o}$ curves discussed in chapter 7.7. The $VICC = 0$ contour coincides with the condition corresponding to an outlet dry-channel temperature of $26\,°C$ ($T_{set-point}$). The $VICC$ values are strongly dependent on the processed dry-air mass flow rate: at a fixed recirculation ratio, increasing the mass flow rate leads to a marked increase in $VICC$ over the entire temperature–humidity domain. At a given mass flow rate, increasing the recirculation ratio enhances $VICC$ up to intermediate values of recirculation, while a further increase causes a reduction in performance due to the decrease in supply air flow. Finally, the highest $VICC$ values are consistently observed at low inlet temperatures and low specific humidities. Although such conditions may correspond to situations in which cooling demand is limited, this behavior can be relevant for

applications involving moderate ambient temperatures combined with high internal heat generation.

The analysis presented so far has shown that, depending on the inlet air temperature and humidity, the $VICC$ is maximized at different combinations of inlet dry-air mass flow rate and recirculation ratio. Consequently, the next step of the analysis consists in identifying, for each inlet condition, the maximum attainable $VICC$ within the explored domain of operating parameters. Figure 9.9 reports the maximum $VICC$ achievable for each $T_{d,i}$-$\omega_{d,i}$ condition considering all the investigated values of inlet mass flow rate and recirculation ratio. At low inlet temperatures and specific humidities, the iso-$VICC_{max}$ curves are more inclined, whereas they progressively flatten as both temperature and humidity increase. The iso-$VICC_{max} = 0$ contour identifies the inlet conditions for which it is not possible to reduce the dry channel outlet temperature below the indoor set-point of 26 °C. This line is nearly horizontal and approaches the iso-$\omega_{d,i}$ curve corresponding to a dew-point temperature of 26 °C. Above this curve, the operation of a cooling system based solely on the M-cycle would result in a net sensible heat gain to the conditioned space.

Figure 9.10 provides additional insight by reporting, for each inlet condition, the values of inlet dry-air mass flow rate (Figure 9.10-A) and recirculation ratio (Figure 9.10-B) that maximize $VICC$. In the region close to saturation, starting from low inlet temperatures, the optimal condition corresponds to the maximum investigated mass flow rate without recirculation, resulting in a full outdoor air ventilation mode. Moving away from saturation, the optimal recirculation ratio increases progressively. Conversely, the optimal mass flow rate reaches its maximum at low temperatures and then progressively decreases.

Outside the near-saturation band, high inlet mass flow rates remain advantageous up to high temperatures, approximately 28 °C for very dry condition. Beyond this point, they rapidly decrease. The optimal recirculation ratio varies more gradually. It

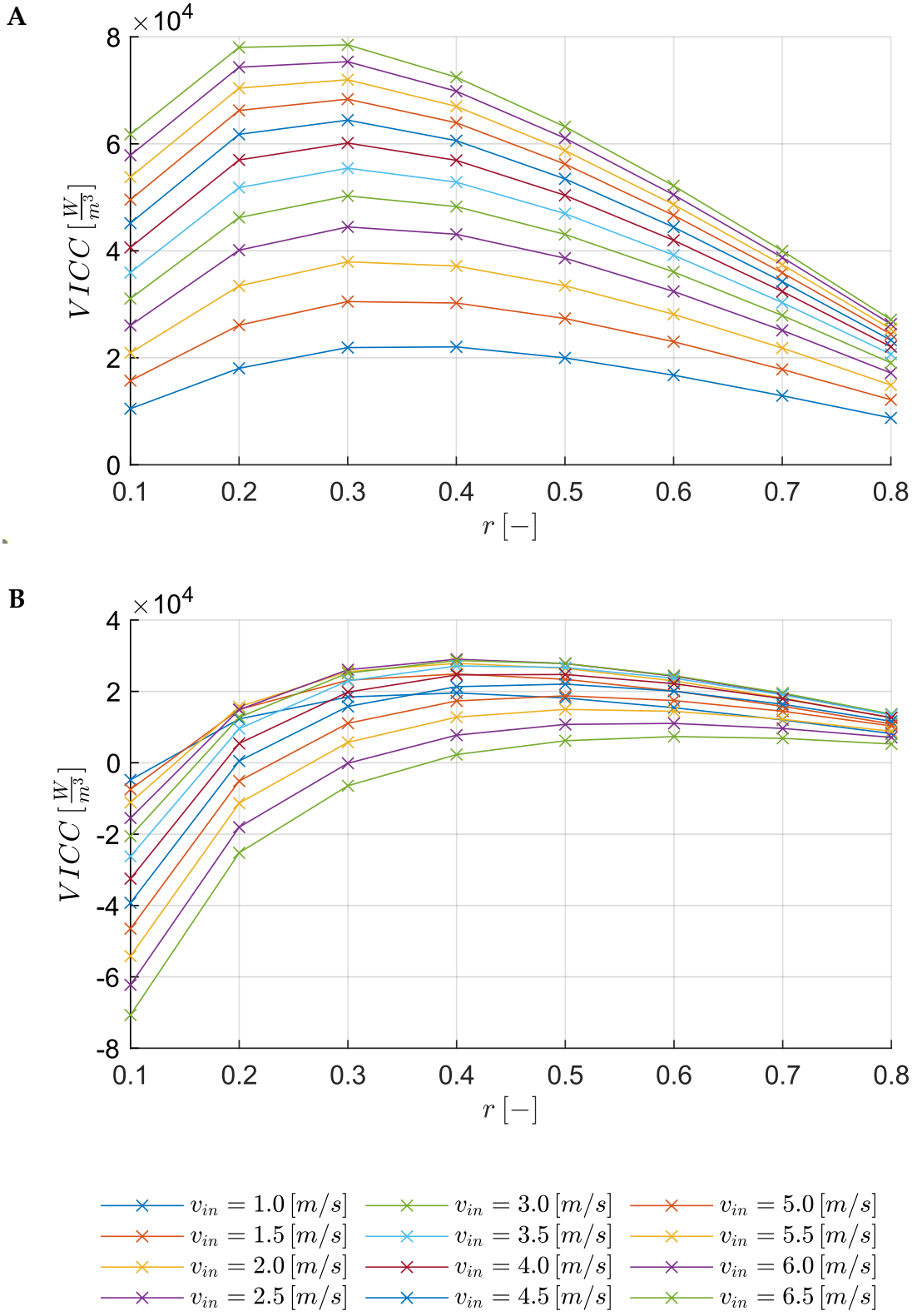

Figure 9.3. Volumetric Indoor Cooling Capacity as a function of the recirculation ratio for different inlet air velocities. Operating conditions: inlet specific humidity of 6 g_v/kg_{da} and inlet air temperatures of 25°C (A) and 40°C (B).

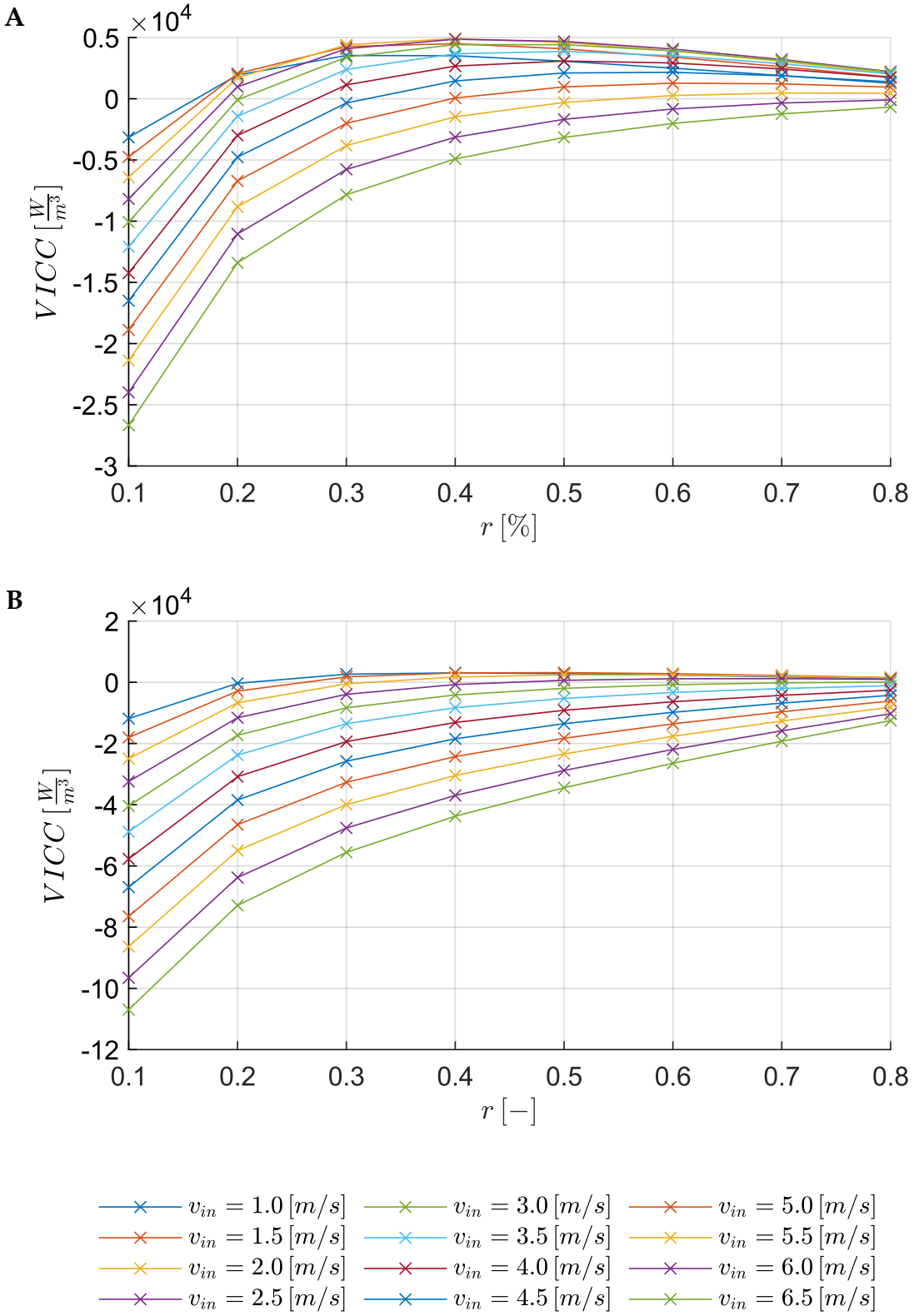

Figure 9.4. Volumetric Indoor Cooling Capacity as a function of the recirculation ratio for different inlet air velocities. Operating conditions: inlet specific humidity of 18 g_v/kg_{da} *and inlet air temperatures of* 30°C *(A) and* 40°C *(B).*

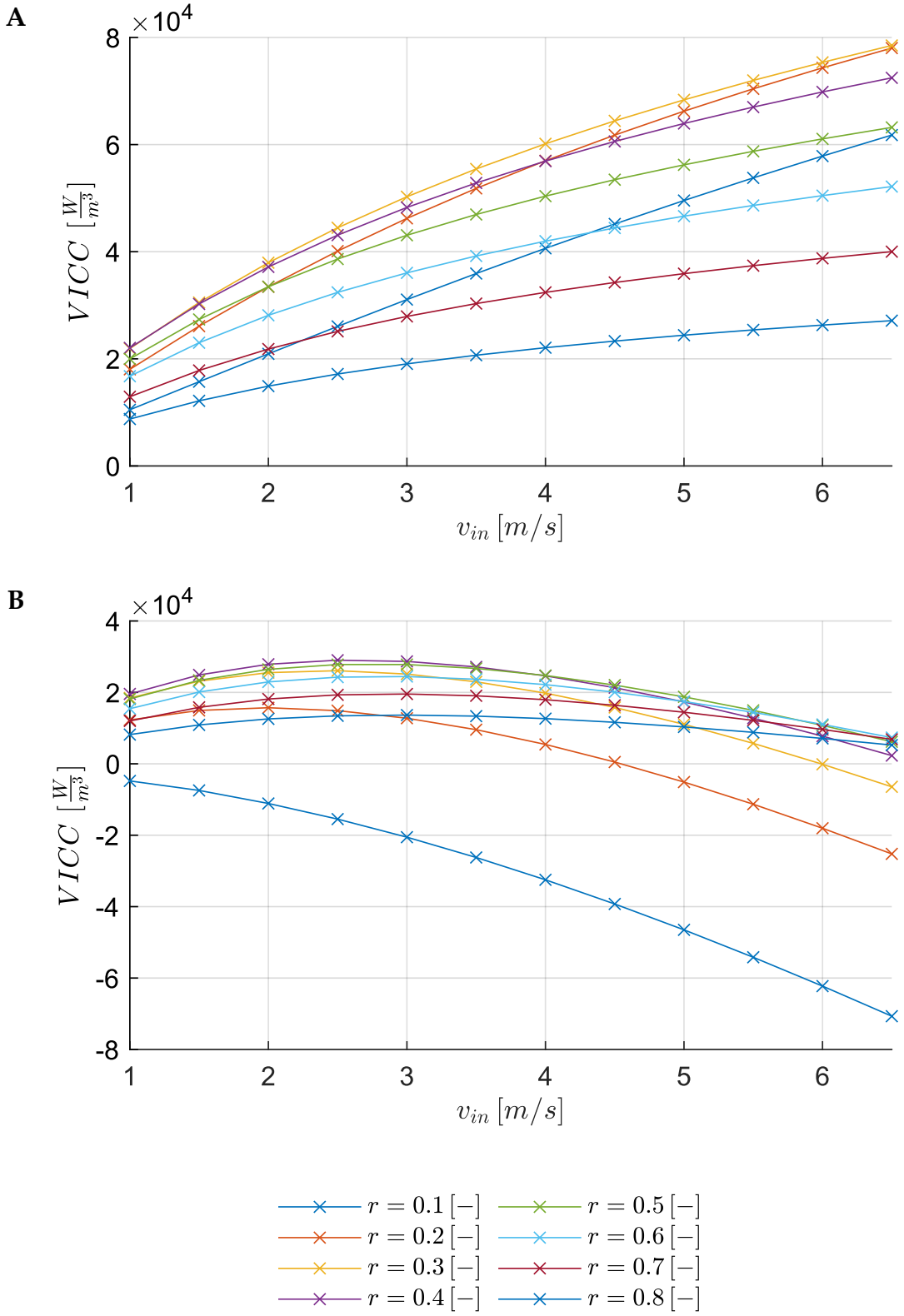

Figure 9.5. Volumetric Indoor Cooling Capacity as a function of inlet air velocity for different recirculation ratios. Operating conditions: inlet specific humidity of 6 g_v/kg_{da} *and inlet air temperatures of* 25°C *(A) and* 40°C *(B).*

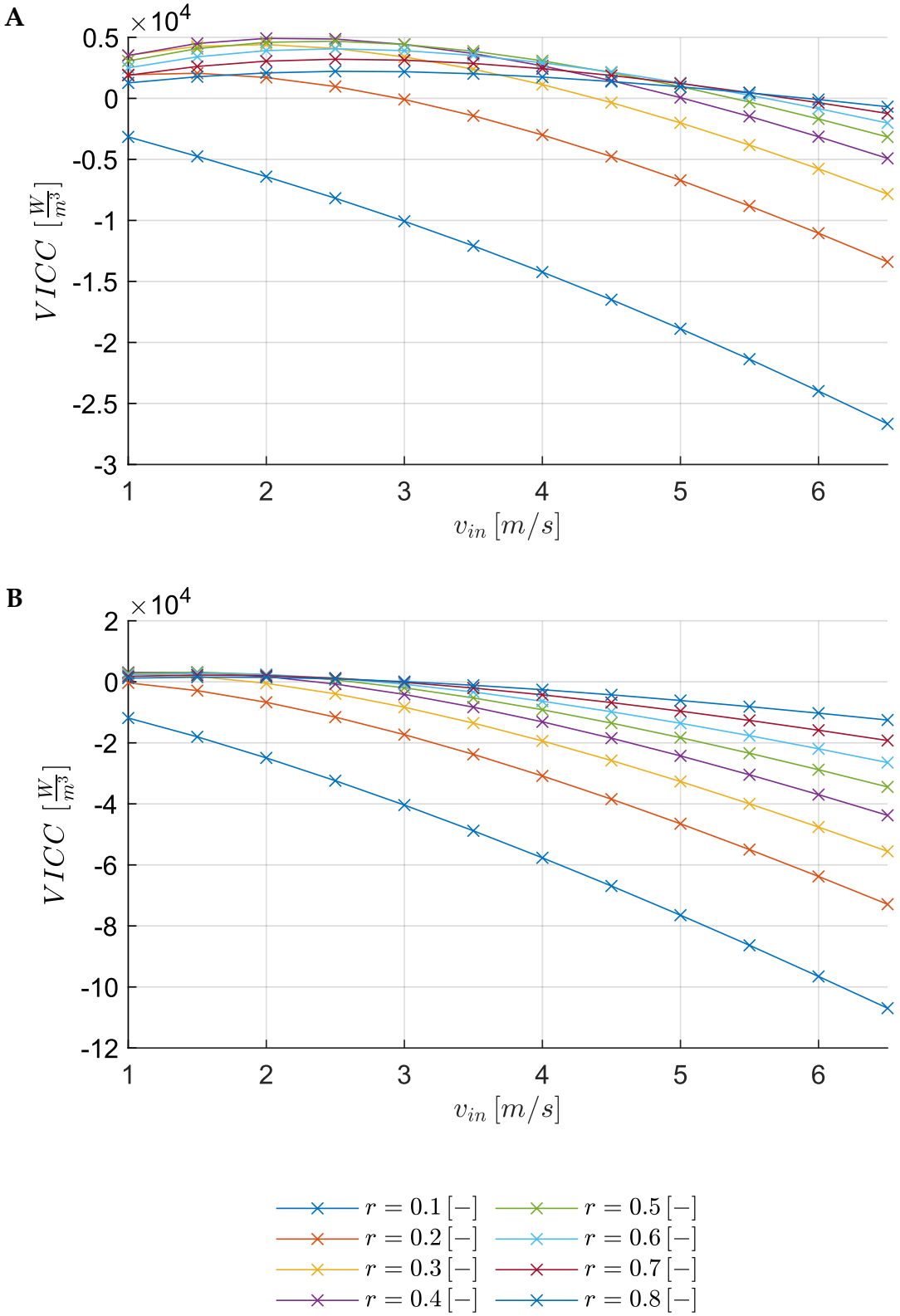

Figure 9.6. Volumetric Indoor Cooling Capacity as a function of inlet air velocity for different recirculation ratios. Operating conditions: inlet specific humidity of 18 g_v/kg_{da} *and inlet air temperatures of* 30°C *(A) and* 40°C *(B).*

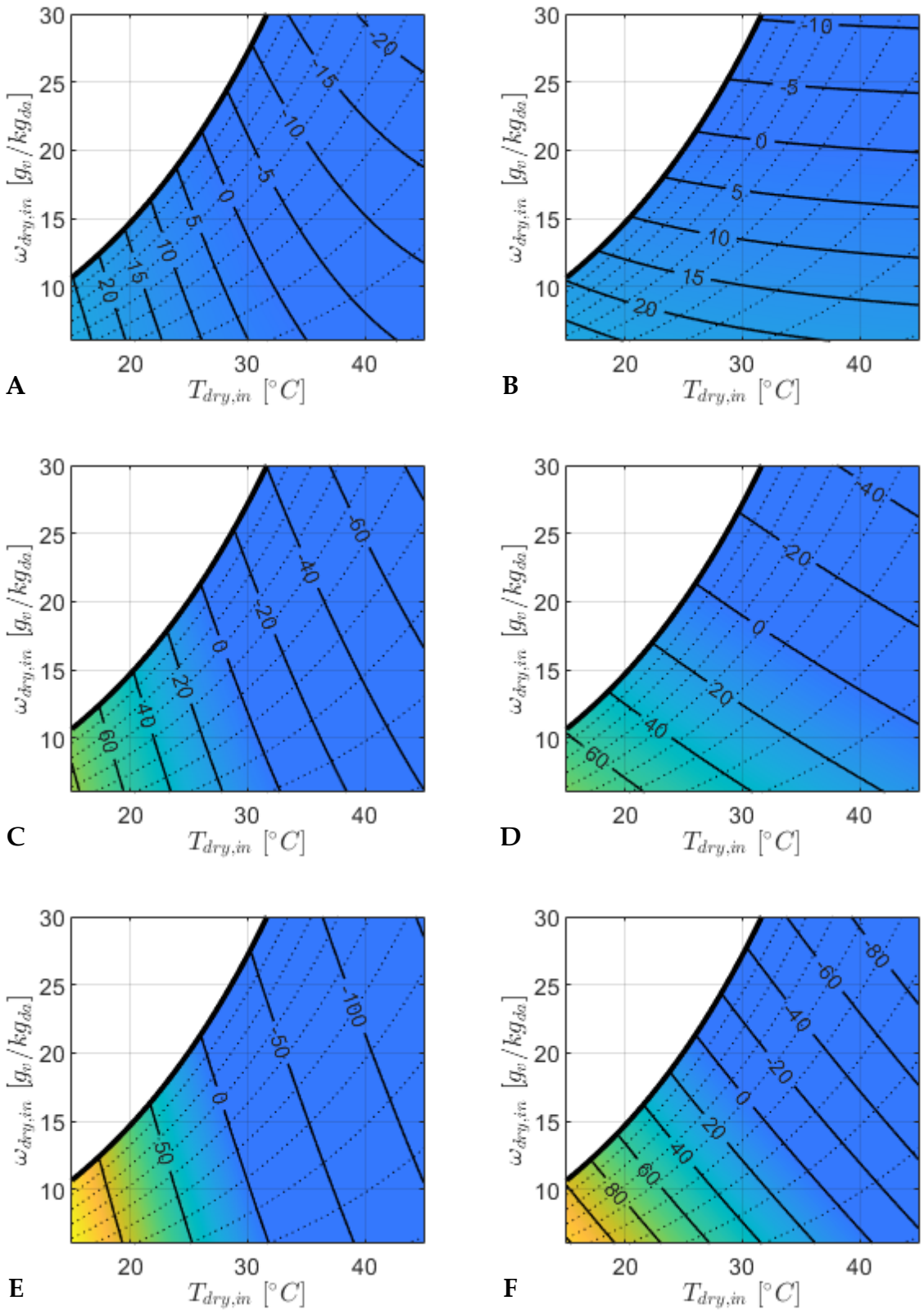

Figure 9.7. Volumetric Indoor Cooling Capacity $[kW/m^3]$ *as a function of inlet temperature* ($T_{d,i}$) *and specific humidity* ($\omega_{d,i}$). *Dry channel dry air mass flow rates* $\dot{m}_{da,d} = 0.1$ *(A, B),* 0.3 *(C, D),* 0.5 *(E, F)* kg/s. *Recirculation ratios* $r_m = 0.1$ *(A, C, E) and* $r_m = 0.3$ *(B, D, F).*

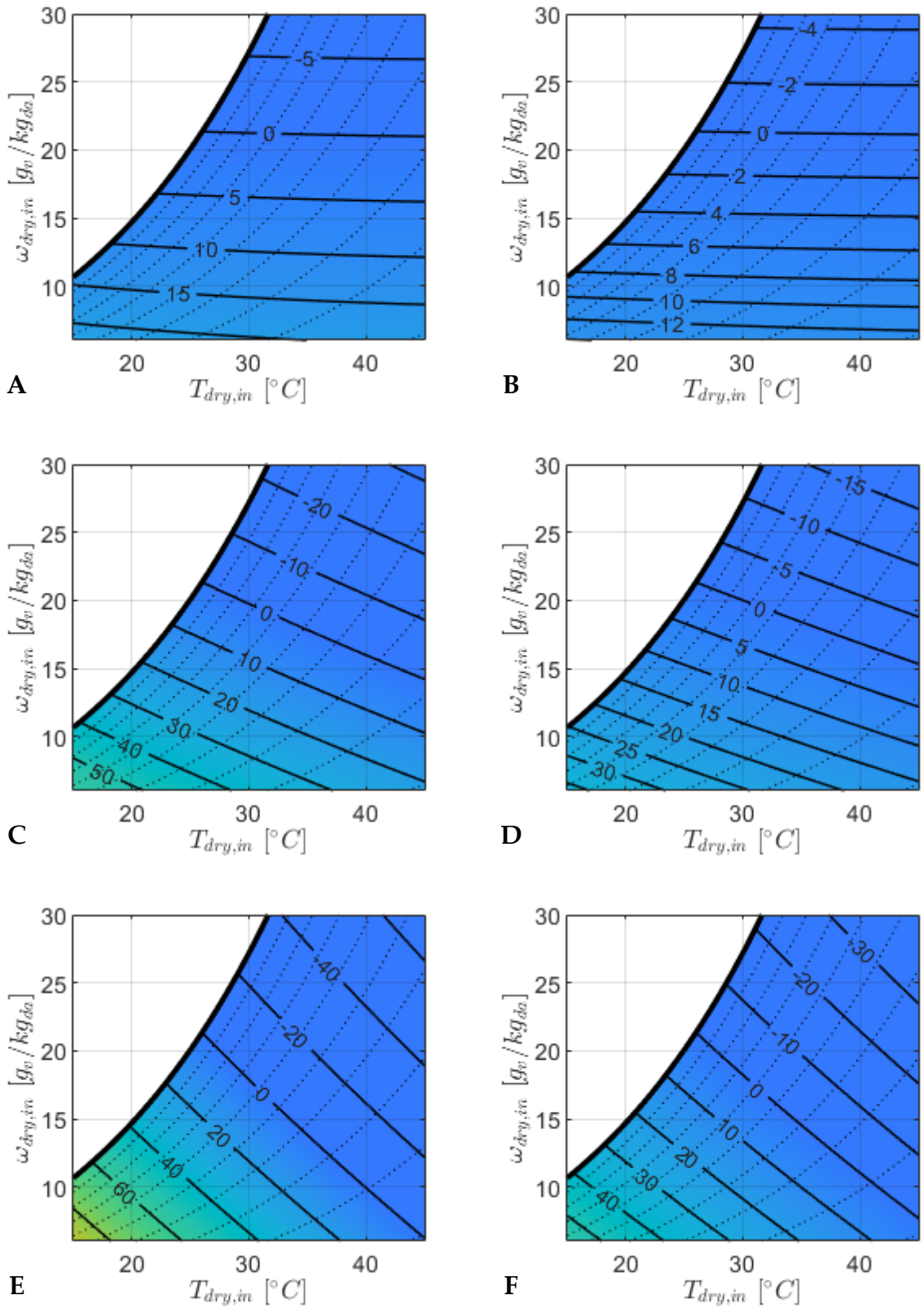

Figure 9.8. Volumetric Indoor Cooling Capacity $[kW/m^3]$ *as a function of inlet temperature* ($T_{d,i}$) *and specific humidity* ($\omega_{d,i}$). *Dry channel dry air mass flow rates* $\dot{m}_{da,d} = 0.1$ *(A, B),* 0.3 *(C, D),* 0.5 *(E, F)* kg/s. *Recirculation ratios* $r_m = 0.5$ *(A, C, E) and* $r_m = 0.7$ *(B, D, F).*

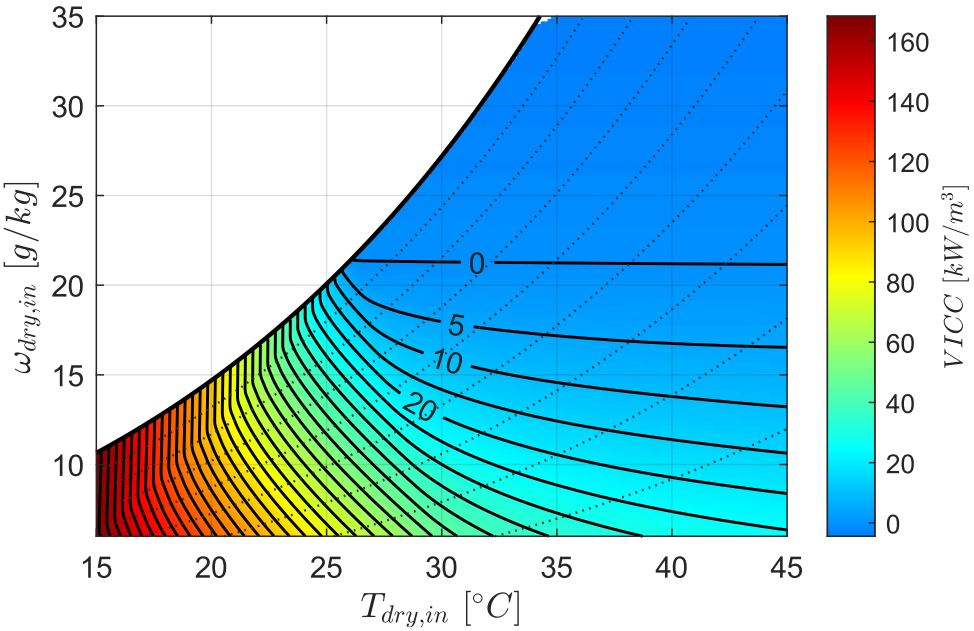

Figure 9.9. Maximum attainable Volumetric Indoor Cooling Capacity $VICC$ $[kW/m^3]$ within the investigated domain of inlet mass flow rate $\dot{m}_{da,in}$ and recirculation ratio r_m for different inlet conditions.

increases to $r_m = 0.5$ at high temperature and high humidity. A narrow region close to the iso-$VICC_{max} = 0$ contour is characterized by a sharp increase in the optimal recirculation ratio. Beyond this boundary, the entire domain exhibits optimal conditions at minimum inlet mass flow rate and maximum recirculation ratio. These operating points minimize the dry-channel outlet temperature among the analyzed configurations and therefore yield the least negative VICC values; however, since they still correspond to a net heat addition to the space, this region has limited practical relevance for cooling applications.

9.4. Energy efficiency ratio of the M-cycle cooling system

Assessing the overall energy performance of the standalone M-Cycle cooling system requires a comprehensive evaluation. This evaluation extends beyond the thermodynamic cooling capacity to include the electrical energy consumption of auxiliary components. In a standalone configuration, the fan power required to overcome hydraulic resistance represents the dominant contribution to electrical

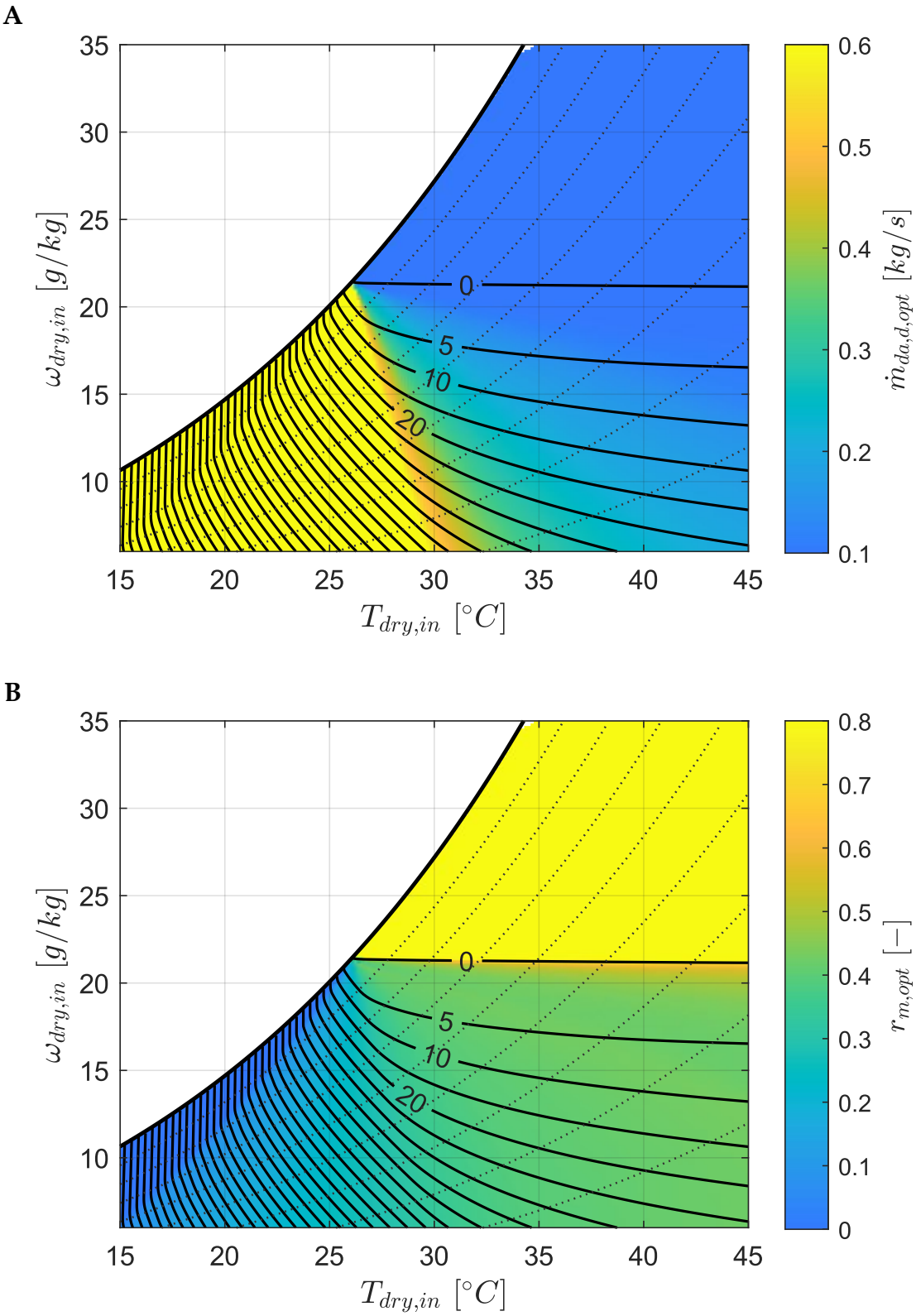

Figure 9.10. Optimal operating parameters plotted on the psychrometric chart to maximize the Volumetric Indoor Cooling Capacity VICC for each inlet condition: optimal inlet dry air mass flow rate $\dot{m}_{da,in}$ $[kg/s]$ *(A) and optimal recirculation ratio* r_m $[-]$ *(B).*

consumption. Consequently, a physically consistent estimation of the EER requires explicit modeling of the pressure drops along the air paths and the resulting mechanical work required from the ventilation system.

Pressure losses within the system are governed by both distributed and localized mechanisms. In addition to the losses within the HMX, pressure losses occur in the inlet and outlet ducts, geometric discontinuities, and flow splitting and mixing at the recirculation junction. For distributed losses, assuming fully developed laminar flow between parallel plates, the Darcy friction factor f can be expressed as a function of the Reynolds number

$$f = \frac{96}{Re} \tag{9.5}$$

This relation is widely adopted in the analysis of compact plate heat exchangers. The corresponding frictional pressure drop Δp_f over a channel of length L and hydraulic diameter D_h is then computed as

$$\Delta p_f = f \, \frac{L}{D_h} \frac{\rho \, v^2}{2} \tag{9.6}$$

where ρ is the air density and v is the mean flow velocity within the channel.

Localized pressure losses are estimated using conventional loss coefficients K, such that

$$\Delta p_{loc} = K \, \frac{\rho \, v^2}{2} \tag{9.7}$$

These occur in regions where the flow direction changes, velocity redistribution, and mixing phenomena are involved. These regions are modeled via the loss coefficients: $K_{in,d}$ for the system entrance, $K_{rec,d}$ for the straight-through supply stream, $K_{out,d}$ for the HMX exit and $K_{rec,w}$ for the diverted recirculated stream. While the primary

dissipation occurs in the diverted recirculated stream (wet channel inlet), the geometric discontinuity at the dry channel outlet induces a minor pressure drop also in the straight-through supply stream. Although secondary, this contribution is retained in the formulation to ensure a rigorous approach. Based on these considerations, the total pressure drop associated with the dry channel air path Δp_d is written as

$$\Delta p_d = \Delta p_{in,d} + \Delta p_{f,d} + \Delta p_{rec,d} + \Delta p_{out,d} \quad 9.8$$

Similarly, the total pressure drop associated with the wet-channel path Δp_w is expressed as

$$\Delta p_w = \Delta p_{rec,w} + \Delta p_{f,w} + \Delta p_{out,w} \quad 9.9$$

To determine the fan power requirements, the system is modeled assuming two distinct pressure loads. The supply air fan is positioned downstream of the conditioned space, acting in extraction to pull the air through the entire supply chain. This configuration ensures that any heat dissipated by the fan motor is rejected directly to the environment, avoiding unwanted thermal gains in the supply air. To sustain this flow, the fan must also overcome pressure losses in the filtration stage Δp_{filt}, in the supply ductwork Δp_{supply} delivering air to the room, and in the extraction path from the conditioned zone Δp_{extr}. To optimize efficiency, the filter is positioned exclusively on the supply branch, downstream of the recirculation split, so that it processes only the net airflow delivered to the room. Finally, the kinetic energy loss associated with the air release into the atmosphere is accounted for by a discharge term $\Delta p_{disch,dry}$. Accordingly, the total pressure rise required from the supply fan is

$$\Delta p_{fan,d} = \Delta p_d + \Delta p_{filt} + \Delta p_{supply} + \Delta p_{extr} + \Delta p_{disch,d} \quad 9.10$$

The working air for the wet channels originates from the dry channel outlet and subsequently traverses the wet channel path. Therefore, the fan responsible for the wet

channel stream must compensate for the cumulative pressure losses along the common section of the dry channels, the wet channel of the HMX, and the final discharge to the atmosphere $\Delta p_{disch,wet}$. The required pressure rise is given by

$$\Delta p_{fan,w} = \Delta p_{in,d} + \Delta p_{f,d} + \Delta p_{w} + \Delta p_{disch,w} \quad 9.11$$

The electrical power consumption for each fan is computed based on the respective volumetric flow rate $\dot{V}$ and total pressure rise

$$P_{el,fan,d} = \frac{\dot{V}_{fan,d}\, \Delta p_{fan,d}}{\eta_{fan,d}} \quad 9.12$$

$$P_{el,fan,w} = \frac{\dot{V}_{fan,w}\, \Delta p_{fan,w}}{\eta_{fan,w}} \quad 9.13$$

where η_{fan} denotes the overall fan efficiency, including electrical, mechanical, volumetric and fluid dynamic losses. The total electrical power demand of the ventilation system is the sum of these contributions

$$P_{el,tot} = P_{el,fan,d} + P_{el,fan,w} \quad 9.14$$

Finally, assuming the power consumption for water distribution is negligible compared to air handling, the EER of the M-Cycle cooling system is defined as the ratio between the useful Indoor Cooling Capacity delivered to the conditioned zone ICC (equivalent to the $VICC$ multiplied by the HMX volume) and the total electrical power demand $P_{el,tot}$

$$EER = \frac{ICC}{P_{el,tot}} \quad 9.15$$

This definition provides a comprehensive metric of system energy performance. It explicitly couples the useful cooling effect with the electric power required to sustain the airflow, enabling consistent comparison with conventional air-conditioning

technologies. The application of the fluid dynamic model and thermodynamic predictions enables the synthesis of system performance into a comprehensive operational map. This map correlates the independent control parameters, specifically the $\dot{m}_{da,d}$ and the r_m, with the system EER and ICC. These outputs serve as a fundamental decision-making tool, allowing for the identification of the M-Cycle system thermal potential while accounting for the operational constraints imposed by current regulations and the strategies required to maximize the EER. A crucial element for the practical validation of the system is the hygienic ventilation curve, represented on the plot as an impassable boundary based on the UNI EN 16798-1:2019 standards. This line defines the minimum outdoor air flow rate threshold required to guarantee adequate air change for both the occupants and the room volume. Consequently, any operating points with flow rates below this curve are considered non-permissible, restricting the operational space to only those configurations that simultaneously satisfy thermal comfort and indoor air quality requirements. The systematic analysis of these surfaces allows for the derivation of an optimization path, graphically depicted as a continuous line traversing the map. For any given thermal load required by the building, this path identifies the specific combination of flow rate and recirculation that minimizes the total electrical consumption of the fans. This optimal-point search algorithm ensures that the system consistently operates along the ridge of maximum EER compatible with the hygienic constraint, extending to the point of maximum possible ICC for the given boundary conditions. In this manner, system management evolves from a simple reactive control into a predictive strategy that dynamically adjusts the operating point to balance cooling demand with the reduction of energy losses. To visualize the principles, the performance evaluation is conducted through the generation of operational maps that illustrate the interplay between thermophysical parameters and regulatory constraints. Within these representations, the x-axis reports $\dot{m}_{da,d}$, while the y-axis indicates r_m. The background chromatic

gradient illustrates the EER field, highlighting the regions of peak electrical performance. Overlaid on this gradient, dashed black isolines denote the levels of ICC, expressed in kW. A further distinctive element is the magenta dash-dotted curve, which delimits the minimum hygienic ventilation requirement; this serves as an operational boundary, excluding all operating points that would fail to guarantee the necessary air exchange for the occupants. The synthesis of these data allows for the identification of the optimization path, represented by a continuous line that identifies the locus of operating points maximizing the EER for every specific ICC and boundary conditions. This path serves as a dynamic control guide: starting from the hygienic ventilation limit, it tracks the most efficient combination of $\dot{m}_{da,d}$ and r_m as the thermal load increases, effectively identifying the trajectory of optimum operating points that yields the highest EER across the entire power range of the system, up to its maximum ICC. The performance of the HMX is based on the neural network predictions described in the previous chapters; however, the results have been scaled to simulate an HMX composed of 200 dry channels rather than the 100 dry channels of the reference geometry. This scaling operation is feasible because, in a parallel channel system, the addition of modules with identical geometric does not alter the transfer phenomena or the outlet temperatures provided that the new dimensions are accounted for in the definition of the inlet flow rate. Instead, it allows changing the total processed flow rate and air velocity, allowing the system to meet the typical thermal loads of a building. To analyze the system behavior across different climatic scenarios, four cases with varying boundary conditions are presented. These scenarios first explore low specific humidity conditions, fixed at $6\ g_v/kg_{da}$, with outdoor air temperatures of 30 $°C$ and 40 $°C$, respectively (Figure 9.11). Subsequently, the analysis shifts to higher humidity scenarios of $13\ g_v/kg_{da}$, maintained at the same temperatures of 30 $°C$ and 40 $°C$ (Figure 9.12). For the ICC calculation in all cases, the return air temperature is assumed to be equal to the summer set-point of 26 $°C$, while

the humidity is assumed to be 11 g_v/kg_{da} for the dry cases and 18 g_v/kg_{da} for the humid cases. These comparisons demonstrate how the system can dynamically adapt its operating point to maintain the highest possible EER, even under less favorable environmental conditions. For the low-humidity case at $T_{d,i} = 30\,°C$ (Figure 9.11-A), the maximum ICC is achieved at high flow rates. This behavior stems from the HMX ability to maintain an outlet temperature significantly below the room set-point across a broad operational range. Consequently, the ICC remains positive even at low r_m for all explored flow rates. The optimization path follows the hygienic ventilation curve up to a r_m of approximately 0.35; beyond this point, meeting higher ICC demands requires an increase in inlet mass flow rate coupled with a gradual reduction in recirculation. For the dry case at $T_{d,i} = 40\,°C$ (Figure 9.11-B), the peak ICC occurs at $r_m \cong 0.41$, with an inlet flow rate only slightly exceeding the minimum hygienic requirement. The optimization path tracks the hygienic limit until r_m reaches 0.4, subsequently detaching the hygienic curve with a slight increase in recirculation toward the maximum ICC point. Under humid conditions at $T_{d,i} = 30\,°C$ (Figure 9.12-A), ICC increases are limited to intermediate flow rates, with absolute values significantly lower than the dry counterparts. The optimization path diverges from the hygienic boundary at $r_m \cong 0.35$, followed by a progressive increase in recirculation. The most constrained behavior is observed at $T_{d,i} = 40\,°C$ and $\omega_{d,i} = 13\ g_v/kg_{da}$ (Figure 9.12-B), where the theoretical maximum ICC falls below the hygienic ventilation threshold. This renders such points invalid for indoor climate control; thus, within the permissible domain, the optimization path remains strictly coincident with the hygienic curve, as the maximum EER and ICC are both found at this boundary. The EER behavior exhibits common trends across all scenarios. Reducing the inlet flow rate generally enhances the EER, with optimal performance occurring at recirculation ratios between 0.3 and 0.4. The detrimental impact of humidity is reflected in the EER

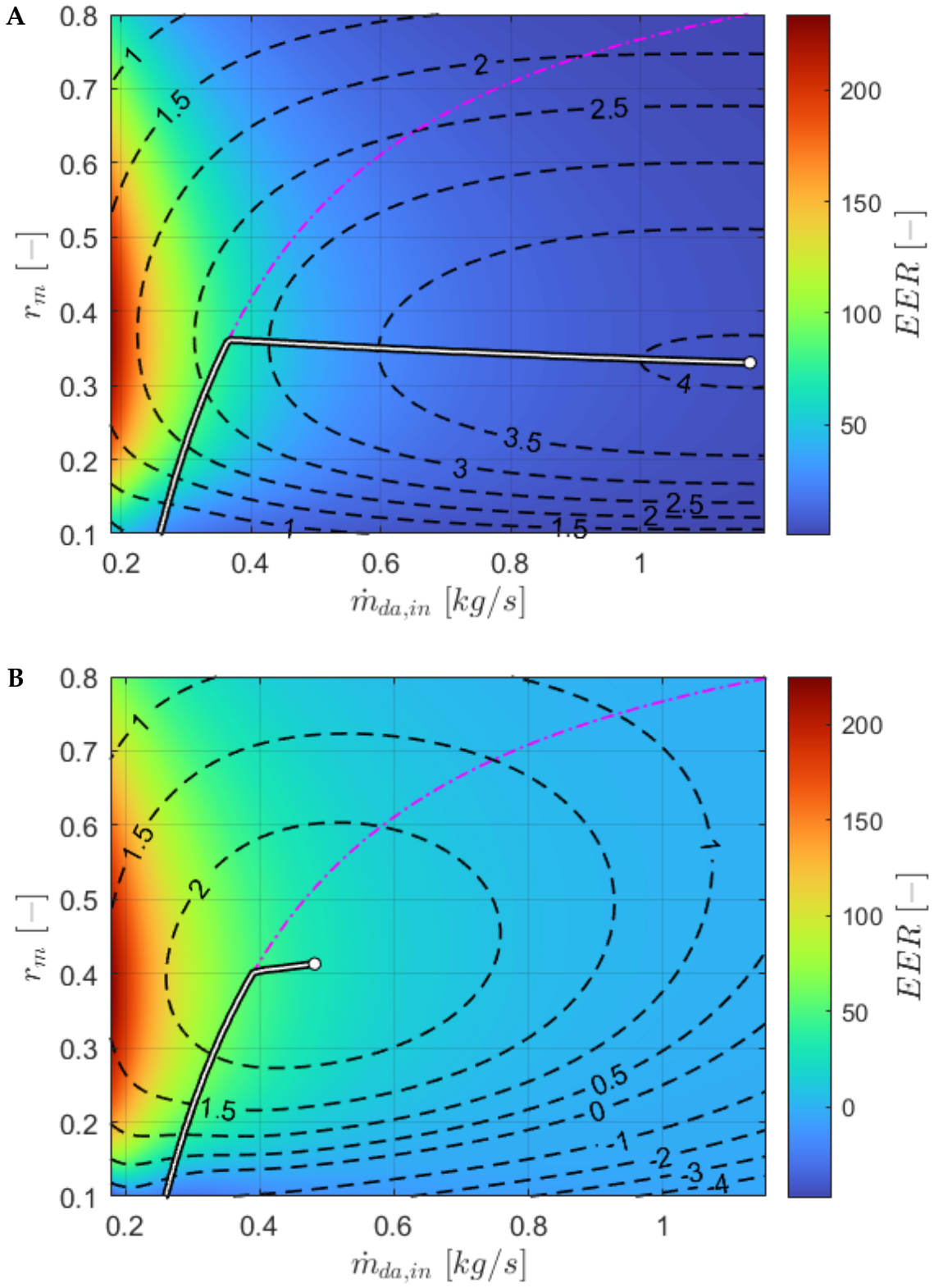

Figure 9.11. EER and ICC distributions, optimization paths and minimum hygienic ventilation as a function of r_m and $\dot{m}_{da,d,i}$ for: (A) Temperate and dry climate ($T_{d,i} = 30\ °C$, $\omega_{d,i} = 0.006\ g_v/kg_{da}$); (B) Hot and dry climate ($T_{d,i} = 40\ °C$, $\omega_{d,i} = 0.006\ g_v/kg_{da}$).

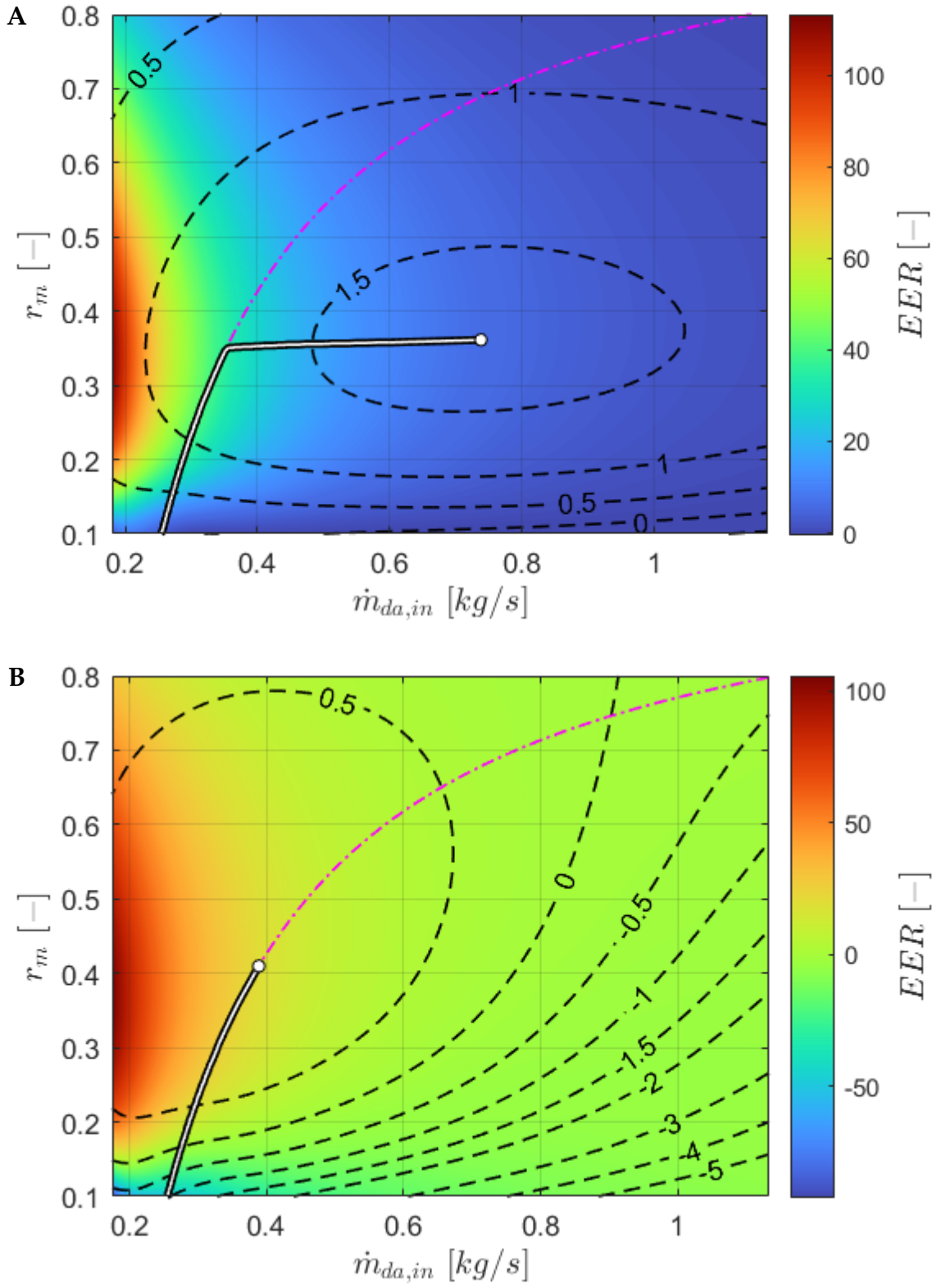

Figure 9.12. EER and ICC distributions, optimization paths and minimum hygienic ventilation as a function of r_m and $\dot{m}_{da,d,i}$ for: (A) Temperate and humid climate ($T_{d,i} = 30\ °C$, $\omega_{d,i} = 0.013\ g_v/kg_{da}$); (B) Hot and humid climate ($T_{d,i} = 40\ °C$, $\omega_{d,i} = 0.013\ g_v/kg_{da}$).

values, which are markedly lower than those achieved in arid conditions due to the diminished evaporative driving force.

From Figure 9.13 to Figure 9.16 show the evolution of EER, recirculation ratio, flow rates, and power consumption along the optimization paths relative to the ICC. For the $T_{d,i} = 30\ °C$, low-humidity case (Figure 9.13), the EER displays a bell-shaped profile, peaking just before the divergence from the hygienic curve. This transition is marked by a discontinuity in the recirculation profile as the algorithm leaves the ventilation constraint to prioritize thermal load. While the supply volume remains constant along the hygienic limit, confirming it as the minimum required air change, the inlet mass flow rate increases sharply, reaching $\dot{m}_{da,d,i} = 1.17\ kg/s$ at maximum ICC. Despite the constant supply volume in the initial stage, the rising total inlet flow increases pressure drops within the HMX dry channels, causing a steady growth in supply-side fan power. Total power consumption escalates from 16 W at low loads to over 800 W at peak ICC, with the supply fan remaining the primary consumer due to its higher volumetric load.

For the $T_{d,i} = 40\ °C$ dry case (Figure 9.14), the EER peak shifts toward higher ICC values, as the optimization path only briefly diverges from the hygienic limit near the maximum capacity point. Although the inlet mass flow rate increases, its peak remains less than half of that observed in the 30 °C case. Total power consumption reaches approximately 80 W, with the wet channel fan power eventually approaching that of the supply fan at maximum ICC due to increasing wet-side pressure drops.

In the humid scenario at $T_{d,i} = 30\ °C$ (Figure 9.15), the EER peak shifts toward higher flow rates, though both EER and ICC values remain significantly lower than in dry conditions. The optimization path diverges from the hygienic limit only for the final 150 W of capacity, with wet-side pressure drops consistently exceeding supply-side losses (up to 200 Pa). Notably, despite the lower cooling output, the total electrical

power exceeds 250 W, considerably higher than the power required for an equivalent ICC in dry conditions.

Finally, the hot and humid case at $T_{d,i} = 40\ °C$ (Figure 9.16) shows no divergence from the hygienic curve. The EER peak is near the maximum ICC, but the overall performance is severely degraded. While the supply volume remains fixed, the working air volume gradually increases, and its associated pressure drops (up to 70 Pa) drive the total power consumption above 40 W for a cooling capacity under 1 kW.

The integrated analysis of thermodynamic performance and electrical consumption demonstrates that the M-Cycle system performance is deeply coupled with ambient conditions and ventilation constraints. The identification of the optimization path reveals that the system can achieve peak EER values by dynamically modulating the recirculation ratio and mass flow rate, effectively balancing cooling demand with hydraulic resistance. Notably, the estimated EER values consistently outperform those of conventional cooling technologies; even under moderate humidity conditions, where EER significantly decreases compared to arid scenarios, the system maintains a performance advantage over traditional air-conditioning systems.

9.5. Optimized path search algorithm

The performance maps discussed in the previous sections show that the cooling performance of the M-cycle system is highly sensitive to the operating parameters. In the context of building cooling, the system must respond to environmental conditions and thermal loads that fluctuate on an hourly or sub-hourly scale. Employing a "brute-force" approach to map the entire operational domain at each time step would be computationally prohibitive. It would also be inefficient for long-term dynamic simulations. Consequently, there is a clear necessity for a dedicated search algorithm to identify the optimal operating point without exhaustive testing of all parameter

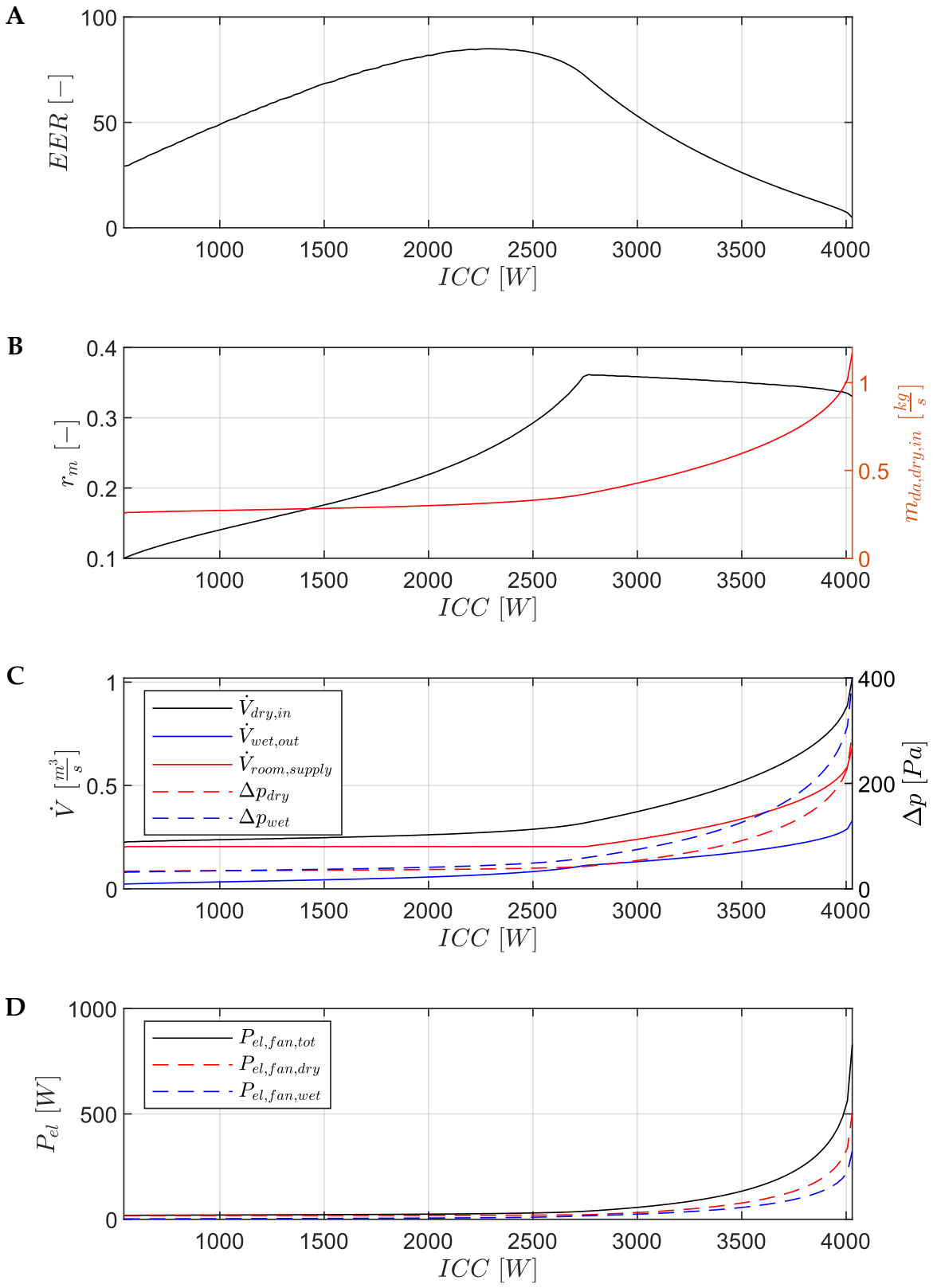

Figure 9.13. Performance profiles along the optimization path for $T_{d,i} = 30\ °C$ and $\omega_{d,i} = 0.006\ g_v/kg_{da}$. System evolution as a function of the Indoor Cooling Capacity (ICC): EER (A); Optimal control parameters (r_m and $\dot{m}_{da,d,i}$) (B); Volumetric flow rates and circuit pressure drops (C); Fans Electrical power consumption (D).

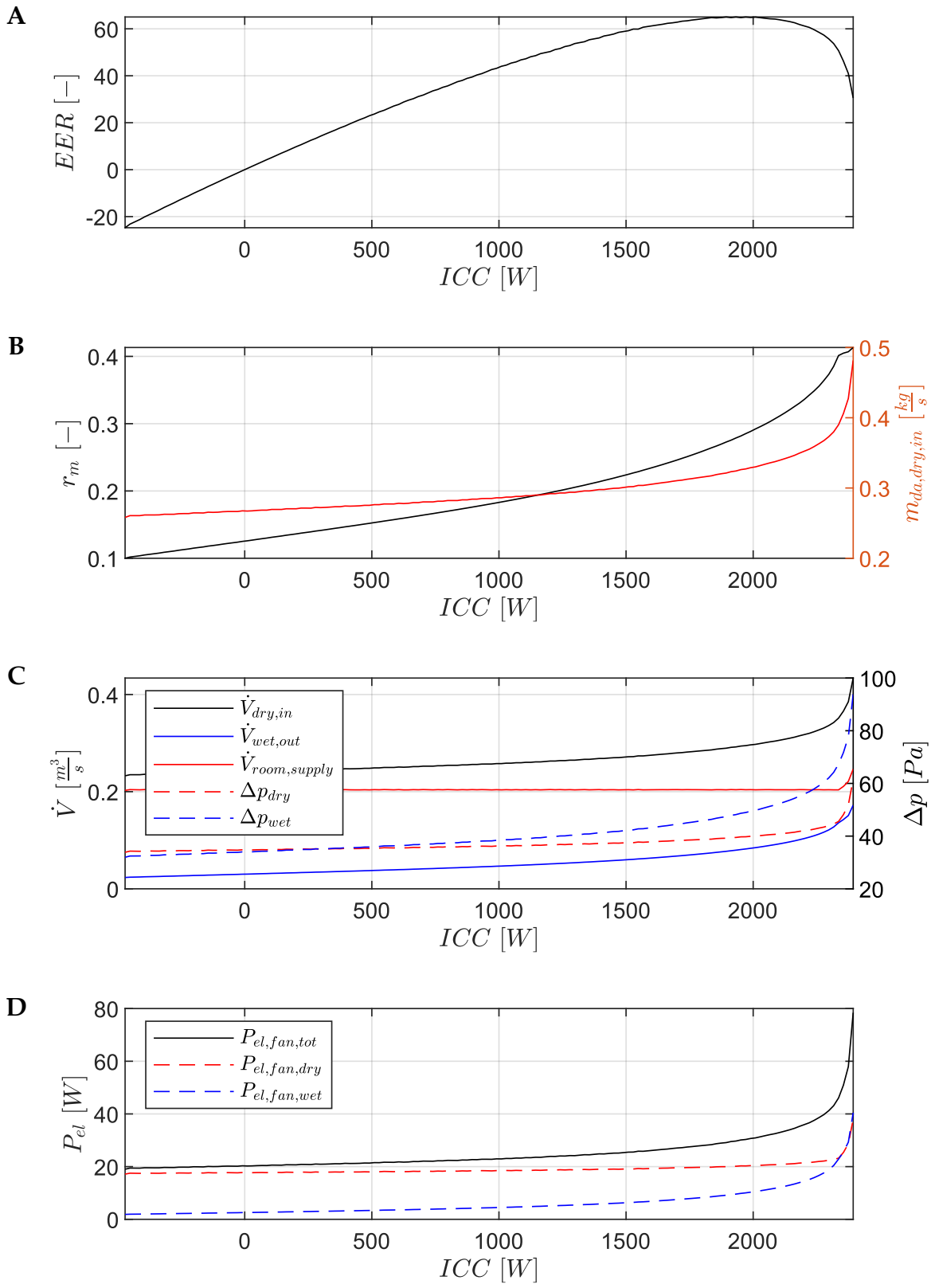

Figure 9.14. Performance profiles along the optimization path for $T_{d,i} = 40\ °C$ and $\omega_{d,i} = 0.006\ g_v/kg_{da}$. System evolution as a function of the Indoor Cooling Capacity (ICC): EER (A); Optimal control parameters (r_m and $\dot{m}_{da,d,i}$) (B); Volumetric flow rates and circuit pressure drops (C); Fans Electrical power consumption (D).

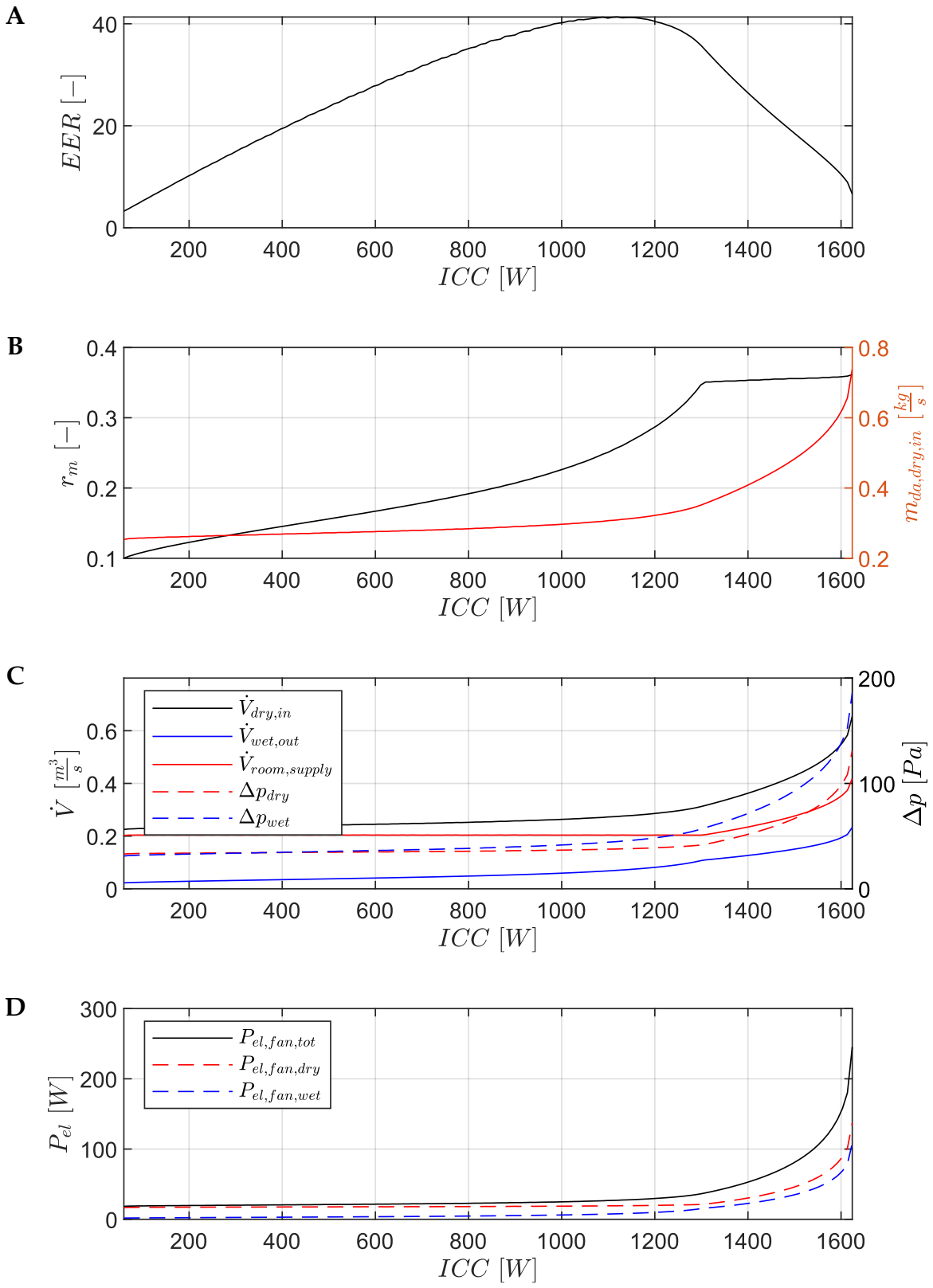

Figure 9.15. Performance profiles along the optimization path for $T_{d,i} = 30\ °C$ and $\omega_{d,i} = 0.013\ g_v/kg_{da}$. System evolution as a function of the Indoor Cooling Capacity (ICC): EER (A); Optimal control parameters (r_m and $\dot{m}_{da,d,i}$) (B); Volumetric flow rates and circuit pressure drops (C); Fans Electrical power consumption (D).

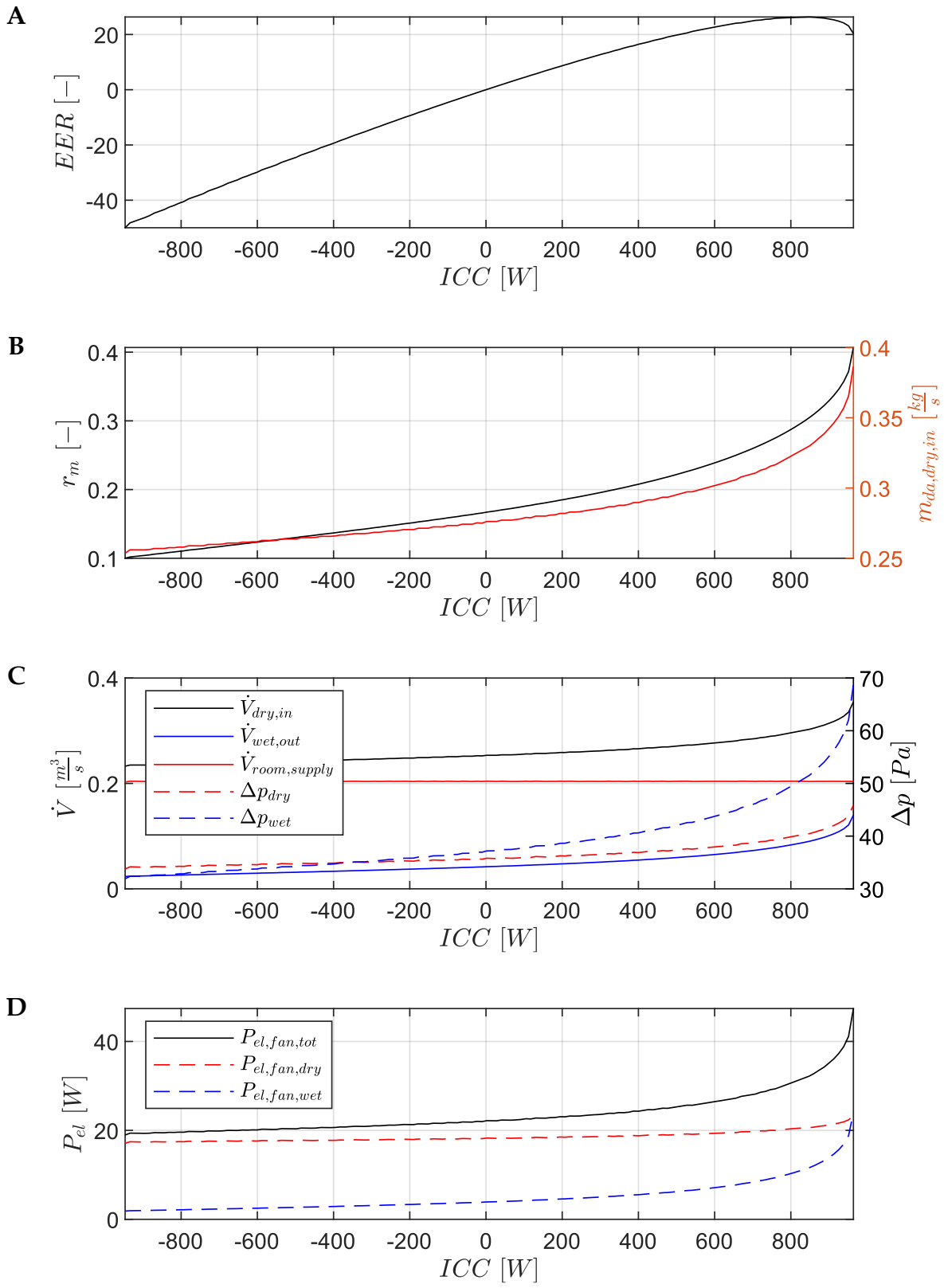

Figure 9.16. Performance profiles along the optimization path for $T_{d,i} = 40\ °C$ and $\omega_{d,i} = 0.013\ g_v/kg_{da}$. System evolution as a function of the Indoor Cooling Capacity (ICC): EER (A); Optimal control parameters (r_m and $\dot{m}_{da,d,i}$) (B); Volumetric flow rates and circuit pressure drops (C); Fans Electrical power consumption (D).

combinations. Since M-cycle performance strictly depends on inlet air conditions, the optimization path must be recalculated at each time step to determine the operational range between the minimum and maximum ICC for the specific boundary conditions. The search algorithm initializes from a state of pure ventilation ($r_m = 0$), with the supply temperature assumed to be equal to the HMX inlet temperature. From this starting point, the algorithm explores the adjacent operational domain using a localized search pattern. Each candidate point in the neighborhood is evaluated sequentially. An initial flow-rate check is performed to determine whether the candidate satisfies the minimum hygienic ventilation requirement. If this condition is met, the algorithm proceeds to calculate the system thermal performance and electrical consumption for that specific operating condition. Among all analyzed points that yield ICC higher than the current state, the algorithm selects the one that maximizes the "EER gain slope", defined as the ratio between the increase in EER and the corresponding increase in ICC between the candidate and the current point. Once the best candidate is identified, it is designated as the new "current point" and the process iterates until the absolute maximum ICC for those boundary conditions is reached. The simplest search pattern involves testing the eight points in a rectangular neighborhood. If the current point lies on the hygienic boundary, an additional point along that curve is also evaluated. If the current point is sufficiently close to the hygienic boundary such that some neighboring candidates fall outside the admissible domain, these points are projected onto the boundary to ensure that only physically valid operating conditions are assessed in that direction. The step sizes for $\dot{m}_{da,d}$ and r_m represent a trade-off between search precision and computational speed. At the conclusion of this iterative cycle, the algorithm generates a set of operational and performance parameters, fully ordered from minimum to maximum ICC, that constitute the optimization path for the given time step. This allows the dynamic

simulation to select the most efficient operating point that satisfies the building's instantaneous thermal demand.

The following section synthesizes the results of the localized search algorithm and evaluates its computational efficiency relative to the previously discussed exhaustive mapping. Figure 9.17 illustrates the results generated by the search algorithm for dry boundary conditions at $30\,°C$ and $40\,°C$. These trajectories were obtained by employing a discretization step of 0.05 for r_m and 0.05 kg/s for $\dot{m}_{da,d}$. The comparison indicates that, despite the significantly lower number of computed points, the algorithm successfully reproduces the optimization paths identified in the previous chapter. It should be noted that the subtle inclination of the path segments diverging from the hygienic boundary cannot be perfectly captured with the current discretization resolution. However, a deviation within a few percentage points represents an acceptable engineering compromise for long-term dynamic simulations. This level of discretization ensures sustainable computational times while providing a sufficiently accurate identification of the most efficient operating points for building energy management. In summary, the transition from a global domain analysis to a step-by-step gradient search allows for the practical integration of complex M-cycle thermodynamics into building energy software. By prioritizing the EER gain slope at each iteration, the algorithm maintains the system high-performance characteristics while minimizing the computational burden associated with full-domain analysis.

9.6. Ventilation and cooling control logic

The control strategy implemented for the M-cycle system integrates guaranteed-flow mechanical ventilation with feedback-based cooling regulation designed for dynamic operation. The primary objective of the system is to maintain thermal comfort within the conditioned zone while minimizing energy expenditure, without ever compromising the hygienic air exchange requirements defined by current standards.

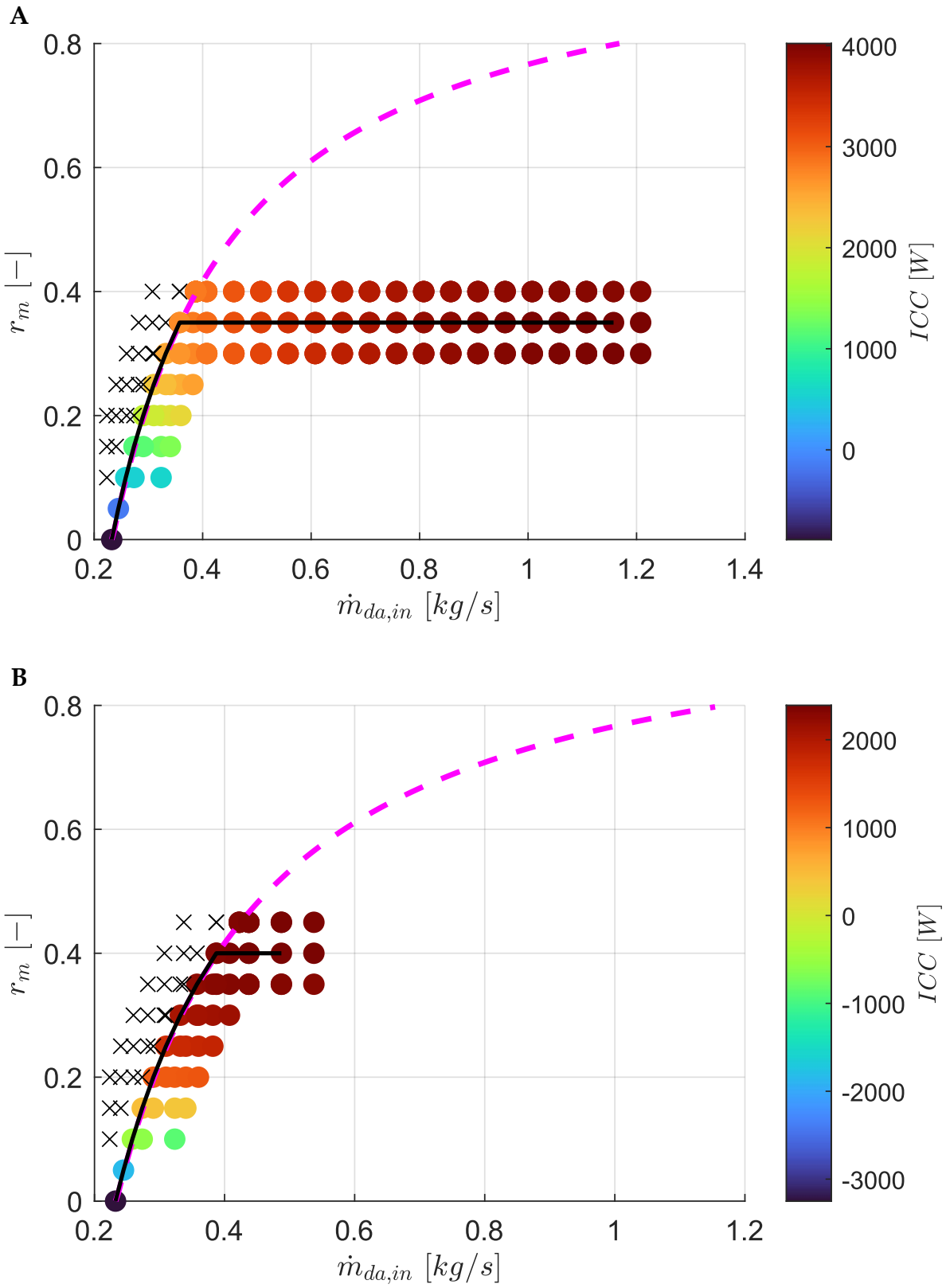

Figure 9.17. Evaluated points from the optimization path discrete points search algorithm for: (A) Temperate and dry climate ($T_{d,i}$ = 30 °C, $\omega_{d,i}$ = 0.006 g_v/kg_{da}); (B) Hot and dry climate ($T_{d,i}$ = 40 °C, $\omega_{d,i}$ = 0.006 g_v/kg_{da}).

At each simulation time step t during which the cooling system is enabled, a discrete-time Proportional-Integral (PI) controller monitors the zone air temperature. The controller evaluates the temperature error $e(t)$ between the current indoor temperature and the established set-point ($26\ °C$)

$$e(t) = T_{space}(t) - T_{set-point} \qquad 9.16$$

The resulting control signal $\alpha(t)$ is calculated as follows

$$\alpha(t) = K_p\, e(t) + K_i \int e(t)\, dt \qquad 9.17$$

Unlike conventional control systems, where the regulator output signal acts directly on a mechanical or electrical quantity (such as inverter frequency or valve opening), the parameter α generated here acts as a modulator of the required Indoor Cooling Capacity ICC_{req}. This value represents the cooling power required by the space at that specific instant. Once the cooling request is calculated, the control system applies dynamic saturation based on the physical limits of the heat exchanger at the current time step. The required power is instantaneously compared with the limits $ICC_{min}(t)$ (under pure ventilation) and $ICC_{max}(t)$ (maximum cooling at the end of the optimized trajectory) derived from the optimization path. If $ICC_{req}(t)$ exceeds these boundaries, it is clamped to the corresponding limit value, ensuring that the operating point always remains within the HMX physical validity domain. Only after this saturation phase does the algorithm proceed backward along the optimization path to identify the mechanical variables necessary for regulation ($\dot{m}_{da,d}$, r_m). This approach allows for optimal management of the anti-windup action. Since the signal α is not numerically bounded, the integral of the temperature error could grow indefinitely when the building thermal load exceeds the system physical capabilities. To prevent this, the plugin monitors the physical saturation state: the growth of the integral term is suspended when the delivered capacity reaches the unit $ICC_{min}(t)$ or $ICC_{max}(t)$ limits.

In this manner, the controller avoids computational drift during overload periods, remaining ready to respond promptly as soon as environmental conditions or internal loads return within the system regulation range. Finally, to ensure stability during typical building transients (such as morning or afternoon startups), the integral term is reset at the beginning of each operational schedule. This reset eliminates the accumulation of non-physical states that occurred during system inactivity, ensuring a predictable dynamic response based solely on instantaneous thermal requirements.

9.7. Simulation methodology

The dynamic integration of the M-cycle system into the EnergyPlus environment is achieved through a dedicated Python plugin. This software interface acts as a bridge between the building thermal model and the physical modeling of the heat exchanger, enabling the execution of the control logic described in the previous section. The implementation relies on the EnergyPlus Python API, which allows the plugin to intercept the simulation at each time step. The first operational phase involves establishing data exchange handles. These handles allow the plugin to access environmental variables (outdoor dry-bulb temperature and humidity ratio) and zone-specific data (indoor temperature and exhaust air state) directly from the simulation engine. At the same time, the plugin manages actuators that override the default behavior of the *Coil:UserDefined* object, imposing the calculated mass flow rates and temperatures onto the air loop. A key technical aspect of the simulation is the real-time execution of the search algorithm. Unlike static modeling, the plugin invokes the localized search function at every time step to generate a transient optimization path. This ensures that the system operational boundaries ($ICC_{min}(t)$ and $ICC_{max}(t)$) are always consistent with the instantaneous psychrometric potential of the outdoor air. The physics of pressure drops and the thermodynamic predictions provided by the neural networks are thus processed in real time to update the system state. Since the optimization path consists of a discrete set of points, the plugin implements linear

interpolation logic. If the required capacity falls between two calculated points, the system determines the values for the inlet mass flow rate and the recirculation ratio through linear weighting between adjacent points. Finally, the plugin manages the coupling between the PI controller and the simulation energy balance. Once the required capacity is determined and interpolated along the optimization path, the plugin translates these values into physical set-points for the air terminals. This architecture establishes the M-cycle unit as an autonomous, self-optimizing component within the building energy model, ensuring that airflow and recirculation are modulated to maximize the EER while maintaining full adherence to prescribed ventilation schedules and transient thermal requirements.

9.8. Simulation results

This section presents the results concerning the technical feasibility of a fully evaporative cooling system applied to school buildings, using a case study of a building located in Bologna and a final comparison with the same case study in Riyadh. The analysis focuses on the thermal response of a typical classroom during the summer season, evaluating how various environmental and operational variables influence the maintenance of indoor comfort. In the generated graphical analyses, the daily operational profile is characterized by specific-colored regions that allow for the immediate distinction of the different phases of space utilization. The areas highlighted in orange represent the lesson periods, during which maximum classroom occupancy is assumed; consequently, the highest internal thermal loads due to the presence of students occur during these times. Conversely, the yellow regions indicate the phases in which the system is active in the absence of occupants, defining the transition periods. Specifically, the short ten-minute intervals preceding the start of the morning and afternoon sessions serve the strategic function of pre-cooling. This phase is necessary to reduce the accumulated latent and sensible heat loads, ensuring optimal thermo-hygrometric conditions upon the students' arrival. In contrast, the final hour

of the afternoon involves the activation of mechanical ventilation only ($r_m = 0$), a choice aimed exclusively at diluting pollutants and CO_2 accumulated during the day to restore indoor air quality. For the study of the boundary conditions, June 10th was selected, identified as one of the most critical days of the school calendar due to an outdoor air temperature reaching a peak of 30 °C. In this initial phase, a sensitivity analysis was conducted regarding the orientation of the classroom external wall to determine how solar exposure affects the system control capacity. Considering the installation of a single unit equipped with a 200-dry-channel heat exchanger, the performance comparison included East, South, South-West, and West exposures. The analysis of the thermal profiles shown in Figure 9.18 reveals, first and foremost, that with the proposed configuration, the system is unable to strictly guarantee the set-point of 26 °C throughout all hours of the day, indicating a partial saturation of the cooling capacity relative to the magnitude of the summer loads. The East orientation is particularly critical during the morning hours due to direct solar radiation through the glazed surfaces; however, the maximum temperature recorded in this phase reaches 26.9 °C, a value that can still be considered acceptable within a tolerance band of 1 °C relative to the target value. The afternoon period is characterized by the highest thermal peaks for all orientations considered. Among the various options, the South exposure ensures the lowest maximum temperature (27.8 °C), followed closely by the East orientation at 28 °C. The most burdensome condition is confirmed to be the West-facing wall, where a thermal peak of 28.9 °C is recorded, a value comparable to that found for the South-West orientation. Based on this evidence, the subsequent detailed analyses in this chapter will be conducted using the West-facing classroom on June 10th as the worst-case reference, in order to test the system under the most challenging environmental conditions.

The next analysis provides a detailed examination of the numerical results for the classroom case study in Bologna with a West-facing external wall, a configuration

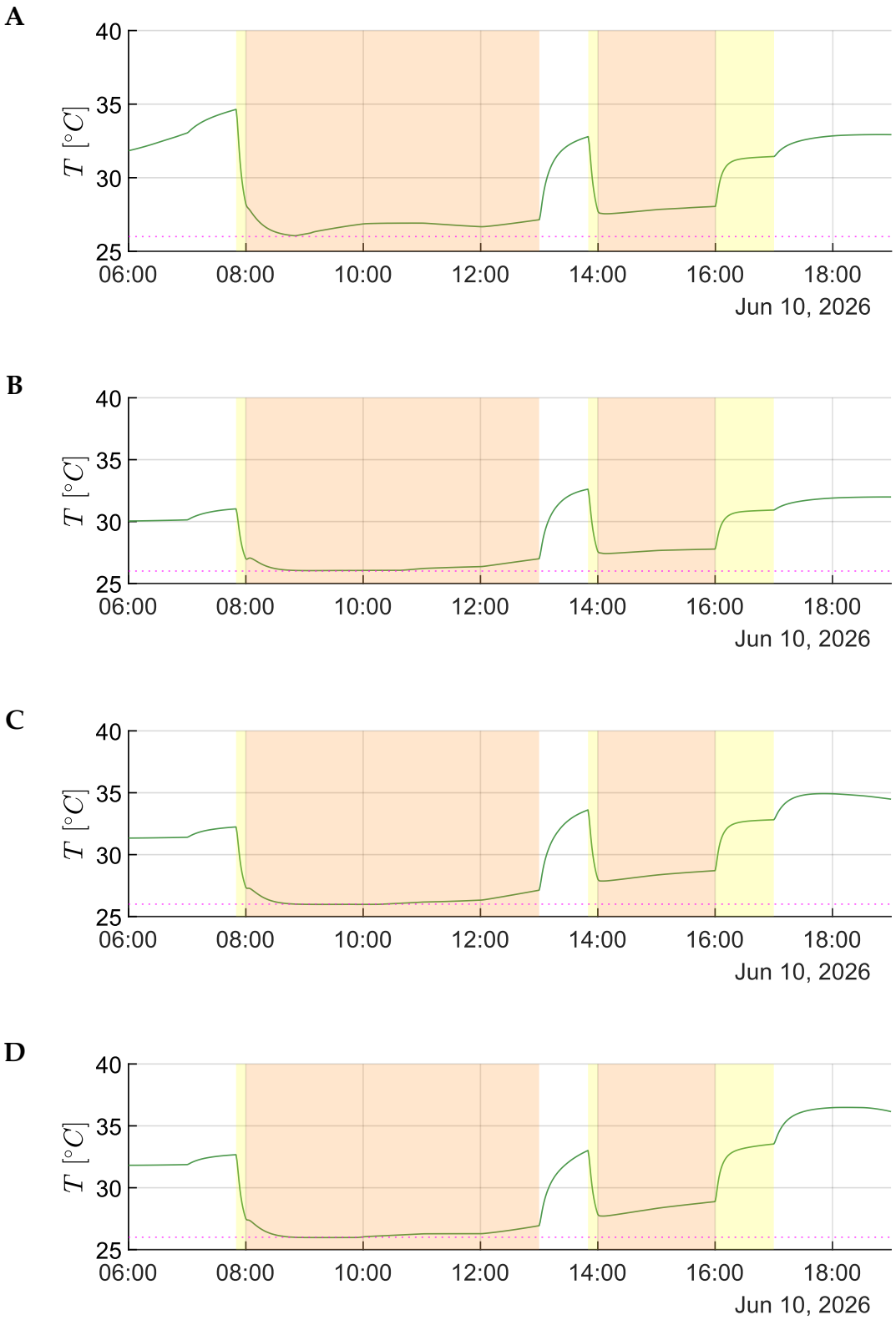

Figure 9.18. Indoor temperature profiles for different classroom orientations: East (A), South (B), South-West (C), and West (D) on June 10th in Bologna (200 channels).

previously identified as the worst-case scenario. The in-depth analysis specifically addresses three different system configurations, characterized by HMX units with 200 dry channels (Figure 9.19 and Figure 9.20), 400 dry channels (Figure 9.21 and Figure 9.22), and 600 dry channels (Figure 9.23 and Figure 9.24). It should be noted that all graphical representations exhibit stepped trends in the operational parameters of the cooling system. This phenomenon is a direct consequence of the discrete optimum path search algorithm used to identify the operating point. Despite this discrete nature, the resolution is sufficient to provide a comprehensive and consistent overview of the system dynamics. To give a clear understanding of the system performance, the results presented below include several key profiles: outdoor and indoor temperature and humidity levels, HMX air mass flow rates and recirculation ratios, inlet air velocity, classroom CO_2 concentrations, the ratio between the required and maximum available ICC, and the EER.

Regarding the first configuration, Figure 9.19-A illustrates the temporal evolution of outdoor and indoor temperatures and specific humidity, alongside the air temperature at the M-Cycle exchanger outlet. As previously mentioned, the use of an HMX pack limited to 200 dry channels is insufficient to counteract the summer thermal loads, causing the indoor temperature to exceed the 28 $°C$ during the afternoon. The analysis of environmental parameters clearly shows that the critical conditions at the end of the day are closely linked to the increase in outdoor specific humidity, which significantly limits the cooling potential at the supply outlet due to the physical constraints of the evaporative process. Simultaneously, Figure 9.19-B shows the intake and supply mass flow rates, together with the recirculation ratio selected at each time step as the optimal operating point. From this analysis, it is observed that the optimal recirculation value remains nearly constant throughout the simulation. Conversely, the intake mass flow rate exhibits a much more pronounced dynamic, reaching the maximum allowable value early in the morning to address the rapid increase in thermal loads and

maintaining this saturation regime for the remainder of the classroom occupancy period.

Figure 9.20-A corroborates previous observations, highlighting how the inlet air velocity quickly converges toward a value near the maximum allowable limit of 6.5 m/s, as identified by the optimal path search algorithm. Simultaneously, the analysis of CO_2 levels reveals a high air change rate. The elevated flow rates required to abate sensible thermal loads ensure CO_2 concentrations remain consistently below 600 ppm for almost the entire simulation period. This value is well within the safety margins compared to the 1000 ppm limit commonly suggested in the literature to guarantee indoor air quality. Finally, Figure 9.20-B confirms that the cooling capacity required by the system promptly reaches saturation relative to the maximum capacity available under local boundary conditions. A particularly noteworthy aspect concerns the system EER. In the initial operational phases during the morning, extremely high values (exceeding 100) are recorded, thanks to the limited thermal loads and favorable outdoor air conditions. However, when the system is pushed to its maximum power to address the afternoon thermal peak, the EER stabilizes at values slightly above 3. This reduction in EER is driven by the high air flow rates utilized to maximize thermal power dissipation.

Analyzing the results obtained using an HMX with 400 intake channels, Figure 9.21-A highlights a significant improvement in thermal performance compared to the previous configuration. Throughout the entire morning period, the system demonstrates improved control capability, successfully reaching and stably maintaining the target set-point. During this phase of the day, the supply air temperature delivered to the environment is consistently lower than that recorded in the 200-channel case. However, despite the increased size of the heat exchanger, the set-point is still not fully met during the afternoon hours, with the indoor temperature tending to rise until it exceeds 27 °C threshold in conjunction with peak loads.

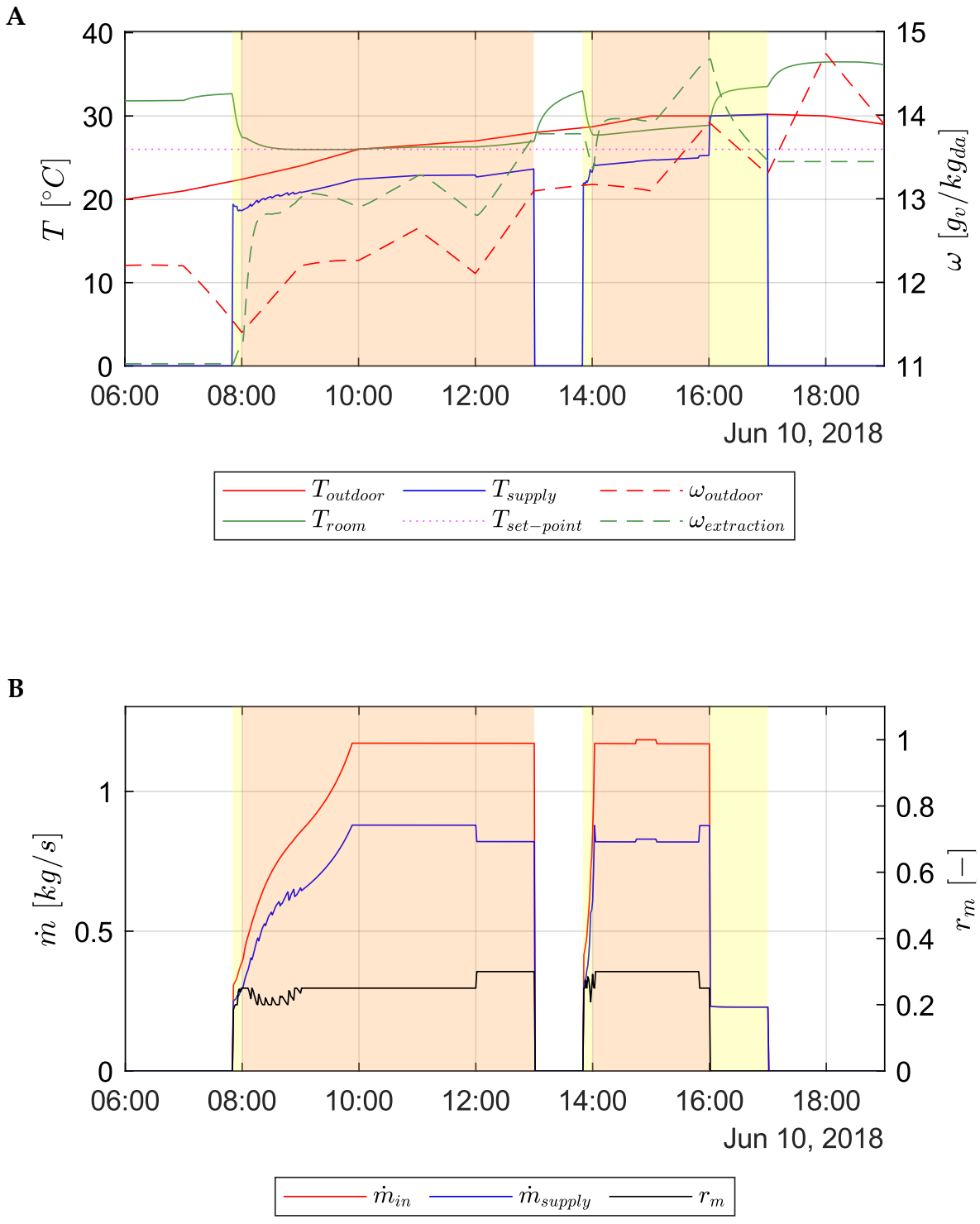

Figure 9.19. Indoor/outdoor temperature and humidity profiles and supply temperature (A); HMX operational parameters (B) for June 10th in Bologna (West exposure, 200 channels).

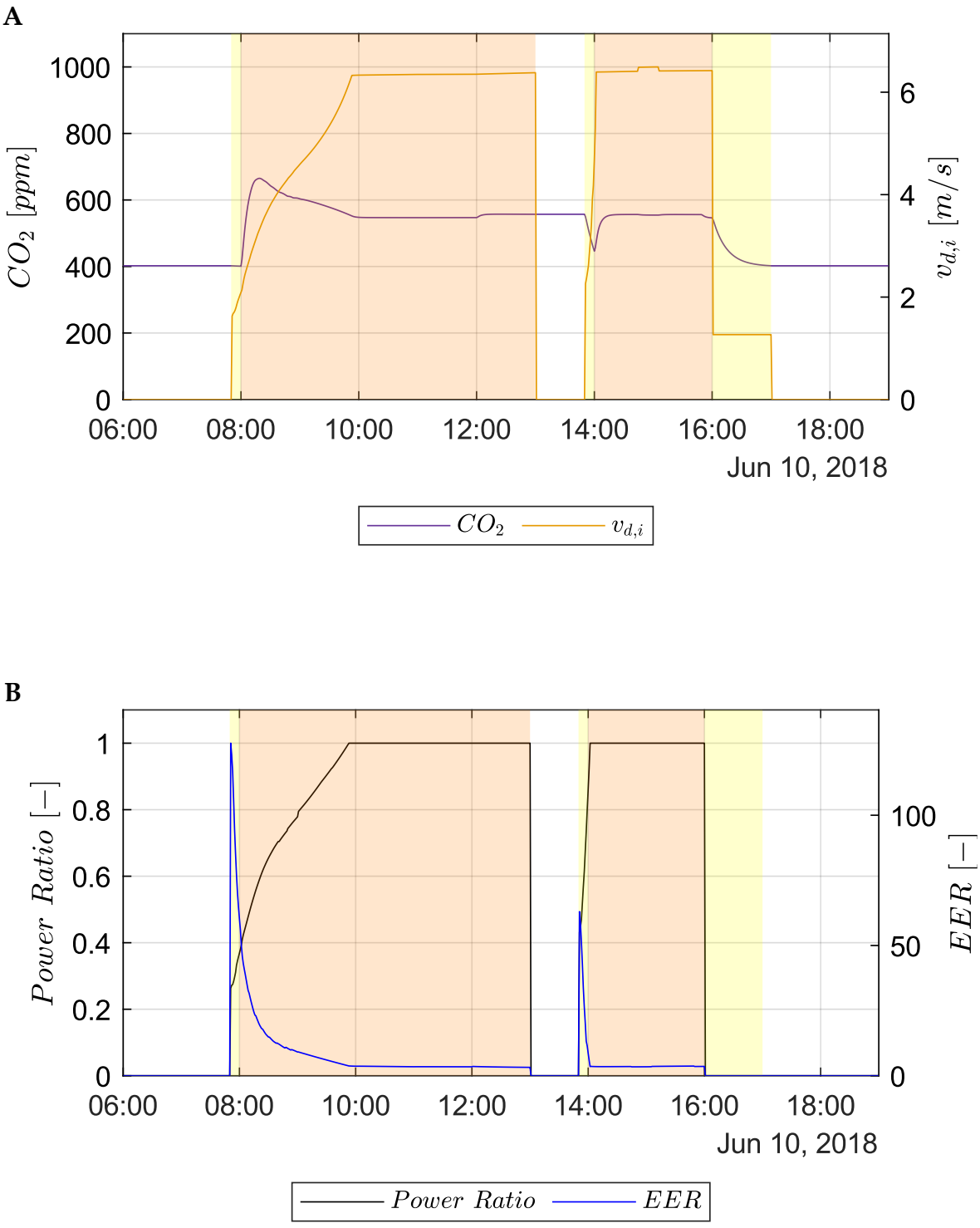

Figure 9.20. Inlet air velocity and indoor CO_2 levels (A); required-to-maximum ICC ratio and EER (B) for June 10th in Bologna (West exposure, 200 channels).

In parallel, the analysis of the operational variables reported in Figure 9.21-B reveals a more complex control dynamic. In the morning, the system operates under a continuous regulation regime, modulating the functional parameters to maintain a limited intake air flow rate, generally below 1 kg/s, a value sufficient to compensate for partial thermal loads. Conversely, with the onset of the afternoon hours and the simultaneous worsening of climatic conditions, the unit is forced to increase ventilation rates, reaching flow rates close to the maximum available limit to counteract the rising ambient temperature, despite the physical constraints previously noted.

Figure 9.22-A illustrates that CO_2 levels during the morning period are higher than those observed in the 200-channel configuration. This dynamic is attributable to the fact that, due to the larger exchange surface of the heat exchanger, the thermal load is effectively dissipated without requiring the maximum available air flow rate, as confirmed by the intake flow velocity profile. Despite this relative increase, CO_2 concentrations consistently remain below the threshold suggested for indoor comfort. Conversely, during the afternoon hours, the flow velocity is forced to higher values to cope with the increase in sensible loads, consequently leading to a significant reduction in the concentration of pollutants within the classroom. Regarding energy performance, Figure 9.22-B shows that during the morning session, the required ICC varies within a range between 20% and 80% of the maximum available capacity. With the transition to the afternoon hours, the system rapidly reaches operational saturation. In terms of EER, a general increase is observed compared to the previous case. This is due to the lower air velocity within the channels, a condition that optimizes the evaporative cooling process in the HMX unit. In the initial phase of the day, efficiency peaks exceeding 250 are recorded, later stabilizing at values that progressively decrease from 40 to 20. During the afternoon, in correspondence with the delivery of maximum power, EER values remain within a range between 3 and 4.

The analysis of the results for the configuration featuring an HMX exchanger with 600 intake channels demonstrates, as illustrated in Figure 9.23-A, significantly more effective thermal control compared to the previous solutions. Although the indoor temperature does not remain perfectly stable at the nominal set-point of $26\,°C$ during the afternoon hours, the thermal peak at the end of the day reaches only $26.5\,°C$. This deviation falls well within the $1\,°C$ tolerance interval relative to the set-point, providing acceptable environmental conditions according to the predefined comfort criteria. Regarding flow management, Figure 9.23-B shows that slightly lower intake air flow rates are employed during the morning session compared to the 400-channel configuration; however, toward the end of the morning, there is a shift toward higher average recirculation values. In the second part of the afternoon, similar to the findings in previous cases, the air flow rates undergo a sudden increase, a necessary measure to counteract heat gain and maintain the indoor temperature within acceptable limits.

Figure 9.24-A highlights that, during the morning period, CO_2 levels reach the highest values among the three analyzed cases, while remaining within acceptable thresholds and stabilizing around $700\,ppm$. The air velocity profile confirms this dynamic, showing that, except for the afternoon hours, values remain slightly above $1\,m/s$. Even during the afternoon peak loads, the maximum intake velocity stands at approximately $4.5\,m/s$, which is the lowest among all the configurations examined. Regarding the energy demand, Figure 9.24-B shows that the maximum available ICC is required only in the latter part of the afternoon, while during the morning, the thermal demand remains consistently below 50% of the nominal capacity. In this scenario, the EER values are the highest in the entire analysis, with a morning peak exceeding 300 and values ranging between 60 and 70 in the second part of the morning. In the final afternoon phase, despite the system operating at maximum capacity to cope with thermal loads, the EER values remain above 4, confirming the excellent energy performance of the upsized configuration.

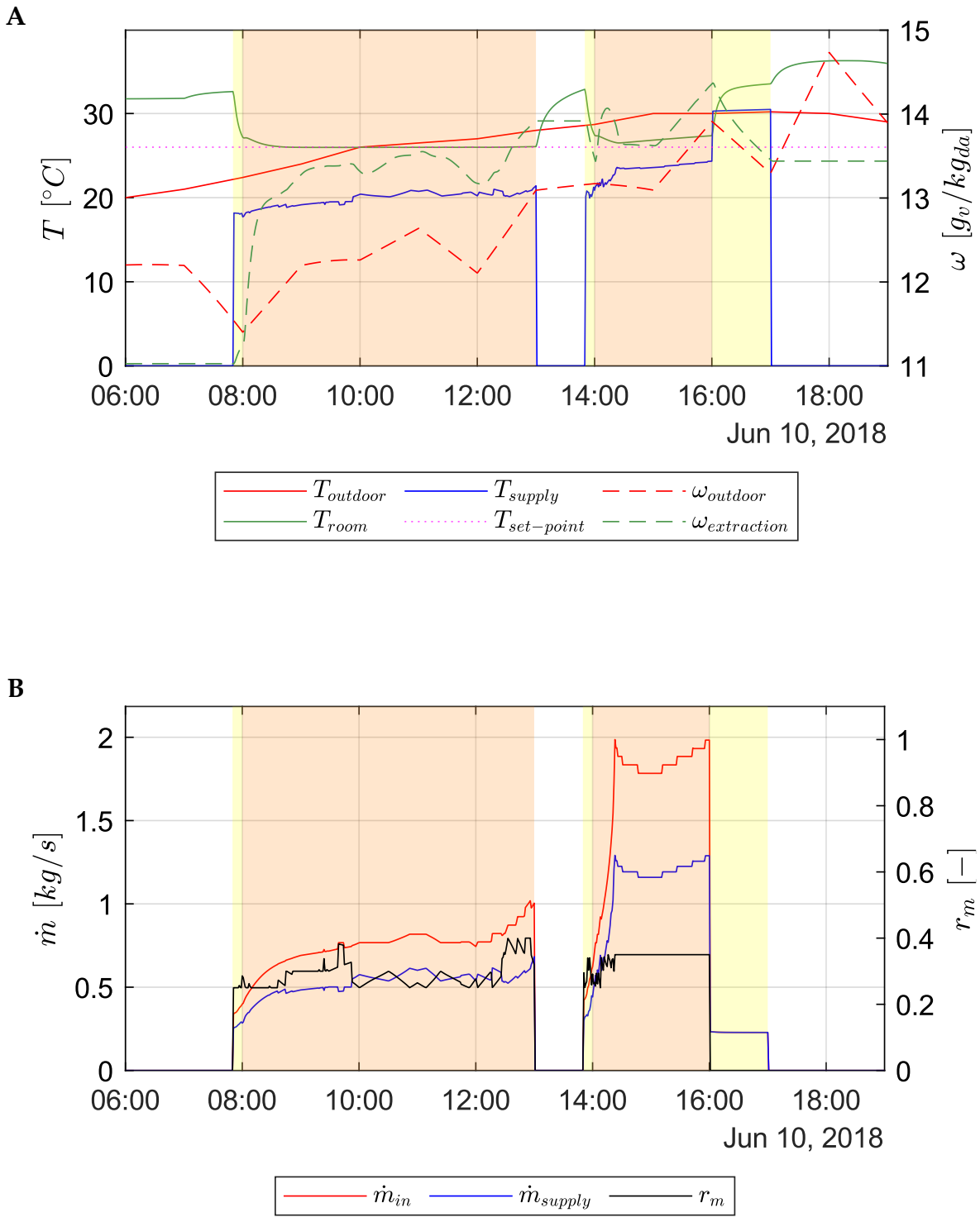

Figure 9.21. Indoor/outdoor temperature and humidity profiles and supply temperature (A); HMX operational parameters (B) for June 10th in Bologna (West exposure, 400 channels).

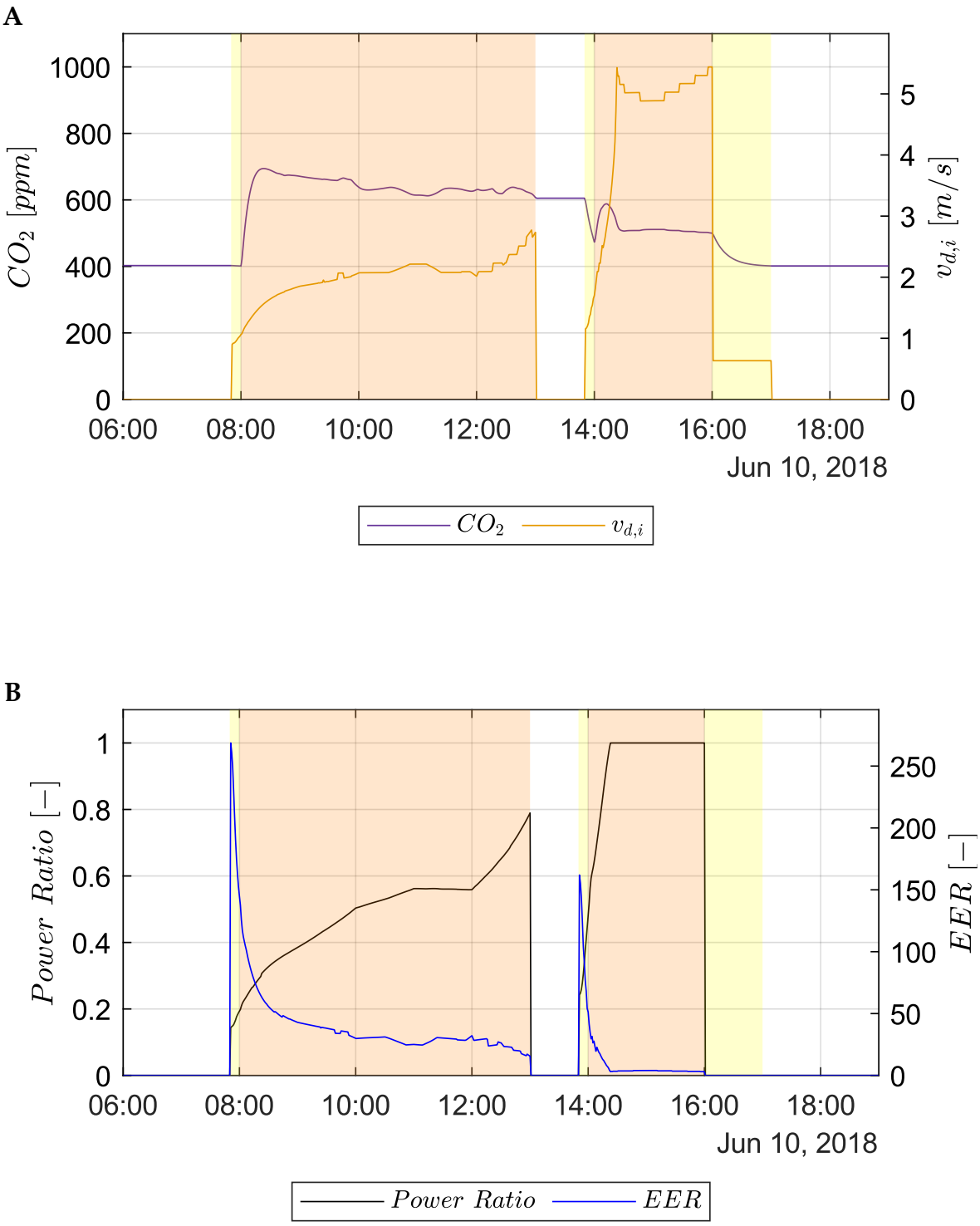

Figure 9.22. Inlet air velocity and indoor CO_2 levels (A); required-to-maximum ICC ratio and EER (B) for June 10th in Bologna (West exposure, 400 channels).

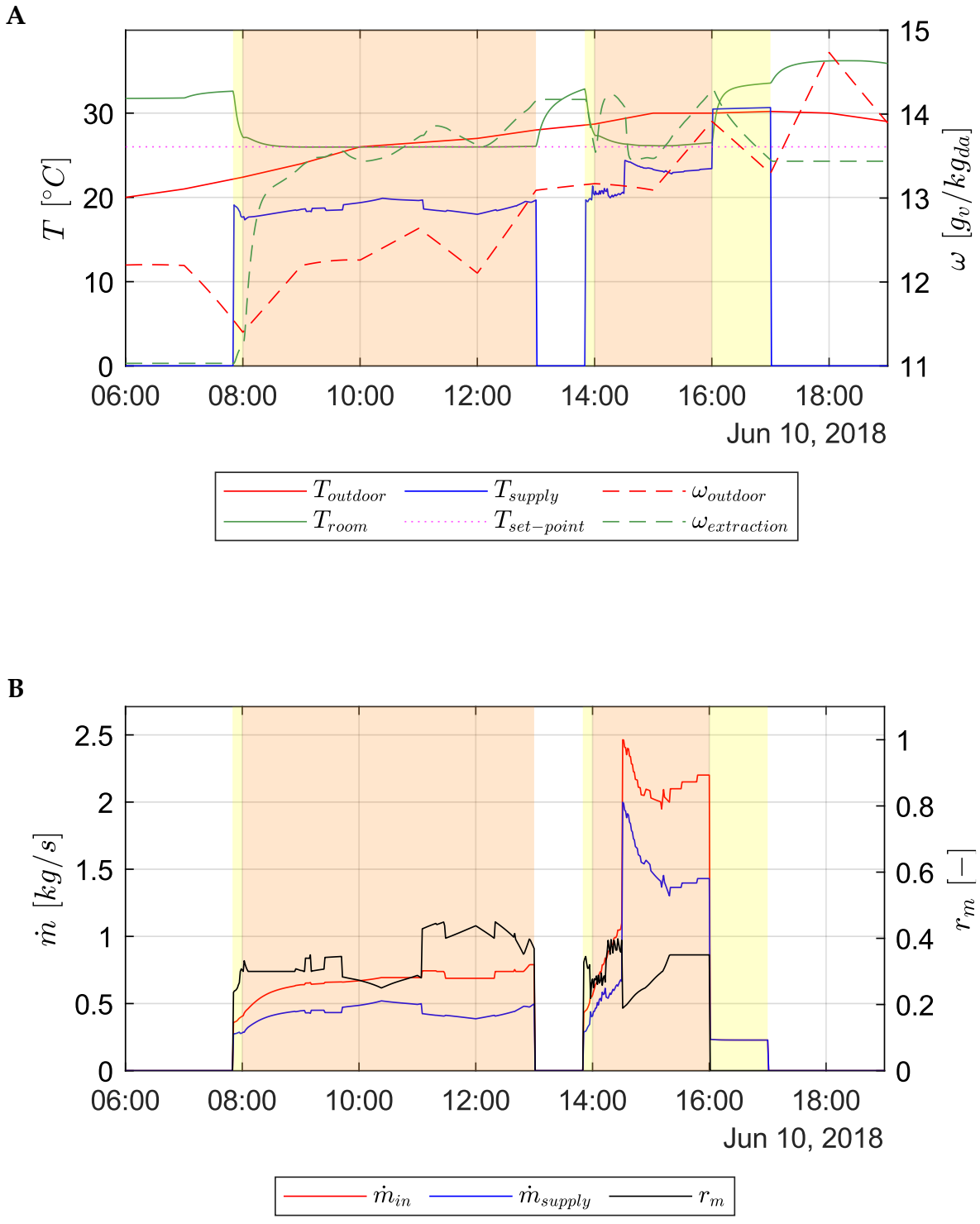

Figure 9.23. Indoor/outdoor temperature and humidity profiles and supply temperature (A); HMX operational parameters (B) for June 10th in Bologna (West exposure, 600 channels).

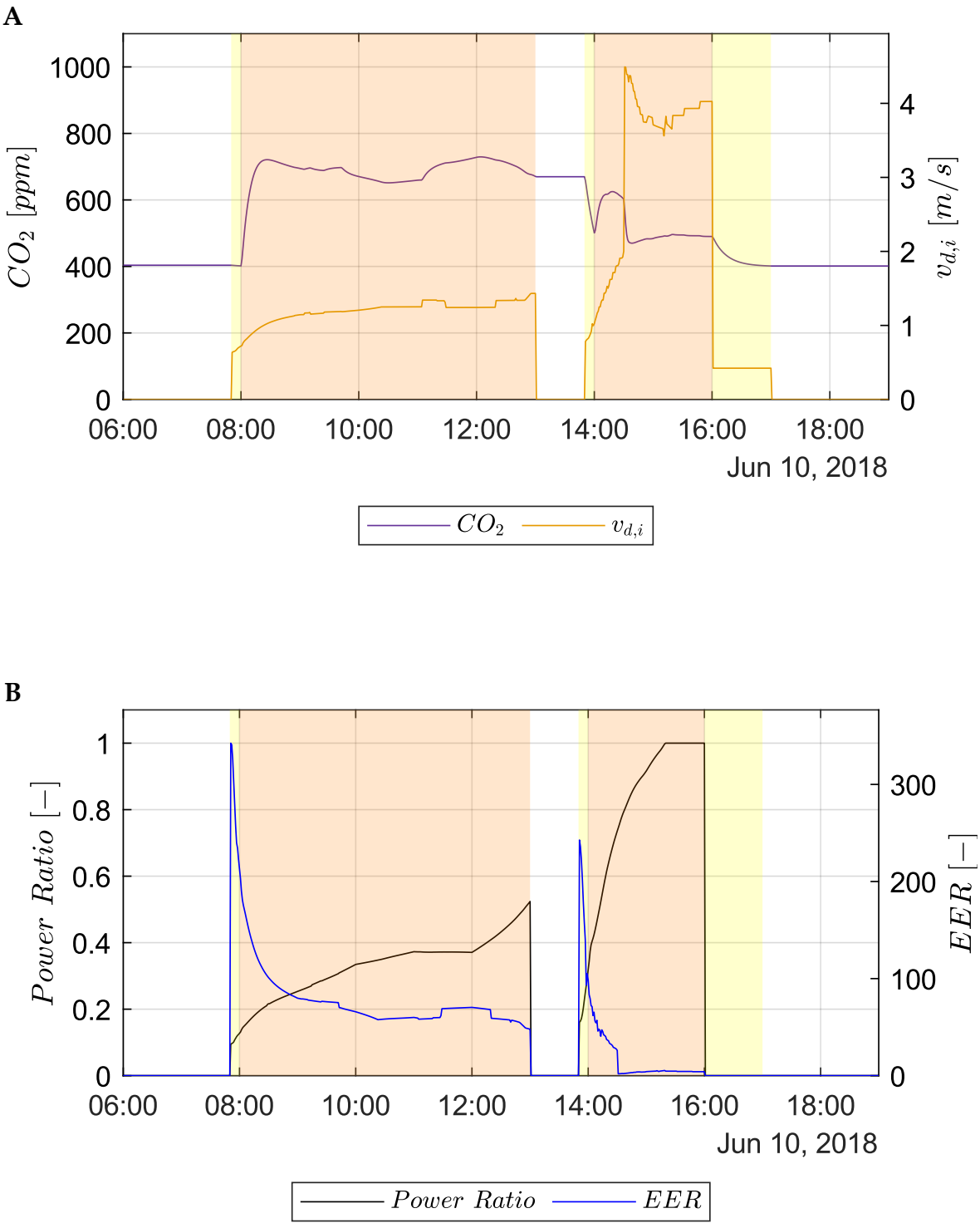

Figure 9.24. Inlet air velocity and indoorCO_2 levels (A); required-to-maximum ICC ratio and EER (B) for June 10th in Bologna (West exposure, 600 channels).

By extending the analysis to a day characterized by less severe climatic conditions, such as June 7th, it is possible to further observe the system potential under intermediate load conditions. On this date, the outdoor temperature does not exceed $28\,°C$, and the specific humidity remains at slightly lower values compared to the previous case, settling around $11\,g_v/kg_{da}$. As illustrated in Figure 9.25-A, these boundary conditions allow the system to operate with extreme effectiveness, guaranteeing that the $26\,°C$ set-point is reached and maintained throughout the entire school schedule without any deviation. From an energy perspective, Figure 9.25-B highlights how the required cooling capacity remains constantly below 50% of the maximum capacity, resulting in extremely high performance indices. Indeed, peak EER values close to 400 are recorded in the initial phases, while during the morning with the ambient temperature stabilized at $26\,°C$, the efficiency oscillates within a range between 125 and 145. Even under the highest demand in the late afternoon, the minimum EER value does not fall below 53, confirming that the M-Cycle system expresses its maximum operational advantage in the presence of moderate thermal loads.

Finally, the configuration for June 10th is examined with the addition of internal insulation on the ceiling and the external perimeter wall, the results of which are reported in Figure 9.26. In this scenario, thermal performance during the morning session shows no significant deviations compared to the non-insulated configuration; however, during the afternoon, a higher cooling demand is recorded, leading the system to reach ICC saturation earlier. This results in a slightly higher ambient temperature at the end of the day ($26.8\,°C$), although still within the acceptable tolerance range, and a subsequent increase in electrical consumption. This phenomenon is explained by the dynamics of internal radiative and convective heat exchange: as the glazing is West-facing, it directly intercepts afternoon solar radiation. The incoming radiant energy is absorbed by the internal surfaces which, due to the

presence of thermal insulation on the inner side of the glazed wall and the ceiling, exhibit a reduced capacity to dissipate heat toward the building structure and the exterior. The resulting surface overheating of the walls increases the convective heat gain transferred to the classroom air, penalizing summer performance compared to the non-insulated case. Such evidence underscores the importance of an integrated design approach. Although the internal insulation solution is disadvantaged in managing summer cooling, it is essential to conduct an extended evaluation that includes the winter heating regime. The final decision on the insulation strategy must therefore stem from an analysis of energy consumption over the entire calendar year, to balance summer criticalities related to internal overheating with the thermal benefits obtainable during the cold season.

For comparative purposes, the following analysis examines the system performance under climatic conditions particularly favorable to evaporative cooling, characterized by extremely hot and dry air. The study focuses on the same typical classroom previously analyzed, without insulation and with a West-facing orientation, but applied to the climate of Riyadh. The reference scenario selected is June 9th, during which the outdoor temperature reaches a peak of 43.4 $°C$ with extremely low specific humidity levels ranging between 2 and 4 g_v/kg_{da}. For this simulation, the most performing HMX configuration from the Bologna case study was adopted, featuring 600 dry channels. As illustrated in Figure 9.27-A, the system demonstrates remarkable control capability, successfully maintaining the indoor temperature in line with the 26 $°C$ set-point for nearly the entire timeframe. During the afternoon hours, a slight deviation from the target value is observed, with the temperature reaching 26.4 $°C$ by the end of the day. This value, although slightly above the set-point, remains fully compatible with indoor thermo-hygrometric comfort requirements. The analysis of operational parameters, reported in Figure 9.27-B, reveals a distinctive flow dynamic. In the early morning phase, the system employs high air flow rates that progressively

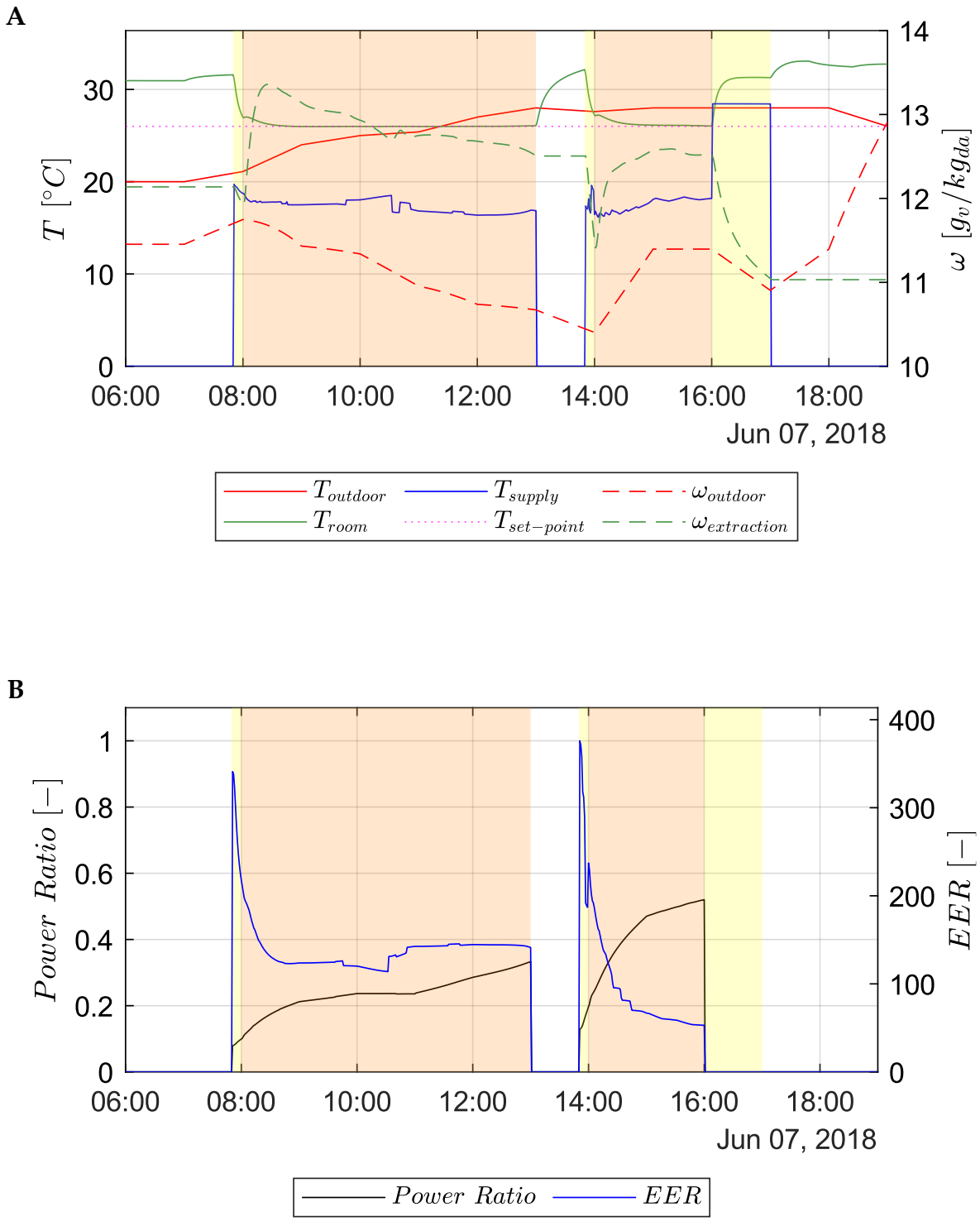

Figure 9.25. Indoor/outdoor temperature and humidity profiles (A); required-to-maximum ICC ratio and EER (B) for June 7th in Bologna (West exposure, 600 channels).

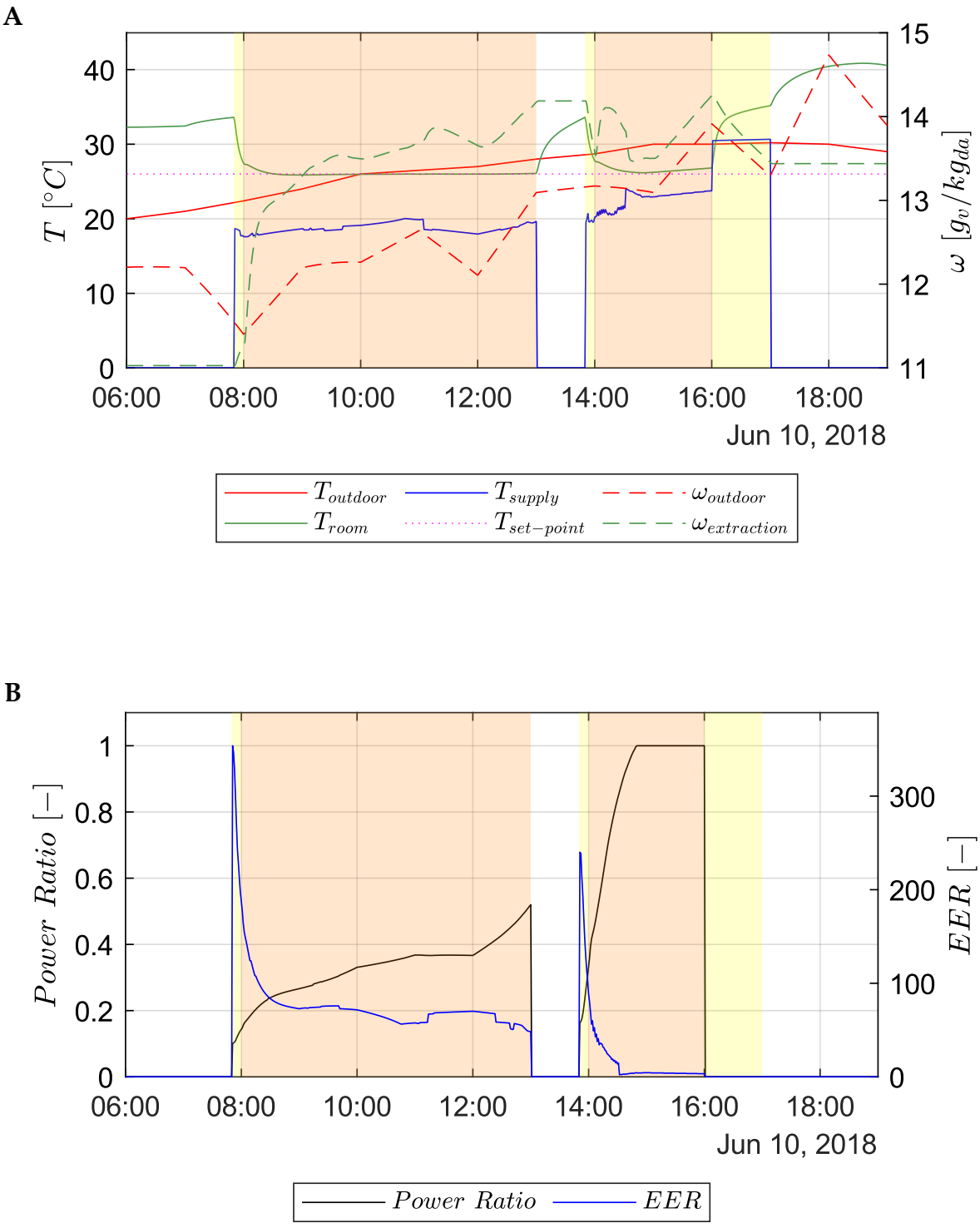

Figure 9.26. Indoor/outdoor temperature and humidity profiles (A); required-to-maximum ICC ratio and EER (B) for June 10th in Bologna (West exposure, 600 channels, insulated classroom).

decrease toward the midday break, while maintaining a constant recirculation ratio of approximately 30%. In the afternoon, the inlet air flow rate stabilizes at nearly constant values, while the recirculation factor increases from 20% to 40%, remaining stable until the end of the school session. This flow management highlights how, in arid climates, the high thermal gradient between outdoor and supply air allows for more flexible regulation and optimal control of sensible thermal loads.

Evaluating the additional indices shown in Figure 9.28-A, the intake flow velocity profile exhibits a decreasing dynamic during the morning, dropping from 4.3 m/s to 2.2 m/s, before stabilizing at values near 2.6 m/s throughout the afternoon session. Simultaneously, air quality monitoring confirms the effectiveness of the air exchange: CO_2 levels remain constantly below 600 ppm, ensuring a healthy environment well within regulatory limits. Regarding the thermal balance, as reported in Figure 9.28-B, the required ICC remains above 80% of the maximum available capacity, though it never reaches saturation during the morning period. In the afternoon, the system operates at the limit of its maximum cooling power, yet succeeds in maintaining the ambient temperature within the previously discussed acceptability margins. From an energy efficiency perspective, the EER values highlight the extraordinary potential of the M-Cycle in dry air conditions. An initial peak exceeding 600 is observed in the early morning hours, followed, after an initial sharp drop, by a steady increase from 4 to 34 during the set-point maintenance phase. In the afternoon, following an initial transient, the EER stabilizes at a value near 30 until the end of the day. These findings underscore a crucial design aspect: a system sized to barely meet comfort conditions in a Mediterranean climate proves to be significantly over-dimensioned and extraordinarily efficient when applied to an extremely hot and arid context, where the evaporative potential of the outdoor air is fully exploited.

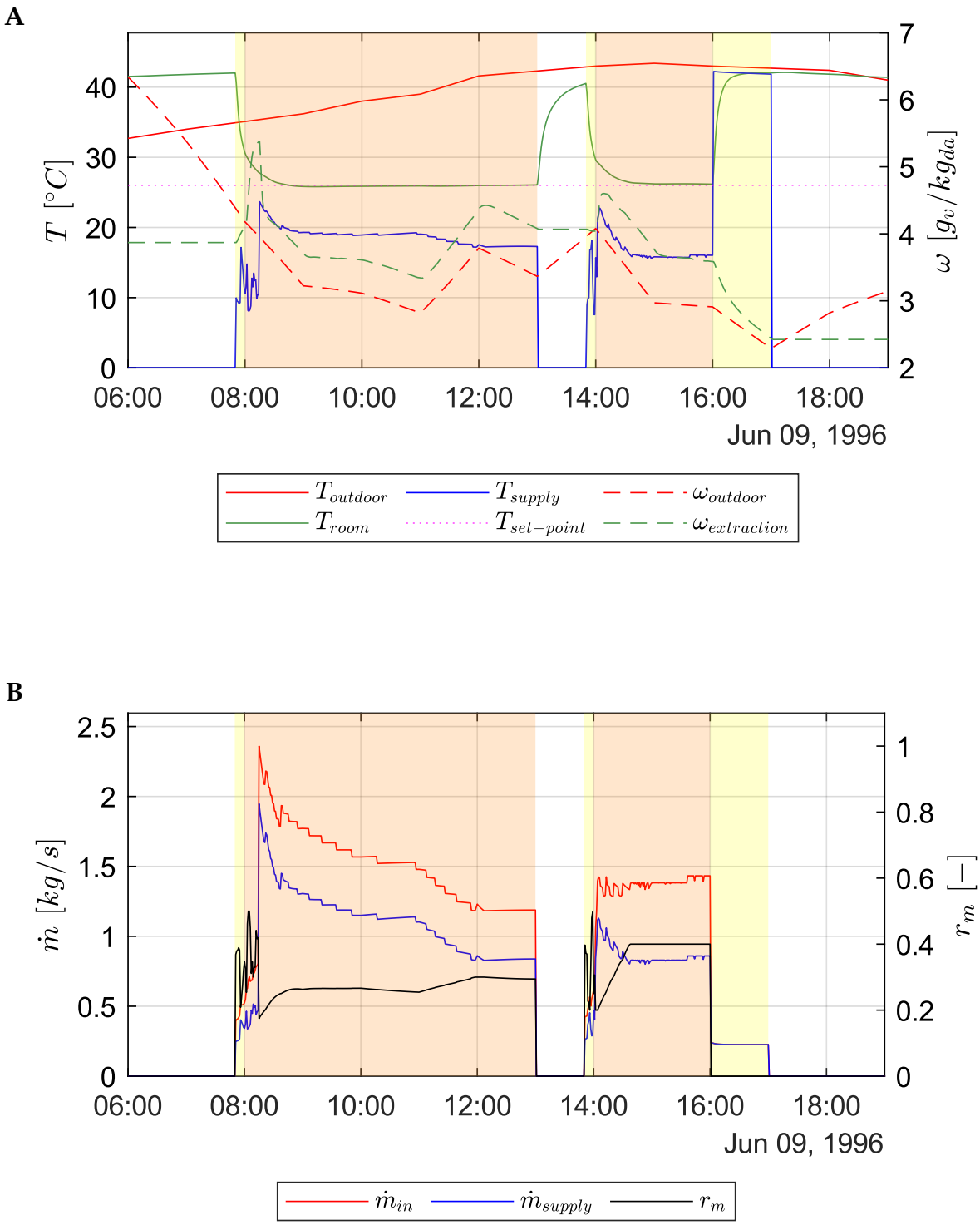

Figure 9.27. Indoor/outdoor temperature and humidity profiles and supply temperature (A); HMX operational parameters (B) for June 09th in Riyadh (West exposure, 600 channels).

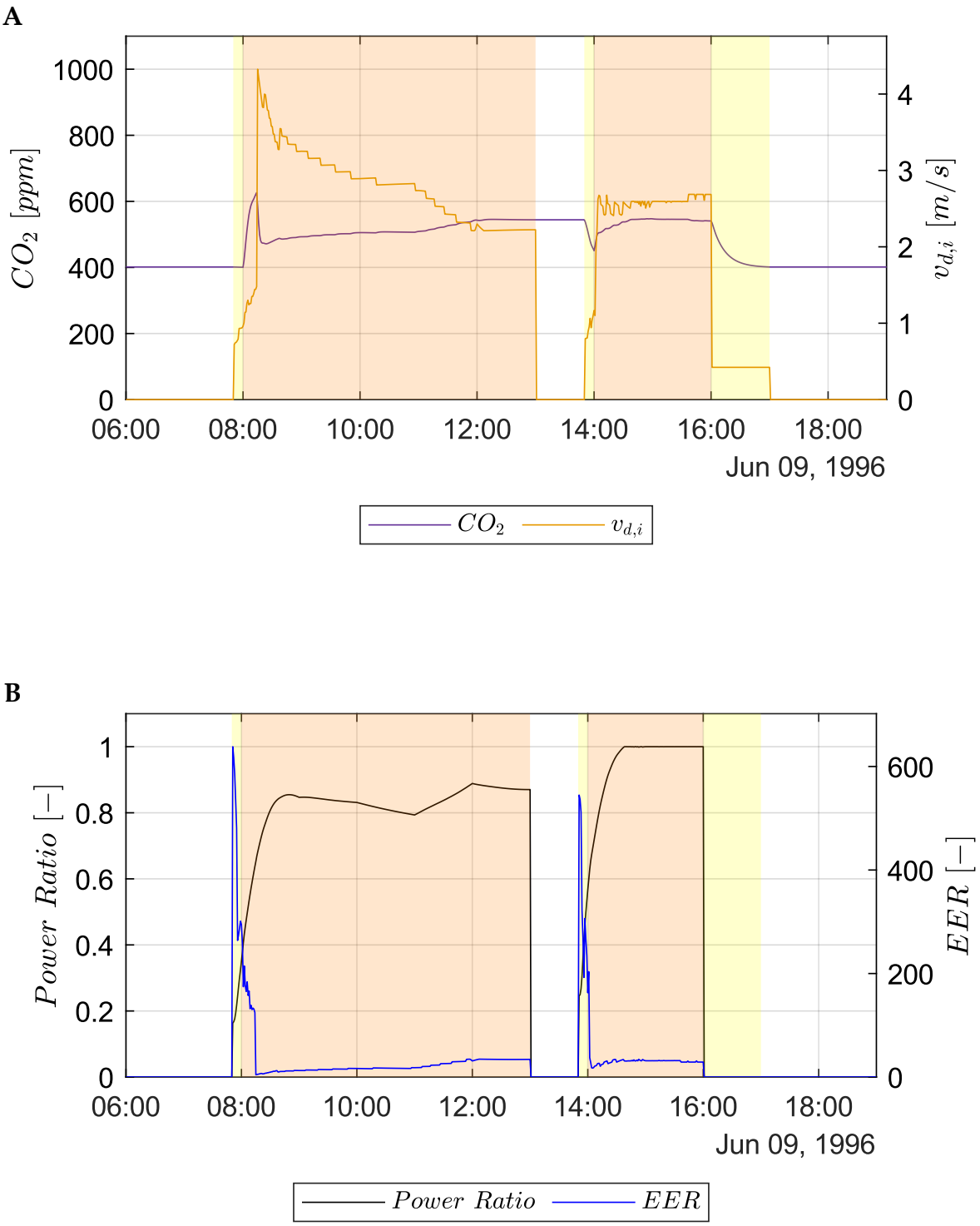

Figure 9.28. Inlet air velocity and indoor CO_2 levels (A); required-to-maximum ICC ratio and EER (B) for June 09th in Riyadh (West exposure, 600 channels).

10. Conclusions

The present thesis has provided a systematic investigation into the potential of evaporative cooling systems based on the Maisotsenko cycle (M-cycle). The research followed a comprehensive methodology that combined theoretical modeling, advanced computational tools, and experimental and applicative validations.

A significant portion of this research focused on the physical modeling of the phenomenon. Initially, extensive use was made of the Hasan model, as it represents a consolidated solution in the literature, widely verified by other authors and characterized by high computational efficiency. However, a critical analysis of this model highlighted several strong simplifying assumptions.

To overcome these limitations, an alternative calculation method was proposed to achieve a deeper understanding of the complex heat and mass transfer phenomena occurring within the exchanger. This new approach allowed for a more rigorous physical modeling of the interaction between the air streams, providing a detailed description of the temperature and humidity gradients along the channels.

Using the Hasan model, an extensive parametric analysis was conducted, which allowed for the mapping of system performance as a function of various operating parameters. The trends of the output variables and specific performance indices were accurately identified, providing a valuable framework for the practical application of the system in real-world scenarios and under varying environmental conditions.

To make these findings applicable in dynamic design contexts, an Artificial Neural Network (ANN) was developed. The ANN proved to be a fundamental tool for:

- Evaluating intermediate operating points that were not covered by the time-consuming and labor-intensive original numerical calculations.

- Enabling the integration of the model into dynamic simulations, which require instantaneous evaluation of outlet conditions at each time-step in response to continuously changing boundary conditions.

The verification activities included a preliminary experimental validation phase. Tests conducted on a test rig specifically developed for a single module of a commercial heat exchanger yielded encouraging results, fully confirming the performance trends and behaviors previously observed through the numerical models.

The application of the developed models to real-world case studies in the building sector led to several strategically significant conclusions:

- Efficiency Optimization: It was observed that for any given boundary condition and required cooling load, a specific combination of air flow rate and recirculation ratio exists that maximizes the Energy Efficiency Ratio (EER). This allows the system to be managed such that, at any moment of the day, cooling is provided with the highest possible efficiency.
- Performance in Temperate and Humid Climates: In these contexts (such as the Bologna case study), although a substantial exchange battery is necessary to meet peak cooling demands, sizing for the most critical days ensures operation with extremely high EER values during all intermediate conditions, when the exchanger is not operating at its limits.
- Performance in Arid Climates: In low-humidity conditions, the system achieves exceptionally high EER values. Remarkably, due to the high evaporative potential of dry air, the required exchanger size does not exceed that needed for temperate climates, despite the significantly higher outdoor temperatures characteristic of the most critical days.
- Air Quality and Energy Savings: The system ensures excellent indoor air quality with minimal energy expenditure. Notably, air quality improves precisely when the cooling demand is at its peak, as the fresh air flow rates far exceed the

minimum hygiene ventilation requirements. Furthermore, by cooling the environment through air supply at temperatures consistently above the dew point, the dehumidification typical of conventional vapor compression systems is avoided. This eliminates the energy cost associated with latent heat removal, further optimizing the building's summer energy balance.

In conclusion, the Maisotsenko cycle proves to be a mature and versatile technology, capable of delivering excellent and sustainable performance, positioning itself as a viable alternative to conventional air conditioning systems across a wide range of climatic contexts.

Bibliography

[1] IEA, “Energy Technology Perspectives,” 2017. [Online]. Available: https://www.iea.org/reports/energy-technology-perspectives-2017

[2] IEA, “CO2 Emissions in 2023,” 2023. [Online]. Available: https://www.iea.org/reports/co2-emissions-in-2023

[3] IEA, “The Future of Cooling,” 2018. [Online]. Available: https://www.iea.org/reports/the-future-of-cooling

[4] A. M. Bahman, “Advancements in vapor compression air conditioning systems for high ambient temperature applications: A comprehensive review,” *Therm. Sci. Eng. Prog.*, vol. 67, 2025. doi: 10.1016/j.tsep.2025.104227.

[5] O. M. Zaki, R. H. Mohammed, and O. Abdelaziz, “Separate sensible and latent cooling technologies: A comprehensive review,” *Energy Convers. Manag.*, vol. 256, 2022. doi: 10.1016/j.enconman.2022.115380.

[6] A. Mota-Babiloni, J. Navarro-Esbrí, Á. Barragán-Cervera, F. Molés, and B. Peris, “Analysis based on EU Regulation No 517/2014 of new HFC/HFO mixtures as alternatives of high GWP refrigerants in refrigeration and HVAC systems,” *Int. J. Refrig.*, vol. 52, pp. 21-31, 2015. doi: 10.1016/j.ijrefrig.2014.12.021.

[7] United Nations Environment Programme (UNEP), “Annual report 2023,” 2023.

[8] W. Ketwong, T. Deethayat, and T. Kiatsiriroat, “Performance enhancement of air conditioner in hot climate by condenser cooling with cool air generated by direct evaporative cooling,” *Case Stud. Therm. Eng.*, vol. 26, 2021. doi: 10.1016/j.csite.2021.101127.

[9] IEA, “The Future of Cooling in China,” 2019. [Online]. Available: https://www.iea.org/reports/the-future-of-cooling-in-china

[10] P. M. Cuce and S. Riffat, "A state of the art review of evaporative cooling systems for building applications," *Renew. Sustain. Energy Rev.*, vol. 54, pp. 1240-1249, 2016. doi: 10.1016/j.rser.2015.10.066.

[11] K. J. Chua, S. K. Chou, W. M. Yang, and J. Yan, "Achieving better energy-efficient air conditioning - A review of technologies and strategies," *Applied Energy*, vol. 104, pp. 87-104, 2013. doi: 10.1016/j.apenergy.2012.10.037.

[12] ASHRAE, *ASHRAE handbook -heating, ventilating, and air-conditioning systems and equipment*, Atlanta, GA, USA: ASHRAE, 2012.

[13] D. Fitzgerald, "Evaporation," *American Society of Civil Engineers,* 1886.

[14] ASHRAE, *ASHRAE Handbook-Fundamentals*. Atlanta, GA, USA: ASHRAE, 2001.

[15] O. Amer, R. Boukhanouf, and H. Ibrahim, "A review of evaporative cooling technologies," *Int. J. Environ. Sci. Dev.*, vol. 6, no. 2, pp. 111-117, 2015. doi: 10.7763/IJESD.2015.V6.571.

[16] J. Lv, H. Xu, M. Zhu, Y. Dai, H. Liu, and Z. Li, "The performance and model of porous materials in the indirect evaporative cooling system: A review," *J. Build. Eng.*, vol. 41, 2021. doi: 10.1016/j.jobe.2021.102741.

[17] X. Zhao, S. Liu, and S. B. Riffat, "Comparative study of heat and mass exchanging materials for indirect evaporative cooling systems," *Build. Environ.*, vol. 43, no. 11, pp. 1902–1911, Nov. 2008. doi: 10.1016/j.buildenv.2007.11.009.

[18] D. M. Swindon, N. Chen, S. Mahoney, and R. W. Gilbert, Patent No.: US 10,151,497 B2, 2018

[19] P. Xu, X. Ma, T. M. O. Diallo, X. Zhao, K. Fancey, D. Li, and H. Chen, "Numerical investigation of the energy performance of a guideless irregular heat and mass exchanger with corrugated heat transfer surface for dew point cooling," *Energy*, vol. 109, pp. 803–817, 2016. doi: 10.1016/j.energy.2016.05.062.

[20] D. Pandelidis, A. Pacak, A. Cichoń, W. Gizicki, W. Worek, and S. Cetin, "Experimental study of plate materials for evaporative air coolers," *Int. Commun. Heat Mass Transf.*, vol. 120, 2021. doi: 10.1016/j.icheatmasstransfer.2020.105049.

[21] F. Al-Sulaiman, "Evaluation of the performance of local fibers in evaporative cooling," *Energy Convers. Manag.*, vol. 43, no. 16, pp. 2267-2273, 2002. doi: 10.1016/S0196-8904(01)00121-2.

[22] D. Abada, C. Maalouf, O. Sotehi, D. Rouag-Saffidine, G. Polidori, A. F. Boudjabi, and Z. Derghout, "Performance evaluation of fabrics for evaporative cooling applications," *Energy Build.*, vol. 266, 2022. doi: 10.1016/j.enbuild.2022.112120.

[23] J. Zhi, C. Dong, M. Guo, R. Qi, and L.-zhi Zhang, "Wettability and performance enhancement with durable super-hydrophilic surfaces for plastic liquid desiccant dehumidification systems," *Energy Build.*, vol. 187, pp. 77–85, 2019. doi: 10.1016/j.enbuild.2019.01.041.

[24] Z. Duan, X. Zhao, C. Zhan, X. Dong, and H. Chen, "Energy saving potential of a counter-flow regenerative evaporative cooler for various climates of China: Experiment-based evaluation," *Energy Build.*, vol. 148, pp. 199–210, 2017. doi: 10.1016/j.enbuild.2017.04.012.

[25] Z. Duan, M. Wang, X. Dong, J. Liu, and X. Zhao, "Experimental and numerical investigation of wicking and evaporation performance of fibrous materials for evaporative cooling," *Energy Build.*, vol. 255, 2022. doi: 10.1016/j.enbuild.2021.111675.

[26] E. V. Gómez, F. J. R. Martínez, F. V. Diez, M. J. M. Leyva, and R. H. Martín, "Description and experimental results of a semi-indirect ceramic evaporative cooler," *Int. J. Refrig.*, vol. 28, no. 5, pp. 654–662, 2005. doi: 10.1016/j.ijrefrig.2005.01.004.

[27] S.-H. Sellam, A. Moummi, C.-E. Mehdid, A. Rouag, A. H. Benmachiche, M.-A. Melhegueg, and A. Benchabane, "Experimental performance evaluation of date palm fibers for a direct evaporative cooler operating in hot and arid climate," *Case Studies in Thermal Engineering*, vol. 35, 2022. doi: 10.1016/j.csite.2022.102119.

[28] D. Bishoyi and K. Sudhakar, "Experimental performance of a direct evaporative cooler in composite climate of India," *Energy Build.*, vol. 153, pp. 190–200, 2017. doi: 10.1016/j.enbuild.2017.08.014.

[29] J. K. Jain and D. A. Hindoliya, "Experimental performance of new evaporative cooling pad materials," *Sustain. Cities Soc.*, vol. 1, no. 4, pp. 252–256, 2011. doi: 10.1016/j.scs.2011.07.005.

[30] P. Abohorlu Doğramacı, S. Riffat, G. Gan, and D. Aydın, "Experimental study of the potential of eucalyptus fibres for evaporative cooling," *Renew. Energy*, vol. 131, pp. 250–260, 2019. doi: 10.1016/j.renene.2018.07.005.

[31] R. Rawangkul, J. Khedari, J. Hirunlabh, and B. Zeghmati, "Performance analysis of a new sustainable evaporative cooling pad made from coconut coir," *Int. J. Sustain. Eng.*, vol. 1, no. 2, pp. 117–131, 2008. doi: 10.1080/19397030802326726.

[32] N. Soponpongpipat and S. Kositchaimongkol, "Recycled high-density polyethylene and rice husk as a wetted pad in evaporative cooling system," *Am. J. Appl. Sci.*, vol. 8, no. 2, pp. 186–191, 2011. doi: 10.3844/ajassp.2011.186.191.

[33] T. Gunhan, V. Demir, and A. K. Yagcioglu, "Evaluation of the suitability of some local materials as cooling pads," *Biosyst. Eng.*, vol. 96, no. 3, pp. 369–377, 2007. doi: 10.1016/j.biosystemseng.2006.12.001.

[34] X. Chen, Y. Su, D. Aydin, X. Zhang, Y. Ding, D. Reay, R. Low, and S. Riffat, "Experimental investigations of polymer hollow fibre integrated evaporative

cooling system with the fibre bundles in a spindle shape," *Energy Build.*, vol. 154, pp. 166–174, 2017. doi: 10.1016/j.enbuild.2017.08.068.

[35] A. Laknizi, A. Ben Abdellah, M. Faqir, E. Essadiqi, and S. Dhimdi, "Performance characterization of a direct evaporative cooling pad based on pottery material," *Int. J. Sustain. Eng.*, vol. 14, no. 1, pp. 46–56, 2021. doi: 10.1080/19397038.2019.1677800.

[36] E. Ibrahim, L. Shao, and S. B. Riffat, "Performance of porous ceramic evaporators for building cooling application," *Energy Build.*, vol. 35, no. 9, pp. 941–949, 2003. doi: 10.1016/S0378-7788(03)00019-7.

[37] K. Tan, Y. Qin, T. Du, L. Li, L. Zhang, and J. Wang, "Biochar from waste biomass as hygroscopic filler for pervious concrete to improve evaporative cooling performance," *Constr. Build. Mater.*, vol. 287, 2021. doi: 10.1016/j.conbuildmat.2021.123078.

[38] S. He, Z. Guan, H. Gurgenci, K. Hooman, Y. Lu, and A. M. Alkhedhair, "Experimental study of film media used for evaporative pre-cooling of air," *Energy Convers. Manag.*, vol. 87, pp. 874–884, 2014. doi: 10.1016/j.enconman.2014.07.084.

[39] S. A. Nada, H. F. Elattar, M. A. Mahoud, and A. Fouda, "Performance enhancement and heat and mass transfer characteristics of direct evaporative building free cooling using corrugated cellulose papers," *Energy*, vol. 211, 2020. doi: 10.1016/j.energy.2020.118678.

[40] M. Barzegar, M. Layeghi, G. Ebrahimi, Y. Hamzeh, and M. Khorasani, "Experimental evaluation of the performances of cellulosic pads made out of Kraft and NSSC corrugated papers as evaporative media," *Energy Convers. Manag.*, vol. 54, no. 1, pp. 24–29, 2012. doi: 10.1016/j.enconman.2011.09.016.

[41] A. Malli, H. R. Seyf, M. Layeghi, S. Sharifian, and H. Behravesh, "Investigating the performance of cellulosic evaporative cooling pads," *Energy Convers. Manag.*, vol. 52, no. 7, pp. 2598–2603, 2011. doi: 10.1016/j.enconman.2010.12.015.

[42] L. Rong, P. Pedersen, T. L. Jensen, S. Morsing, and G. Zhang, "Dynamic performance of an evaporative cooling pad investigated in a wind tunnel for application in hot and arid climate," *Biosyst. Eng.*, vol. 156, pp. 173–182, 2017. doi: 10.1016/j.biosystemseng.2017.02.003.

[43] A. E. Kabeel and M. M. Bassuoni, "A simplified experimentally tested theoretical model to reduce water consumption of a direct evaporative cooler for dry climates," *Int. J. Refrig.*, vol. 82, pp. 487–494, 2017. doi: 10.1016/j.ijrefrig.2017.06.010.

[44] T. Adekanye, K. O. Babaremu, A. Okunola, and K. Babaremu, "Evaluation of an active evaporative cooling device for storage of fruits and vegetables," *CIGR Journal*, vol. 21, no. 1, 2019.

[45] E. A. Awafo, S. Nketsiah, M. Alhassan, and E. Appiah-Kubi, "Design, Construction, and Performance Evaluation of an Evaporative Cooling System for Tomatoes Storage," *Agric. Eng.*, vol. 24, no. 4, pp. 1–12, 2020. doi: 10.1515/agriceng-2020-0031.

[46] A. Franco, D. L. Valera, A. Madueño, and A. Peña, "Influence of water and air flow on the performance of cellulose evaporative cooling pads used in mediterranean greenhouses," *Trans. ASABE*, vol. 53, no. 2, pp. 565–576, 2015. 10.13140/RG.2.1.4506.3522.

[47] M. Hnayno, A. Chehade, H. Klaba, G. Polidori, and C. Maalouf, "Experimental investigation of an optimized indirect free cooling system including a dry cooler equipped with evaporative cooling pads for data center," *Energy Rep.*, vol. 9, pp. 460–469, 2023. doi: 10.1016/j.egyr.2023.12.005.

[48] Stabat P., D. Marchio, and M. Orphelin, "Pre-design and design tools for evaporative cooling," *ASHRAE Trans.*, vol. 107, pp. 643-652, 2001.

[49] J. K. Jain and D. A. Hindoliya, "Correlations for saturation efficiency of evaporative cooling pads," *J. Inst. Eng. India Ser. C*, vol. 95, no. 1, pp. 5–10, 2014. doi: 10.1007/s40032-014-0098-0.

[50] J. M. Wu, X. Huang, and H. Zhang, "Theoretical analysis on heat and mass transfer in a direct evaporative cooler," *Appl. Therm. Eng.*, vol. 29, no. 5–6, pp. 980–984, 2009. doi: 10.1016/j.applthermaleng.2008.05.016.

[51] J. R. Camargo, C. D. Ebinuma, and J. L. Silveira, "Experimental performance of a direct evaporative cooler operating during summer in a Brazilian city," *Int. J. Refrig.*, vol. 28, no. 7, pp. 1124–1132, 2005. doi: 10.1016/j.ijrefrig.2004.12.011.

[52] G. Heidarinejad, M. Bozorgmehr, S. Delfani, and J. Esmaeelian, "Experimental investigation of two-stage indirect/direct evaporative cooling system in various climatic conditions," *Build. Environ.*, vol. 44, no. 10, pp. 2073–2079, 2009. doi: 10.1016/j.buildenv.2009.02.017.

[53] B. Porumb, P. Ungureşan, L. F. Tutunaru, A. Şerban, and M. BĂlan, "A Review of Indirect Evaporative Cooling Operating Conditions and Performances," *Energy Procedia*, vol. 85, pp. 452–460, 2016. doi: 10.1016/j.egypro.2015.12.226.

[54] F. Comino, S. Milani, S. De Antonellis, C. M. Joppolo, and M. Ruiz de Adana, "Simplified performance correlation of an indirect evaporative cooling system: Development and validation," *Int. J. Refrig.*, vol. 88, pp. 307–317, 2018. doi: 10.1016/j.ijrefrig.2018.02.002.

[55] S. De Antonellis, L. Cignatta, C. Facchini, and P. Liberati, "Effect of heat exchanger plates geometry on performance of an indirect evaporative cooling

system," *Appl. Therm. Eng.*, vol. 173, 2020. doi: 10.1016/j.applthermaleng.2020.115200.

[56] W. Y. Li, Y. C. Li, L.-yue Zeng, and J. Lu, "Comparative study of vertical and horizontal indirect evaporative cooling heat recovery exchangers," *Int. J. Heat Mass Transf.*, vol. 124, pp. 1245–1261, 2018. doi: 10.1016/j.ijheatmasstransfer.2018.04.041.

[57] S. De Antonellis, C. M. Joppolo, P. Liberati, S. Milani, and L. Molinaroli, "Experimental analysis of a cross flow indirect evaporative cooling system," *Energy Build.*, vol. 121, pp. 130–138, 2016. doi: 10.1016/j.enbuild.2016.03.076.

[58] W. Shi, Y. Min, X. Ma, Y. Chen, and H. Yang, "Performance evaluation of a novel plate-type porous indirect evaporative cooling system: An experimental study," *J. Build. Eng.*, vol. 48, 2022. doi: 10.1016/j.jobe.2021.103898.

[59] W. Shi, Y. Min, X. Ma, Y. Chen, and H. Yang, "Dynamic performance evaluation of porous indirect evaporative cooling system with intermittent spraying strategies," *Appl. Energy*, vol. 311, 2022. doi: 10.1016/j.apenergy.2022.118598.

[60] L. Gillan, "Maisotsenko cycle for cooling processes," *Int. J. Energy Clean Environ.*, vol. 9, no. 1-3, pp. 47-64, 2008. doi: 10.1615/InterJEnerCleanEnv.v9.i1-3.50

[61] Z. Duan, C. Zhan, X. Zhang, M. Mustafa, X. Zhao, B. Alimohammadisagvand, and A. Hasan, "Indirect evaporative cooling: Past, present and future potentials," *Renewable and Sustainable Energy Reviews*, vol. 16, no. 9, pp. 6823-6850, 2012. doi: 10.1016/j.rser.2012.07.007.

[62] U. Sajjad, N. Abbas, K. Hamid, S. Abbas, I. Hussain, S. M. Ammar, M. Sultan, H. M. Ali, M. Hussain, T.-ur-Rehman, and C. C. Wang, "A review of recent advances in indirect evaporative cooling technology," *Int. Commun. Heat Mass Transf.*, vol. 122, 2021. doi: 10.1016/j.icheatmasstransfer.2021.105140.

[63] R. H. Mohammed, M. El-Morsi, and O. Abdelaziz, "Indirect evaporative cooling for buildings: A comprehensive patents review," *J. Build. Eng.*, vol. 50, 2022. doi: 10.1016/j.jobe.2022.104158.

[64] B. Porumb, P. Ungureşan, L. F. Tutunaru, A. Şerban, and M. BĂlan, "A Review of Indirect Evaporative Cooling Technology," *Energy Procedia*, vol. 85, pp. 461-471, 2016. doi: 10.1016/j.egypro.2015.12.228.

[65] F. Bruno, "On-site experimental testing of a novel dew point evaporative cooler," *Energy Build.*, vol. 43, no. 12, pp. 3475–3483, 2011. doi: 10.1016/j.enbuild.2011.09.013.

[66] X. Cui, W. Tian, X. Yang, Q. Kong, Y. Chai, and L. Jin, "Experimental study on a cross-flow regenerative indirect evaporative cooling system," *Energy Procedia*, vol. 152, pp. 395-400, 2018. doi: 10.1016/j.egypro.2018.09.163.

[67] S. Kashyap, J. Sarkar, and A. Kumar, "Comparative performance analysis of different novel regenerative evaporative cooling device topologies," *Appl. Therm. Eng.*, vol. 176, 2020. doi: 10.1016/j.applthermaleng.2020.115474.

[68] M. S. Alam, M. N. B. M. Zubir, M. R. B. Muhamad, S. N. Kazi, H. F. Öztop, S. Abdullah, and K. Shaikh, "A technological review of dew point evaporative cooling: experimental, analytical, numerical and optimization perspectives," *J. Build. Eng.*, vol. 91, 2024. doi: 10.1016/j.jobe.2024.109544.

[69] B. Rahmati, A. M. Jadidi, and M. S. Valipour, "Enhancing the performance of an M-cycle based tubular indirect evaporative cooler by mesh screens," *Int. Commun. Heat Mass Transf.*, vol. 156, 2024, doi: 10.1016/j.icheatmasstransfer.2024.107575.

[70] D. Zube and L. Gillan, "Evaluating Coolerado Corporation's heat-mass exchanger performance through experimental analysis," *Int. J. Energy Clean*

Environ., vol. 12, no. 2-4, pp. 101-116, 2011. doi: 10.1615/InterJEnerCleanEnv.2012005839

[71] J. Lin, R. Z. Wang, M. Kumja, T. D. Bui, and K. J. Chua, "Modelling and experimental investigation of the cross-flow dew point evaporative cooler with and without dehumidification," *Appl. Therm. Eng.*, vol. 121, pp. 1–13, 2017. doi: 10.1016/j.applthermaleng.2017.04.047.

[72] M. Jradi and S. Riffat, "Experimental and numerical investigation of a dew-point cooling system for thermal comfort in buildings," *Appl. Energy*, vol. 132, pp. 524–535, 2014. doi: 10.1016/j.apenergy.2014.07.040.

[73] O. Khalid, M. Ali, N. A. Sheikh, H. M. Ali, and M. Shehryar, "Experimental analysis of an improved Maisotsenko cycle design under low velocity conditions," *Appl. Therm. Eng.*, vol. 95, pp. 288–295, 2016. doi: 10.1016/j.applthermaleng.2015.11.030.

[74] D. Pandelidis and S. Anisimov, "Numerical analysis of the heat and mass transfer processes in selected M-Cycle heat exchangers for the dew point evaporative cooling," *Energy Convers. Manag.*, vol. 90, pp. 62–83, 2015. doi: 10.1016/j.enconman.2014.11.008.

[75] J. Lee and D.-Y. Lee, "Design, fabrication, and testing of a compact regenerative evaporative cooler with finned channels," *Int. J. Energy Clean Environ.*, vol. 12, no. 2-4, pp. 221-237, 2011. doi: 10.1615/InterJEnerCleanEnv.2012006393.

[76] R. Boukhanouf, H. G. Ibrahim, A. Alharbi, and M. Kanzari, "Investigation of an evaporative cooler for buildings in hot and dry climates," *J. Clean Energy Technol.*, vol. 2, no. 3, pp. 221–225, 2014. doi: 10.7763/jocet.2014.v2.127.

[77] J. Lee, B. Choi, and D. Y. Lee, "Comparison of configurations for a compact regenerative evaporative cooler," *Int. J. Heat Mass Transf.*, vol. 65, pp. 192–198, 2013. doi: 10.1016/j.ijheatmasstransfer.2013.05.068.

[78] Y. Liu, Y. G. Akhlaghi, X. Zhao, and J. Li, "Experimental and numerical investigation of a high-efficiency dew-point evaporative cooler," *Energy Build.*, vol. 197, pp. 120–130, 2019. doi: 10.1016/j.enbuild.2019.05.038.

[79] P. Xu, X. Ma, X. Zhao, and K. Fancey, "Experimental investigation of a super performance dew point air cooler," *Appl. Energy*, vol. 203, pp. 761–777, 2017. doi: 10.1016/j.apenergy.2017.06.095.

[80] A. E. Kabeel and M. Abdelgaied, "Numerical and experimental investigation of a novel configuration of indirect evaporative cooler with internal baffles," *Energy Convers. Manag.*, vol. 126, pp. 526–536, 2016. doi: 10.1016/j.enconman.2016.08.028.

[81] K. Wu, S. Wang, J. Lin, Y. Shao, F. Gao, and K. J. Chua, "The enhanced dew-point evaporative cooling with a macro-roughened structure," *Int. J. Heat Mass Transf.*, vol. 219, 2024. doi: 10.1016/j.ijheatmasstransfer.2023.124898.

[82] R. Boukhanouf, O. Amer, H. Ibrahim, and J. Calautit, "Design and performance analysis of a regenerative evaporative cooler for cooling of buildings in arid climates," *Build. Environ.*, vol. 142, pp. 1–10, 2018. doi: 10.1016/j.buildenv.2018.06.004.

[83] J. Castillo-González, F. Comino, F. J. Navas-Martos, and M. Ruiz de Adana, "Manufacturing and experimental analysis of a dew-point indirect evaporative cooler using fused deposition modelling 3D printing and polymeric materials," *Appl. Therm. Eng.*, vol. 230, 2023. doi: 10.1016/j.applthermaleng.2023.120683.

[84] B. Hua, H. Sadighi Dizaji, F. Aldawi, H. Loukil, A. Mouldi, and M. A. E. Damian, "Developing an experiment-based strong machine learning model for performance prediction and full analysis of Maisotsenko dewpoint evaporative air cooler," *Energy*, vol. 310, 2024. doi: 10.1016/j.energy.2024.133179.

[85] P. Atkins and J. de Paula, *Atkins' physical chemistry*, 8th ed. New York, NY, USA: W. H. Freeman and Company, 2006.

[86] F. W. Murray, "On the computation of saturation vapor pressure," *J. Appl. Meteorol. Climatol.*, vol. 6, no. 1, pp. 203-204, 1967. doi: 10.1175/1520-0450(1967)006<0203:OTCOSV>2.0.CO;2

[87] R. K. Shah and A. L. London, Laminar flow forced convection in ducts, New York, NY, USA: Academic Press, 1978.

[88] R. Di Cess and E. C. Shaffer, "Heat transfer to laminar flow between parallel plates with a prescribed wall heat flux," *Appl. Sci. Res.*, vol. 8, pp. 339–344, 1959. doi: 10.1007/BF00411758.

[89] R. Siegel, E. M. Sparrow, and T. M. Hallman, "Steady laminar heat transfer in a circular tube with prescribed wall heat flux," *Appl. Sci. Res.*, vol. 7, pp. 386–392 1958. doi: 10.1007/BF03184999.

[90] W. K. Lewis, "The evaporation of a liquid into a gas," *Trans. ASME*, vol. 44, pp. 332-340, 1922. doi: 10.1115/1.4058176.

[91] A. Quarteroni, R. Sacco, and F. Saleri, *Numerical Mathematics*, New York, NY, USA: Springer, 2000.

[92] A. Hasan, "Indirect evaporative cooling of air to a sub-wet bulb temperature," *Appl. Therm. Eng.*, vol. 30, no. 16, pp. 2460–2468, 2010, doi: 10.1016/j.applthermaleng.2010.06.017.

[93] F. Merkel, Verdunstungskühlung, VDI Forschungsarbeiten, no. 275, Berlin, Germany, 1925.

[94] S. A. Kalogirou, "Artificial neural networks in renewable energy systems applications: a review," *Renew. Sustain. Energy Rev.*, vol. 5, no. 4, pp. 373-401, 2001. doi: 10.1016/S1364-0321(01)00006-5.

[95] S. S. Haykin, *Neural networks and learning machines*, 3rd ed., Upper Saddle River, NJ, USA: Pearson, 2009.

[96] C. M. Bishop, *Pattern recognition and machine learning*, New York, NY, USA: Springer, 2006.

[97] K. Hornik, M. Stinchombe, and H. White, "Multilayer feedforward networks are universal approximators," *Neural Networks*, vol. 2, no. 5, pp. 359-366, 1989. doi: 10.1016/0893-6080(89)90020-8.

[98] I. Goodfellow, Y. Bengio, and A. Courville, *Deep Learning*, Cambridge, MA, USA: MIT Press, 2016.

[99] G. Montúfar, R. Pascanu, K. Cho, and Y. Bengio, "On the Number of Linear Regions of Deep Neural Networks," *Neural Information Processing System*, 2014. doi: 10.48550/arXiv.1402.1869.

[100] S. Hochreiter, "The vanishing gradient problem during learning recurrent neural nets and problem solutions," *Int. J. Uncertainty Fuzziness Knowl.-Based Syst.*, vol. 6, no. 2, pp. 107-116, 1998. doi: 10.1142/S0218488598000094.

[101] Y. LeCun, L. Bottou, G. B. Orr, and K.-R. Müller, "Efficient BackProp," *Neural Networks: Tricks of the Trade*, vol. 1524, 1998. doi: 10.1007/3-540-49430-8_2.

[102] D. E. Rumelhart, G. E. Hinton, and R. J. Williams, "Learning representations by back-propagating errors," *Nature*, vol. 323, pp. 533–536, 1986. doi: 10.1038/323533a0.

[103] D. J. C. Mackay, "A practical bayesian framework for backpropagation networks," *Neural Computation*, vol. 4, no. 3, pp. 448-472, 1992. doi: 10.1162/neco.1992.4.3.448.

[104] D. W. Marquardt, "An algorithm for least-squares estimation of nonlinear parameters," *J. Soc. Ind. Appl. Math.*, vol. 11, no. 2, pp. 431-441, 1963. [Online]. Available: http://www.jstor.org/stable/2098941.

[105] X. Glorot and Y. Bengio, "Understanding the difficulty of training deep feedforward neural networks," *Proceedings of Machine Learning Research*, vol. 9, pp. 249-256, 2010. [Online]. Available: https://proceedings.mlr.press/v9/glorot10a.html.

[106] F. P. Incropera, D. P. Dewitt, T. L. Bergman, and A. S. Lavine, *Fundamentals of heat and mass transfer*, 6th ed. John Wiley & Sons, 2007.

[107] C. A. Harper, *Modern Plastics Handbook,* New York, NY, USA: McGraw-Hill, 2000.

[108] B. Riangvilaikul and S. Kumar, "An experimental study of a novel dew point evaporative cooling system," *Energy Build.*, vol. 42, no. 5, pp. 637–644, 2010. doi: 10.1016/j.enbuild.2009.10.034.

[109] F. Fakhrabadi and F. Kowsary, "Optimal design of a regenerative heat and mass exchanger for indirect evaporative cooling," *Appl. Therm. Eng.*, vol. 102, pp. 1384–1394, 2016. doi: 10.1016/j.applthermaleng.2016.03.115.

[110] M. T. Hagan and M. B. Menhaj, "Training feedforward networks with the Marquardt algorithm," *IEEE Trans. Neural Netw.*, vol. 5, no. 6, pp. 989-993, 1994. doi: 10.1109/72.329697.

[111] L. Pérez-Lombard, J. Ortiz, and C. Pout, "A review on buildings energy consumption information," *Energy Build.*, vol. 40, no. 3, pp. 394–398, 2008. doi: 10.1016/j.enbuild.2007.03.007.

[112] Y. Al horr, M. Arif, M. Katafygiotou, A. Mazroei, A. Kaushik, and E. Elsarrag, "Impact of indoor environmental quality on occupant well-being and comfort: A review of the literature," *Int. J. Sustain. Built Environ.*, vol. 5, no. 1, pp. 1-11, 2016. doi: 10.1016/j.ijsbe.2016.03.006.

[113] Y. Al Horr, M. Arif, A. Kaushik, A. Mazroei, E. Elsarrag, and S. Mishra, "Occupant productivity and indoor environment quality: A case of GSAS," *Int. J. Sustain. Built Environ.*, vol. 6, no. 2, pp. 476–490, 2017. doi: 10.1016/j.ijsbe.2017.11.001.

[114] R. J. de Dear, T. Akimoto, E. A. Arens, G. Brager, C. Candido, K. W. D. Cheong, B. Li, N. Nishihara, S. C. Sekhar, S. Tanabe, J. Toftum, H. Zhang, and Y. Zhu, "Progress in thermal comfort research over the last twenty years," *Indoor Air*, vol. 23, no. 6, pp. 442-461, 2013. doi: 10.1111/ina.12046.

[115] W. J. Fisk, "Review of health and productivity gains from better IEQ," 2000. [Online]. Available: https://digital.library.unt.edu/ark:/67531/metadc782978/

[116] M. G. Apte, W. J. Fisk, and J. M. Daisey, "Associations between indoor CO2 concentrations and sick building syndrome symptoms in U.S. office buildings: an analysis of the 1994-1996 BASE study data," *Indoor Air*, vol. 10, no. 4, pp. 246–257, 2000. doi: 10.1034/j.1600-0668.2000.010004246.x

[117] P. V. Dorizas, M. N. Assimakopoulos, and M. Santamouris, "A holistic approach for the assessment of the indoor environmental quality, student productivity, and energy consumption in primary schools," *Environ. Monit. Assess.*, vol. 187, 2015. doi: 10.1007/s10661-015-4503-9.

[118] J. M. Daisey, W. J. Angell, and M. G. Apte, "Indoor air quality, ventilation and health symptoms in schools: An analysis of existing information," *Indoor Air*, vol. 13, no. 1, pp. 53-64, 2003. doi: 10.1034/j.1600-0668.2003.00153.x.

[119] Y. Fan, X. Cao, J. Zhang, D. Lai, and L. Pang, "Short-term exposure to indoor carbon dioxide and cognitive task performance: A systematic review and meta-analysis," *Build. Environ.*, vol. 237, 2023. doi: 10.1016/j.buildenv.2023.110331.

[120] B. Du, M. C. Tandoc, M. L. Mack, and J. A. Siegel, "Indoor CO2 concentrations and cognitive function: A critical review," *Indoor Air*, vol. 30, no. 6, pp. 1067-1082, 2020. doi: 10.1111/ina.12706.

[121] N. Zhang, C. Liu, C. Hou, W. Wang, Q. Yuan, and W. Gao, "The impact of indoor carbon dioxide exposure on human brain activity: A systematic review and meta-analysis based on studies utilizing electroencephalogram signals," *Build. Environ.*, vol. 259, 2024. doi: 10.1016/j.buildenv.2024.111687.

[122] W. J. Fisk, "The ventilation problem in schools: literature review," *Indoor Air*, vol. 27, no. 6, pp. 1039-1051, 2017. doi: 10.1111/ina.12403.

[123] P. Wargocki and D. P. Wyon, "The effects of moderately raised classroom temperatures and classroom ventilation rate on the performance of schoolwork by children (RP-1257)," *HVAC&R Res.*, vol. 13, no. 2, pp. 193–220, 2007. doi: 10.1080/10789669.2007.10390951.

[124] P. Wargocki, "The effects of ventilation in homes on health," *Int. J. Vent.*, vol. 12, no. 2, 2013. doi: 10.1080/14733315.2013.11684005.

[125] O. A. Seppänen, W. J. Fisk, and M. J. Mendell, "Association of ventilation rates and CO2 concentrations with health and other responses in commercial and institutional buildings," *Indoor Air*, vol. 9, no. 4, pp. 226-252, 1999. doi: 10.1111/j.1600-0668.1999.00003.x

[126] B. K. Thirunagari, R. Garaga, and S. H. Kota, "Association of ventilation rates with building design in various built environments: A Critical Review," *Curr Pollution Rep*, vol. 9, pp. 569-589, 2023. doi: 10.1007/s40726-023-00271-w.

[127] S. S. Korsavi, A. Montazami, and D. Mumovic, "The impact of indoor environment quality (IEQ) on school children's overall comfort in the UK; a regression approach," *Build. Environ.*, vol. 185, 2020. doi: 10.1016/j.buildenv.2020.107309.

[128] P. Wargocki and D. P. Wyon, "Providing better thermal and air quality conditions in school classrooms would be cost-effective," *Build. Environ.*, vol. 59, pp. 581–589, 2013. doi: 10.1016/j.buildenv.2012.10.007.

[129] P. Wargocki and D. P. Wyon, "Ten questions concerning thermal and indoor air quality effects on the performance of office work and schoolwork," *Build. Environ.*, vol. 112, pp. 359–366, 2017. doi: 10.1016/j.buildenv.2016.11.020.

[130] I. Sarbu and C. Pacurar, "Experimental and numerical research to assess indoor environment quality and schoolwork performance in university classrooms," *Build. Environ.*, vol. 93, no. P2, pp. 141–154, 2015. doi: 10.1016/j.buildenv.2015.06.022.

[131] R. Kosonen and F. Tan, "Assessment of productivity loss in air-conditioned buildings using PMV index," *Energy Build.*, vol. 36, no. 10, pp. 987–993, 2004. doi: 10.1016/j.enbuild.2004.06.021.

[132] M. J. Mendell, G. M. Naco, T. G. Wilcox, and W. K. Sieber, "Environmental risk factors and work-related lower respiratory symptoms in 80 office buildings: An exploratory analysis of NIOSH data," *Am. J. Ind. Med.*, vol. 43, no. 6, pp. 630–641, 2003. doi: 10.1002/ajim.10211.

[133] M. J. Mendell, W. J. Fisk, K. Kreiss, H. Levin, D. Alexander, W. S. Cain, J. R. Girman, C. J. Hines, P. A. Jensen, D. K. Milton, L. P. Rexroat, and K. M. Wallingford, "Improving the health of workers in indoor environments: priority research needs for a national occupational research agenda," *Am. J. Public Health*, vol. 92, no. 9, pp. 1430-1440, 2002. doi: 10.2105/AJPH.92.9.1430.

[134] M. Guo, P. Xu, T. Xiao, R. He, M. Dai, and S. L. Miller, "Review and comparison of HVAC operation guidelines in different countries during the COVID-19 pandemic," *Build. Environ*, vol. 187, 2021. doi: 10.1016/j.buildenv.2020.107368.

[135] T. Lipinski, D. Ahmad, N. Serey, and H. Jouhara, "Review of ventilation strategies to reduce the risk of disease transmission in high occupancy buildings," *Int. J. Thermofluids*, vol. 7–8, 2020. doi: 10.1016/j.ijft.2020.100045.

[136] L. V. de Abreu-Harbich, V. L. A. Chaves, and M. C. G. O. Brandstetter, "Evaluation of strategies that improve the thermal comfort and energy saving of a classroom of an institutional building in a tropical climate," *Build. Environ.*, vol. 135, pp. 257–268, 2018. doi: 10.1016/j.buildenv.2018.03.017.

[137] UNI/TR 11552:2014. Abaco delle strutture costituenti l'involucro opaco degli edifici - Parametri termofisici.

[138] UNI 10351:2021. Materiali da costruzione - Proprietà termoigrometriche - Procedura per la scelta dei valori di progetto.

[139] UNI EN ISO 10456:2008. Materiali e prodotti per edilizia - Proprietà igrometriche - Valori tabulati di progetto e procedimenti per la determinazione dei valori termici dichiarati e di progetto.

[140] UNI EN ISO 6946:2018. Componenti ed elementi per edilizia - Resistenza termica e trasmittanza termica - Metodi di calcolo.

[141] UNI CEN/TR 16798-2:2020. Prestazioni energetiche degli edifici - Ventilazione per gli edifici - Parte 2: Interpretazione dei requisiti della norma EN 16798-1 - Parametri di input ambientale interno per la progettazione e la valutazione delle prestazioni energetiche degli edifici in relazione alla qualità dell'aria interna, all'ambiente termico, all'illuminazione e all'acustica (Modulo M1-6).

[142] UNI EN 16798-1:2019. Prestazione energetica degli edifici - Ventilazione per gli edifici - Parte 1: Parametri di ingresso dell'ambiente interno per la progettazione e la valutazione della prestazione energetica degli edifici in relazione alla qualità dell'aria interna, all'ambiente termico, all'illuminazione e all'acustica - Modulo M1-6.

[143] UNI EN ISO 8996:2022. Ergonomia dell'ambiente termico - Determinazione del metabolismo energetico.

[144] UNI EN ISO 7730:2006. Ergonomia degli ambienti termici - Determinazione analitica e interpretazione del benessere termico mediante il calcolo degli indici PMV e PPD e dei criteri di benessere termico locale.

Appendix

This appendix provides a comprehensive collection of 3D performance maps generated using the Hasan model. These figures illustrate the sensitivity of $T_{d,o}$ to the full range of inlet temperatures and specific humidities investigated. By presenting the results for various combinations of r_m and $v_{d,in}$, these global representations provide an overall visualization of the HMX behavior under different operating conditions, complementing the detailed parametric analysis discussed in Chapter 6.2.3.

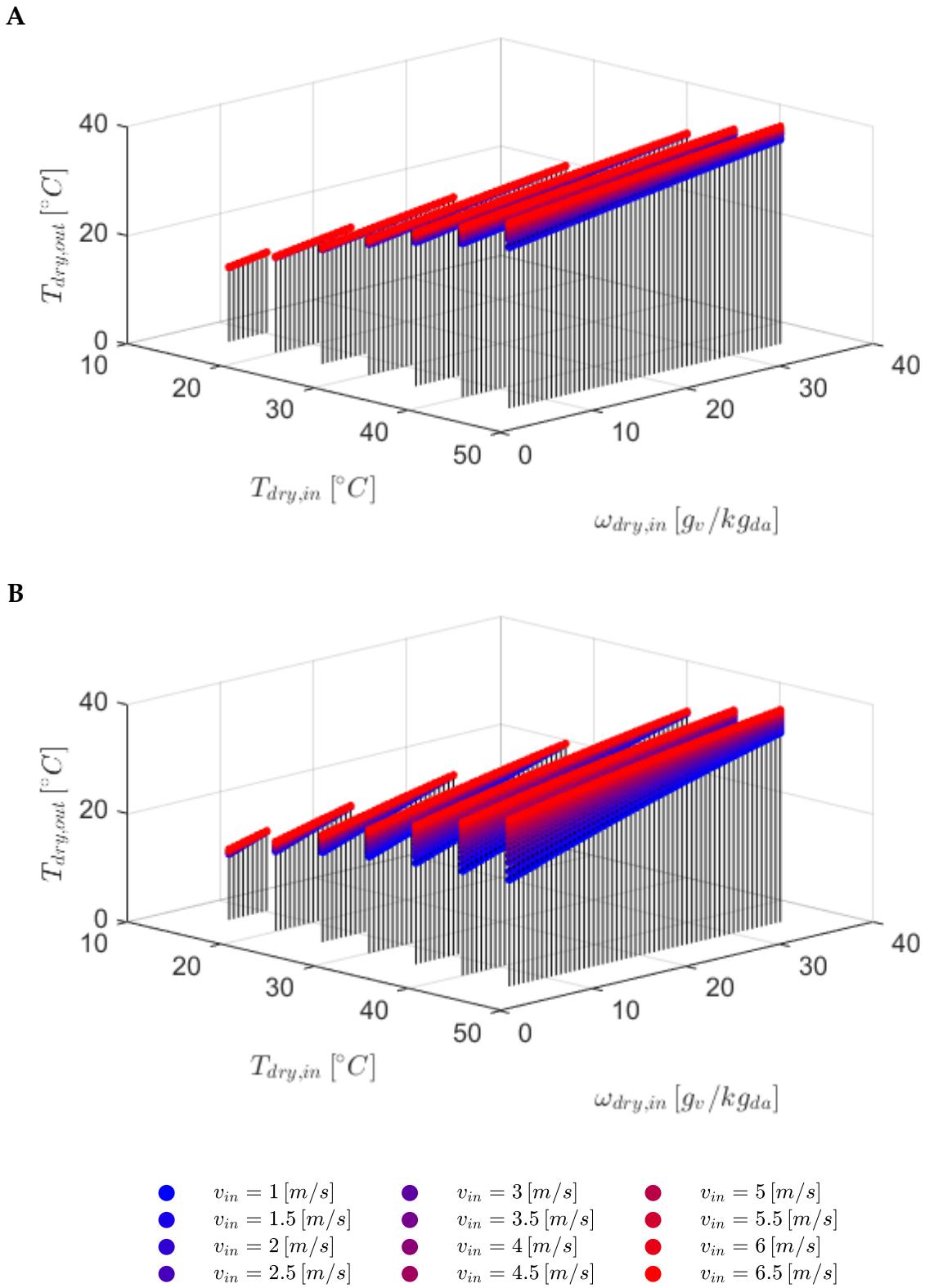

Figure A.1. Product temperature for an M-cycle HMX with a length of 0.2 m *and a channel height of* 2 mm*, obtained using the Hasan model, as a function of inlet dry-bulb temperature, inlet specific humidity, and inlet fluid velocity for recirculation ratio of* 10 % *(A) and* 20 % *(B).*

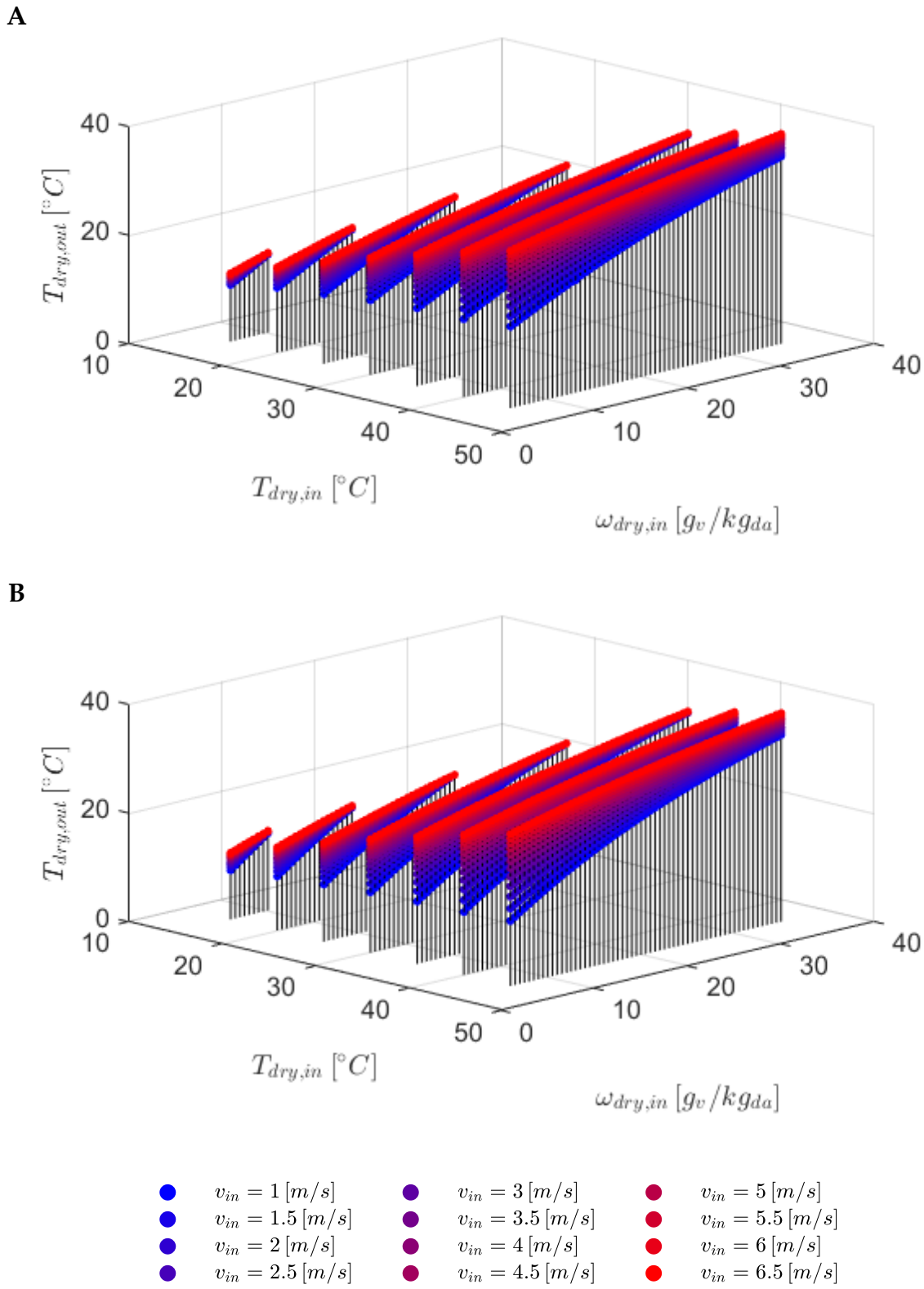

Figure A.2. Product temperature for an M-cycle HMX with a length of 0.2 m *and a channel height of* 2 mm*, obtained using the Hasan model, as a function of inlet dry-bulb temperature, inlet specific humidity, and inlet fluid velocity for recirculation ratio of* 30 % *(A) and* 40 % *(B).*

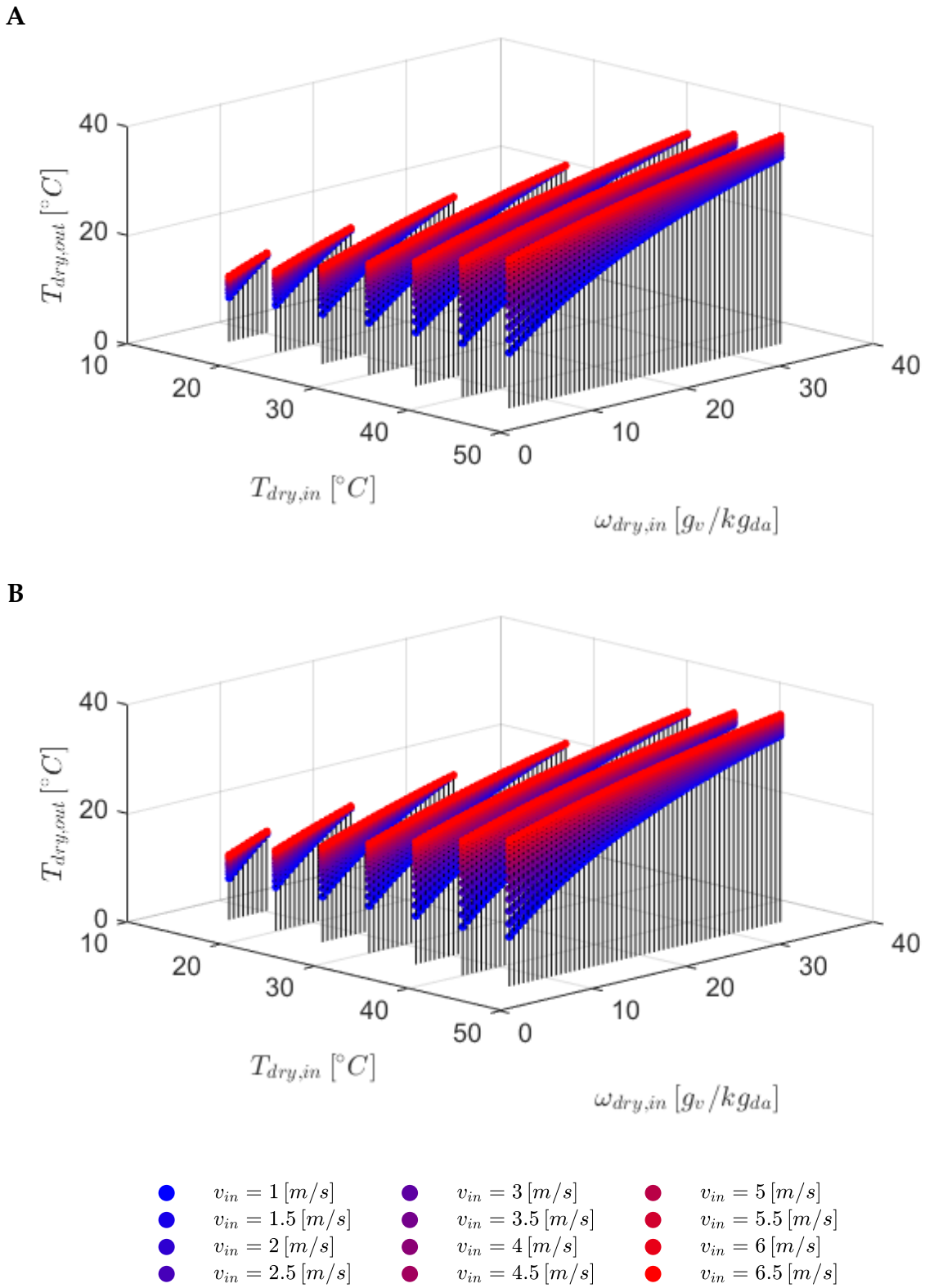

Figure A.3. Product temperature for an M-cycle HMX with a length of 0.2 m *and a channel height of* 2 mm*, obtained using the Hasan model, as a function of inlet dry-bulb temperature, inlet specific humidity, and inlet fluid velocity for recirculation ratio of* 50 % *(A) and* 60 % *(B).*

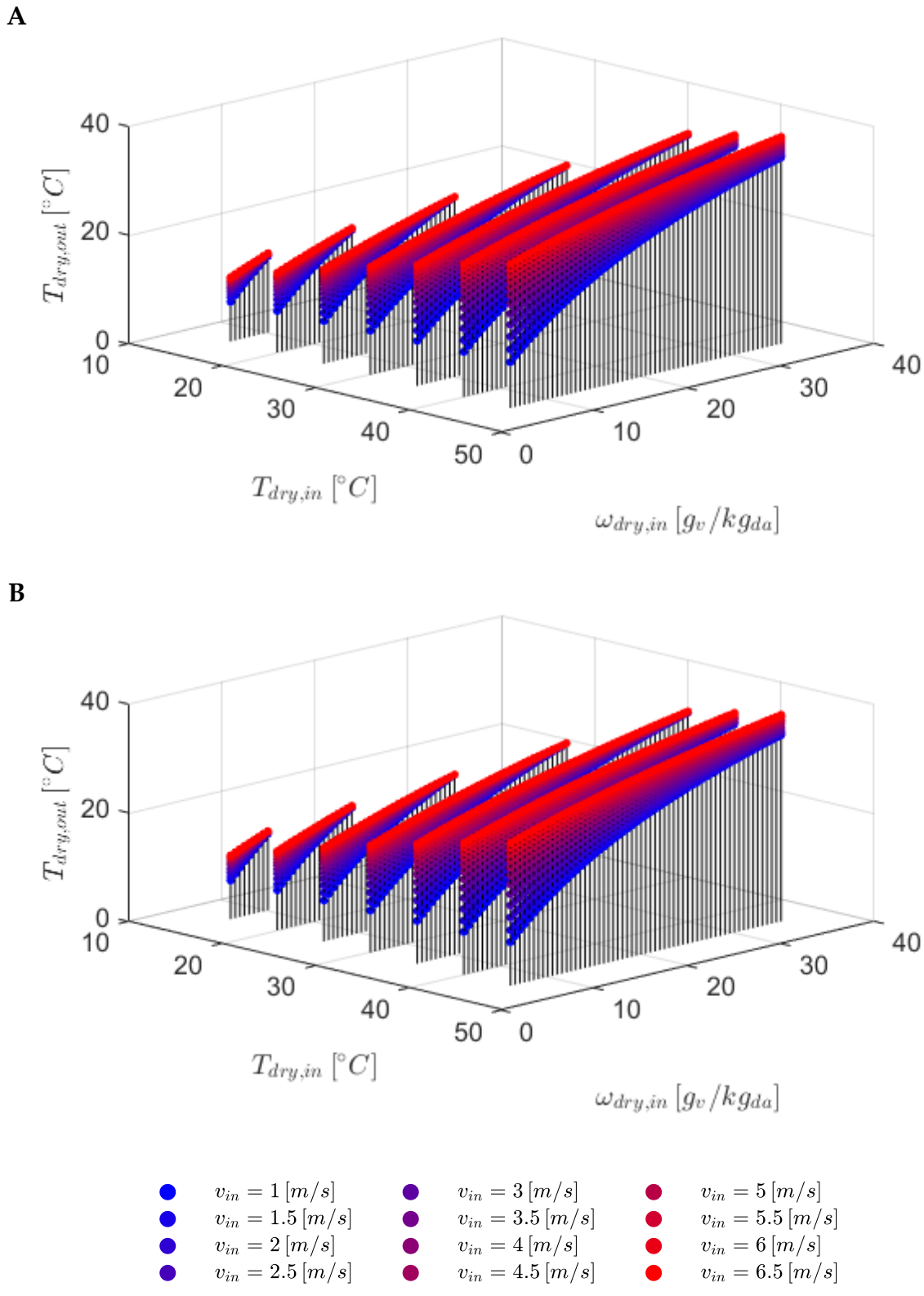

Figure A.4. Product temperature for an M-cycle HMX with a length of 0.2 m *and a channel height of* 2 mm*, obtained using the Hasan model, as a function of inlet dry-bulb temperature, inlet specific humidity, and inlet fluid velocity for recirculation ratio of* 70 % *(A) and* 80 % *(B).*

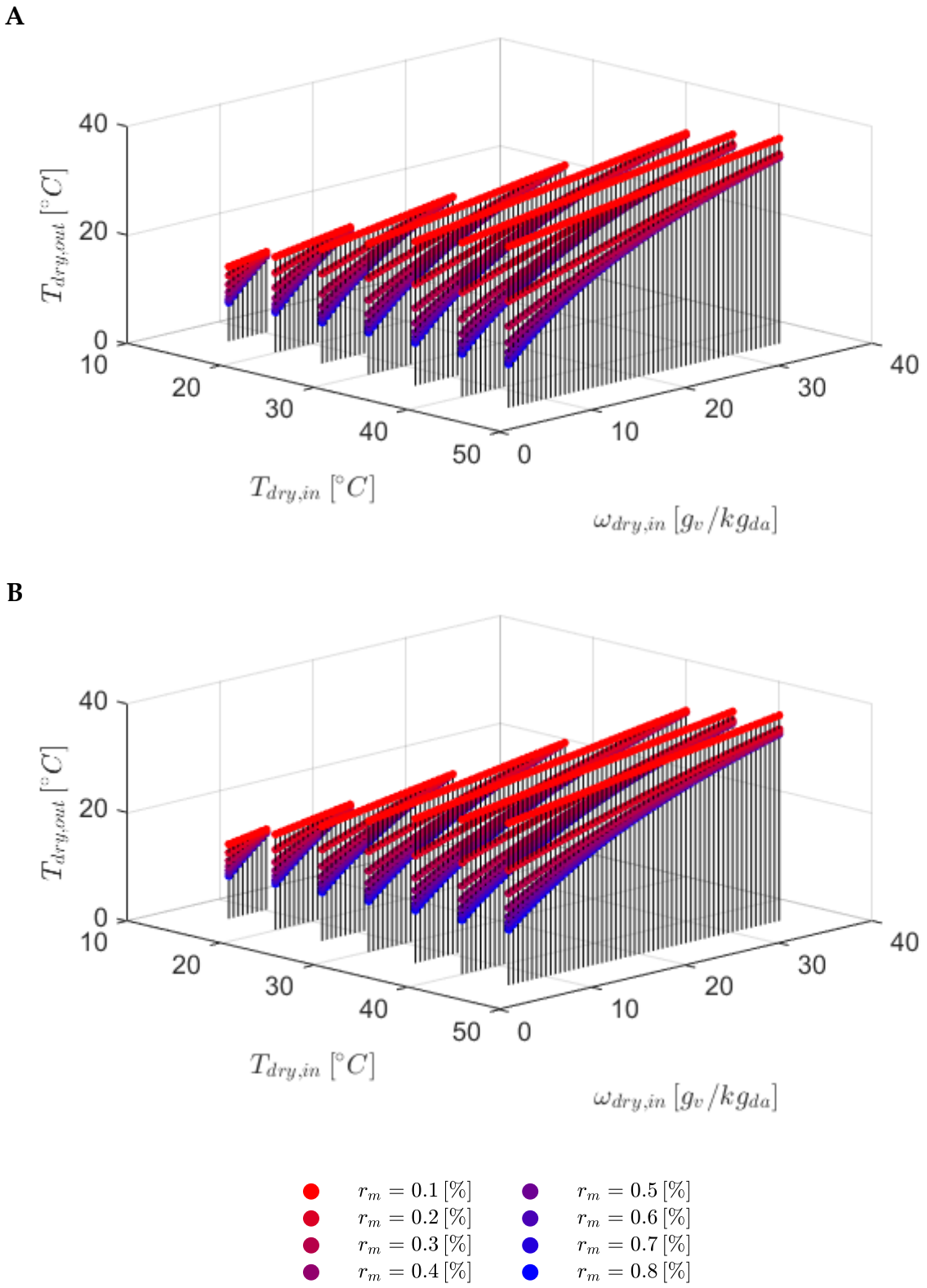

Figure A.5. Product temperature for an M-cycle HMX with a length of 0.2 m *and a channel height of* 2 mm*, obtained using the Hasan model, as a function of inlet dry-bulb temperature, inlet specific humidity, and recirculation ratio for inlet fluid velocities of* 10 m/s *(A) and* 15 m/s *(B).*

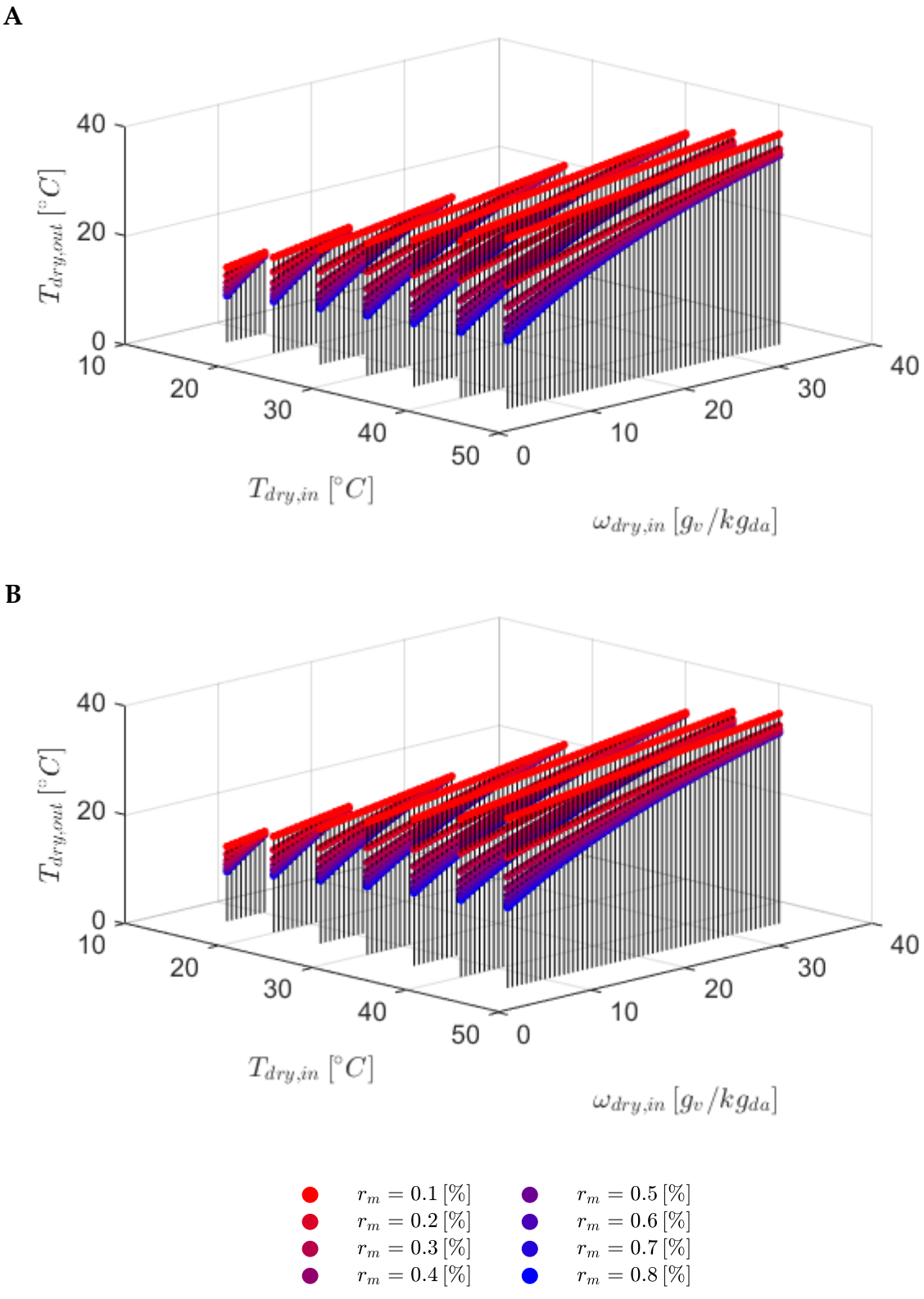

Figure A.6. Product temperature for an M-cycle HMX with a length of 0.2 m *and a channel height of* 2 mm*, obtained using the Hasan model, as a function of inlet dry-bulb temperature, inlet specific humidity, and recirculation ratio for inlet fluid velocities of* 20 m/s *(A) and* 25 m/s *(B).*

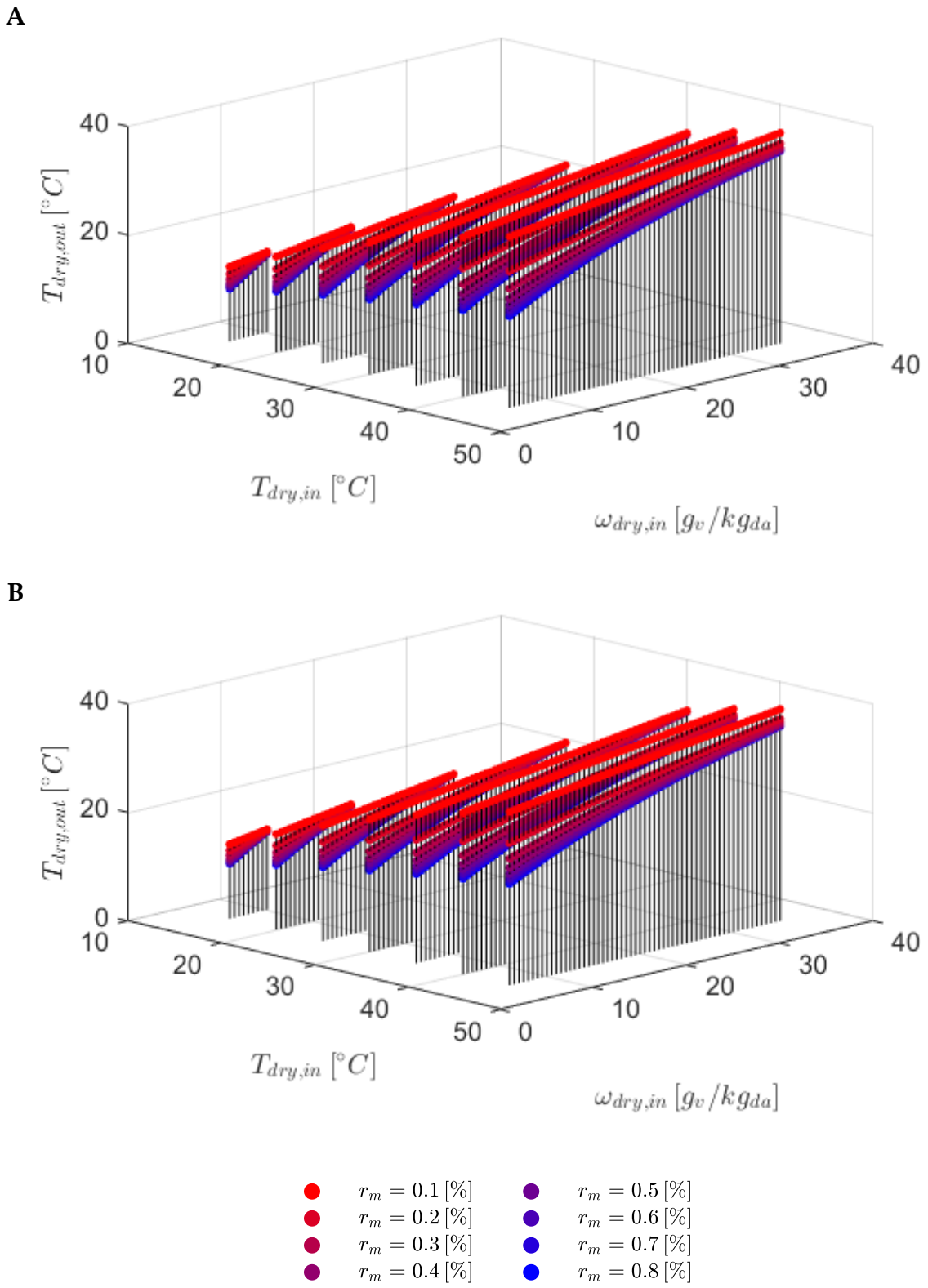

Figure A.7. Product temperature for an M-cycle HMX with a length of 0.2 m *and a channel height of* 2 mm*, obtained using the Hasan model, as a function of inlet dry-bulb temperature, inlet specific humidity, and recirculation ratio for inlet fluid velocities of* 30 m/s *(A) and* 35 m/s *(B).*

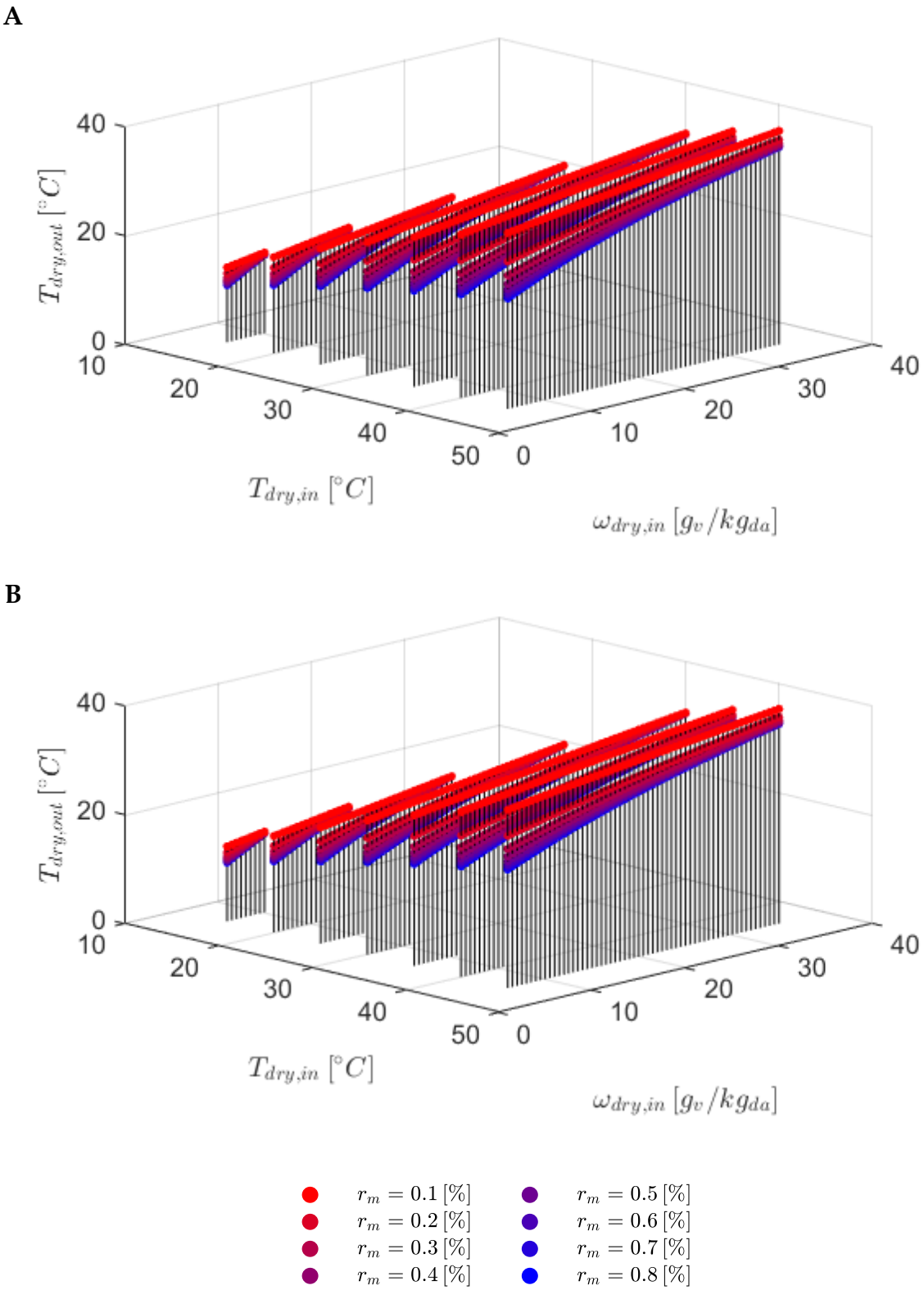

Figure A.8. Product temperature for an M-cycle HMX with a length of 0.2 m *and a channel height of* 2 mm*, obtained using the Hasan model, as a function of inlet dry-bulb temperature, inlet specific humidity, and recirculation ratio for inlet fluid velocities of* 40 m/s *(A) and* 45 m/s *(B).*

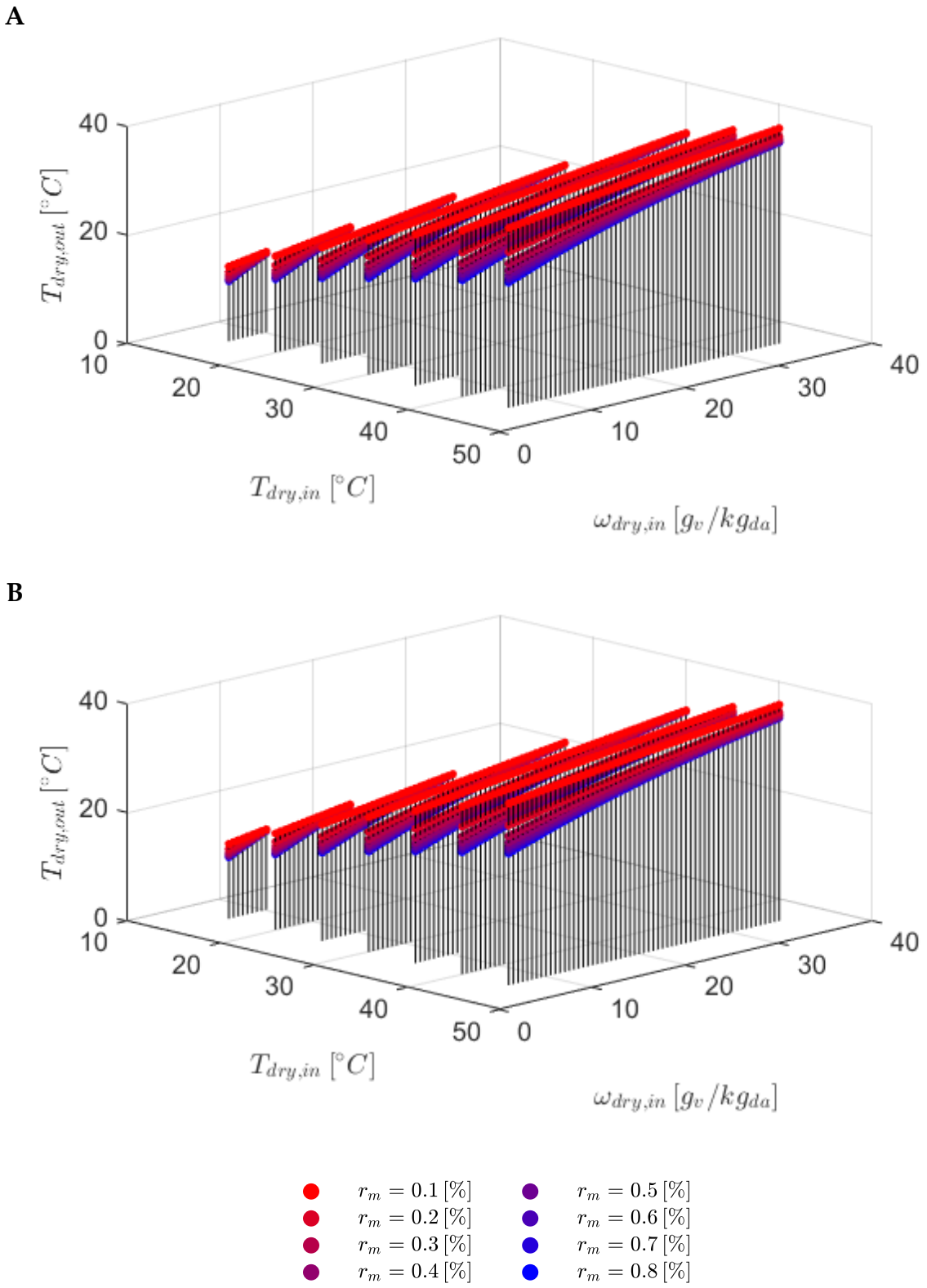

Figure A.9. Product temperature for an M-cycle HMX with a length of 0.2 m *and a channel height of* 2 mm*, obtained using the Hasan model, as a function of inlet dry-bulb temperature, inlet specific humidity, and recirculation ratio for inlet fluid velocities of* 50 m/s *(A) and* 55 m/s *(B).*

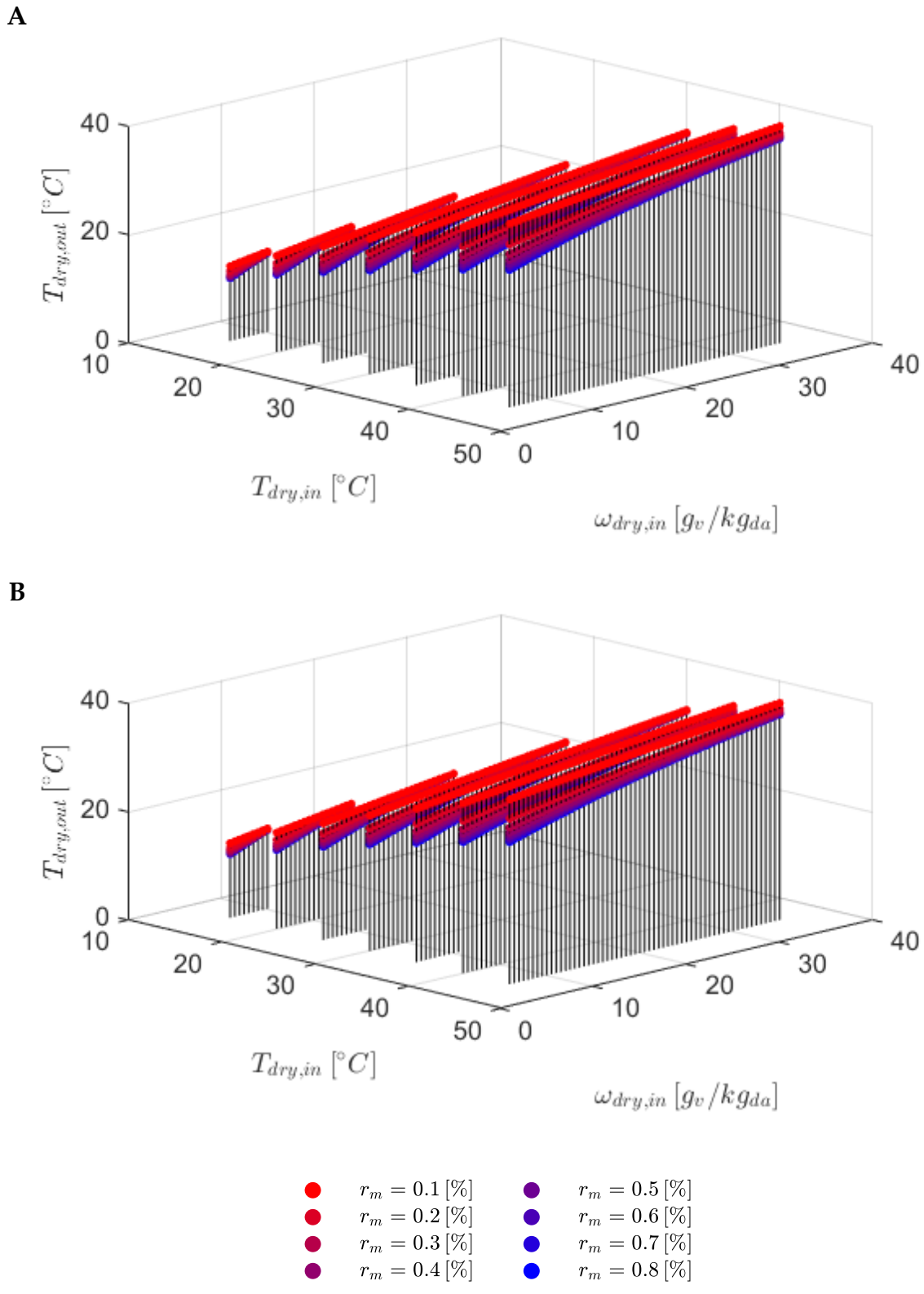

Figure A.10. Product temperature for an M-cycle HMX with a length of 0.2 m *and a channel height of* 2 mm*, obtained using the Hasan model, as a function of inlet dry-bulb temperature, inlet specific humidity, and recirculation ratio for inlet fluid velocities of* 60 m/s *(A) and* 65 m/s *(B).*